UNIVERSITÉ DE STRASBOURG

ÉCOLE DOCTORALE DE PHYSIQUE ET CHIMIE PHYSIQUE

INSTITUT PLURIDISCIPLINAIRE HUBERT CURIEN

UMR 7178 CNRS/IN2P3

THÈSE présentée par :

Bartolomeo DE CANDITIIS

soutenue le : **24 Juin 2020**

pour obtenir le grade de : **Docteur de l'université de Strasbourg**

Discipline/ Spécialité : physique

Caractérisation 3D de détecteurs germanium hyper purs multi-segmentés – Simulation et validation de la technique de PSCS et son application à diverses énergies gamma à l'aide d'une source de ^{152}Eu

3D characterization of multi-segmented HPGe detectors - Simulation and validation of the PSCS technique and its application for different energies with a ^{152}Eu source

THÈSE dirigée par :

Monsieur DUCHÊNE GIlbert	Directeur de recherches, Institut Pluridisciplinaire Hubert Curien

RAPPORTEURS :

Monsieur GERL Jurgen	Docteur, GSI Helmholtzzentrum für Schwerionenforschung GmbH
Madame LOPEZ MARTENS Araceli	Directrice de recherches, Laboratoire de Physique des deux Infinis Iréne Joliot-Curie

---

AUTRES MEMBRES DU JURY :

Madame COURTIN Sandrine	Professeur, Institut Pluridisciplinaire Hubert Curien
Monsieur FINCK Christian	Chargé de recherches, Institut Pluridisciplinaire Hubert Curien
Monsieur LJUNGVALL Joa	Chargé de recherches, Laboratoire de Physique des deux Infinis Iréne Joliot-Curie
Monsieur MARIAN Vlad	Ingénieur, MIRION Technologies

Acknowledgments

This work has been supported by

- ◇ the MIRION Technologies Canberra Company under the contract N°152521,
- ◇ the OASIS ANR grant under the contract ANR-17-CE31-0026-02.

I'd like to thank Gilbert Duchêne for guiding me through this PhD. Thanks also to Benoit Pirard from MIRION Technologies Canberra for the founding provided for the project.

Many thanks to Araceli Lopez-Martens, Jurgen Gerl, Christian Fink, Sandrine Curtin and Joa Ljungvall for reading this document and providing constructive feedback.

This work would not have been possible without the precious help of the Strasbourg AGATA group, so a special thanks goes to Marie-Hélène Sigward, Kseniia Rezynkina, François Didierjean and Michel Filliger.

A great thank you goes to Michael Ginsz, Vlad Marian, Damian Ralet and all the people from MIRION Technologies Canberra for their support for this work and during my great time spent at the company production site.

Thanks to the people of the AGATA collaboration for the ideas and suggestions provided during the collaboration meetings. In particular, thanks to the OASIS group for the economical support to the upgrade of the scanning table. Also, many thanks to Herbert Hess for the test box used for the response function measurement and for the precious advice given. Finally, thanks to Andy Boston, Joa Ljungvall, Fraser Holloway, Marco Siciliano and Rouven Hirsch for the great feedback and inputs supplied.

I would like to thank Benoît Gall, Louise Stuttgé, Dominique Curien, Olivier Dorvaux, Christelle Schmitt, Mohamad Moukaddam, Kamila Sieja and Frederic Nowacki, members of the DNE group and colleagues "from the corridor", for the support given during these years in the form of chats, "pots", and of course ideas.

Almost four years of PhD would not have been possible without all the beers and moments shared with all my friends.

Thanks to my Strasbourg friends. Irene and Mateo, for your loud laughs echoing in the corridor and the stupid jokes. Daniel and Nico, for all the afternoons spent with Nico's fancy cocktails and with Daniel's "special treats" while listening music. Douja, Julie and Loris, for standing my randomness moments. Sviat, Rodrigo, Marketa, Reem, Feifei, Guillaume, Alex, Dylan, Jean, Robin, Clément, for all the beers, the games and the cool moments.

A huge thanks to my "Italian" Strasbourg friends. Federica, Fabiana, Annabella, Daniela, Giovanni, Nicla, Michele, Federico, Debora, Valentina, Margherita, for all the "sunday lunches", fried eggplants, promenades, "medaglia d'oro" wines and cheerful laughs. A special mention goes to Fabiana for the too-long-to-do-a-list lovely things she provides me with.

A fuzzy thanks to Federico and Swapnesh "Schweppes", members of the "Deploy the Cowcatcher", for all the time spent in the rehearsal room and the moments shared together on the stage playing very noisy stoner rock. I hope to step on the stage together again soon.

Thanks to my childhood and high-school friends for being always there every time I go back "home". Marianna, my "newfound" friend (ma che cunferenza s'ha pigliato 'o tiempo a ce vede' spartute). Felice, Nicola, Mario, Antonio and the other Antonio for all the time we messed around since we were kids. Salvo, Ciccio, Nando, Davide, Simone, Stefano, Umberto, Pasquale and Michele for the trips and holidays, the rugby games, the "fantacalci", the fishing sessions, the "stuzzicheria secca" and the five-a-side football games.

Thanks to my friends from the university of Naples. Chiara, Teresa, Roberta, Michela, Ciro, Federico, Alessandro, Simone, even if we are scattered around Europe we always manage to keep in touch and hang around. To Marta for the amazing concerts we attended together and the trekking in the Schwarzwald. To Daniele, Alessandro, Giusj and Magda for the time spent together in the EDEN lab in Naples.

Finally the biggest thanks goes to my family. To my brother Diego and especially to my mother Alba who through all the difficulties managed to support me up to this point.

Contents

Introduction

Despite the knowledge collected in more than one century of research, the descriptive and predictive power of nuclear physics models is wide but still limited. The nuclear structure can't be yet described by a single universal model but it is instead described by a variety of models that fit the data more or less well depending in which part of the chart of the nuclides the nucleus of interest is located. In addition, the predictions of the different models diverge more significantly when approaching the proton and neutron drip lines. Obviously, new data are required in order to improve the actual models and modern nuclear physics looks with particular interest to the study of nuclei under extreme conditions such as large atomic number, very large angular momentum, very neutron rich or deficient isotopes and high temperatures. Such nuclei are produced in a variety of reactions such as fusion-evaporation, fusion-fission, multi-nucleon transfer, nucleon transfer, knock-out, Coulomb excitation, etc... where the nucleus is produced in an excited state that decays finally by gamma-ray emission. The latter gives information on the structure of the residual nucleus as its level scheme can be build through gamma-ray spectroscopy. Generally, the production rates of these nuclei is several orders of magnitude smaller with respect to reactions in which stable nuclei are produced. Moreover, they are produced in large background conditions and generally at much larger recoil velocities. This calls for development, construction and exploitation of state of the art gamma-ray detectors in order to maximize the quality of the information obtainable in an experimental run.

The development of techniques for the production of GeLi detectors [1, 2] in the 1960s allowed for the building of progressively thicker planar detectors (with relative efficiencies of few percents). These GeLi detectors marked the birth of high-resolution gamma-ray spectroscopy but had the disadvantage of having long production times and the fact that they needed to be constantly maintained at low temperatures. The first high purity germanium (HPGe) detectors, developed in Berkley [3, 4] and put on the market in the late 1970s, solved both the issues. The size of these detectors grew during the following decades reaching, for a cylindrical geometry (diameter $\times$ lenght), $50\,mm \times 50\,mm$ during the 1980s, $70\,mm \times 70\,mm$ at the beginning of the 1990s up to $80\,mm \times 90\,mm$ in the current days. The size increase meant a better photopeak detection efficiency of the germanium crystals. In parallel, during the mid 1970s, the first Compton shields, composed by NaI(Tl) scintillators [5, 6], were developed, pushing further the progress in gamma-ray spectroscopy. These shields, surrounding the HPGe detector, reduced the Compton background but because of their large size ($25\,cm \times 20\,cm$) an array could be

composed of only few shielded germanium crystals. It was at the beginning of the 1980s that the first BGO scintillator detectors were used as Compton shields, implemented in HERA (high energy resolution array) at the Berkley National Laboratory [7, 8]. BGO detectors are about three times more efficient per interaction length than NaI(Tl) detectors. Thus the shield size could be reduced and this allowed for the allocation of more germanium detectors into the array. Moreover HERA used the newly developed n-type coaxial detectors with $\sim 25\%$ relative efficiency[1]. These new technologies prompted during the 1980s the building of several national arrays in Canada, Denmark, France, Germany, Italy, UK, and USA. As the price of the new larger detectors rose quickly, the late 1980s and the beginning of the 1990s saw the first international efforts to build large 4π arrays of shielded germanium detectors resulting in ESSA30, EUROGAM I and GASP in Europe and GAMMASPHERE in USA [9, 10, 11, 12]. These arrays were composed of large germanium crystals with relative efficiencies of $\sim 70\%$. The next major improvement at the beginning of the 1990s consists in the assembly of four germanium detectors compacted in a single cryostat [13], each one with a relative efficiency of $\sim 21\%$ at $1332.5\,keV$ ([2]). The use of this new technology brought EUROGAM II in which 2 rings composed of 12 such detectors were added around 90° with respect to the beam axis. This configuration granted substantial improvement for Doppler correction and allowed the measurement of linear polarization of gamma rays. In the mid 1990s, a new detector encapsulation technology was developed by IKP Cologne in collaboration with Eurisys Mesures (today MIRION Technologies). The detectors could be encased under ultra-vacuum in thin sealed aluminum canisters [14]. This compact design was used to build EUROBALL [15, 16, 17], a new European array in operation from 1996 to 2003. The backward 1π of the array was paved by 15 cluster detectors each composed by 7 large volume crystals (with a relative efficiency of $\sim 60\%$) each in a single cryostat, surrounded by BGO shields. The first electric segmentation of coaxial crystals was developed at the end of the 1990s. The technique was first used on some of the GAMMASPHERE detectors (placed around 90° with respect to the beam axis) which were segmented in two longitudinal sectors. This allowed reduced detector angular aperture and increased the granularity of the array. The segmentation technology continued to progress and at the beginning of the 2000s, IKP and MIRION developed new 6-fold longitudinally segmented detectors which composed the MINIBALL array [18, 19]. These detectors were later further segmented in a 2-fold transversal fashion (reaching 12 segments per detector). MINIBALL was one of the first segmented detector array to be used in a radioactive ion facility (REX-ISOLDE at CERN) together with EXOGAM (SPIRAL in GANIL) and SeGa (at NSCL)[20, 21].

The concept of an array without Compton shield arose in the mid 1990s on both sides of Atlantic ocean and developments of prototypes for a proof of concept were performed up to 2001. The success of this *R&D* lead to the launch of the AGATA (Advanced

[1] For a given detector, the relative efficiency is defined as the ratio of its absolute efficiency at $1332.5\,keV$ when irradiated by a ^{60}Co source placed at $25\,cm$ from the center of the detector front face, to the efficiency of a 3" × 3" NaI irradiated in the same conditions (this reference value is $1.244 \cdot 10^{-3}$).

[2] In case of multiple crystals fired simultaneously, the energies released in such crystals are added up (add-back mode) and a total relative efficiency of up to 130% can be reached for one clover detector.

GAmma Tracking Array) collaboration in 2003 and of the GRETA (Gamma-Ray Energy Tracking Array) collaboration a bit earlier [22, 23]. The main feature of these two arrays is the ability to reconstruct the history of the interactions of a gamma ray interacting in the array (tracking), which is possible thanks to a dedicated tracking algorithm. This implies two main perks. The first one is that the tracking makes obsolete the use of Compton shields, which occupy a sizable portion of the solid angle, increasing the geometrical efficiency of germanium by typically a factor 2 relatively to EUROBALL and GAMMASPHERE. Note that the add-back of energies released by one gamma ray in different crystals leads to an additional gain factor of almost 2. The efficiency of such a tracking array is therefore about a factor 4 larger than the arrays of precedent generation at gamma-ray multiplicity 1. The second one is that the reconstruction of trajectories allows a precise determination of the first interaction point which leads to a substantial improvement of the Doppler correction. The knowledge of the second interaction point enables, in addition, to extract the linear polarization of the gamma rays useful for the determination of the parity of the nuclear states studied.

In order to reconstruct an event, the tracking algorithm needs as input the positions of each interaction of the gamma ray. These are determined with a pulse shape analysis (PSA) algorithm. For a given interaction, the algorithm compares the associated pulse shape with a database of calculated pulse shapes associated with spatial coordinates within the volume of the detector. Presently, databases of pulse shapes can be calculated via software leading to good tracking performances, although calculations don't take properly into account some characteristics of the detectors which are difficult to implement or not known, such as the real impurity distribution and the thickness of dead layers (passivated surface and Li diffused contact). A novel approach to database construction is the execution of full volume characterization of the detectors via three-dimensional gamma-ray beam scans. These measurements are realized with dedicated tools called scanning tables.

A scanning table is based at the IPHC laboratory of Strasbourg and is realized within the framework of the AGATA collaboration. This scanning table is designed to perform three-dimensional scans with a good spatial resolution, large amount of scanned points and short running times. The table exploits the Pulse Shape Comparison Scan (PSCS) technique that allows the reconstruction of a database by comparing two datasets of pulses. The two datasets are obtained by performing, with a collimated ^{137}Cs source, two two-dimensional scans in which the detector is oriented in two different directions perpendicular to each other (eg. vertical and horizontal orientations).

The scanning table was already tested in precedent works [24, 25], showing good performances although no systematic study of its characteristics by the means of Monte Carlo simulations was never performed. In this light, a part of the work presented in this thesis aims to quantify the characteristics of the PSCS technique implemented by the Strasbourg scanning table. The whole scanning procedure is recreated with Monte Carlo simulations and the data obtained are analyzed with the same algorithms used for the real measurements. Two different detector geometries are tested: a planar pixelated detector and an AGATA detector unit (tapered coaxial geometry).

Recently, the scanning table received several improvements which open new perspec-

tives. In particular, the collimator diameter can now be chosen among three different options ($1\,mm$, $0.5\,mm$ and $0.2\,mm$) and a ^{152}Eu source has been acquired. The latter allows to create databases of pulses with different energy ranges in a single scan procedure. This new feature is unique and was never tested within the scanning tables of the AGATA collaboration. The second part of this thesis presents the results obtained by several scans of an AGATA detector unit performed with ^{241}Am, ^{137}Cs and ^{152}Eu sources. In particular the main aim of the measurements is to prove that, by comparing the various databases with different energies obtained with the PSCS technique, the pulse shapes generated by a gamma ray interaction is independent from the interaction energy. This principle, which comes from theoretical assumptions, is at the base of the above mentioned PSA algorithms.

The present PhD document is structured as follows. In the first two chapters general knowledge on the interaction of gamma rays with the matter and on the functioning of germanium detectors are given. In the third chapter the AGATA array is presented along with the description of it's HPGe detector units. In the forth chapter the PSCS technique and the Strasbourg scanning table are described, together with some preliminary results of simulations and measurements of the gamma-ray beam irradiating from the collimated sources. In the fifth chapter details on the simulation methods and on the general analysis are provided. Chapter six describes the results of the simulation on the PSCS technique implemented for the IPHC scanning table. Simulations of both a planar and an AGATA detector unit are presented and several conclusions are drawn. Finally, chapter seven contains the results of real scans performed on an AGATA detector unit. Both two-dimensional and three-dimensional scans with the ^{241}Am, ^{137}Cs and ^{152}Eu sources are shown, analyzed and compared, and several conclusions are drawn and perspectives are suggested.

Chapter 1

Interaction of gamma rays with matter

Gamma rays interact with matter through several mechanisms, although only three major ones play an important role for detection purposes: *photoelectric absorption* (or *photoelectric effect*), *Compton scattering* and *pair production*. Photoelectric absorption dominates at low energy for gamma rays with up to few hundred keV, while pair production predominates at high energies (above 5 — 10 MeV). In the range between this two

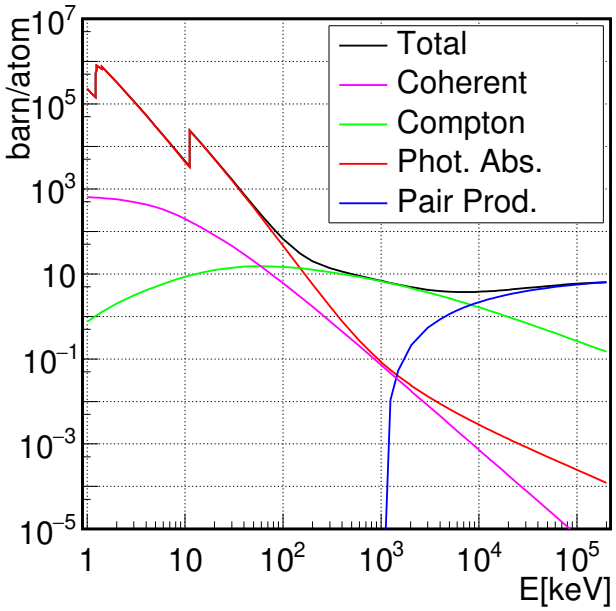

Figure 1.1: Photon absorption cross section for germanium with the various contributions to the total cross section. Data from [26].

energy limits Compton effect is the most probable mechanism (see figure 1.1). Atomic number Z of the interaction medium also has a strong influence on the relative probabilities of these three interactions; for example, photoelectric absorption probability varies approximately as $Z^{4.5}$. All of these processes, as it will be shown, lead to the partial or complete transfer of the photon energy to one electron, which lead to two features: gamma rays are many times more penetrating in matter than charged particles with the same energy and beams of photons are not degraded in energy as they pass through the matter, but only attenuated in intensity. The first feature is due to the much smaller cross section of the interaction processes relative to the inelastic electron collision cross section that characterizes charged particles. The second feature, however, is due to the fact that the described processes remove the photon from the beam entirely, either by absorption or scattering, while the photons which pass straight through are those which have not suffered any interaction at all. Detection of gamma rays is therefore critically dependent on the mechanism causing transfer of all or part of the photon energy to an electron in the absorbing material. In the present chapter the interaction mechanism listed previously will be briefly reviewed along with the respective expected response of a generic gamma-ray detector.

1.1 Photoelectric absorption

Photoelectric absorption is an interaction in which an incident gamma ray interacts with an absorber atom disappearing completely. In its place, an energetic *photoelectron* is produced from one of the electron shells of the absorber atom with a kinetic energy given by the incident photon energy $h\nu$ minus the binding energy of the electron in its original shell (E_b) as shown in the figure 1.2. The interaction is with the atom as a whole and cannot take place with free electrons; as result of conservation laws, the atom recoils in this process, but its recoil energy is very small and usually neglected.

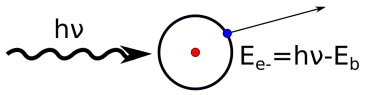

Figure 1.2: Simple photoelectric effect scheme.

For typical gamma-ray energies, the photoelectron is most likely to emerge from the K shell, for which typical binding energies range from a few keV for low-Z materials to tens of keV for materials with higher atomic number. The interacting atom is left in an excited state. It inherits a surplus of energy equal to the binding energy of the expelled electron. It will then return this energy by emitting characteristic X-rays due to the rearrangement of its structure, were higher shells electrons fill the vacancies in the lower shells. These X-rays will be generally reabsorbed through new photoelectric interactions. If the electron and the X-ray are detected, then the sum of their energy is equal to the original energy of the incident gamma ray.

The photoelectric process is predominant for gamma rays of relatively low energy, typically below $130\,keV$ for Ge (figure 1.1). The process is also enhanced for absorber materials of high atomic number Z. No analytic expression is valid for the probability of photoelectric absorption per atom (τ) over all ranges of E_γ and Z, but a rough approximation is

$$\tau \cong const. \times \frac{Z^n}{E_\gamma^{3.5}}$$

where the exponent n varies between 4 and 5 over the gamma-ray energy region of interest.

1.2 Compton scattering

The interaction process of Compton scattering takes place when a gamma ray strikes a weakly bound electron in the absorbing material. The result of the interaction is the creation of a recoil electron and a scattered gamma ray, with the division of energy between the two dependent on the scattering angle (figure 1.3). The energy $h\nu'$ of the scattered gamma ray in terms of its scattering angle θ is given by

$$h\nu' = \frac{h\nu}{1 + (h\nu/m_0c^2)(1 - cos\,\theta)} \tag{1.1}$$

where m_0c^2 is the mass energy at rest of the electron ($0.511\,MeV$). The kinetic energy of the recoil electron is therefore

$$E_{e^-} = h\nu - h\nu' = h\nu \left(\frac{(h\nu/m_0c^2)(1 - cos\,\theta)}{1 + (h\nu/m_0c^2)(1 - cos\,\theta)} \right) \tag{1.2}$$

Two extreme cases can be identified when $\theta \approx 0$ and $\theta \approx \pi$. In the first case equations 1.1 and 1.2 predict that $h\nu \approx h\nu'$ and $E_{e^-} \approx 0$, meaning the Compton electron has very little energy and the scattered gamma ray has nearly the same energy as before the interaction. In the second case the gamma ray is subjected at a head on collision in which it is back scattered toward its direction of origin, whereas the electron recoils along the direction of incidence and maximum energy is transferred.

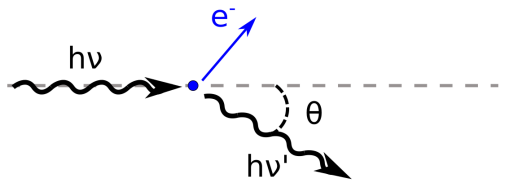

Figure 1.3: Simple Compton scattering effect scheme.

Between this two extreme cases, a continuum of energies can be transferred to the electron and for any specific gamma-ray energy the electron energy distribution has the

general shape shown in figure 1.4. The gap between the maximum Compton recoil-electron energy (called *Compton edge*) and the incident gamma-ray energy is given by

$$E_C = \frac{h\nu}{1 + 2h\nu/m_0c^2} \tag{1.3}$$

and in the limit that the incident gamma-ray energy is large ($h\nu \gg m_0c^2/2$) this difference tends to the constant value of $E_C \approx 0.256\,MeV$.

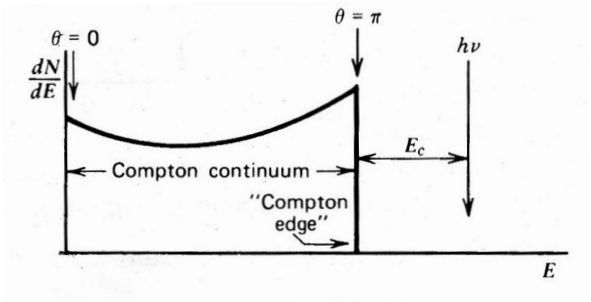

Figure 1.4: Compton scattering spectrum. A continuum of energies can be transferred to the electron within the interval $[0, \pi]$. The Compton edge corresponds to $\theta = \pi$. E_c is the energy difference between the actual incident gamma-ray energy and the Compton edge. From [27].

The cross section for Compton scattering was one of the first to be calculated using quantum electrodynamics and is known as the Klein-Nishina formula. For an unpolarized gamma ray it can be written as

$$\frac{d\sigma}{d\Omega} = Z\frac{r_e^2}{2}\frac{1}{[1+\gamma(1-cos\,\theta)]^2}\left(1 + cos^2\theta + \frac{\gamma^2(1-cos\,\theta)^2}{1+\gamma(1-cos\,\theta)}\right) \tag{1.4}$$

where r_e is the classical electron radius and $\gamma = h\nu/m_0c^2$. The distribution is shown graphically in fig. 1.5 and illustrates the strong tendency for forward scattering for large values of the gamma-ray energies ($E_\gamma \geq 511\,keV$).

1.2.1 Coherent scattering

Related to Compton scattering is the classical process of *Rayleigh scattering* where the photons are scattered by atoms as a whole. In this process, all the electrons in the atom participate in a coherent manner, thus the name *coherent scattering*. The scattering is characterized by the fact that no energy is transfered to the medium. The atoms are neither excited nor ionized and only the direction of the photon is changed. The probability of coherent scattering is significant only for low photon energies (typically below a few hundred keV for common materials).

1.3 Pair production

The process of pair production involves the transformation of a photon into a electron-proton pair. In order to conserve momentum, this can only occur in the presence of

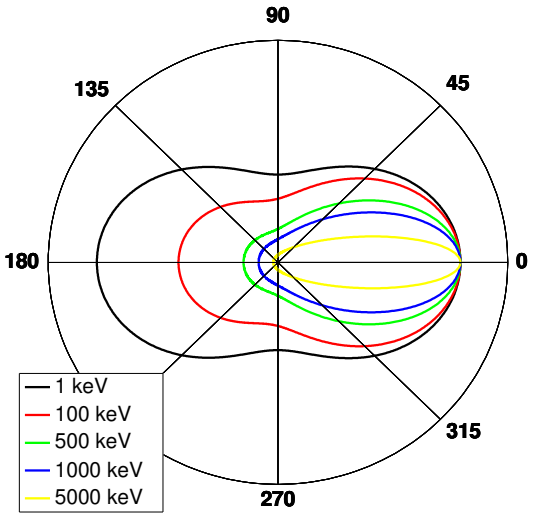

Figure 1.5: A polar plot of the number of gamma rays (incident from the left) Compton scattered into a unit solid angle at the scattering angle θ (in degrees).

the intense electric field of a target nucleus. To create an electron-positron pair, an energy of $2m_0c^2$ is required, thus the incident gamma ray must have at least an energy of $1.02\,MeV$ in order that the process is energetically possible. If the incident gamma ray exceeds this value, the excess energy appears in the form of kinetic energy E_{e^-} and E_{e^+} shared by the pair of particles. One has

$$E_{e^-} + E_{e^+} = h\nu - 2m_0c^2$$

The electron and the positron travel in the medium before loosing all their energy (a few millimeters for germanium). The shape of the distribution in energy from a monochromatic beam of gamma rays is then, again, a delta function whose peak is $2m_0c^2$ below the actual incident gamma-ray energy (as shown in figure 1.6). However,

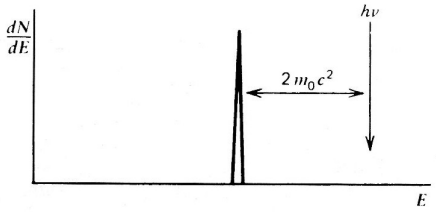

Figure 1.6: Schematic spectrum of pair-production event. The peak of the distribution (a delta function) is shifted by $2m_0c^2$ from the actual energy of the interacting gamma ray due to the energy required to create the electron-positron pair. From [27].

the pair-production process is complicated by the fact that the positron is not a stable

particle. Once it's kinetic energy becomes very low (thermal energy), the positron will annihilate or combine with an electron in the absorbing medium. The particles are then replaced by two annihilation photons of energy m_0c^2 ($0.511\,MeV$) each. The time required for the positron to slow down and annihilate is so that the annihilation radiation appears in virtual coincidence with the original pair-production interaction.

The magnitude of probability of pair production per nucleus varies approximately as the square of the absorber atomic number and it raises sharply with energy as indicated in figure 1.1. Finally figure 1.7 shows the relative importance of each of the three processes described above for different absorber materials and gamma-ray energies.

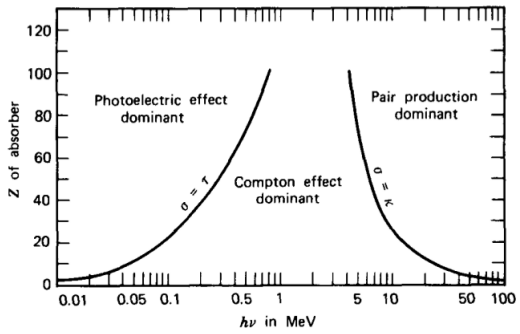

Figure 1.7: Relative importance of the three major types of gamma−ray interaction. The lines show the values of Z and $h\nu$ for which the occurrence probability of two neighboring effects are just equal. From [27].

1.4 Predicted response to gamma rays

If all the considerations done previously are taken into account, one can predict the response function for a typical, medium-sized, gamma-ray detector hit by a monochromatic beam. The possible outcomes of a gamma ray entering the detector are shown in figure 1.8. If the energy of a gamma ray of the incident beam is in the low or medium range (where pair production is not significant) the predicted spectrum will show a Compton continuum and a photopeak. The Compton continuum is populated by all those gamma rays that undergo single or multiple Compton scattering before escaping the detector. These gamma rays populate also the region between the photopeak and the Compton edge (see figure 1.4). The photopeak has contributions both from gamma rays that are absorbed by photoelectric absorption and from gamma rays that undergo multiple Compton scattering, losing energy at each interaction, before getting absorbed. The ratio between the two areas depends on the energy of the incident beam and the size of the detector. The lower the incident gamma-ray energy, the lower will be the average energy of a Compton scattered photon and the corresponding average distance of migration. Thus the probability for a gamma ray to get absorbed and the relative area under the photopeak increase with decreasing incident photon energy. At very low energies ($E < 100\,keV$) the Compton continuum may effectively disappear.

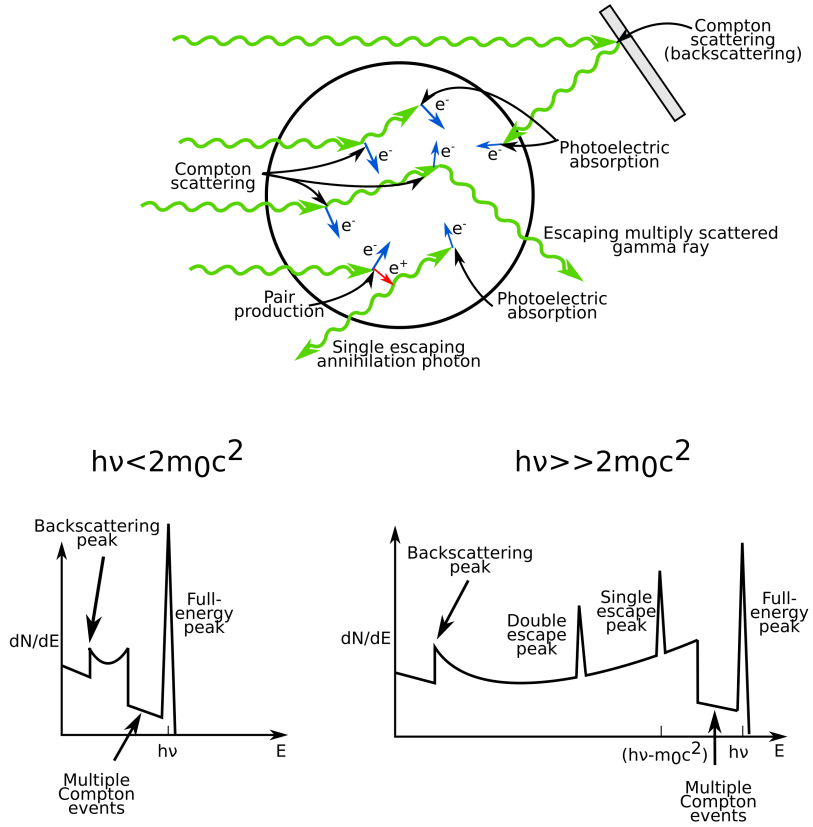

Figure 1.8: Possible gamma-ray interactions outcomes in a medium sized detector and respective predicted response function for low and medium-high energies.

If the gamma-ray energy is high enough to make pair production significant, a more complicated situation prevails. The annihilation photons may either escape or undergo further interactions within the detector. These additional interactions may lead to either partial or full-energy absorption of either one or both of the annihilation photons. If both annihilation photons escape without interaction, only the electron and positron kinetic energies are deposited. The net effect is to add a *double escape peak* to the spectrum located at an energy $2m_0c^2$ $(1.02\,MeV)$ below the photopeak. Another relatively frequent occurrence is the escaping of one annihilation photon while the other is totally absorbed. These events contribute to a *single escape peak*, which now appears in the spectrum at an energy m_0c^2 $(0.511\,MeV)$ below the photopeak. A continuous range of other possibilities exists in which one or both of the annihilation photons are partially converted to electron energy through Compton scattering and subsequent escape of the scattered photon. Such events accumulate in a broad continuum in the pulse height spectrum lying between the double escape peak and the photopeak.

As final remark one should note that the response function to be expected for a real

gamma-ray detector will depend on the size, shape and composition of the detector, and also the geometric details of the irradiation conditions. In general, the response function is too complicated to predict in detail other than through the use of Monte Carlo calculations, which simulate the histories actually taking place in a detector of the same size and composition.

1.5 Gamma-ray attenuation

As it was written in the introduction to this chapter, gamma rays are not degraded in energy as they pass through the matter, they get attenuated only in intensity. The sum of the probabilities of occurrence per unit path length that a gamma ray is removed from the beam hitting an absorber is called *linear attenuation coefficient*

$$\mu = \tau_{photoelectric} + \sigma_{Compton} + \kappa_{pair} \tag{1.5}$$

It corresponds to the inverse of the mean free path of the photon $\lambda = \frac{1}{\mu}$. The number of transmitted photons I with respect to the initial number of photons I_0 is then

$$\frac{I}{I_0} = e^{-\mu x} \tag{1.6}$$

where x is the length of matter passed through.

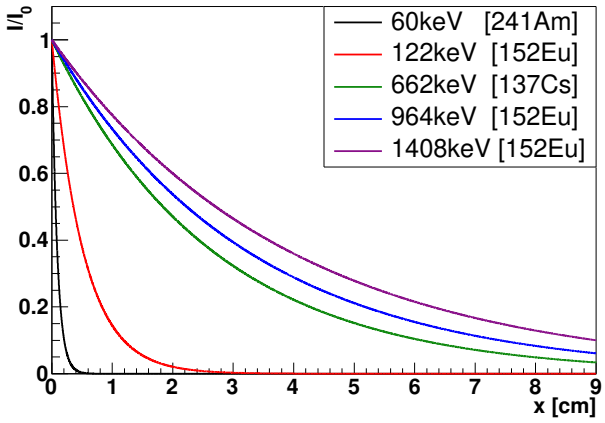

Figure 1.9: Transmission ratio of gamma rays in germanium as a function of the length of matter passed through for various energies. Data from [26].

As it will be shown later, the majority of the measurements done during the study presented here were performed using gamma-ray beams emitted by sources of ^{241}Am, ^{137}Cs and ^{152}Eu. For these sources the transmission ratios in germanium is shown in figure 1.9. The ^{241}Am gamma rays and the lowest energy gamma rays of the ^{152}Eu are absorbed by the first layers of germanium. This two sources can be used to study effects on the surface of the germanium detector. ^{137}Cs gamma ray and high energy

gamma rays of the ^{152}Eu, instead, can travel several cm into the germanium without interacting.

Chapter 2

Semiconductors and HPGe detectors

Semiconductor detectors, or solid-state detectors, are based on crystalline semiconductor materials, most notably silicon and germanium. Their operating principle consists in the fact that an ionizing radiation creates electron-hole pairs that are then moved under the effect of an electric field, generating a signal on the electrodes of the detector. Among the advantages of semiconductor detectors one can count the small energy required to create an electron-hole pair ($2.96\,eV$ in Germanium at the operational temperature of $77\,K$), a good energy resolution ($\sim 2\,keV$ FWHM at $1\,MeV$), the rather fast time response ($\sim 7\,ns$ response for ^{60}Co and rise times of ~ 150 to $400\,ns$) and their compact size. For these reasons semiconductor detectors are often chosen for high precision gamma-ray spectroscopy, especially germanium that is preferred to silicon for his higher Z which guaranties a larger interaction cross-section for gamma rays. The above mentioned advantages are counterbalanced by the fact that, being crystalline materials, they have a greater sensitivity to radiation damage which limits their long term use. Also, and this is true for germanium detectors, they operate at very low temperature (generally liquid nitrogen temperature, $77\,K$) which implies the usage and maintenance of an additional cryogenic system.

In the following chapter a brief review of semiconductor properties and operations will be presented. Germanium crystals will be used as main reference since they play a main role in the present work.

2.1 Band structure in semiconductors

The electrons of a perfect crystalline solid occupy the energy states in well established intervals called *allowed energy bands*. The energy bands are regions populated by many discrete levels so closely spaced that they can be considered as a continuum. The band structure arises from the overlapping of the electron wavefunctions caused by the close and periodic arrangement of the atoms of the crystal; since the Pauli principle forbids more than one electron in the same state, the degeneracy in the outer atomic shell energy

levels breaks to form many discrete levels slightly separated from each other. In between two allowed energy bands lay the *forbidden energy gap* which is a region in which levels are not available.

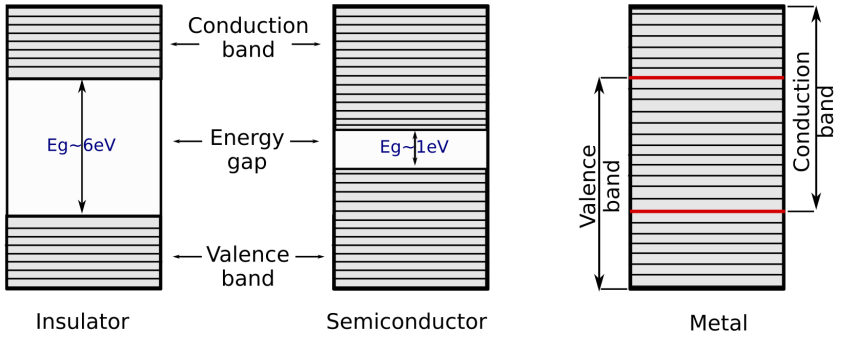

Figure 2.1: Band structure schemes for insulator, semiconductor and conductor materials.

A simplified version of the band structure is shown in figure 2.1. The lower band is called the *valence band* and corresponds to those outer-shell electrons that are bound to specific lattice sites within the crystal (covalent bonding electrons). The higher-lying band is called *conduction band* and represents electrons that are free to migrate through the crystal. The two bands are separated by the already mentioned forbidden energy gap, which size is determined by the lattice spacing between the atoms of the crystal, which also depends from external parameters such as temperature and pressure of the crystal.

The size of the energy gap determines whether the material is classified as an *insulator*, a *conductor* (*metal*) or a *semiconductor* (see figure 2.1). In an insulator at normal temperatures, all the electrons are in the valence band and the thermal energy is insufficient to excite electrons across the gap. When an external field is applied to the medium there is no movement of electrons and thus no current. For a conductor, on the contrary, there is no gap between the two bands. The thermally excited electrons can jump easily in the conduction band where they are free to move in the crystal. When an electric field is applied a current flows through the medium. Finally, in a semiconductor, the gap size is intermediate between the two above mentioned cases. At room temperature, electrons are excited into the conduction band by thermal energy and when an electric field is applied, a current can be observed[1]. If the semiconductor is cooled down, the electrons will fall into the valence band and the conductivity of the semiconductor will decrease.

[1] In some semiconductors devices a current can flow even without an external voltage. For example, it is the case of thin CMOS detectors, where the charges drift for a very short distance (few tens of microns).

2.2 Charge carriers

Germanium has four valence electrons, all participating in four covalent bonds. At a temperature of $0\,K$ all bonds are in the lowest energy state of the semiconductor (see figure 2.2a). At room temperature, however, a valence electron can pass to the conduction band by the action of the thermal energy. This event will leave a *hole* in the original position of the electron. At this point a neighboring valence electron can easily jump from its site to fill the hole, leaving another hole in its original position. If this process is repeated with another neighboring electron and so on, one can state that the hole is moving through the crystal. Since the hole is positive relative to the sea of negative electrons in the valence band, one can consider the hole as a positive *charge carrier*. In a semiconductor, thus, the electric current arises from two sources that are the movement of free electrons in the conduction band and the movement of holes in the valence band.

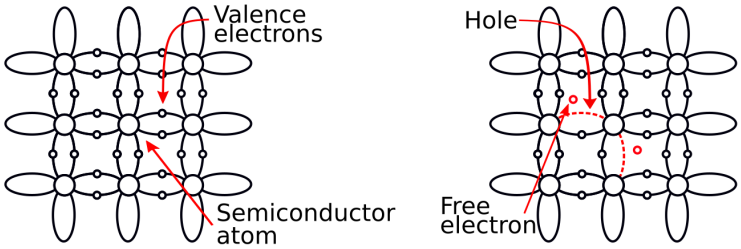

(a)

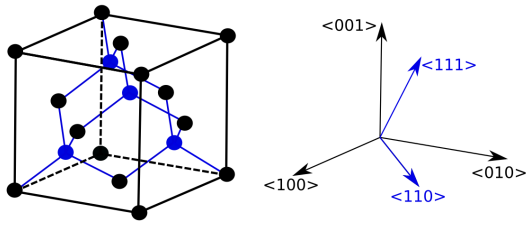

(b)

Figure 2.2: (a) Germanium (silicon) covalent bonding. On the left all the electrons participate to the bonding, on the right one bond due to thermal energy is freeing an electron and leaving a hole. (b) Germanium cubic diamond structure with the crystallographic axes.

Electron-hole pairs are constantly generated by thermal energy, while at the same time there are a certain number of them which recombine. Recombination happens when an electron drops from the conduction band to the valence band, emitting a photon in the process. The creation and recombination of pairs happens in dynamic equilibrium and the concentration of the electron-hole pairs remain stable. If n_i is the concentration

of electron (holes), T the temperature, E_g the energy gap at $0\,K$ and k the Boltzmann constant, then

$$n_i = AT^{3/2} exp\left(\frac{-E_g}{2kT}\right) \tag{2.1}$$

where A is a constant independent of the temperature. A typical value of n_i for germanium at $T = 300\,K$ is of the order of $2.5 \times 10^{13}\,cm^{-3}$ which, related to the density of the crystal of $10^{22}\,atoms/cm^3$, means that only 1 in 10^9 germanium atoms is ionized, leading to a very low concentration of charge carriers.

2.3 Charge mobility

If a low-to-moderate electric field is externally applied to the semiconductor, and the difference in temperature between electrons or holes and the lattice is not excessive, the *drift velocity* of the electrons and holes can be written as

$$\begin{aligned} v_e &= \mu_e \mathcal{E} \\ v_h &= \mu_h \mathcal{E} \end{aligned} \tag{2.2}$$

where $\mathcal{E}$ is the intensity of the electrical field and μ_e and μ_h are the *mobilities* of the electron and holes, respectively. For a given material, the velocities are function of $\mathcal{E}$ and the temperature T (see table 2.1). At moderate electric field values, the drift velocities v_e and v_h vary linearly with $\mathcal{E}$ (equation 2.2). At higher electric field values, v_e and v_h increase slower with $\mathcal{E}$. A *saturation velocity* may be reached at very high electric field (see figure 2.3a).

When the temperature of the charge carriers rises above the temperature of the lattice, the electron drift velocity will not be parallel to the applied electrical field but will be influenced and determined by the crystal lattice orientation. Germanium has a Face Centered Cubic (FCC) lattice structure and Cartesian coordinates can be used to define the lattice axes (or planes). In the figure 2.2b the three crystallographic axes $\langle 1,0,0\rangle$, $\langle 1,1,0\rangle$ and $\langle 1,1,1\rangle$ are shown. Along the three crystallographic directions

	Si	Ge
Dielectric Constant (relative)	12	16
Intrinsic Resistivity (300K) [Ωcm]	230000	45
Energy gap (300K) [eV]	1.115	0.665
Energy gap (0K) [eV]	1.165	0.746
Electron mobility (300K) [cm^2/Vs]	1350	3900
Hole mobility (300K) [cm^2/Vs]	480	1900
Electron mobility (77K) [cm^2/Vs]	$2.1 \cdot 10^4$	$3.6 \cdot 10^4$
Hole mobility (77K) [cm^2/Vs]	$1.1 \cdot 10^4$	$4.2 \cdot 10^4$
Pair creation energy (77K) [eV]	3.76	2.96

Table 2.1: Physical properties of silicon and germanium. From [28].

the mobility has to be always aligned with the electrical field due to the crystal lattice symmetry in germanium. Figure 2.3b shows the velocity of the charge carriers as a function of the electric field for the three crystallographic axes. One can observe that the main axis $\langle 1,0,0\rangle$ is the fastest while the $\langle 1,1,1\rangle$ axis is the slowest.

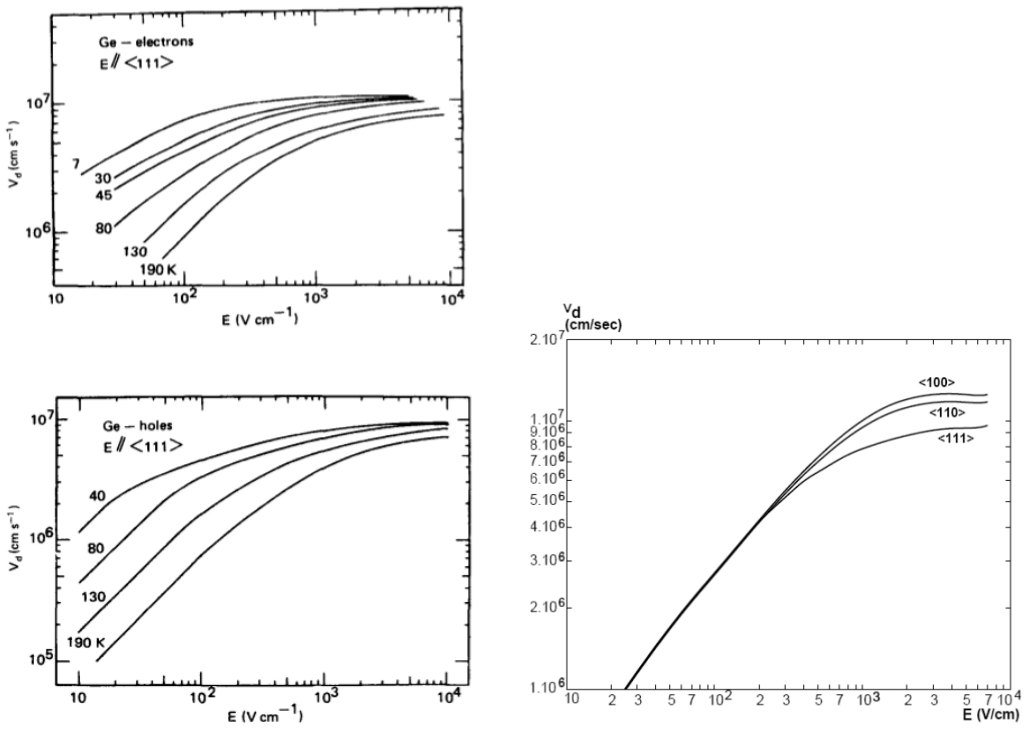

(a) (b)

Figure 2.3: (a)Drift velocity in germanium along axis $< 111 >$ as a function of the electrical field. From [27]. (b)Drift velocity in germanium along the three main crystallographic axes as a function of the electrical field. From [29] and references therein.

2.4 Impurities and doping of the crystal

In section 2.2 it was mentioned that electrons and holes can recombine. In a perfect crystal this process is very rare and electron-hole pairs show lifetimes of the order of seconds. However, experimentally it is shown that charge carrier have a lifetime ranging from nanoseconds to hundreds of microseconds. This means that impurities that work as *recombination centers* (or *trapping centers*) are present even in the purest of the crystals. These elements perturb the energy band structure by adding additional levels in the forbidden energy gap. These states can capture an electron (hole) from the conduction (valence) band and than one of the following things may happen: after a certain time the electron (hole) is released back in the conduction (valence) band or during holding

time the impurity captures a hole (electron) which annihilates with the trapped electron (hole). The presence of impurities reduces the mean time in which charge carriers remain free and thus some of the charges will be lost during charge collection. This worsen the energy resolution of the semiconductor which is a major problem for radiation detection.

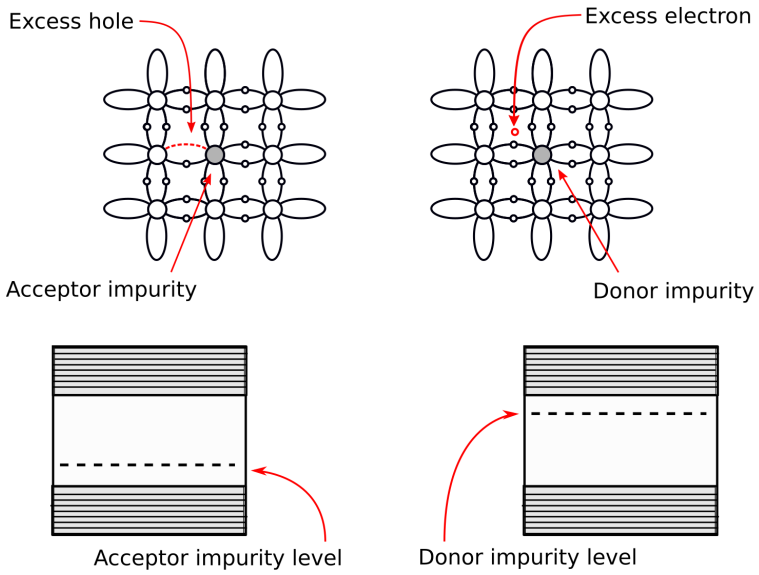

Figure 2.4: Scheme of donor and acceptor impurity levels induced in the energy bands by doping agents.

Nevertheless the addition of certain elements to pure semiconductors may also enhance the characteristics of the material. These elements, called *doping agent*, can change the electron-hole ratio in the conduction band. The characteristic of a *dopant* is that it possesses one more or one less valence electron than germanium in the outer atomic shell. When integrated into the crystal lattice it creates what are called *doped* or *extrinsic* semiconductors. The effect of the dopant is to add discrete levels that lay close to the *valence* or *conductive band* as shown in figure 2.4.

If the dopant is *pentavalent* (*donor dopant*), the electrons fill up the valence band and the extra electron, since there is no place to fit in the band, will reside in a discrete energy level located in the energy gap which is very close to the conduction band. Unlike a trapping state, this level will enhance the conductivity of the semiconductor because at normal temperatures an electron will be more easily excited into the conduction band. In these semiconductors, electrons are the primary charge carriers and they are called *n-type* semiconductors.

Vice versa, if the dopant is trivalent (*acceptor dopant*) there will be not enough electrons to fill the valence band and there will be an excess of holes in the crystal. Now the additional level will be placed close to the valence band and electrons will be easily excited into this level leaving extra holes behind. In these semiconductors, holes are the

primary charge carriers and they are called *p-type* semiconductors.

2.5 The pn semiconductor junction

If a semiconductor possesses one p-type region in contact with a n-type region a so called *pn junction* is formed. This special zone is created at the interface between the two materials (see figure 2.5) where the difference in concentration of electrons and holes between them generates a drift of electrons towards the p-region and a drift of holes towards the n-region. As a consequence the diffusing electrons fill up holes in the p-region while the diffusing holes capture electrons on the n-side. This recombination of charges causes a charge build-up to occur on either side of the junction; the p-region becomes negative while the n-region becomes positive. This creates an electric-field gradient across the junction which will eventually stops the diffusion process leaving a region of fixed space charge. The potential difference across the junction is called *contact potential* (which is generally of the order of $1\,V$).

The region of changing potential is known as *depletion zone* (*space charge region*). It is devoid of all the mobile charge carriers. This region is of particular interest for radiation detection because any electron or hole generated in this zone, say by an interacting gamma ray, will be dragged out by the electric field. If electrical contacts are placed on the end of the junctions, it is possible to collect the resulting current which intensity is proportional to the ionization (thus to the energy of the incident gamma ray).

However, the pn junction as described above does not work at its best. In fact, the intrinsic electric field is too weak to provide efficient charge collection and the depletion zone is too thin (of the order of few microns) to stop high energy particles. A third negative effect also arises from the fact that the small thickness present a large capacitance that interacts with the detector electronics generating noise on the output signals. A way to improve the junction is to apply a *reverse-bias voltage* to the junction, i.e. a negative voltage to the p-side, as shown in figure 2.6. This voltage will attract holes in the p-region and electrons in the n-region towards the contacts and far away from the junction. Consequently, the depletion zone will expand enlarging the sensitive volume for radiation detection.

The thickness of the depletion zone is given by the equation

$$d = \left(\frac{2\epsilon V}{eN}\right)^{1/2} \tag{2.3}$$

where V is the reverse bias voltage and N is the net impurity concentration in the bulk semiconductor material, ϵ is the dielectric constant and e is the electronic charge[2]. The maximum voltage that can be applied to the junction, however, is limited by the resistance of the semiconductor; once a threshold is crossed, the junction will breakdown and the semiconductor will behave as a conductor.

[2]In reality the depletion zone has soft edges. If this is taken into account, the exponent in equation 2.3 can be replaced with an empirical factor α that varies between 1/2 and 1/3.

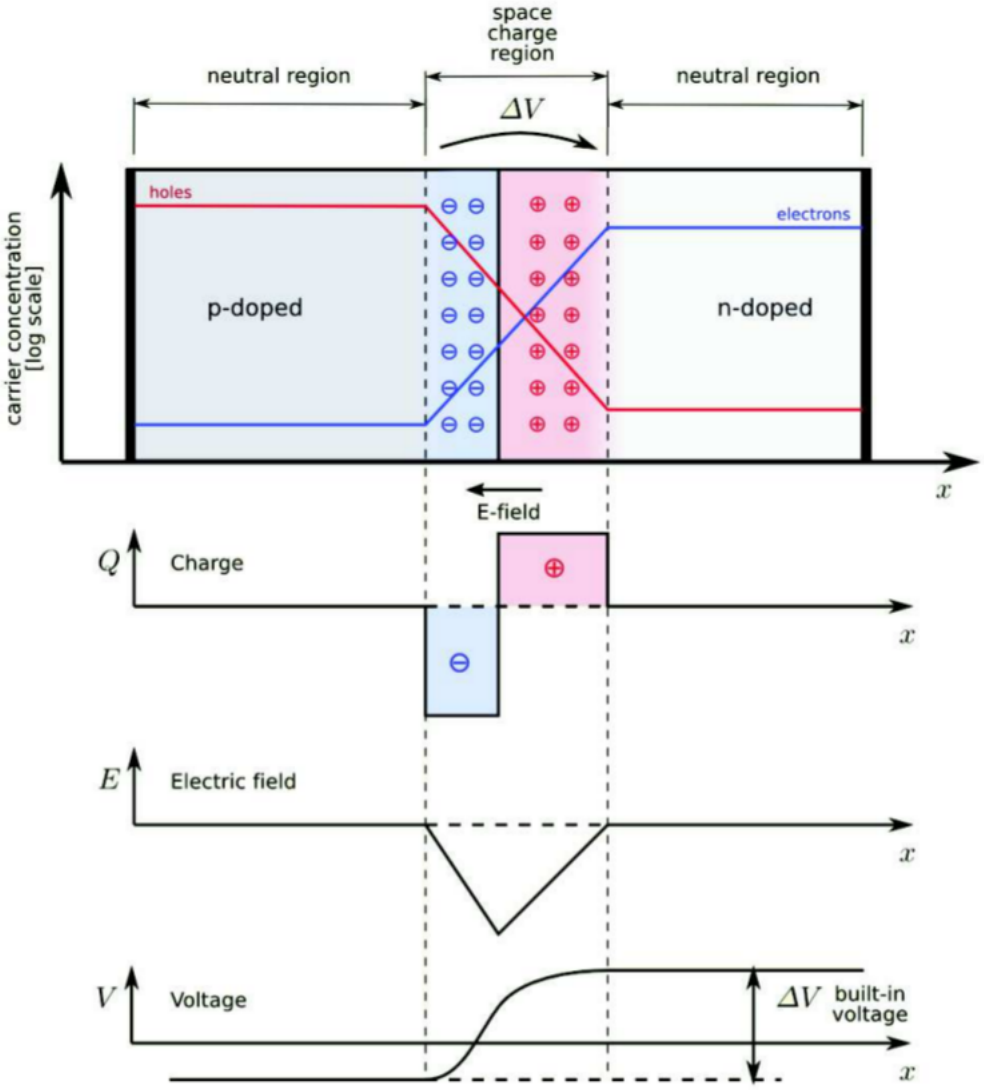

Figure 2.5: pn junction principle scheme. The charges drift from their original doped region creating a charge gradient Q which generates the electric field E and its respective contact potential V. From [24].

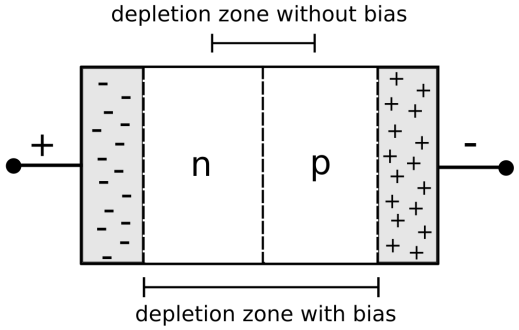

Figure 2.6: pn junction scheme with an applied reverse-bias voltage.

2.6 HPGe detectors

The two most common semiconductors used for radiation detection are silicon and germanium. Between the two, germanium is generally preferred for gamma-ray spectroscopy. Two advantages lead to this. The first reason is that the higher atomic number of germanium ($Z_{Ge} = 32$ compared to $Z_{Si} = 14$) leads to a much higher cross section for gamma-ray interactions (see section 1.1). The second reason is linked to the electro-chemical properties of the material itself. In fact, at normal semiconductor purity, germanium (and silicon) can't reach depletion depths bigger than 2 or 3 mm despite having bias voltages near the breakdown level. Equation 2.3 shows that greater depletion depths can be achieved by reducing the impurity concentration N. Modern refining techniques, developed for germanium but not for silicon, reduce the impurity concentration to approximately $10^{10}\, atoms/cm^3$ that allows depletion depths of $10\, mm$ with a $1000\, V$ bias voltage for germanium. Detectors that are manufactured from this pure germanium are called *high purity germanium* (*HPGe*) detectors. Depending on what is the predominant remaining low-level impurity type, the germanium can be classified as a *p-type* germanium (surplus of acceptors) or *n-type* (surplus of donors).

Two geometrical configurations of germanium detectors can be commonly found off-the-shelf: *planar* and *coaxial* (figure 2.7). In a planar configuration, the electric contacts are provided on the two flat surfaces of a germanium disk. The diameter of the cylindrical crystal from which the wafer is cut may be as large as $10\, cm$ and its thickness (i.e. depletion depth) is limited to about $2\, cm$. Thus, active volumes up to $160\, cm^2$ may be achieved. Bigger volumes, which are favorable for gamma-ray spectroscopy, can be achieved if the detector is constructed in cylindrical or *quasi-coaxial* configuration. In this case, one electrode is fabricated at the outer cylindrical surface of a long germanium cylindrical crystal. A second cylindrical contact is provided by removing the core of the crystal and placing a contact over the inner cylindrical surface. In this way the crystal can be made long in the axial direction still keeping a moderate distance (few centimeters) between the electrodes. This geometry allows reaching much larger active volumes. This configuration allows also to achieve lower capacitance with respect to the

planar geometry (lower capacitance leads to better energy resolution).

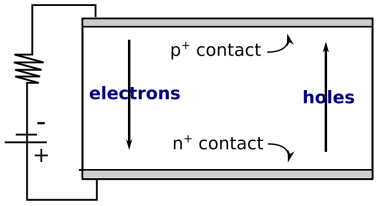

(a)

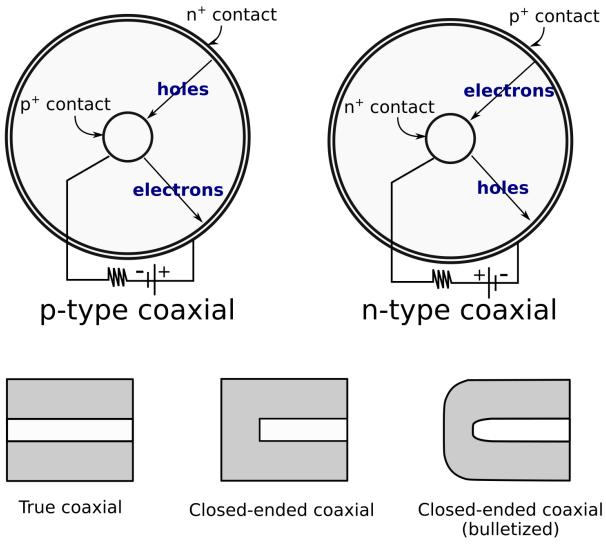

(b)

Figure 2.7: Common geometrical configurations for germanium detectors: (a) planar configuration; (b) coaxial configurations.

At normal temperature the germanium present a small band gap ($0.7\,eV$) which does not allow optimal operational conditions due to the large thermally-induced leakage current. In order to not spoil the energy resolution, the detector has to be operated at temperatures of around $77\,K$ through the use of an insulated Dewar in which liquid nitrogen is kept in thermal contact with the detector. The detector must be kept in a vacuum-tight cryostat to inhibit thermal conductivity between the crystal and the surrounding air. It is worth to mention that in some applications it may be convenient to allow the detector temperature to rise above liquid nitrogen temperature (this will not have major impact on the detector as long as the temperature does not reach $130\,K$), in these cases a mechanical or electrical cooling system may be paired with the detector at the place of the nitrogen filled Dewar. Finally, the detector is usually coupled with a preamplifier which purpose is to amplify and shape the incoming raw signals (see section 3.3.1). The input or first stage of the preamplifier is generally kept in the cold part of

the cryostat in order to reduce electronics noise.

As mentioned before, HPGe detectors are excellent in gamma-ray spectroscopy due to their high energy resolution which allows to resolve many closely spaced gamma-ray energies. The overall energy resolution depends on the combination of three factors: the inherent statistical spread in the number of charge carriers, the variation in the charge collection efficiency and the contribution of electronics noise. The full width half maximum W_T of a typical peak in the spectrum can thus be written as

$$W_T^2 = W_D^2 + W_X^2 + W_E^2 \tag{2.4}$$

The first factor W_D^2 represents the inherent statistical fluctuation of the number of charge carriers created and is given by

$$W_D^2 = (2.35)^2 F \epsilon E \tag{2.5}$$

where F is the Fano factor, ϵ is the energy necessary to create one electron-hole pair and E is the gamma-ray energy. Taking $\epsilon = 2.96\,eV$ for germanium, and $F = 0.08$ as Fano factor for large germanium volumes, the above equation predicts a full width half maximum (FWHM) of $1.32\,keV$ at $1.33\,MeV$. The contribution of the second term W_X^2 is due to the incomplete charge collection due to charge trapping (see section 2.9 later in this chapter). This is most significant in detectors with large volume and low average electric field. Finally the third factor W_E^2 represents the broadening effects of all electronics components and intrinsic capacitance of the detector. Energy resolution for germanium detectors are often specified at $5.9\,keV$ (^{55}Fe), $122\,keV$ (^{57}Co), $662\,keV$ (^{137}Cs), or $1333\,keV$ (^{60}Co). Large coaxial detectors will produce FWHM values of $0.8 - 1.2\,keV$ at $122\,keV$, rising to $1.9 - 2.3\,keV$ at $1333\,keV$.

Finally, it is wort to mention that further peak broadening can come from the Doppler effect when HPGe detectors are used in in-beam experiments. Doppler broadening depends exclusively from experimental conditions and its effects can be corrected if the velocity vector of the interacting gamma ray is known (i.e. the position of its first interaction).

2.7 Electric-field calculation for planar and coaxial detectors

As previously said (2.3) the drift velocity of the charge carriers in germanium detectors depends on the electric field in the detector volume. For a given geometry, the electric potential φ can be calculated by solving the Poisson's equation

$$\nabla^2 \varphi = -\frac{\rho}{\epsilon} \tag{2.6}$$

where ρ is the charge density and ϵ is the dielectric constant. The charge density, in the case of a p-type germanium detector, is equal to $\rho = -eN_A$, where e is the electron charge and N_A is the density of the acceptor impurities. In the same way, for a n-type

detector $\rho = eN_D$ where N_D is the density of donor impurities. The spacial variation of the field strength across the active volume is different in a planar and a coaxial detector geometry. In the following the two geometries will be treated separately.

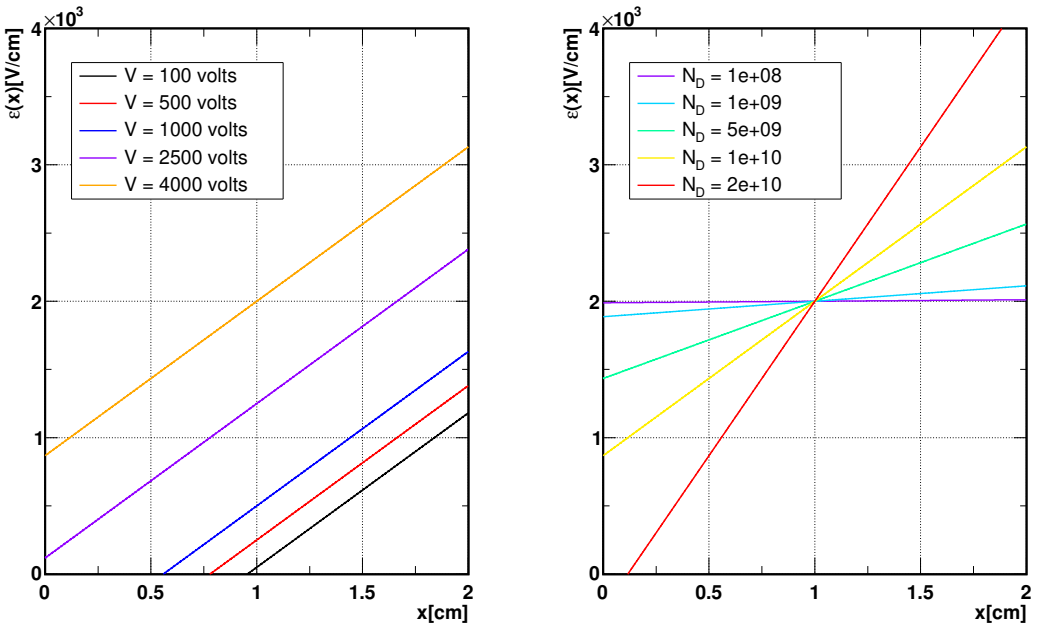

(a) (b)

Figure 2.8: Variation of the electric–field strength, along the depth of a $2\,cm$ thick planar detector. In (a) the impurity density V_D is set at $10^{10}\,cm^{-3}$ and the variation is shown for different values of the applied bias V. In (b) the applied bias V is fixed at $4000\,V$ and the variation is shown for different impurity densities V_D.

The thickness of the depletion zone of a pn-junction for a given voltage is given by equation 2.3. If a detector with planar geometry of thickness T is considered, the full depletion will require an applied voltage of

$$V_d = \frac{\rho T^2}{2\epsilon} \tag{2.7}$$

For a mono-dimensional geometry, equation 2.6 can be written as

$$\frac{d^2\varphi}{dx^2} = -\frac{\rho}{\epsilon} \tag{2.8}$$

and since the electric field is

$$\mathcal{E} = -d\varphi/dx \tag{2.9}$$

by solving eq. 2.8 with the boundary condition $\varphi(d) - \varphi(0) = V$, one obtains

$$-\mathcal{E}(x) = \frac{V}{d} + \frac{\rho}{\epsilon}\left(\frac{d}{2} - x\right) \tag{2.10}$$

Figure 2.8 shows the electric-field variation in the crystal depth for different applied voltage values and different impurities concentrations as predicted by equation 2.10.

For a coaxial geometry, the Poisson's equation can be written in cylindrical coordinates

$$\frac{d^2\varphi}{dr^2} + \frac{1}{r}\frac{d\varphi}{dr} = -\frac{\rho}{\epsilon} \tag{2.11}$$

If the considered detector has inner and outer radii of r_1 and r_2 and the boundary condition $\varphi(r_2) - \varphi(r_1) = V$ is imposed, by solving equation 2.11 for $\mathcal{E}(r) = -d\varphi/dr$ one obtains

$$-\mathcal{E}(r) = -\frac{\rho}{2\epsilon}r + \frac{V + (\rho/4\epsilon)(r_2^2 - r_1^2)}{r\, ln(r_2/r_1)} \tag{2.12}$$

Plots of the electric-field intensity along the crystal radius are shown in figure 2.9 for

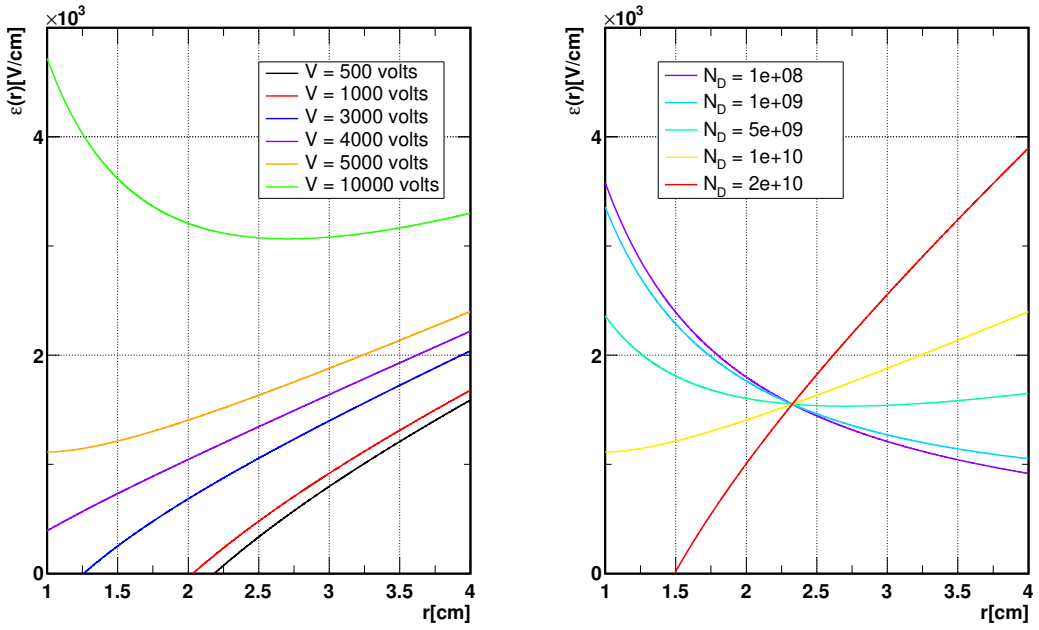

(a) (b)

Figure 2.9: Variation of the electric–field strength, along the radius of a coaxial detector. In these examples, the crystal radii are $r_1 = 1.0\,cm$ and $r_2 = 4.0\,cm$. In (a) the impurity density V_D is set at $10^{10}\,cm^{-3}$ and the variation is shown for different values of the applied bias V. In (b) the applied bias V is fixed at $5000\,V$ and the variation is shown for different impurity densities V_D.

different applied voltage values and different impurities concentrations. The voltage V_d

needed to deplete the detector can be found by setting $\mathcal{E}(r_1) = 0$ in equation 2.12, resulting in

$$V_d = \frac{\rho}{2\epsilon}\left[r_1^2\, ln\left(\frac{r_2}{r_1}\right) - \frac{1}{2}(r_2^2 - r_1^2)\right] \tag{2.13}$$

2.8 Signal formation

As introduced in the previous sections the mechanism of gamma-ray detection for germanium (or semiconductor detectors in general) consists in the following steps: a gamma ray interacts with the semiconductor creating a number of charge carriers proportional to the energy deposited; the carriers move in the electric field applied to the detector inducing electric charges at each electrode[3]; the charge is converted into a voltage signal, the amplitude of which is proportional to the energy of the interacting gamma ray.

The induced charge Q on the electrodes can be calculated by determining the instantaneous electric field $\mathbf{E}$ when the moving charge q is at each point of its trajectory and then integrate the normal component of $\mathbf{E}$ over the surface S surrounding the electrode

$$Q = \oint_S \varepsilon \mathbf{E} \cdot d\mathbf{S} \tag{2.14}$$

where ε is the dielectric constant of the material. Nevertheless, a simpler method to calculate the induced charge was independently derived from equation 2.14 by Shockley and Ramo [30, 31, 32]. The Shockley-Ramo theorem states that the charge Q and the current i on an electrode induced by a moving point charge q are given by

$$Q = -q\phi_0(\mathbf{x}) \tag{2.15}$$

$$i = q\mathbf{v} \cdot \mathbf{E}_0(\mathbf{x}) \tag{2.16}$$

where $\mathbf{v}$ is the instantaneous velocity of charge q. The quantities $\phi_0(\mathbf{x})$ and $\mathbf{E}_0(\mathbf{x})$ are called the *weighting potential* and *weighting field*, respectively. They correspond to the electric potential and field that would exist at the charge q instantaneous position $\mathbf{x}$ if the selected electrode is considered at $1\,V$, all the other electrodes being at $0\,V$ and all the charges being removed. As supplementary assumptions, it is considered that the magnetic effects are negligible and that the electric field propagates instantaneously (quasi-static approximation). Summing up, the elements required for the calculation are: the electrical field in the detector, the trajectory of the charge carriers under its action and the weighting potentials.

The electrical field can be calculated analytically or numerically (depending on the complexity of the geometry of the detector) by solving the Poisson equation

$$\triangle\phi = -\frac{\rho}{\epsilon} \tag{2.17}$$

[3]Counter-intuitively, the detector signal is not formed only when the charge carriers reach the electrodes. That would imply a time delay between the interaction and start of the signal formation. No such delay exists and the signal formation begins as soon as the carriers start to drift towards the electrodes as result of their movement within the field.

Typically, simple symmetric detector geometries, such as planar or true coaxial configurations, have analytical solutions. The solution to the Poisson equation for more complex geometries is obtained numerically by finite differencing techniques on a point grid.

The weighting potentials can be obtained by solving the Laplace equation

$$\nabla^2 \phi_i(\mathbf{x}) = 0 \tag{2.18}$$

where, if S_j is the surface of the electrode j,

$$\phi_i | S_j = \delta_{i,j} \tag{2.19}$$

as said before. From equations 2.15 and 2.16 one can see that if a charge q, located at position $\mathbf{x}$, is traveling towards the electrode S_i, this electrode will collect a charge proportional to the weighting potential $\phi_i(\mathbf{x})$. At the same time the other electrodes $S_{j \neq i}$ will collect a charge proportional to value of their respective weighting potential $\phi_j(\mathbf{x})$. However, for the equation 2.18, when q will reach the electrode S_i the net charge induced on it will be $Q = -q$, while the net charge collected on the other electrodes will be $Q = 0$. The charge collected on the electrodes $S_{j \neq i}$ is called *transient charge* (or *image charge*) and the signals obtained from it are called *transient signals* (or *image signals*).

Since the weighting potentials strongly depend on the spatial coordinates, the signals generated on the electrodes (especially for the transient signals) can be used to deduce the position of the gamma-ray interaction that generated the charge, making segmented HPGe detectors position sensitive, as it will be later shown.

In the next two sections examples of analytical calculation of pulse shapes for planar and coaxial geometries will be presented.

2.8.1 Pulse-shapes for planar detectors

Let consider a planar detector where V_0 is the voltage applied and d the distance between its electrodes. If a positive charge q_0 moves from x_0 to x through the medium, the energy absorbed is

$$\Delta E = \frac{q_0 V_0}{d} (x - x_0) \tag{2.20}$$

and the signal voltage will be

$$\Delta V_R = \frac{\Delta E}{C V_0} = \frac{q_0}{C} \frac{(x - x_0)}{d} \tag{2.21}$$

where C is the intrinsic capacitance of the detector. This corresponds to an induced charge on the electrodes of

$$\Delta Q = C \Delta V_R = q_0 \frac{(x - x_0)}{d} \tag{2.22}$$

The induced charge can be expressed in terms of growth of time-dependent induced charge $Q(t)$. The induced charge starts at zero when electrons and holes are formed and

reaches it's maximum of q_0 when the two clouds of charge carriers are collected. If it is assumed that the charges are formed at a distance x from the n^+ contact of the detector (see figure 2.10) and the following definitions are used

$$\begin{array}{rl} t_e = x/v_e & \textit{electron collection time} \\ t_h = \frac{d-x}{v_h} & \textit{hole collection time} \end{array} \tag{2.23}$$

(with v_e and v_h electrons and holes saturation velocity, respectively) then four possible time domain can be defined (see figure 2.10).

If both electrons and holes are drifting ($t < t_h$ and $t < t_e$)

$$Q(t) = q_0 \left(\frac{v_e}{d} t + \frac{v_h}{d} t \right) \tag{2.24}$$

If electrons have been collected and holes are still drifting ($t_e < t < t_h$)

$$Q(t) = q_0 \left(\frac{x}{d} + \frac{v_h}{d} t \right) \tag{2.25}$$

If holes have been collected and electrons are still drifting ($t_h < t < t_e$)

$$Q(t) = q_0 \left(\frac{v_e}{d} t + \frac{(d-x)}{d} \right) \tag{2.26}$$

Finally, if both holes and electrons have been collected ($t > t_h$ and $t > t_e$)

$$Q(t) = q_0 \tag{2.27}$$

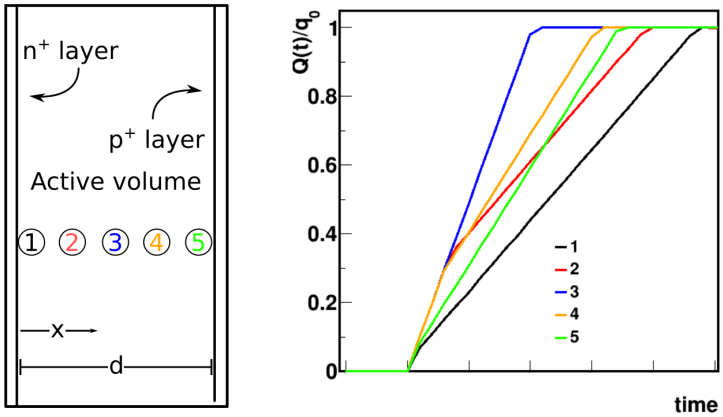

Figure 2.10: Pulse shapes examples in a planar detector.

2.8.2 Pulse-shapes for coaxial detectors

The considerations made in the previous section can be proposed again for a detector with coaxial geometry with an external (internal) radius r_2 (r_1). For a cylindrical geometry, if a positive charge q_0 moves from r_0 to r through the medium, the energy variation will be

$$\Delta E = q_0\alpha(r^2 - r_0^2) + q_0\beta\, ln\frac{r}{r_0} \tag{2.28}$$

where

$$\alpha = \frac{eN_A}{4\epsilon} \qquad \beta = \frac{V_0\alpha(r_2^2 - r_1^2)}{ln(r_2/r_1)} \tag{2.29}$$

e is the charge of the electron, N_A is the acceptors concentration and ε is the dielectric constant in the medium. The time-dependent charge induced by the motion of electrons and holes can be written in terms of the radial positions $r_e(t)$ and $r_h(t)$

$$Q^-(t) = \frac{\Delta E^-}{V_0} = \frac{q_0\alpha}{V_0}[r_e^2(t) - r_0^2] + \frac{q_0\beta}{V_0}\, ln\frac{r_e(t)}{r_0} \tag{2.30}$$

$$Q^+(t) = \frac{q_0\alpha}{V_0}[r_0^2 - r_h^2(t)] + \frac{q_0\beta}{V_0}\, ln\frac{r_0}{r_h(t)} \tag{2.31}$$

The shape of $Q(t) = Q^-(t) + Q^+(t)$ will differ from the one for the planar detector

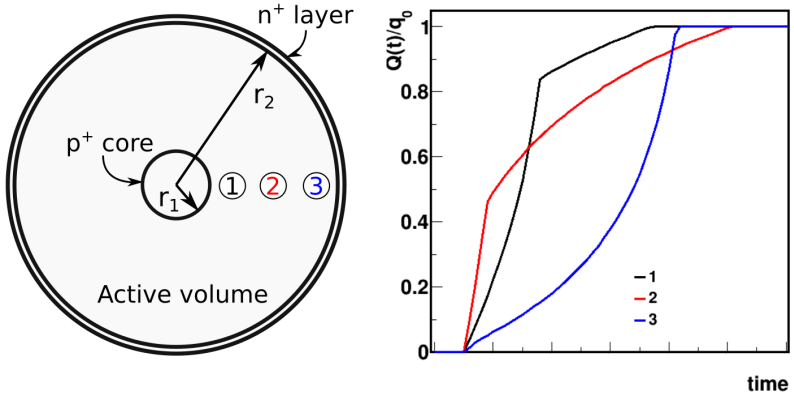

Figure 2.11: Pulse-shape examples in a coaxial detector.

because the electric field in a coaxial geometry varies radially and since the asymmetric nature of the germanium mobility (see section 2.3) the drift velocities of the charge carriers may vary during collection time. One can assume an empirical form for the drift velocity of the charge carriers [27] which is

$$v_i = \frac{\mu_{0i}\mathcal{E}(r)}{[1 + (\mathcal{E}(r)/\mathcal{E}_{0i})^{\gamma_i}]^{1/\gamma_i}} \tag{2.32}$$

with $i \equiv e, h$ where $\mathcal{E}(r)$ is the electrical field value at radius r, μ_{0i} is the mobility at low field values, γ_i and $\mathcal{E}_{0i}$ are adjustable parameters fitted to experimental drift velocity data. As the radial position can be determined numerically, it is possible to calculate the signal pulse shape for a coaxial detector (figure 2.11).

2.9 Impact of trapping on the signals

It was already mentioned in section 2.4 that once the charge carriers are generated, they can find on their drifting path some trapping centers in which they can be captured. These trapping centers are basically impurities of the crystal which add levels in the forbidden band. These levels can be more or less close to the conducting or valence band depending on their nature. Dopants, which enhance the semiconductor conduction, create levels very close to the conducting or valence band and, for this reason, they are called shallow impurities. Other impurities, due to crystal imperfections such as discontinuities, radiation damages[4] and extraneous atoms[5] occupying lattice positions, create levels further away from the conduction and valence bands, toward the middle of the forbidden band and, for this reason, they are called deep impurities.

When a charge carrier is trapped, it can be de-trapped after a certain amount of time. The mean lifetime $\theta_{e,h}$ of a trapped electron or hole before de-trapping occurs can be calculated with the following equation [33]

$$\theta_{e,h} = \frac{1}{\sigma_{e,h} v_{th} n_{e,h}} \tag{2.33}$$

where $\sigma_{e,h}$ is the effective capture cross section for electrons or holes, v_{th} is the thermal velocity ($\sim 10^7\, cm/s$) and $n_{e,h}$ is the density of the charge carriers in the conducting band which can be written as

$$n_e = N_C \cdot e^{-\frac{E_C - E_t}{kT}} \tag{2.34}$$

$$n_h = N_V \cdot e^{-\frac{E_t - E_V}{kT}} \tag{2.35}$$

where N_C (N_V) is the density of levels in the conduction (valence) band, $E_C - E_t$ ($E_t - E_V$) is the energy difference among the trapping level and the conduction (valence) band, k is the Boltzmann constant and T is the temperature of the crystal. Likewise, one can consider the mean free drift time of the charge carriers, written as

$$\tau_{e,h} = \frac{1}{\sigma_{e,h} v_{th} N_t} \tag{2.36}$$

where N_t is the level density in the forbidden band with energy E_t. In the case of shallow impurities, charge carriers are de-trapped quite rapidly, with times $< 100\, ns$.

[4] Typically induced by neutrons. Coaxial detector are more affected by this phenomenon since they are designed to detect high energies gamma rays which is compensated for n-type detectors by the charge collection configuration.

[5] Typically metallic atoms such as gold, zinc, cadmium.

Deep impurities, instead, trap the charges for longer times that range widely from microseconds to seconds. Finally, other types of deep impurities can act as recombination centers where both electrons and holes are captured causing them to annihilate. The time delay between trapping and de-trapping is often sufficiently long to prevent the trapped carriers from contributing to the shape and amplitude of the measured pulse, although this also depends on the main amplifier shaping times used for pulse analysis. Pulses can then be affected by trapping and three scenarios may arise that can be described taking a planar detector as example. In an interaction near the p^+ contact, the holes are immediately collected and one can set $x = d$ in equation 2.26. If no trapping is considered, then

$$Q(t) = q_0 \frac{t}{t_e} \qquad (t \leq t_e) \tag{2.37}$$

where t_e is the transit time of the electrons. In this case the pulse has the expected shape and amplitude as shown by signal (a) in figure 2.12.

If now it is assumed that an uniform concentration of electron traps is present along the charge carrier path, then, if the electrons are not de-trapped or are de-trapped after a time longer than the shaping time, one obtains

$$Q(t) = q_0 \frac{\tau_e}{t_e} \left(1 - e^{-t/\tau_e}\right) \qquad (t \leq t_e) \tag{2.38}$$

where τ_e is the mean free drift time of the electrons (equation 2.36). In this case trapping has an influence on the leading edge of the signal and its final amplitude, as exemplified by signal (b) in figure 2.12.

Finally, if the electrons are partially de-trapped in a fast enough time, a fast and a slow component will appear in the resulting pulse. The fast component consists in the leading edge of the pulse and is characterized by

$$Q(t) = q_0 \frac{\Theta_e}{t_e} \left(\frac{t}{\theta_e} + \frac{\Theta_e}{\tau_e}(1 - e^{-t/\Theta_e})\right) \qquad (t \leq t_e) \tag{2.39}$$

where θ_e is given by equation 2.36 and

$$\Theta_e = \frac{\tau_e \theta_e}{\tau_e + \theta_e} \tag{2.40}$$

while the slow component don't have a simple analytic expression. The resulting signal is schematised by signal (c) of figure 2.12. To summarize, trapping can influence both the timing and the energy reading of a signal. The latter is helped by de-trapping, but only if it occurs on a short time scale compared with pulse-shaping times in the subsequent electronics.

Furthermore, trapping can cause a deterioration in energy resolution due to the variable amount of charges lost per pulse. The term W_X^2 of equation 2.4, in fact, is not uniform inside the volume of the detector and depends on the interaction positions.

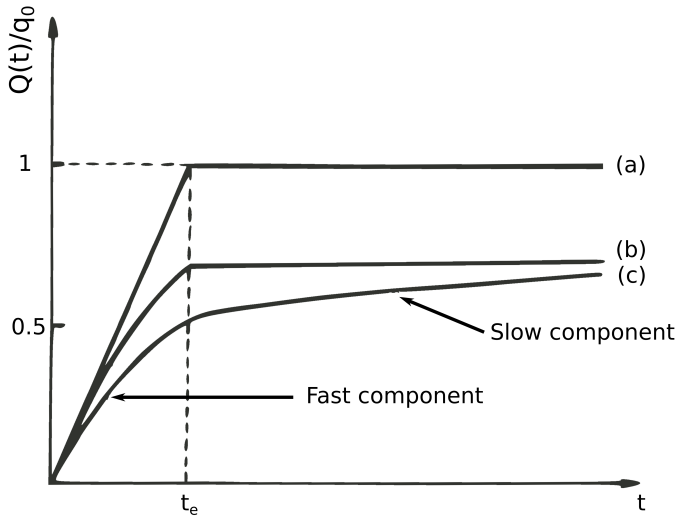

Figure 2.12: Pulse shapes for interactions in a planar detector at one extreme of the active volume. (a)Absence of trapping, (b) permanent trapping and (c) trapping with de-trapping. The fast and the slow components of signal (c) are indicated by the arrows. Adapted from [33].

An exact analytical form of W_X^2 does not exist and experimental formulas are generally proposed starting from collimated beam measurements. In [34], the following semi-empirical formula is proposed for a n-type coaxial detector biased on the external p^+ contact

$$W_X^2(r) = \epsilon K E_0 \left[1 - \eta(r)\right] \tag{2.41}$$

where K is a constant similar to the Fano factor related to the fluctuation of the number of trapped charges, E_0 is the energy of the gamma-ray interaction, ϵ is the energy needed to produce an electron-hole pair and $\eta(r) = \eta_e(r) + \eta_h(r)$, comprised between 0 and 1, is the total charge collection efficiency as a function of the radius. The two terms $\eta_e(r)$ and $\eta_h(r)$ have the form

$$\eta_e(r) = -\frac{e^{-r/\lambda_e}}{ln(r_2/r_1)}\left[ln\frac{r_1}{r} - \frac{1}{\lambda_e}(r - r_1) - \frac{1}{4\lambda_e^2}\left(r^2 - r_1^2\right)\right] \tag{2.42}$$

$$\eta_h(r) = \frac{e^{r/\lambda_h}}{ln(r_2/r_1)}\left[ln\frac{r_2}{r} - \frac{1}{\lambda_h}(r_2 - r) + \frac{1}{4\lambda_h^2}\left(r_2^2 - r^2\right)\right] \tag{2.43}$$

where $\lambda_e(\lambda_h)$ is the mean free path of the electrons (holes) in the crystal and r_1 and r_2 are the inner and outer radii of the detector. The larger the charge carrier path, the wider the peak at position r in the case of a collimated irradiation.

As the resolution depends from the radius of the interaction (or the depth for a planar detector) if a collimated gamma beam would irradiate the detector at different radii, the FWHM of the resulting peaks would increase going towards one contact to

the other[6]. An example of this phenomenon is shown in figure 2.13. If a free source irradiates uniformly a detector, then the total peak can be seen as the sum of several Gaussian functions with different centroids and FWHMs. The centroid and FWHM of the total peak is influenced by the ones of the many individual Gaussian functions obtained with collimated irradiation and its peak shape appears asymmetrical with a tail on the low-end.

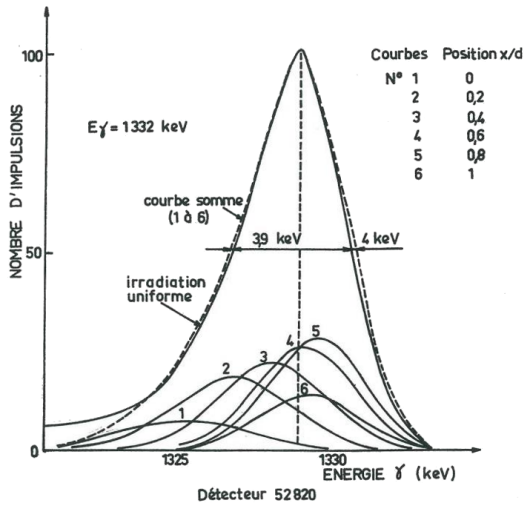

Figure 2.13: Photopeaks at $1332\,keV$ measured with a planar, $\sim 6\,mm$ thick, GeLi detector. The detector is irradiated laterally at different positions x in the crystal depth (listed at the top right of the figure, with d the crystal thickness of the active volume) by the collimated ^{60}Co source. The dashed line represents the sum of all the photopeaks and is compared with a photopeak obtained with a free ^{60}Co source (uniform irradiation). From [33].

[6]This is true if one of the two contribution to the trapping is negligible, ie. holes are less likely to be trapped if the crystal has not sufered from neutron damages.

Chapter 3

The AGATA detector

3.1 AGATA collaboration

The study of the nuclear structures far from stability through gamma-ray spectroscopy plays an important role in modern nuclear physics. Efforts are made into the production and investigation of nuclear system under extreme values of isospin, masses, angular momentum and temperature [35]. These unstable nuclei exhibit peculiar structures (eg. nuclear halo, nuclear skin, clusterization, hyperdeformation) and by exploring their level structure is possible to obtain data needed to improve existing nuclear models. Existing Radioactive Ion Beams (RIBs) accelerator facilities, such as SPIRAL1 at GANIL and ISOLDE at CERN, are already capable to access a wide range of proton- and neutron-rich nuclei and new generation facilities, currently under construction, like FAIR at GSI, SPIRAL2 at GANIL and SPES at LNL, will be capable of explore even more the exotic areas of the chart of nuclides.

Since the production rates of such exotic nuclei are very low, experiments involving these species require gamma-ray arrays with large detection efficiency and excellent energy resolution. The *Advanced GAmma Tracking Array* (AGATA) is an European project that involves over 40 institutions from 11 countries. The aim of the collaboration is to design, build and develop a new generation HPGe detector array that delivers the required performances for the study of the nuclei far from the valley of stability. A parallel project is carried out in the USA by the GRETA/GRETINA collaboration [23] with which the AGATA collaboration cooperates on technical developments of common interest.

In the coming sub-sections a description of the array, the single detector unit, pulse-shape analysis, gamma-ray tracking and characterization will be given. AGATA is a mobile instrument, that will be moved between the major European laboratories to take advantage of the different beams, ancillary detectors and equipments available at the different facilities. Several experimental campaigns already made use of AGATA at LNL, GSI and GANIL.

3.2 The AGATA array

The previous generation of HPGe detector arrays covering a solid angle of 4π such as EUROBALL and GAMMASPHERE [15, 17, 36] were already efficiently developed and built respectively in Europe and USA during the 1990s. These arrays were equipped with escape-suppression shields which enhanced the peak-to-total ratio in gamma-ray spectra (see figure 3.1). In these kind of arrays the shields are generally composed of BGO detectors, which have low energy resolution but high intrinsic detection efficiency. An event is rejected when a gamma ray Compton-interacts with a germanium detector of the array and then escape it interacting with the surrounding BGO. This technique has two main disadvantages. The first one is that BGO shields occupy space, limiting the solid angle occupied by the germanium detectors and thus reducing the geometrical efficiency. The second disadvantage lays in the loss of intrinsic efficiency due to suppression event. This efficiency loss could be avoided if, somehow, information on the escaped gamma rays could be recovered.

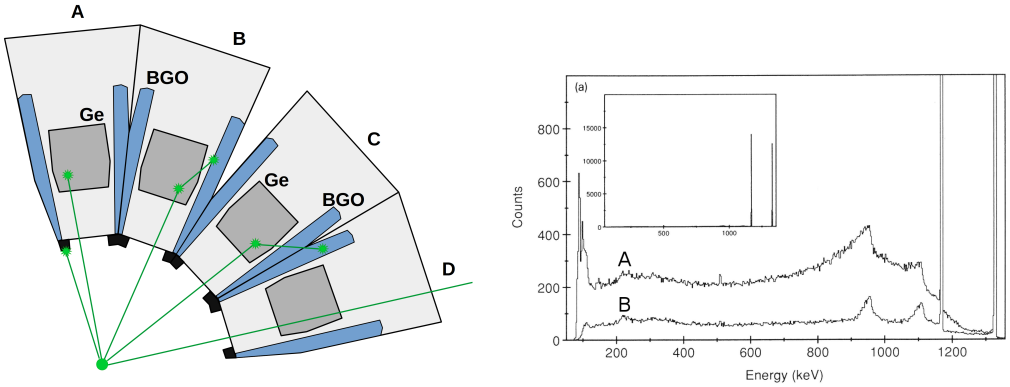

Figure 3.1: (a) Simple schematics of EUROBALL detectors. The germanium detectors are shielded by BGO detectors that suppress the events in which a gamma ray doesn't release all its energy in a single detector (cases B and C). (b) Spectrum of a ^{60}Co source measured with Eurogam array detector. For the spectrum labeled with the letter A the Compton escaping events are not suppressed. The spectrum labeled with the letter B shows the sizable background reduction due to the Compton suppression. From [10].

The AGATA detector array [22] exploits the position sensitive properties of segmented HPGe detectors (see sections 2.8 and 3.4) to get the information on the position of a gamma ray for each of its interaction. The gamma-ray tracking feature make the use of Compton-suppression unnecessary and results in a gain of geometrical and intrinsic efficiency of the detector with respect to the previous detector generation. Moreover, the direction of emission and scattering of each individual gamma ray can be determined with higher precision (first interaction point within $5\,mm$) allowing better Doppler correction (see figure 3.2) and linear polarization determination (extracted from the knowledge of

the positions of the two first interaction points).

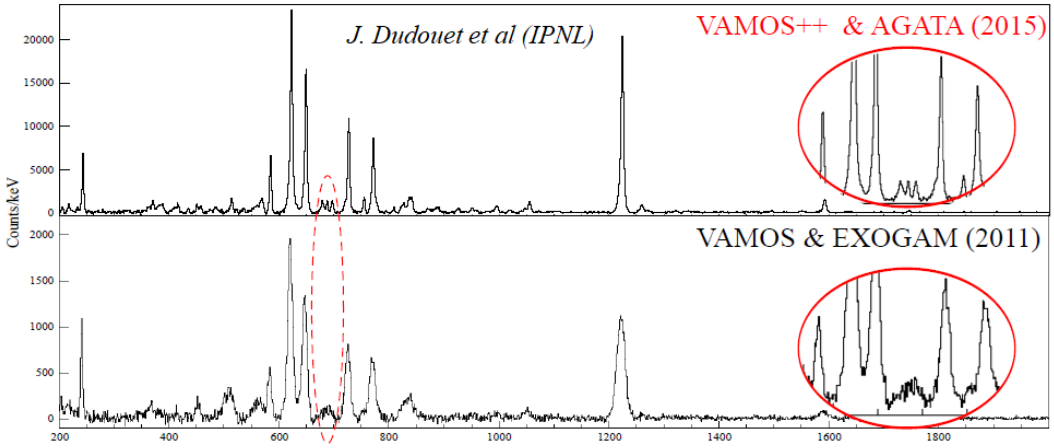

Figure 3.2: Spectra obtained with AGATA (in a limited, nine detectors, configuration) and EXOGAM coupled with VAMOS in two different experimental runs. Gamma−ray energies are gated on ^{98}Zr produced in the $^{238}U(6.5\,MeV/A) +^{9} Be$ fusion−fission reaction. The two spectra are obtained in the same experimental conditions, although the two runs had different durations, with the AGATA one being shorter. AGATA spectrum shows clearly a better resolution and the potentiality of the complete array. (J. Dudouet, IP2I, Private Communication).

The completed AGATA array (in figure 3.3a) will consist in 180 segmented HPGe detectors arranged in a 4π configuration that will cover 82% of the solid angle. The array is currently in construction stage and is composed by 41 working detectors installed at GANIL, as shown in figure 3.3c. In order to maximize the covered solid angle (and thus the geometrical detection efficiency) while minimizing the development and maintenance costs, AGATA is composed by few elementary shapes. The sphere is decomposed in 180 irregular hexagons[1], grouped in clusters of 3 (triplet, see yellow contour in figure 3.3a), and 12 regular void pentagons that can be used for mechanical support, insertion of complementary detectors and beam pipes. Each triplet is formed by different hexagonal shapes named A, B, C (in red, green and blue respectively in figure 3.3a) which are arranged in the same triple cryostat, as shown in figure 3.3b.

[1]The number of hexagons have been chosen based on GEANT4 simulations and the best response in efficiency, peak-to-total and in-beam energy resolution is found for 180 capsules. In addition, this configuration leads to a large inner radius of 23.5 cm which enables the placement of large complementary detectors. See [37, 38].

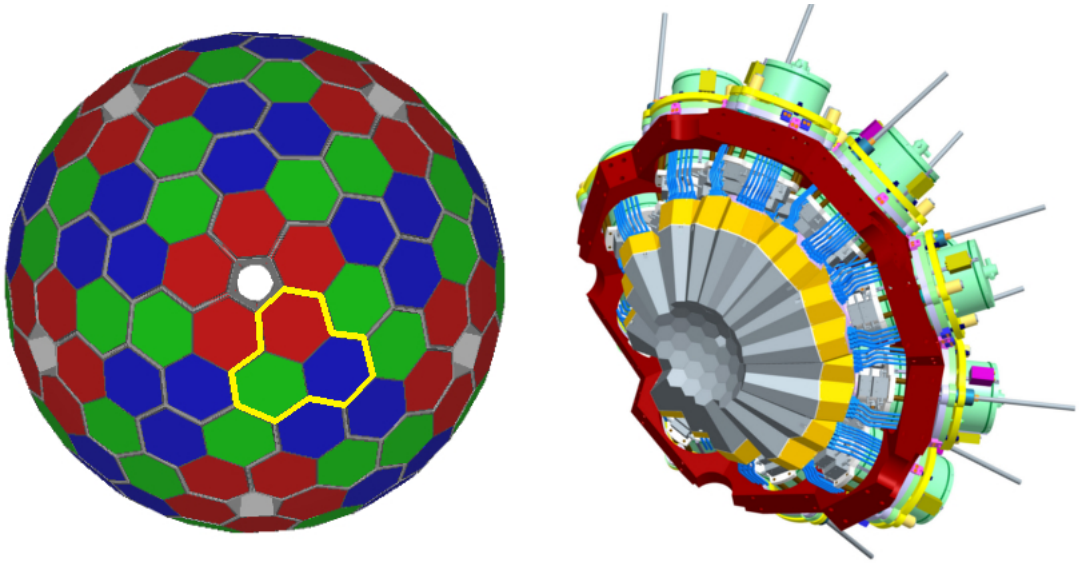

(a) Rendered figures of the AGATA detector array. The full array composed by 180 hexagonal shaped detectors is visible on the left; the yellow line highlights 3 detectors grouped in the same cluster. On the right a realistic 1π assembly of the array is shown.

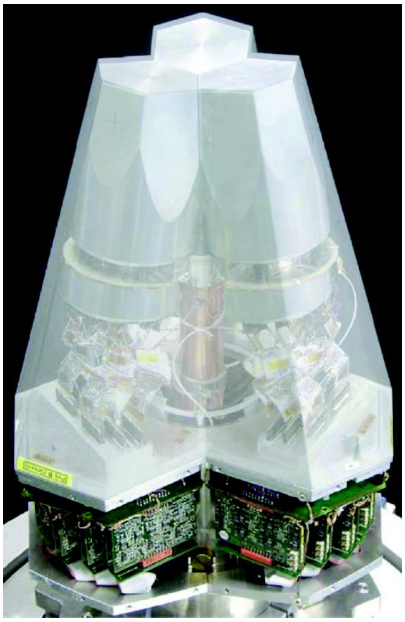

(b) Picture of a triplet mounted in a triple cryostat. The triplet cover is shown in semi transparency for greater clarity.

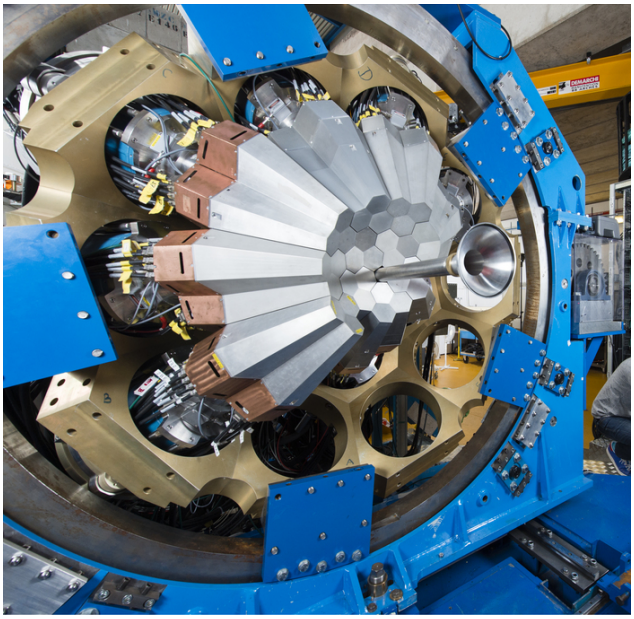

(c) Picture of the AGATA array composed of 11 triple clusters during the GANIL physics campaign.

Figure 3.3

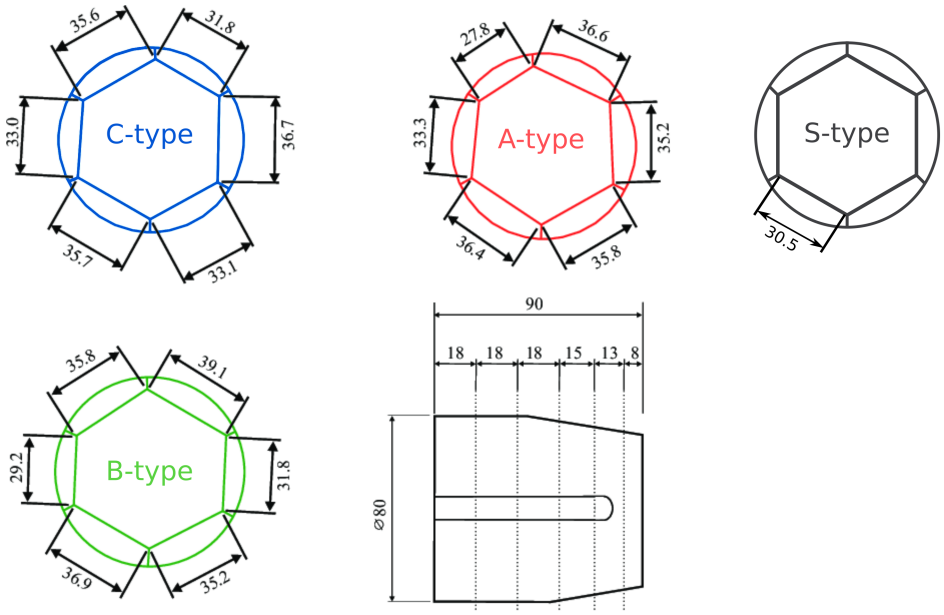

(a)

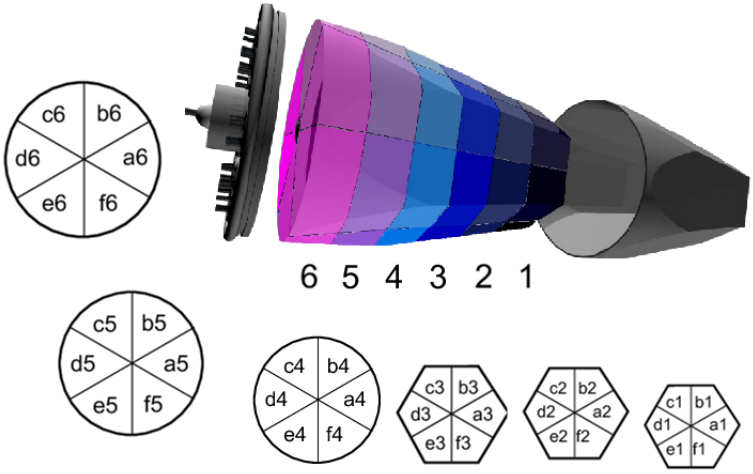

(b)

Figure 3.4: (a) Dimensions (in mm) of the three shapes of the detectors forming the AGATA array (A, B and C), and the prototype S. (b) The six slices of the detector are shown with their respective labeling. The hexagonal shaped slice are toward the front of the detector. The segment labeling corresponds to the detector seen from its back side. (Adapted from [22])

3.3 The AGATA detector unit

The AGATA detector units (figure 3.4) are segmented closed-end coaxial *n-type* HPGe crystals. The units of type A, B and C, which are used in triple clusters [39], have a tapered hexagonal geometry with an asymmetric shape. A fourth unit exists, the type S, which has a tapered hexagonal geometry with a symmetric shape. Three of such units were produced as a prototype and never integrated into the AGATA array. The length of each crystal is $90\,mm$ and the coaxial diameter is $80\,mm$. The central hole has a diameter of $10\,mm$ and extends to $13\,mm$ from the front end. The 6-fold sector-wise segmentation goes through the middle of each flat hexagonal side. The 6-fold longitudinal segmentation forms rings of 8, 13, 15, 18, 18 and 18 mm in thickness starting from the front face. Thus 37 signals are collected from each crystal: 36 segments signals plus 1 total energy signal collected by the central contact (*core*).

Each crystal has a weight of $2\,kg$ with an impurity concentration between 0.4 and $1.8\times10^{10}cm^{-3}$. The crystals are encapsulated in hermetically sealed aluminum canisters with a $0.8\,mm$ wall thickness. Thermal isolation is established by a vacuum with pressure values below $1\times10^{-6}mbar$. The spacing between the crystal and the canister wall varies from $0.4\,mm$ to $0.7\,mm$. At the back of the canister, ceramic feed-through connectors provide access to each of the 36 segment outer contacts and to the core contact. The latter is also used to apply the high voltage.

3.3.1 AGATA electronics

Due to their small amplitude, the current pulses coming from the electrodes of an AGATA detector unit need to be amplified and converted into voltage signals before being further processed. This is accomplished by 37 charge-sensitive preamplifiers

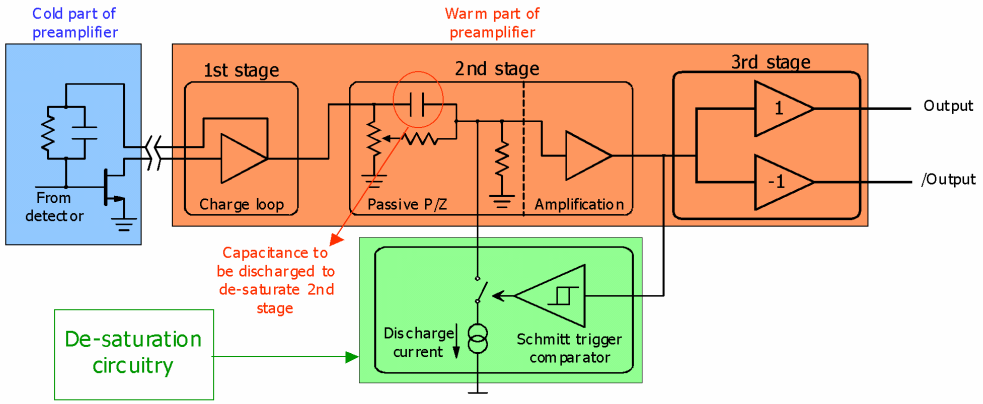

Figure 3.5: Scheme of the AGATA preamplifiers. The cold (warm) stage of the preamplifier is highlighted in blue (orange). The circuit highlighted in green allows the TOT technique (see text for more details). From [40].

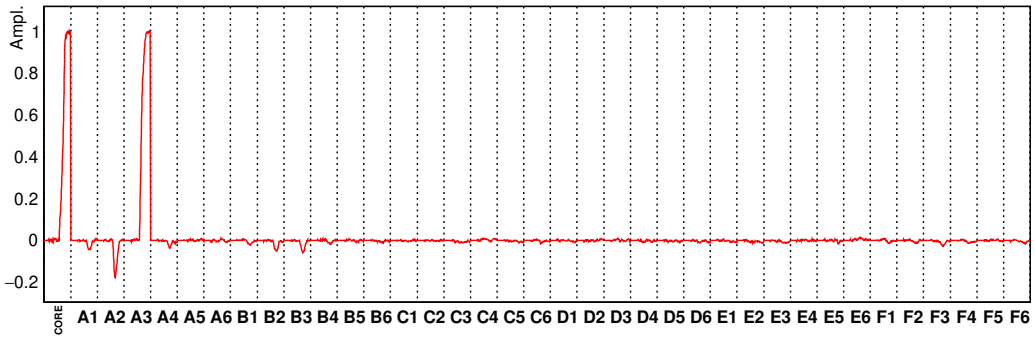

(a)

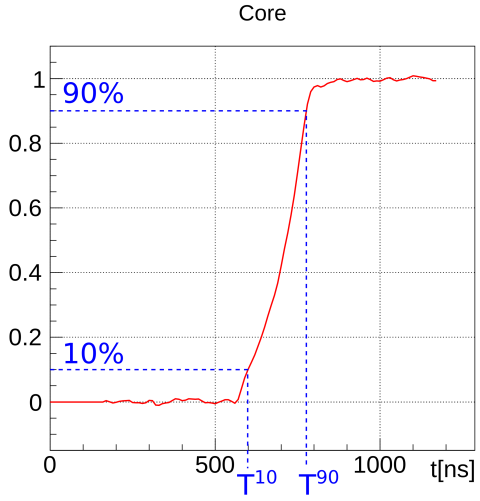

(b)

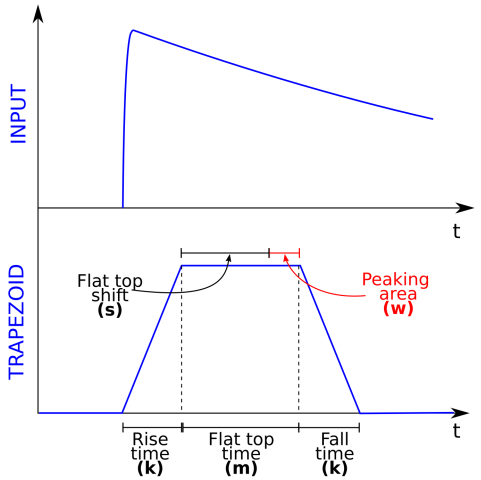

(c)

Figure 3.6: (a)Example of supertrace coming from a S-type AGATA detector plotted as a (see text for detail). The signals are normalized with respect to the amplitude of the core signal. In panel (b) the core signal is shown isolated. T^{10} and T^{90} mark the time at which the signal reach the 10% and 90%, respectively, of its maximum amplitude. The difference between T^{10} and T^{90}, quoted as T^{90}_{10}, corresponds to the rise time of the preamplifier pulse. (c) Simple scheme of the MWD algorithm. The input signal is re-shaped into a trapezoid which characteristics are labeled in the scheme. The energy reading corresponds to the energy average for the samples in the peaking area window, highlighted in red. The sum τ of the rise time, the flat top shift and the peaking area is called shaping time.

[40, 41, 42] (one for each channel) with which AGATA units are equipped. The preamplifiers have a cold and warm stage, as it can be seen in figure 3.5. The cold stage is located in cold, under vacuum part of the cryostat and it is operated close to the liquid nitrogen temperature to ensure low noise performances[2]. The warm stage, instead, is situated outside the vacuum compartment and at room temperature, since it contributes less to the noise. The core preamplifier is characterized by low noise and large dynamic range for energy detection. The board for the core signal delivers two energy-range outputs, $0 - 5.7\,MeV$ and $0 - 20\,MeV$. Actually, it is possible to extend the $0 - 20\,MeV$ range of the preamplifier up to $180\,MeV$, with a resolution of 0.2 % (FWHM), by applying the *time over threshold* technique [42]. The preamplifiers are characterized by a response time of $\sim 25\,ns$. A large bandwidth ensures good resolution for pulse-shape analysis (since the small transient signals are not deformed) and good timing properties.

The outputs of the preamplifiers are sent to digitizers that sample the signals with $14\,bit$ resolution at $100\,MHz$ rate. Figure 3.6a shows an example of signals generated by a $662\,keV$ gamma ray interacting in a S-type AGATA detector. The signals are shown as a *supertrace*, a compact representation of the leading edges of each channel of the detector. The signals coming from AGATA detectors have rise times that range between $\sim 150\,ns$ and $\sim 400\,ns$. The rise time of a signal can be determined calculating the T_{10}^{90}, defined as the time interval in which the amplitude of the considered signal goes from 10% to 90% of the maximum amplitude (see figure 3.6b).

Finally, the energy of a signal is measured with a pre-processing unit that applies a moving window deconvolution (MWD) algorithm (Jordanov trapezoidal filter) [43, 44]. The algorithm transforms the incoming signal into a trapezoidal shape, as exemplified in figure 3.6c, and the energy reading is done by averaging the amplitude value in the peaking area. Different parameters of the trapezoid such as the rise and fall time (k), the flat top window (m), the flat top shift (s) and the peaking area (w) should be set in order to obtain the best energy resolution. Hereafter, the sum $\tau = k + s + w$ of the rising time, flat top shift and peaking area of the trapezoidal signal is called shaping time.

3.4 Tracking and the importance of characterization

As the AGATA array doesn't use BGO shields to suppress Compton scattered gamma rays, a novel technique has been developed to reconstruct the trajectory of each detected gamma ray. The data processing is performed in three steps. In the first step a pulse-shape analysis (PSA) algorithm [45, 46, 47, 48, 49] is used to determine the position of each interaction composing an event[3]. The algorithm compares the experimental pulse shape with a database of calculated pulse shapes associated with spatial coordinates within the volume of the detector. Table 3.1 shows the PSA algorithms tested by

[2] The FETs of the preamplifiers work at an optimal temperature of $130\,K$, where the noise component is minimal.

[3] An event is defined as the interaction history of a gamma ray in the array. It is a time ordered collection of interaction positions and respective energy release.

the collaboration with relative performances and position resolutions. Once all the interaction positions of a detected nuclear event are obtained, a clustering algorithm groups the interactions which most likely belong to the same gamma-ray and a tracking algorithm [45, 50, 51, 52, 53] reconstructs the interaction history for each gamma ray. This last part is done by calculating, for each possible interaction combination, a factor of merit based on the energies, scattering angles and distances of each interaction. At the end of the procedure the reconstructed event associated to the best factor of merit is chosen and if this value is above a certain experimental threshold the event is accepted and stored, otherwise it gets rejected. The whole process is schematised in figure 3.7. The spatial resolution achieved by the array after PSA and tracking is $5\,mm$ FWHM at $1\,MeV$ [54, 55].

Algorithm	Single interaction		Multiple interaction	
	CPU time (norm/GS)	Res. (mm)	CPU time (norm/PS)	Res. (mm)
Grid search (GS)	1	2	–	4
Extensive GS	2.7	1	6×10^4	4
Particle swarm (PS)	0.1	2	1	4
Matrix method	6.7	2.4	10	10
Generic algorithm	330	1.9	2×10^2	8.1
Binary search	0.06	1	Not adapted	Not adapted
Recursive subtraction	Not evaluated	3	Not evaluated	5
Neural network	2	1.5	Not adapted	Not adapted
Wavelets	Not evaluated	2.3	Not adapted	Not adapted

Table 3.1: Overview of the performance of different PSA algorithms tested using simulated data. The performances for single (multiple) interactions are relative to the grid search (particle swarm) algorithm. The position resolution refers to the FWHM. From [22].

The PSA step is fundamental to achieve the best tracking results and this requires accurate databases of pulses. In fact, incorrect spatial attribution of gamma-ray interactions could lead, on the one hand, to the rejection of events which would have contributed to the full energy peak resulting to the decrease of the overall array efficiency and, on the other hand, to the selection of escaped gamma rays contributing to the background of the spectrum and degrading the peak-to-total (P/T) ratio. Presently, the PSA in AGATA is performed with the grid search algorithm [45] which uses databases calculated via AGATA Detector Library (ADL) ([56], see section 5.1). ADL calculates the pulse shape at a certain point of the detector, given the values of the electric field and the weighting potentials of the detector. Criticalities with the tracking algorithm arise for interaction points coming from the front and the back of the detector. In these areas the electric field strongly depends on the local geometry of the detector and particular impurities distribution. Such factors are difficult to implement in the numerical methods for the calculation of databases. Another source of incertitude for the numerical methods is the behavior of charges along the segmentation lines or surfaces, which cannot be easily implemented. A different approach to these problems consists in obtaining the

pulse-shape databases experimentally. Such topic will be discussed in the next chapters of this work.

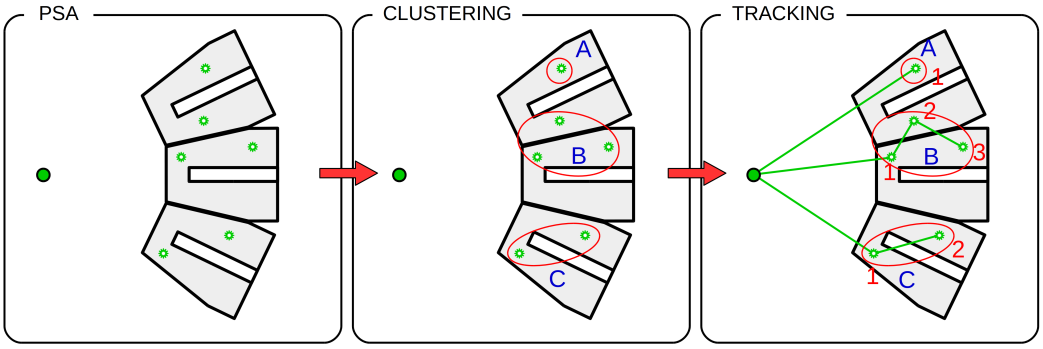

Figure 3.7: Simple representation of the PSA and tracking procedure. The outcome shows three different types of event. In event (A) the gamma ray gets absorbed by photoelectric effect; in event (B) the gamma ray interacts through Compton scatterings in two different detectors of the array and then gets absorbed by photoelectric effect; in event (C) the gamma ray interacts through Compton scatterings in the same detector and then gets absorbed by photoelectric effect.

	Gamma emission properties	AGATA 4π	EUROBALL
Full-energy efficiency	$E_\gamma = 0.1\,MeV,\ M_\gamma = 1,\ 0 < \beta < 0.5$	$67 - 70\%$	$\sim 40\%$
	$E_\gamma = 1\,MeV,\ M_\gamma = 1,\ 0 < \beta < 0.5$	$34 - 38\%$	9.4%
	$E_\gamma = 10\,MeV,\ M_\gamma = 1,\ 0 < \beta < 0.5$	$3.6 - 5\%$	//
Peak-to-total ratio (P/T)	$E_\gamma = 1\,MeV,\ M_\gamma = 1,\ 0 < \beta < 0.5$	$49 - 54\%$	53%
	$E_\gamma = 1\,MeV,\ M_\gamma = 30,\ 0 < \beta < 0.5$	$37 - 41\%$	45%

Table 3.2: Comparison between AGATA and EUROBALL characteristics for different gamma energies E_γ et multiplicities M_γ. From [57].

In table 3.2 the properties of the full AGATA array are compared to the ones of the previous generation array EUROBALL. The table shows that the efficiency of AGATA at $1\,MeV$ is a factor ~ 3.5 times bigger than EUROBALL for multiplicities (M_γ) 1 and 30, although the P/T ratio appears to be 10% lower.

The performance parameters of a gamma-ray spectrometer in real experimental conditions (in-beam, background, etc...) are determined by two quantities, the resolving power (or background reduction factor, R) which indicates how well a peak can be isolated from the background and the total photopeak detection efficiency P_{ph}. The former is related to the P/T ratio and the energy resolution ΔE_γ (FWHM) by the following formula [58]

$$R = 0.76 \cdot \frac{SE_\gamma}{\Delta E_\gamma} \cdot P/T \tag{3.1}$$

where SE_γ is the average separation of the peaks of the spectrum and the 0.76 factor

comes from the fraction of a Gaussian peak which is included in setting a coincidence gate.

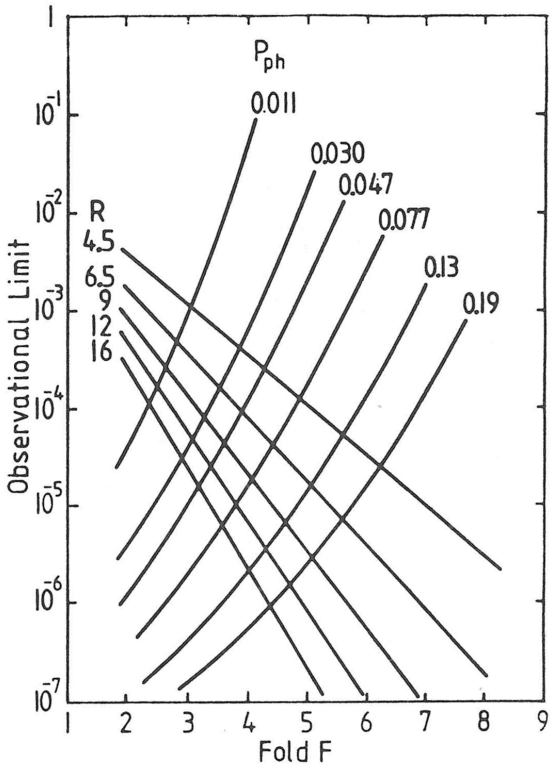

Figure 3.8: Observational limit as a function of fold f for various values of R and P_{ph} respectively. The observational limit is determined by the intersection of the R and P_{ph} curves. From [16].

In high-spin studies, where long cascades of gamma rays are emitted, the resolving power can be estimated as R^f where f is the fold of the cascade ($f-1$ gates are applied to obtain the specific spectrum). It can be seen that as f increases, the parameter R^f increases. This is due to the fact that the background gets "diluted" in a f dimensions data analysis space [58, 16].

On the other hand, by rising the fold number, the counts in the peak of interest will decrease due to the lower probability to populate multi-fold events. The number of counts depends from the total photopeak efficiency P_{ph} [16].

The observational limit of a gamma-ray array as a function of f can be than extracted by considering the resolving power and the total photopeak efficiency. Figure 3.8 shows the observational limit as a function of f for various values of R and P_{ph}, respectively. Since a peak can be observed if the resolving power is sufficiently high and the number of counts is statistically significant, the observational limit is determined by the intersection of the R and P_{ph} curves.

Finally, the array experimental sensitivity is defined as the inverse of the obser-

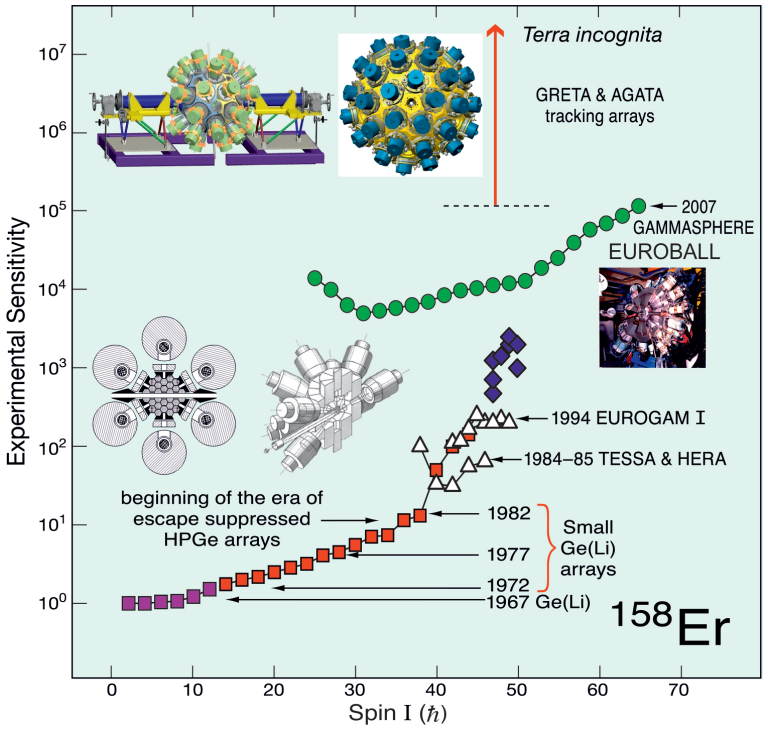

Figure 3.9: Experimental sensitivity of the gamma-ray arrays of the past decades as a function of the nuclear spin of the studied system. (J. Simpson, UKRI STFC, Private Communication.)

vational limit. Figure 3.9 shows the evolution of the experimental sensitivity of the gamma-ray arrays of the past decades as a function of the nuclear spin of the studied system, in this case the good rotor 158Er. It clearly shows that the AGATA and GRETA tracking arrays open a new area for research in nuclear physics.

Chapter 4

IPHC scanning table

As anticipated in the previous chapter, the pulse database of a detector can be alternatively obtained performing a full volume characterization. This operation can be performed by the use of the so called *scanning tables*. The AGATA collaboration uses different kinds of scanning tables which exploits diverse techniques and methods, although the basic operational principle of every scanning table is the same. A detector is fixed to the table structure and irradiated with a gamma ray source; several algorithms are then used to link each pulse shape measured to the position of the respective interaction. Presently, the scanning tables used by the collaboration are located in Liverpool, Orsay, Darmstadt, Salamanca and Strasbourg.

Liverpool scanning table [59] uses coincidence scanning technique. Several BGO detectors are placed around the detector vertically fixed on the structure. A collimated ^{137}Cs source irradiates the detector from below. Metal sledges are placed in front of the BGO detectors, perpendicular with respect to the scanned detector. In this way only gamma rays that are scattered in the detector by 90° relative to the beam direction can hit the BGO scintillators. The position of the interaction is geometrically defined by collimator and the lateral slits. Only coincidence events between the scanned detector and the BGO scintillators are recorded. The Liverpool scanning table spatial precision ranges between $1.5\,mm$ and $3.0\,mm$ and can perform a 3D scan of about 2000 points in about 2 months. The clean selection of events obtained with the technique used by the Liverpool scanning table makes it the reference point for all the others scanning techniques.

Orsay scanning table [60] also uses a coincidence scanning technique. A collimated ^{137}Cs source irradiates the detector from below, while 6 TOHR detectors (NaI scintillators) are placed around it forming a circle. A perforated tungsten mask is placed in front of each TOHR detector. The mask act as many small oriented collimators giving each detector a focal point. The TOHR detectors are installed so that their focal points coincide. By translating vertically the structure holding the TOHR detectors and rotating the scanned detector and translating the collimated source along one axis, it is possible to change the focal point relatively to the scanned crystal and thus perform a full volume scan. The Orsay table scans 2000 points in about one month.

Darmstadt and Salamanca scanning tables [61, 62] share the same technique implemented in a slightly different manner. A ^{22}Na source is placed between a position sensitive detector (PSD) and the scanned detector. The source emits, for each decay, two gamma rays in coincidence with the same energy ($511\,keV$) but opposite directions. The coincidences between the PSD and the detector are measured and the direction of the gamma ray pair is calculated using the position information given by the PSD. Subsequently, for the Darmstadt scanning table, the PSD detector is moved 90° around the scanned detector. The same effect is obtained for the Salamanca scanning table by rotating the scanned detector by 90° around its axis. The scanning operation is then repeated and the position of the interactions can be reconstructed by finding intersects between the two obtained datasets of directions. The recorded pulse shapes in the two perpendicular measurements are compared by a χ^2 test (see next section) and identical pulses are selected and associated to the intersect. Intersects are grouped in voxels which size can be modified. Both Salamanca and Darmstadt scanning tables can scan the full volume (~ 48500 voxels of $2 \times 2 \times 2\,mm^3$ for AGATA crystals) in few days, with a spacial resolution of $\sim 1 - 2\,mm$.

Summarizing, the first two tables have a clean selection but are quite slow in the data acquisition, while the second two tables have fast scanning times but are limited to scan the detector with $511\,keV$ gamma rays. Strasbourg scanning table [25] was designed with the aim of small scan duration, good spatial resolution and variable scanning energy. It relies on the *pulse shape coincidence scan* (PSCS) technique that allows to perform 3D scans, of the full crystal volume in times of the order of 15 days. In this chapter a description of the PSCS technique and the scanning table will be given, along with some preliminary results.

4.1 Pulse Shape Coincidence Scan method

The *pulse shape coincidence scan* (PSCS) [63] method allows full volume characterization of a given detector starting from two sets of data obtained by shooting the detector with a collimated gamma ray source. The detector is put at first in vertical position (see figure 4.1), then the collimated source is moved by regular steps in a plane perpendicular to the detector axis. For each position of the collimator all the pulses generated by the detector along the gamma ray beam are collected and a vertical beam dataset $\mathcal{V}$ is so obtained. The detector is then moved to horizontal position by rotating it by 90° (see figure 4.1) and a horizontal beams dataset $\mathcal{H}$ is obtained by repeating the same scanning procedure. The positions of the beams of the $\mathcal{V}$ and $\mathcal{H}$ datasets are chosen so that they (virtually) cross forming a three-dimensional *scanning grid*.

For a position sensitive detector (such as AGATA) two identical gamma rays that interacts in the same point will produce the same signal. If $\mathcal{V}$ and $\mathcal{H}$ datasets are compared, their pulses will differ except where the beams intersect. The similarity between two pulses can be evaluated with the following χ^2-*like* formula

$$\chi^2 = \frac{\sum_{i=0}^{N} (v_i - h_i)^2}{\sigma \cdot N} \tag{4.1}$$

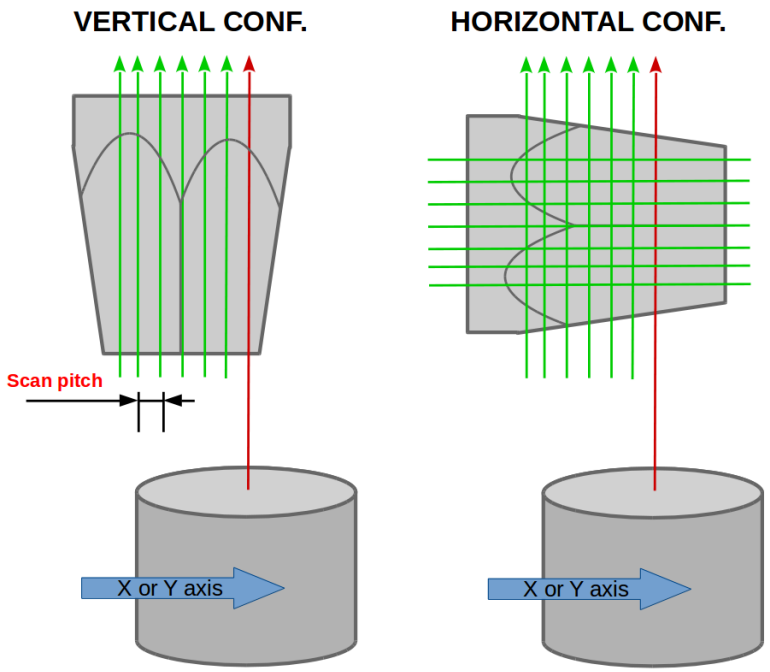

Figure 4.1: Simple scheme representing the operations needed to perform the PSCS technique. On the left the detector is in vertical configuration while on right the detector is in horizontal configuration. In this example the scan has a $2\,mm$ pitch.

where v_i and h_i are the samples of two pulses $\bar{v}$ and $\bar{h}$ coming from $\mathcal{V}$ and $\mathcal{H}$ datasets respectively, N is the total number of samples of each signal (it is implied that $\bar{v}$ and $\bar{h}$ are sampled at the same rate) and σ is the measured noise level of the signals coming from the scanned detector. The lower the χ^2 value, the most alike are the two compared pulses. Unfortunately, it does not exist an absolute threshold for the χ^2 value under which two pulses can be considered identical. This value, in fact, also depends on the experimental conditions, so that only relative evaluations can be done. In this regard, the main disadvantage of the PSCS technique lays in the fact that multiple interaction events could give rise to small χ^2 and appear as fake single-interaction events originated at the crossing point. This kind of events could have a negative impact on the final database quality and should be excluded if possible. As final comment it is worth to mention that a recent study [64] showed that the use of an optimized exponential value in equation 4.1 (χ^α instead of χ^2) could lead to better results for pulse selection and database quality.

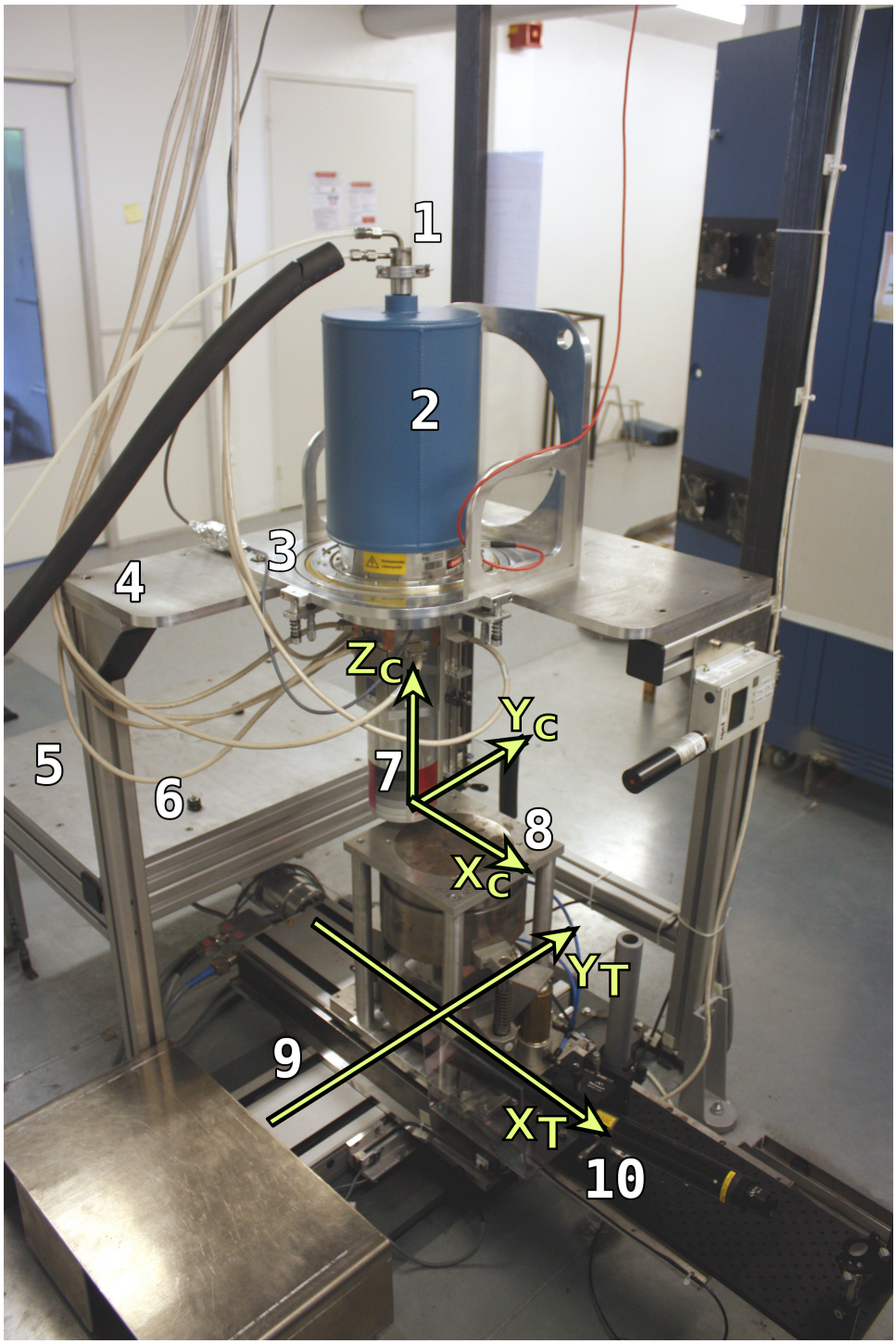

Figure 4.2: Picture of the scanning table: (1) LN2 pipes, (2) test-cryostat Dewar, (3) adjustment frame, (4) holding plate for vertical positioning, (5) holding plate for horizontal positioning, (6) fixing studs, (7) end cap of the detector, (8) collimator, (9) scanning table motorized axes, (10) alignment laser. The reference frame of the table $[X_T, Y_T]$ and the reference frame of the detector (crystal) $[X_C, Y_C, Z_C]$ are shown in green. [25]

4.2 IPHC scanning table setup

4.2.1 The frame

The table setup [24, 25] is shown in picture 4.2. A metal collimator, later described, sits on two motorized perpendicular axes that allow its planar movement in a range of $300\,mm$ in both X_T and Y_T directions. The axes are designed to sustain and move the $170\,kg$ heavy collimator with a precision of about $10\,\mu m$. Above the collimator level, two fixed plates allow the placement of the detector in vertical and horizontal positions. The detector is actually placed in an adjustment frame which is fixed on the plates by two centering studs. The adjustment frame allows the adjustment between the detector and the table axes, by tilting it using micrometric screws and by freehand rotating it (a fine bearing scale is used for measuring rotating angles). Finally, a laser alignment system is set on the mechanical support of the collimator and is used to keep the relative alignment of the detector when going from vertical to horizontal position.

4.2.2 The collimator

The collimator consists of a metallic cylindrical block, $189\,mm$ high with a diameter of $220\,mm$, made by the mechanical union of different components. These components are made of iron, lead and tungsten, materials that absorb the gamma rays which are not traveling through the central hole [25]. A simple representation of the section of the collimator is shown in figure 4.3.

The base of the collimator holds a cylindrical capsule containing the gamma-ray source. The base can slide down in order to open the collimator, allowing the swap of the source capsule. The capsule and the overall collimator are coaxial. Along the central axis of the capsule a channel with $1.6\,mm$ diameter is pierced. This channel runs from the top of the capsule to its center where the source is actually placed. Another channel, $165\,mm$ long, is pierced through the central axis of the collimator and is jointed with the capsules one. There is one capsule per gamma-ray source. Two configurations exist for the central part of the detector. The two will be referred as *original configuration* and *upgraded configuration*.

In the *original configuration*, the central part is made by 5 short pierced cylinders with an internal diameter of $2.5\,mm$ and a length of $23\,mm$. On top of these, 4 lead cylinders lead to the exit of the collimator. Finally, a Ta tube with an external diameter of $2.5\,mm$ and an internal diameter of $1.5\,mm$ runs through the cylinders. The *upgraded configuration*[1] allows to mechanically swap the central part of the collimator. It is possible to choose between three central parts which have diameters of $1.0\,mm$, $0.5\,mm$ and $0.2\,mm$.

[1] The upgrade of the collimator took place during the course of this work.

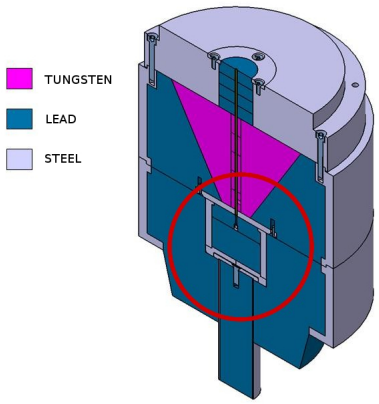

Figure 4.3: Rendered section of the collimator. The materials that compose the collimator are reported in the legend. A red circle highlights the capsule containing the gamma-ray source.

4.2.3 The sources

Three sources are used for scanning. Each emits gamma rays of different energies that can be used accordingly to their penetrating power (see section 1.5). An ^{241}Am source, which emits monochromatic gamma rays with an energy of $59.5\,keV$, is used for surface ($2D$) scans. A ^{137}Cs source, which emits monochromatic gamma rays with an energy of $661.7\,keV$, is used for deep scanning as well for the full volume characterization ($3D$) scans. Finally, a ^{152}Eu source, which emits gamma rays of several energies in the range of $122\,keV \div 1408\,keV$, is used to perform several advanced tests on detectors. The source emits some of its gamma rays in cascade and there's a negligible probability that two gamma rays pass at the same time through the collimator. For example, the $779\,keV$ gamma ray is always followed by the $344\,keV$ gamma ray but, following Geant4 simulations, the two have only 0.06% chance to come out of the collimator simultaneously[2].

For the work here presented, two sets of sources where used. The first set was used with the collimator in the original configuration, while the second set was used mostly with the upgraded configuration. The geometrical and physical parameters of the sources are summarized in table 4.1. Both the geometrical and physical properties have an important role in the estimation of the output rate which will be discussed in the following section.

[2]The cascade between the $344\,keV$ and $779\,keV$ transitions was simulated with Geant4. All the gamma rays with energies $344 \pm 5\,keV$ and $779 \pm 5\,keV$ going out of the collimator were counted. The ratio between this number and all the $779 \pm 5keV$ gamma rays out of the collimator gives the 0.06% probability.

Source	Active ϕ	Active h	Wdw. thk.	Activity
^{241}Am (OLD)	Spherical, $\phi = 1\,mm$		$0.2\,mm$	$0.07\,GBq$
^{137}Cs (OLD)	$2\,mm$	$2\,mm$	$0.2\,mm$	$0.37\,GBq$
^{241}Am (NEW)	$3\,mm$	$3\,mm$	$0.23\,mm$	$1.5\,GBq$
^{137}Cs (NEW)	$3\,mm$	$3\,mm$	$0.38\,mm$	$1.85\,GBq$
^{152}Eu	$3.18\,mm$	$2.2\,mm$	$1\,mm$	$0.74\,GBq$

Table 4.1: Geometrical and physical information for the different sources. All the sources are cylindrical except where noted. The sources are encapsulated in stainless steel and the window thickness is indicated in the fourth column of the table. The source activities are the ones calculated by fall 2018.

4.2.4 Data acquisition (DAQ)

The data acquisition (DAQ) is done with TNT2 cards [65], developed at IPHC. These cards cover both the digitizing and pre-processing of the signals done by the standard AGATA electronics (see section 3.3.1). Each card has 4 channels, so 10 cards are used during the scan of an AGATA detector unit, 9 for the 36 segments and one for the core signal used as trigger. Each channel samples the incoming signal with $14\,bit$ resolution and $100\,MHz$ rate, subsequently the energy is read applying the MWD algorithm (see section 3.3.1). For the measurements shown in this work, the signals were sampled in a time window of $1.2\,\mu s$ (120 samples) and a $5.95\,\mu s$ shaping time ($k = 4\,\mu s$, $m = 2\,\mu s$, $s = 1.75\,\mu s$, $w = 0.2\,\mu s$, see figure 3.6c) was used for the MWD procedure.

The acquisition chain is structured as follows. The differential signals coming from the detector preamplifiers are carried to the DAQ via MDR cables and converted to single-ended signals by dedicated modules before entering the TNT2 cards. The 10 TNT2 cards are linked in a daisy chain, with the core card being the master. The DAQ is triggered each time the master card receives a signal from the core. The DAQ is managed through a workstation linked to the cards via USB. Finally, during the data acquisition, all the data are transferred and stored on a dedicated workstation.

4.3 Tested detectors

Two detectors were involved in the work here presented: a S-type AGATA detector and a planar 3×3 pixelated $HPGe$ detector (which will be referred from now on as "3×3 pixelated detector"). The former was used in both simulations and real measurements while the latter was used exclusively in simulations. The geometrical features of the two detectors were faithfully replicated in the simulations.

The S-type detector is, to be precise, the S001 unit, the first prototype unit commissioned from the collaboration, and its geometry was already discussed in section 3.3. When mounted on the table, the distance of the front face of the collimator from the center of the detector in both vertical and horizontal configuration is $54\,mm$ and $95\,mm$, respectively. A render of the detector as it appears in the simulations is shown in figure 4.4.

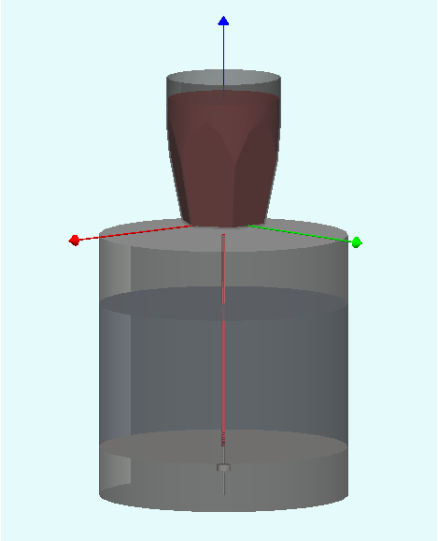

Figure 4.4: Geant4 render of the S001 detector and collimator geometry used for the Monte Carlo simulation.

The 3×3 pixelated detector is also a prototype, owned by the IPHC AGATA group. The detector (in figure 4.5) has a rectangular shape with an active volume of $51 \times 51 \times 19.9\,mm^3$. One side of the active part is segmented by nine $17 \times 17\,mm^2$ boron-implanted electrodes arranged in a 3 rows, 3 columns matrix, while on the opposite side lies the core contact realized with a $0.3\,mm$ thick lithium layer. A *guard ring* of inactive germanium with a thickness of $4.5\,mm$ is placed around the active area and helps to regularize the electrical field at the edges of the detector. The total volume of the germanium crystal is then $60 \times 60 \times 20.2\,mm^3$. The average impurity concentration of the germanium, specified by the manufacturer, is comprised between $0.90 \cdot 10^{10}\,cm^{-3}$ and $0.95 \cdot 10^{10}\,cm^{-3}$. Finally a FR-4 board facing the segmented contact (see figure 4.5) holds the nine cold preamplifiers of the detector on the segmented side.

The detector is mounted in a dedicated cryostat with a cylindrical aluminum end-cap. The cylindrical walls of the cap are $0.8\,mm$ thick, while its front face is $2\,mm$ thick. The detector central axis is not collinear to the cap axis, but is shifted by $10.25\,mm$, so that the cap axis lays along the Li-diffused contact of the detector. When the detector is put on the scanning table in vertical configuration, the distance between the front of the aluminum cap and the top of the collimator is $110\,mm$. The distance between the center of the detector and the face of the collimator is $159\,mm$. With the detector in horizontal configuration the segment contacts face the collimator and the distance of the top of the collimator is $39\,mm$ from the side of the cryostat cap and $80.55\,mm$ from the center of the detector.

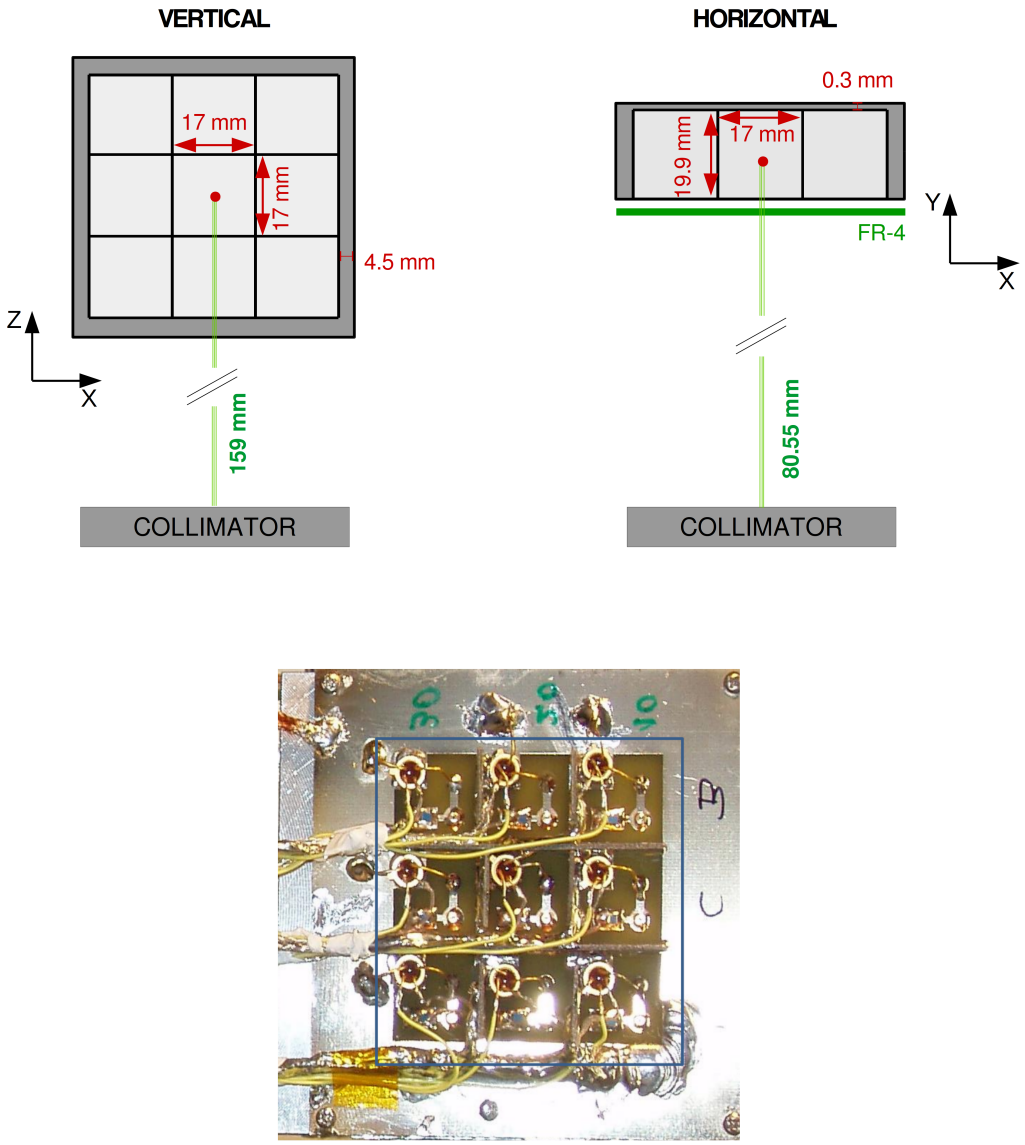

Figure 4.5: Simple schematics of the planar 3×3 pixelated *HPGe* detector. The sizes of the segments and the guard ring are shown in the top panels along with the distances of the center of the detector, placed both in vertical and horizontal configuration, to the front face of the collimator. The picture on the bottom shows the cold electronics of the segments which is facing the pixelated contact and is highlighted by the blue outline.

4.3.1 Response function

In real measurements, the actual signals coming from the acquisition system have different shapes with respect to the theoretical ones. This is due to the fact that the detector-plus-preamplifier system has a limited bandwidth which slows down the output charge pulse. The result is that the leading edge of the real pulses are altered with respect to the expected ones. The output signal $V(t)$ is, in fact, convoluted with a response function $R(t)$ so that

$$V(t) = \int_0^t I(t - t') \cdot R(t')\, dt' \tag{4.2}$$

where $I(t)$ is the input current. It is possible to extract the response function from the preamplifier output signal if the input current is known, by deconvolving equation 4.2. For the simulations presented later in this work, the response functions for both the S001 detector and 3×3 segmented detector were convoluted with the corresponding calculated signals.

The response function used of the S001 detector was extracted from the AGAPRO software source code. AGAPRO [66] is a software used by the AGATA collaboration that contains routines and algorithms to process the data flow coming from the AGATA acquisition system. The response function, shown in figure 4.6, is derived from data taken during the LNL (Laboratori Nazionali di Legnaro) experimental campaign using a pulser. Both the core and segments response functions were sampled, in fact these two possess different characteristics due to the fact that the core contact has different (bigger) intrinsic capacitance with respect to the segment contacts. Due to this, generally core signals have slower leading edges than the segments ones.

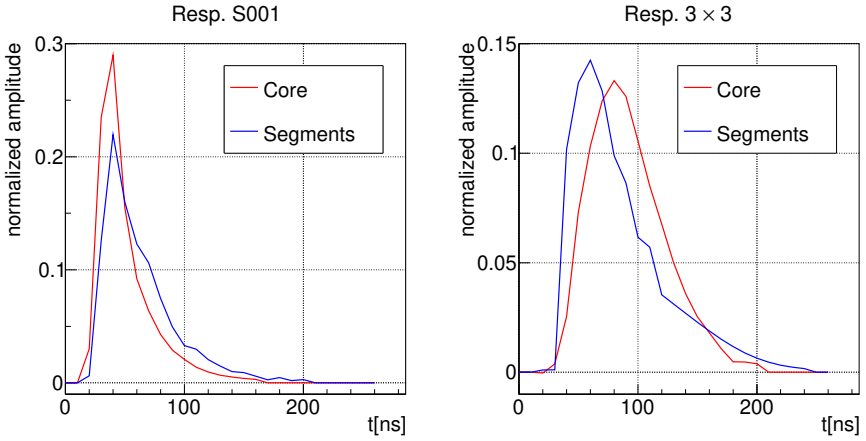

(a) (b)

Figure 4.6: (a) Response functions for the AGATA detector. (b) Response functions for the 3x3 segmented detector.

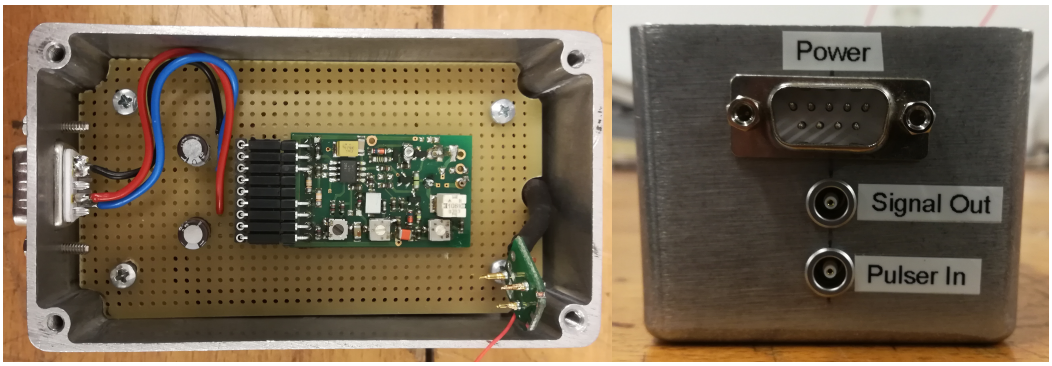

Figure 4.7: Pictures of the test box used to measure the response function of the 3×3 pixelated detector. On the left, a plugged preamplifier can be seen.

The response function of the 3x3 segmented detector was, instead, specifically measured. Since the detector doesn't have a test input (which is instead present on AGATA detectors) the measurements were performed by using a special circuit, courtesy of the IKP Cologne group, which allows to physically simulate the equivalent circuit of the 3×3 detector and to connect it to its preamplifiers (see pictures 4.7). A square pulse (in figure 4.8a) with an amplitude of $1\,V$, duration time of $100\,\mu s$ and rise-time of $5\,ns$ was used to test the core preamplifier and one of the segments preamplifiers[3]. The output was sampled with a digital oscilloscope. The outputs signals (in figures 4.8b and 4.8c) have rise-times of $\sim 40\,ns$ and $\sim 90\,ns$ for the core and the segment preamplifiers, respectively. This goes against what was previously said about response functions and leading edges, but it has to be pointed out that the preamplifiers of the 3×3 pixelated detector were tuned in this peculiar way in order to minimize oscillation problems on the signals. Finally, in order to obtain the response function, the output signals were derived and normalized, giving the results shown in figure 4.6.

4.3.2 Realistic noise extraction

Noise characteristics were extracted from real measurements from both the S001 detector and the 3×3 pixelated detector with the following procedure (schematized in figure 4.9). An uncollimated ^{137}Cs source was used to irradiate the detector. Then, the signals coming from events in which a $662\,keV$ gamma ray was absorbed in a single segment were selected for each segment (including the core). For each pool of signals the samples of the baseline were put on histograms after being normalized as follows. The signal is shifted so that the baseline is centered at zero. Then the amplitude of the signal (difference between the baseline and the plateau) is considered to have a value[4] of $661.7\,keV$ and the samples of the baseline are scaled proportionally to this value. In average, ~ 2000 pulses per segment were used to extract the noise characteristics for the

[3]Since the segment preamplifiers of the 3×3 pixelated detector are of the same type and similarly tuned, only one response function was measured.

[4]The unit here used is arbitrary. Electron-volt where used for the sake of simplicity.

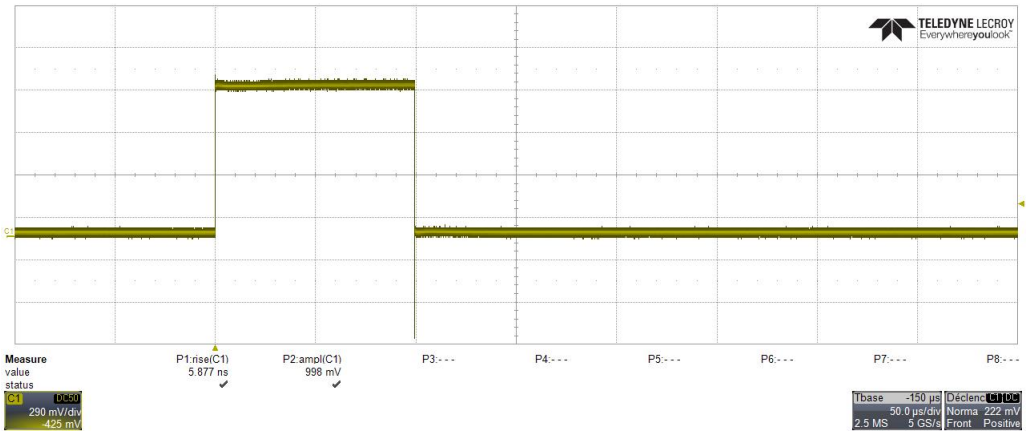

(a)

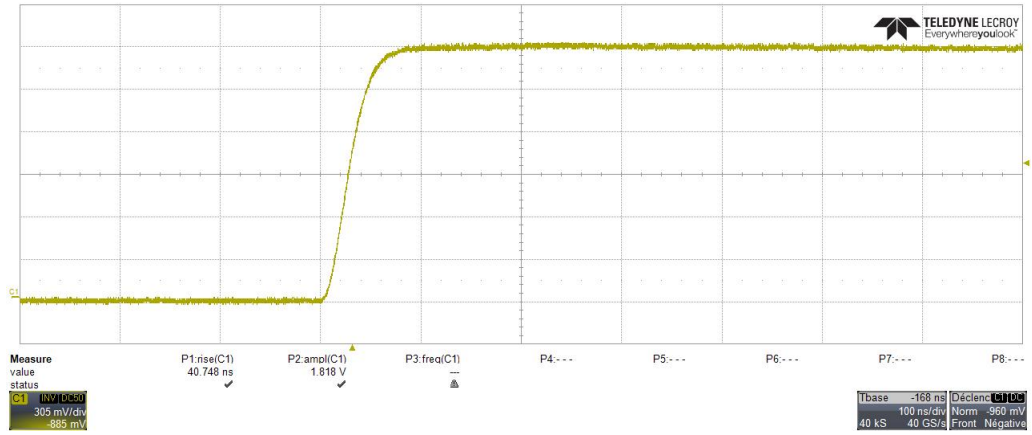

(b)

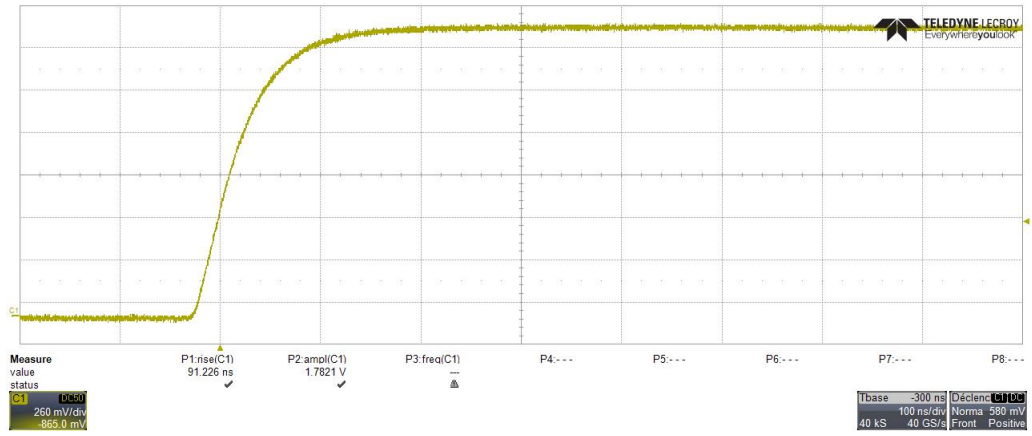

(c)

Figure 4.8: (a) Input signal used to measure the response function of the 3×3 pixelated detector. (b) Inverted output signal measured from the core preamplifier. (c) Output signal measured from one of the segments preamplifier.

S001 detector and $\sim$ 50000 for the 3×3 pixelated detector. The histograms show that, as expected, the noise has a Gaussian profile. Also, it is assumed that the amplitude of the noise is independent of the amplitude of the considered signal. A Gaussian fit allowed the extraction of the noise amplitude as the σ of the curve. The extracted values are reported in table 4.2. It is worth to note that the noise amplitude for the core is higher than the amplitude for the segments for both the S001 and 3×3 pixelated detector.

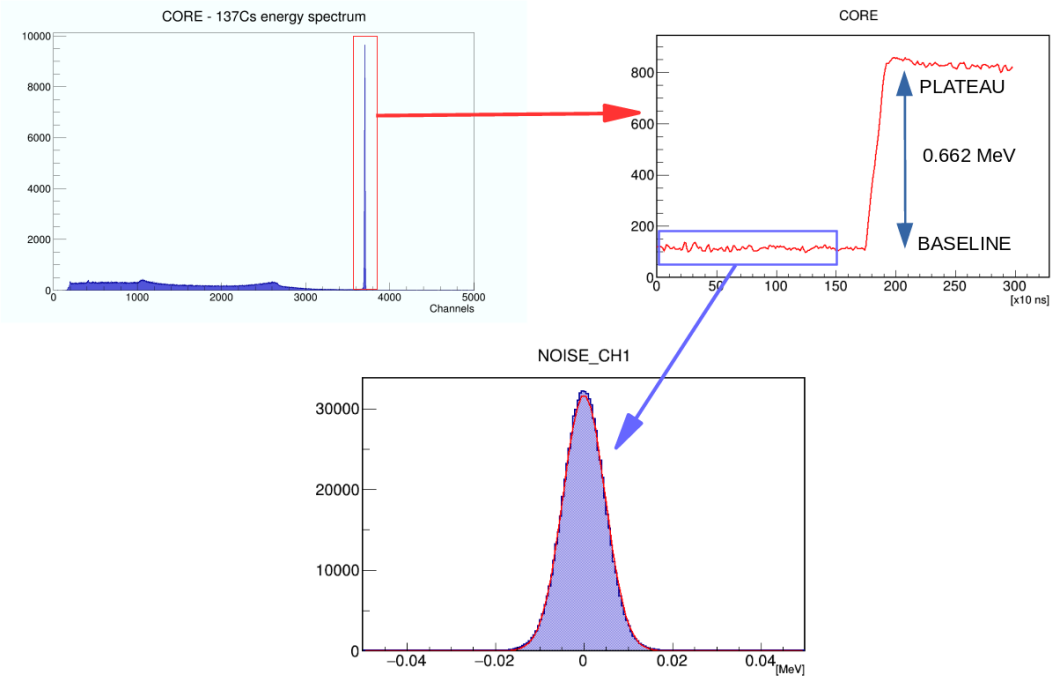

Figure 4.9: Scheme of noise extraction procedure.

	Core	Seg. avg.	Seg. min.	Seg. Max.
S001	5.9 keV	2.1 keV	1.7 keV	2.6 keV
3x3 segmented	4.8 keV	2.1 keV	1.7 keV	2.6 keV

Table 4.2: Measured standard deviation of the signal noise. For the segments the average of all the values is reported together with the minimum and maximum value measured for a single segment.

4.4 Beam simulations and measurements

The gamma ray beam output of the collimator was the object of a preliminary study performed with the use of Geant4 [67], a Monte Carlo software that simulates the interaction of radiation with the matter (see section 5.1). Both the geometry and materials

of the collimator and position and dimensions of the gamma-ray sources were introduced in the simulation. A graphical representation of the collimator as it appears in Geant4 can be seen in figure 4.4.

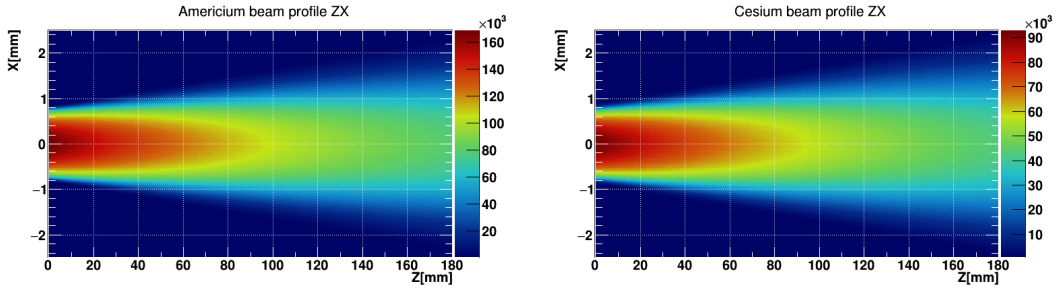

(a) (b)

Figure 4.10: Beam profile projection on the ZX plan for both the americium (a) and cesium (b) sources. The collimator is in the original configuration.

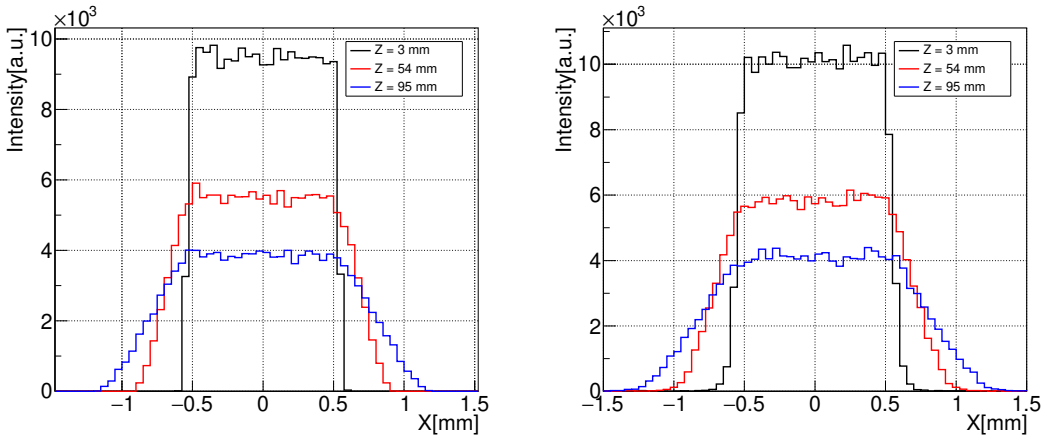

(a) (b)

Figure 4.11: Beam profile sections at different heights above the collimator $Z = z - z_p$ for both americium (a) and cesium (b) sources. The profile sections are obtained by considering the events in a $50\,\mu m$ thick slice at the center of the beam spot.

An event generator uniformly generates the starting point of gamma rays of a chosen energy inside the volume of the simulated source. The gamma rays are then propagated along an isotropically generated direction. If a gamma ray exits the collimator, its position (x_p, y_p, z_p) and momentum direction (v_x, v_y, v_z) are stored and the beam profile

is reconstructed with the following equations

$$\begin{cases} x = (z - z_p) \cdot (v_x/v_z) + x_p \\ y = (z - z_p) \cdot (v_y/v_z) + y_p \\ z \in [0; \infty] \end{cases} \tag{4.3}$$

where the variable z is used as a parameter and $v_z > 0$.

The beam profiles for ^{241}Am and ^{137}Cs with the collimator in the original configuration are shown in figure 4.10. Projections on the x axis for different z values[5] are shown in figure 4.11. As it can be seen the beams haven't a sharp pencil-like output and their spots become larger as the distance $Z = z - z_p$ from the hole of the collimator increases. This becomes more evident by looking at the histograms shown in figure 4.11 and by looking at tables 4.3 and 4.4 where the FWHM of the distributions are reported for the original configuration and for the the new configuration respectively.

	Simulated 1.5 mm collimator	
Z	Am	Cs
3	1.6128 ± 0.0002	1.6443 ± 0.0003
80	2.2879 ± 0.0004	2.4005 ± 0.0006
160	3.009 ± 0.001	3.130 ± 0.001
	Measured 1.5 mm collimator	
3	1.60 ± 0.01	1.69 ± 0.01
80	2.29 ± 0.01	2.41 ± 0.03
160	3.04 ± 0.04	3.46 ± 0.04

Table 4.3: *FWHM* in mm of the beam profile distributions at different distances from the exit of the original collimator. All units are in mm.

	Simulated					
	0.5 mm collimator			1.0 mm collimator		
Z	Am	Cs	$Eu\,(1408\,keV)$	Am	Cs	$Eu\,(1408\,keV)$
3	0.5349 ± 0.0004	0.5525 ± 0.0005	0.5711 ± 0.0007	1.0795 ± 0.0006	1.1133 ± 0.0009	1.147 ± 0.001
54	0.689 ± 0.001	0.728 ± 0.001	0.753 ± 0.002	1.408 ± 0.002	1.453 ± 0.002	1.504 ± 0.003
95	0.804 ± 0.002	0.862 ± 0.002	0.887 ± 0.003	1.658 ± 0.003	1.718 ± 0.004	1.774 ± 0.005
	Measured					
Z	Am	Cs	Eu	Am	Cs	Eu
3	0.531 ± 0.008	0.52 ± 0.02	0.52 ± 0.01	1.074 ± 0.008	1.13 ± 0.01	1.09 ± 0.02
54	0.68 ± 0.01	0.75 ± 0.02	0.76 ± 0.02	1.43 ± 0.01	1.47 ± 0.03	1.39 ± 0.02
95	0.81 ± 0.02	0.89 ± 0.02	0.86 ± 0.02	1.65 ± 0.02	1.81 ± 0.03	1.63 ± 0.03

Table 4.4: *FWHM* in mm of the beam profile distributions at different distances from the exit of the upgraded collimator. All units are in mm.

[5]The z values correspond to three distances of interest: exit of the collimator and position of the center of the S001 AGATA detector in horizontal and vertical positions.

The beam diverges with a maximum angle of $\pm 0.5°$ ($\pm 0.3°$) for the $1.5\,mm$ ($1.0\,mm$) diameter collimator. Further it can be seen that the americium beam is slightly sharper than the cesium one. That's because the gamma rays emitted by americium are less energetic, thus they are more likely to be absorbed inside the tungsten of the very last segment of the collimator hole, while the gamma rays emitted by the ^{137}Cs source can easily pass through the corner of the collimator hole.

The beam profile of the sources for the different configurations of the collimator was measured with an IPIX sensor (see figure 4.12). The sensor is a pixelated $CdTe$ detector. It is made by 256×256 pixels each with an area of $55 \times 55\,\mu m^2$ and a thickness of $1\,mm$. The detector is generally used for imaging purposes and is very compact and easy to handle. The detector was mounted on an adjustable stand and put perpendicularly to the beam at various heights.

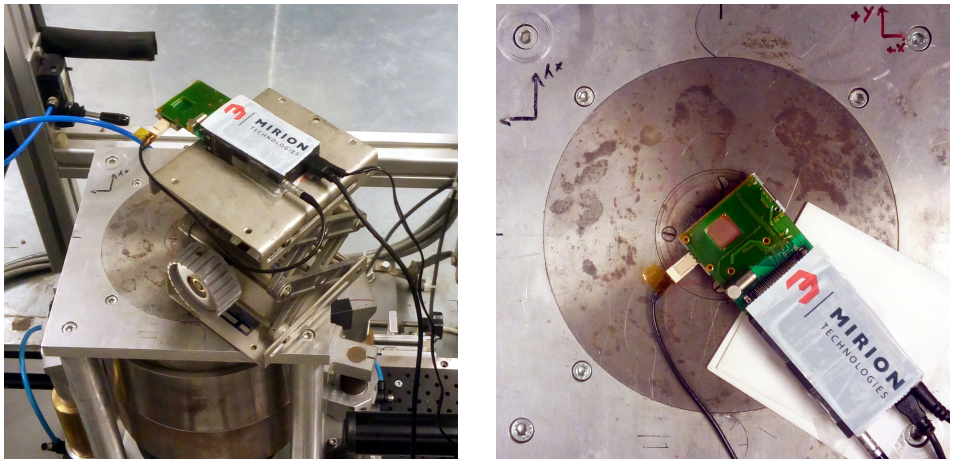

(a) (b)

Figure 4.12: Pictures of the experimental setup for the beam-profile measurement with the IPIX detector. (a)The IPIX detector is placed on a lifting platform (b) perpendicular to the beam direction.

An example of beam spot acquired is shown in figure 4.13. The FWHM of the distribution were calculated by fitting the beam profiles with a Gaussian function convoluted with an error function, which take the form

$$y = A \cdot \left(Erf\left(\frac{x-\mu+r}{\sqrt{2}\cdot\sigma}\right) - Erf\left(\frac{x-\mu-r}{\sqrt{2}\cdot\sigma}\right)\right) \tag{4.4}$$

where A is an amplitude constant, μ and σ are the mean value and the standard deviation, respectively, of the Gaussian part and r is the half-width of the plateau. The values are reported in tables 4.4 and 4.3. The values of the measurements and simulations are in good agreement except for the ^{152}Eu source. This is due to the fact that the IPIX sensor is not thick enough to efficiently detect high energy gamma rays (i.e. $1408\,keV$) and moreover the branching ratio of low energy gamma rays in europium (i.e. $122\,keV$ and $344\,keV$) is quite large compared to the one of high energy gamma rays (see table

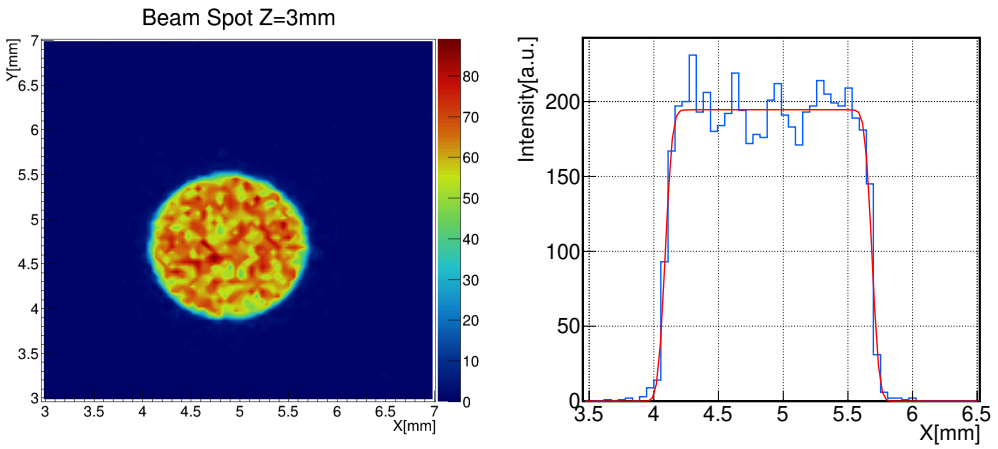

(a) (b)

Figure 4.13: Beam spot distribution of the americium source measured at $Z = 3\,mm$ for the $1.5\,mm$ collimator. (a) $2D$ distribution and (b) beam profile fitted with equation 4.4.

4.6 further in the section). This shifts the measured beam widths to a value closer to the ones of the americium. On the other hand for the simulation of the europium beam, only events with $1408\,keV$ were considered, leading to a larger beam width as expected.

From the simulation it is also possible to evaluate the yield of the source-collimator system, that is the ratio $R_{yield} = \frac{\gamma_{out}}{\gamma_{tot}}$ of gamma rays that exit the collimator on the total number of gamma rays emitted. These evaluations are important to be able to determine the time duration of the data acquisition at each point of the scan, in order to have enough statistics in the photopeak of interest. For this purpose, the geometrical dimensions of the various sources were taken into account (see table 4.1) as well as the absorption of the stainless-steel window of the source encapsulation. If R_{Yield} is multiplied by the activity of the source and the branching ratio (BR) of the gamma ray of interest, it is possible to calculate how many gamma rays per second ($c.p.s.$) are emitted by the collimator. Results are reported in tables 4.5 and 4.6.

Source	Coll. $\emptyset$	R_{yield}	Activity	BR	c.p.s.
^{241}Am (OLD)	$1.5\,mm$	$4.08 \cdot 10^{-6}$	$0.07\,GBq$	0.36	107
^{137}Cs (OLD)	$1.5\,mm$	$4.32 \cdot 10^{-6}$	$0.37\,GBq$	0.851	1446
^{137}Cs (NEW)	$1.0\,mm$	$8.62 \cdot 10^{-7}$	$1.85\,GBq$	0.851	1357
^{152}Eu	$1.0\,mm$	$8.93 \cdot 10^{-7}$	$0.74\,GBq$	1.393	921

Table 4.5: Yield and count per second for the simulated sources. Branching ratios are found in [68].

$E\,(keV)$	BR	c.p.s.
122	0.286	189
245	0.076	50
344	0.265	175
779	0.129	86
867	0.043	28
964	0.146	97
1086	0.102	67
1112	0.136	90
1408	0.210	139

Table 4.6: c.p.s. for the relevant energies of Eu. Branching ratios are found in [68].

4.5 Absorption rate simulations

In the previous section the yield of the collimator for a given source was calculated, as well as the relatives c.p.s.. From this, the rate of absorption in a single segment of gamma rays of a given energy can be calculated. This information is useful to set (and predict) the duration of a scan, since it gives an indication on how many events of interest will be measured per unit of time.

A Geant4 simulation was run to estimate the absorption rate for the segments of an AGATA detector. The simulation was performed for the new ^{137}Cs and ^{152}Eu sources with the $1\,mm$ hole collimator. The detector modeled for the test is an S-type detector (see section 3.3). ADL (which will be be widely presented in section 5.1) was used to determine if a gamma ray is fully absorbed and in which segment.

A monochromatic beam of 2×10^5 gamma rays hit the detector in vertical position. The beam hits the detector in sector D (see figure 3.4 and 4.14) as the collimator is positioned at coordinates $x_c = -20\,mm$ and $y_c = 0\,mm$ in the frame shown in figure 4.14. The absorption rates are shown in tables 4.7, 4.8 and 4.9. As expected from figure 1.9, low energy gamma rays ($122\,keV$, $245\,keV$ and $344\,keV$) are most likely to be fully absorbed in the first segments of the detector. It is worth to note that in the case of gamma rays with $122\,keV$ the rate drops to zero due to the fact that the photons are completely absorbed in the first four segments. Going towards higher energies, gamma rays gain penetrating power but the probability to be absorbed in a single segment drops since now Compton scattered gamma rays have more energy and may travel further in the germanium due to the lower interaction cross section. Absorption rates also depend on the dimensions of the segment in which gamma rays interact. For example, for energies $\geq 662\,keV$ the rate in segment 20 is smaller than in segment 21 since its larger volume compensates for its backward positioning. Finally, tables 4.8 and 4.9 show, respectively, the counts per second (c.p.s.) and the counts per minutes (c.p.m.) of gamma rays absorbed by a segment, calculated for the ^{137}Cs and the ^{152}Eu source. It can be noticed that the ^{137}Cs source can deliver enough statistics in a $\sim 2\,min$ interval, while the same cannot be said for the ^{152}Eu source. It is not possible, in fact, to perform full volume

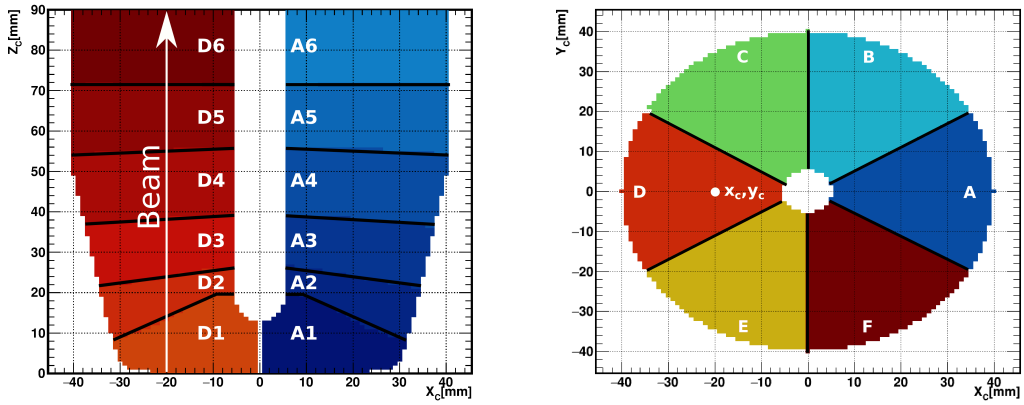

(a) (b)

Figure 4.14: (a) Vertical section of a S-type AGATA detector (cut at $Y_C = 0\,mm$) implemented in ADL. The black lines roughly show the separations between segments. The white line indicates the beam path used for this simulation. The numbers show the name of the respective segments. The D and A sectors are highlighted in shades of red and blue, respectively. (b) Horizontal top section of the same detector. The white dot indicates the x_C, y_C coordinates from which the beam is propagated. The 6 slices are highlighted in different colors.

$E\,(keV)$	Full det.	Seg D1	Seg D2	Seg D3	Seg D4	Seg D5	Seg D6
122	66.79	59.14	3.87	0.77	0.07	0.00	0.00
245	35.63	13.93	3.58	2.64	1.24	0.35	0.12
344	26.37	6.48	2.04	1.85	1.11	0.40	0.16
662	17.35	2.09	0.74	0.91	0.70	0.34	0.17
779	16.04	1.66	0.60	0.79	0.64	0.31	0.17
867	15.25	1.49	0.55	0.72	0.60	0.31	0.17
964	14.56	1.30	0.48	0.67	0.56	0.31	0.16
1086	13.82	1.12	0.45	0.57	0.52	0.29	0.18
1112	13.69	1.09	0.44	0.56	0.52	0.29	0.17
1408	12.39	0.87	0.35	0.49	0.46	0.28	0.19

Table 4.7: Percentage of gamma rays fully absorbed in a single segment when shooting a gamma-ray beam at $x_c = -20\,mm$ and $y_c = 0\,mm$. The second column refers to the percentage of gamma rays absorbed in the full volume of the detector.

$E\,(keV)$	Full det.	Seg D1	Seg D2	Seg D3	Seg D4	Seg D5	Seg D6
122	136	112	7	1	0.1	0.0	0.0
245	18	7	2	1	1	0.2	0.1
344	46	11	4	3	2	1	0.3
662	235	28	10	12	10	5	2
779	14	1.4	0.5	0.7	0.5	0.3	0.1
867	4	0.4	0.2	0.2	0.2	0.1	0.0
964	14	1	0.5	0.7	1	0.3	0.2
1086	9	1	0.3	0.4	0.4	0.2	0.1
1112	12	1	0.4	0.5	0.5	0.3	0.2
1408	17	1	0.5	0.7	1	0.4	0.3

Table 4.8: Counts per second (c.p.s.) of gamma rays fully absorbed in a single segment. The second column refers to the c.p.s. of gamma rays absorbed in the full volume of the detector.

$E\,(keV)$	Full det.	Seg D1	Seg D2	Seg D3	Seg D4	Seg D5	Seg D6
122	7572	6704	438	88	8	0	0
245	1072	419	108	79	37	10	4
344	2772	681	215	194	117	42	17
662	14130	1701	600	741	570	276	134
779	823	85	31	40	33	16	9
867	257	25	9	12	10	5	3
964	843	75	28	39	32	18	9
1086	560	45	18	23	21	12	7
1112	741	59	24	30	28	16	9
1408	1033	72	29	41	38	24	15

Table 4.9: Counts per minutes (c.p.m.) of gamma rays fully absorbed in a single segment. The second column refers to the c.p.m. of gamma rays absorbed in the full volume of the detector.

scans in a reasonable time with the actual ^{152}Eu source. This is due to the fact that the ^{152}Eu source is ~ 3 times less active than the ^{137}Cs source and moreover its activity is divided among different decay branches which leads to rates that are ~ 20 times smaller for gamma rays with energies of $779\,keV$ and $1408\,keV$. Never the less the ^{152}Eu source will be used for advanced testing and 3D scans on limited volumes (e.g. one sector).

Chapter 5

Simulation tools and methods

A simulation of the PSCS technique applied to the 3×3 segmented detector and a S-type AGATA detector is carried out using three software tools: Geant4, SIMION and the AGATA Detector Library (ADL). The simulation includes the gamma-ray propagation, the pulse shape generation and χ^2 selection with the database creation. A simple scheme of the procedure is shown in figure 5.1. In the following sections, a description of the previously mentioned tools will be given, along with the explanation of the data treatment and analysis procedure.

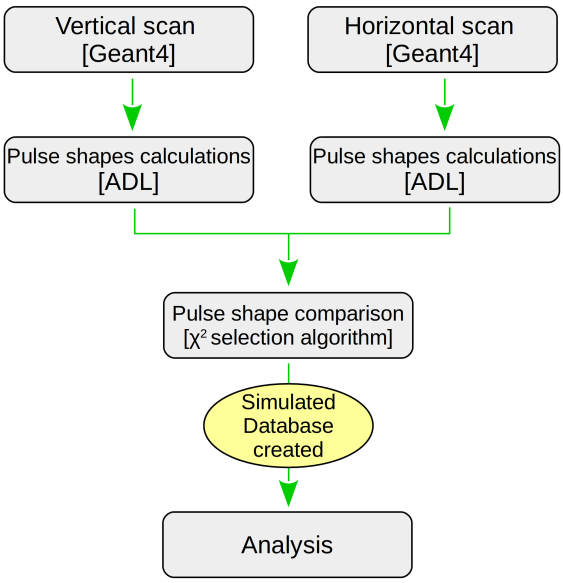

Figure 5.1: Simple work-flow scheme.

5.1 The AGATA Detector Library (ADL)

The *AGATA Detector Library* (ADL) is a software library developed in Köln University by the AGATA collaboration [56]. The library is used for the calculation of signals from highly segmented large volume HPGe detectors. In particular, ADL is actually used by the AGATA collaboration to calculate the signals generated from the AGATA detectors and build the relative signal databases to be used for pulse-shape analysis (PSA). ADL is the last instance of codes used by the AGATA collaboration to numerically characterize the detectors of the array. In the past different softwares where used, such as MGS and JASS [69, 46].

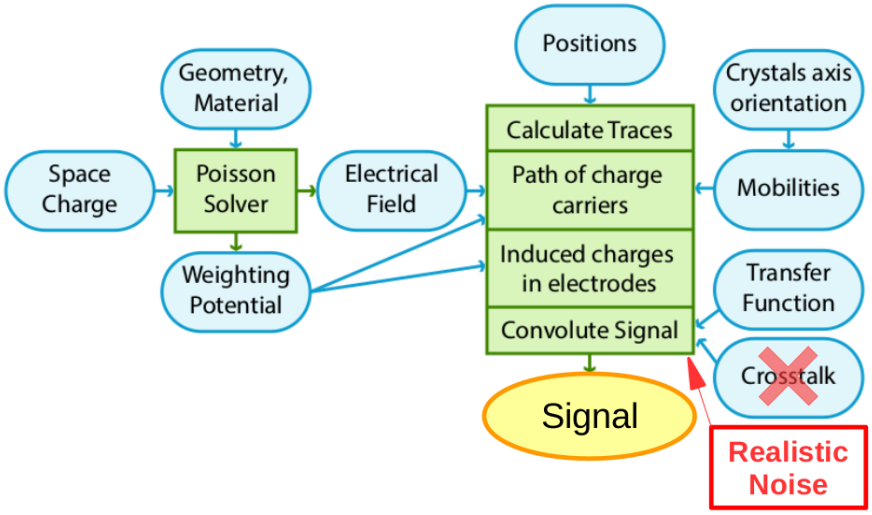

Figure 5.2: ADL I/O scheme (adapted from [56]). In blue and red are represented the parameters or inputs to be set in the code while in green are represented the different routines that form the code.

ADL operates on the theoretical basis described in section 2.8 with the addition of the following supplementary assumptions. The first assumption is that the charge cloud generated by the interaction of the gamma ray in the detector is considered point-like since the range of the electrons in the charge cloud can not be resolved. This is justified by the fact that a single interaction of a gamma ray of $1\,MeV$ in germanium generates a charge cloud with a radius of $0.5\,mm$ [46] which is much lower than the PSA position resolution [54, 55]. Diffusion effects are also neglected in ADL. Under action of diffusion, initial delta distributions of charges will be transformed into a Gaussian distribution with $\sigma = \sqrt{2Dt}$, where D is the diffusion coefficient and t the time. For AGATA detectors at liquid nitrogen temperature, D is typically lower than $300\,cm^2/s$ and collection times will not surpass $0.6\,\mu s$, giving an upper limit of $\sigma_{max} < 0.2\,mm$. Thus, having in mind the considerations previously made, the image charges induced by such Gaussian profile will not differ from the image charge induced by a delta distribution and diffusion effects can be neglected. Finally, the quasi-static field approximation is used, meaning that the

image charges at the electrodes of the detector are created instantaneously in response to the charges created in the bulk of the detector. Furthermore it is assumed that the extra field generated by the charges created by the gamma radiation is negligible compared to the external applied collection field.

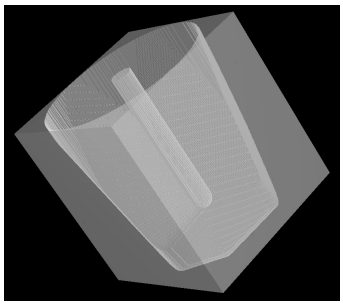

(a)

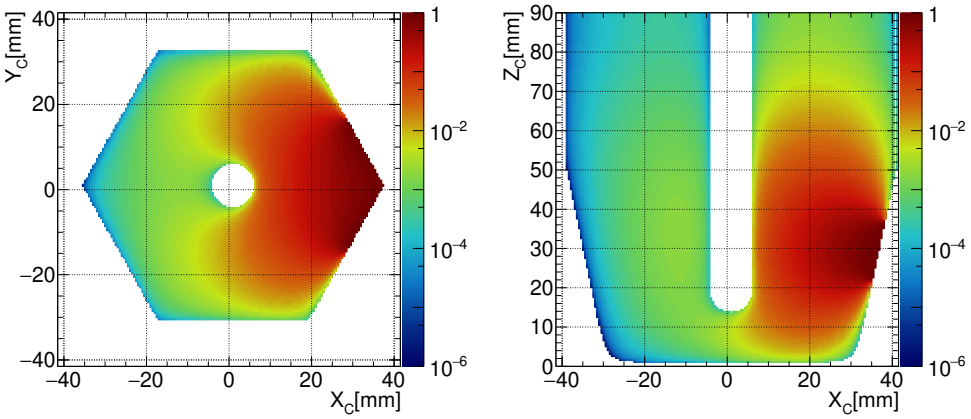

(b) (c)

Figure 5.3: (a) Type-S AGATA detector geometry as it appears in the SIMION visualizer. (b),(c) Weighting fields of segment $A3$ calculated with SIMION. The values are relative to $Z = 32\,mm$ for (b) and $Y = 0\,mm$ for (c).

A simple block scheme of the architecture of ADL is shown in figure 5.2. Different inputs and parameters should be set in the code before running. At first, the geometry and the space charge properties of the detector should be defined. This is done by setting the electrical fields and the weighting potentials for each segments. These two quantities are calculated through a Poisson solver. The ADL software package provides already the weighting potentials and electrical fields for the 4 different types of AGATA detector (type A, B, C and S). These where calculated with SIMION [70], a software that is generally used to design electrostatic lenses and simulate ions optics, but can be also used for discrete calculation of electrical fields for complex geometries. Examples of fields calculated with SIMION can be seen in figure 5.3. The SIMION files distributed with ADL package are the one used by the AGATA collaboration and have been used

in this work. A copy of SIMION was also used to calculate the electrical fields and weighting potentials for the geometries of the other detectors simulated in this work. The second group of parameters to be set are the mobility parameters for the electrons and holes in the crystal and its axis orientation. For the AGATA detectors these values were measured in [71] and are listed in table 5.1.

Electron mobility parameters			
Mobility along $\langle 100 \rangle$		Inter valley scattering rate	
$E_0\,[V/cm]$	507.7	$E_0\,[V/cm]$	1200
β	0.804	ν_0	0.459
$\mu_0\,[cm^2/V\,s]$	37165	ν_1	0.0294
$\mu_n\,[cm^2/V\,s]$	-145	ν_2	0.000054
Hole mobility parameters			
Mobility along $\langle 100 \rangle$		Mobility along $\langle 111 \rangle$	
$E_0\,[V/cm]$	181.9	$E_0\,[V/cm]$	143.9
β	0.735	β	0.749
$\mu\,[cm^2/V\,s]$	62934	$\mu\,[cm^2/V\,s]$	62383

Table 5.1: Mobility table. Values taken from [56].

With the fields and the mobility parameters set, it is possible to calculate the pulse shape generated by an event giving the positions and the deposited energies as input. These are obtained, for the the simulations presented in this work, via Geant4 and in particular it is considered that the energy is released at the gamma-ray interaction point[1]. The simulation uses the *FTFP_BERT* physics list, although the coherent scattering is not taken into account as it has no influence on the PSCS technique[2].

ADL allows to regulate some parameters of the pulse shapes such as the time alignment of the signal (trigger time), the number of time steps (samples) and the step size (time resolution or sampling rate). For this work, the pulses are 100 samples long and are calculated with a step size of $10\,ns$ (sampling rate of $100\,MHz$). The paths of the charges along the electric field are calculated with the 5th-order Runge Kutta integration method with adaptive step size control. The induced signals for every electrode of the detector are calculated depending on the drift of the electrons and holes to the electrodes. For every time step and for each interaction the weighting field evaluated at the position of the electrons is subtracted from the weighting field evaluated at the position of the holes. These differences are multiplied by the charge produced at the individual interaction. The sum of all interactions result in the signal set for the given

[1] This is an approximation, as the signal is generated by the ionization caused by the electron involved in the gamma-ray interaction. For an interaction of $1\,MeV$ in germanium, the electron can travel $1\,mm$ away from the gamma-ray interaction.

[2] In fact, the pulse shape is not affected by the process since no energy is released during the interaction. Although, as stated in [50], the coherent scattering can impact the tracking algorithm performances as it affects the ending parts of the tracks of multi-scattered gamma rays ($\sim 17\%$ of $1.332\,MeV$ events undergo coherent scattering).

event. In order to have a realistic output, the resulting signal can be convoluted with the response function of the preamplifiers and the crosstalk function. The used response functions were discussed in section 4.3.1. The crosstalk, instead, was not considered for this work mainly because the selected events are single segment hits, but also because crosstalk don't have an influence on the final shape of the signal. Finally, realistic noise (see section 4.3.2) was added to the final signals though a Gaussian random generator which was initialized with the measured values.

Examples of calculated signals can be seen in figures 5.4 and 5.5. In the former, a signal generated by a single interaction in the simulated S001 AGATA detector is compared with the corresponding signal extracted from a measured database of the detector S001 (see chapter 7). In the latter, different signals are generated with ADL by single interactions in the S001 AGATA detector at different positions. The top figure shows the signals for different interaction radii: the graph in the center shows the main signal generated by the hit segment, while the four graphs around show the transient signals of the neighboring segments. The graphs also show the difference in the maximum amplitude between the main signal (normalized to 1) and the transient signals. The figure on the bottom shows the signals for different interactions along a fixed radius. As the radius is fixed, the rise-time of the main pulse remains constant (there is a slight change due to the fact that charges speed depends on the germanium crystal orientation). On the other hand the amplitude of the transient signals changes with the interaction position: as the interaction approaches a neighboring segment, the respective transient signal (left or right) grows in amplitude.

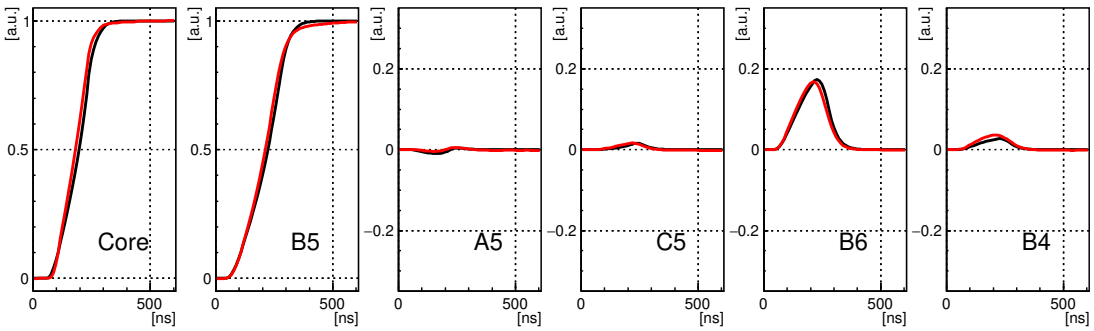

Figure 5.4: Comparison between a signal extracted from a measured database of the detector S001 (in red) and the corresponding signal calculated with ADL (in black). The first two panels show the core and hit segment (B5) signals. A5 and C5 are the right and left neighbor segments, respectively. B6 and B4 are the top and bottom neighbor segments, respectively.

5.2 Treatment of simulated data and χ^2 algorithm

A simple data generation and work-flow scheme has been represented in figure 5.1. As first step, the beam propagation in the detector is simulated with Geant4. The positions

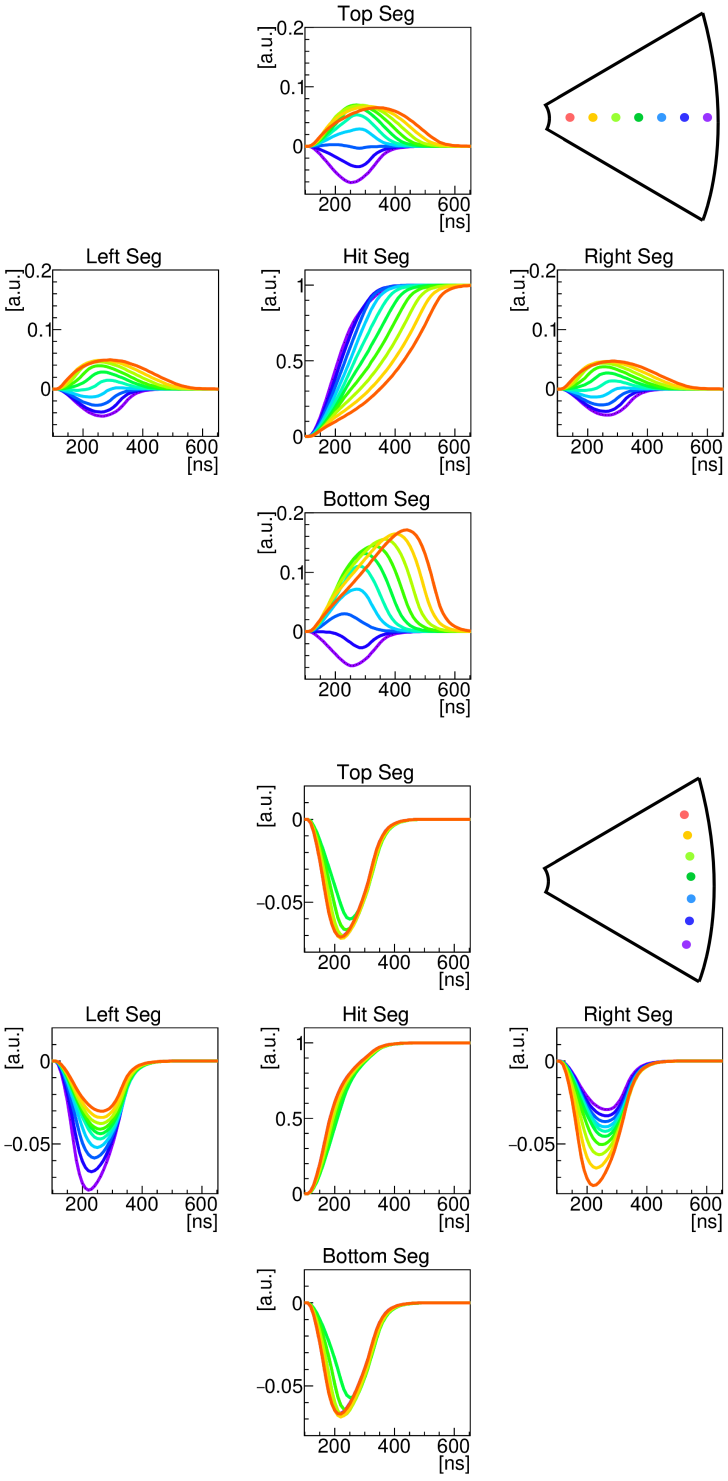

Figure 5.5: Pulse shapes for a S−type detector calculated for interactions at different radii (top panels) and at a fixed radius and at different lateral positions (bottom panel). For each panel the hit segment (central plot) and the top/bottom and left/right segments are represented. See text for details.

at which the beam should be shot are given to Geant4 via a script and for each position an individual output file is generated. The files contain information on the position and energy released by each interaction of each gamma ray that interacts in the detector (event).

The Geant4 generated files are then cleaned from events in which gamma rays are not completely absorbed by the detector and prepared to be inputted into the ADL application which will calculate the pulse shapes. During calculation only the events generated by gamma rays that are fully absorbed in a single segment are saved in the output file. For a typical simulated scan of an AGATA detector 2975 beam files are converted (1257 in vertical and 1718 in horizontal configuration). The average running time to convert 6000 events is $\sim 200\,s$, which means that the total calculation time is of about *one week* (on a 2.60 GHz processor machine) that can be halved if two conversion processes are run in parallel on more than one CPU.

The next step is the pulse-shape comparison, performed with a code that implements the PSCS algorithm presented in section 4.1. The overall code design follows the one described in [24] with several changes in the handling and selection of the traces. The path of the couples of files that have to be compared and the coordinates of the corresponding crossing point are listed in a script that is read by the program. At the beginning, the two files with the traces to compare are loaded in memory. This decreases the running time, since it was observed that accessing directly the original files (.root extension) is ~ 200 times faster. The typical amount of events that are treated for each file is 6000 (this parameter can be set at the beginning of a run). This mean that $3.6 \cdot 10^6$ couples of signals must be compared for each point of the scan grid. Actually, only the signals produced by events happening in the same segment are compared and this reduces the total amount of couples to compare.

The comparison between two pulses is performed by calculating the χ^2 value with equation 4.1, written in the form

$$\chi^2 = \frac{\sum_{seg\in\mathcal{M}}^{M} \sum_{i=i_0}^{i_f} (v_{seg,i} - h_{seg,i})^2}{M \cdot (i_f - i_0)} \tag{5.1}$$

where *seg* is the segment index, $\mathcal{M}$ is the M dimensioned ensemble of segments formed by the Core segment, the hit segment and the neighboring segments of the hit segment (4 segments if the hit segment is in the middle of the detector or 3 segments if the hit segment is at the top or bottom of the detector) and v_i and h_i are the samples of the vertical and horizontal signals, respectively. Finally, the comparison can be performed on a subset of contiguous samples in the window $[i_0, i_f]$, e.g. the window containing the leading edge.

A list with the IDs of the two compared pulse shapes and their calculated χ^2 value is updated after every comparison. The list of N_1 pairs of pulse shapes is sorted in increasing order of χ^2. The number N_1 is set before running the code. A couple of pulse shapes is entered into the list if its χ^2 value is lower than a threshold, otherwise it gets rejected. The threshold value is set high at the beginning of the run and then it self-adjusts, taking the value of the highest χ^2 value of the list. This *sliding threshold*

technique is necessary because the average value of the χ^2 varies widely within the scanned points, making impossible to set a global threshold. The sliding technique ensures that only the N_1 best matching couples of events are selected.

Once all the couples have been compared, it is possible that in the list of N_1 pairs of pulse shapes some leading edges have been selected more than once. These *extra* events are removed so that just one copy for each event ID is considered. The elements of the list are then decoupled forming a new list of N_2 events ready for the next step of the algorithm which is the *mean pulse-shape refin*ement. The refinement rejects the most diverging pulses giving a more coherent final selection of events, since the χ^2 procedure just described don't assure that the selected pairs are similar within each others[3]. The procedure is schematised in figure 5.6. At first the mean pulse of the N_2 events of the list is calculated. Then each pulse is compared with this mean pulse and the respective χ^2 is calculated with equation 5.1. The 5% of the N_2 pulses with the higher χ^2 are rejected and the procedure is repeated several times (usually 10 times). The remaining $N_{final} = N_2(1-0.05)^i$ (where i is the number of iterations) signals are averaged and the resulting signal will be part of the final database. A rejection rate of 5% was chosen to insure that the final pulse would be obtained by the average of more than 100 selected pulses. Finally, all the information related to the final selection of events is saved in an output file that will be further analyzed. The running times for the selection procedure are of the order of $\sim 7\,s$ per grid point (this is highly influenced by the number of couples to be compared) leading to a global running time of ~ 4.7 days for a typical full scan of an AGATA detector (simulated or measured) of ~ 60000 points which produces (considering the tapering) a database of ~ 45000 points.

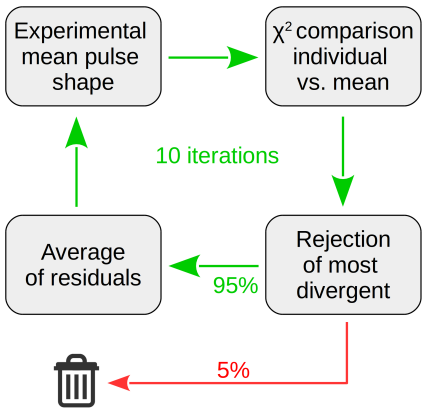

Figure 5.6: Refinement procedure scheme.

[3]This is specially true with experimental data, as explained in [24]. In fact it can happen that an event coming from the natural radioactive background can be accidentally selected even if its pulse shape is totally different from the expected one.

Chapter 6

Simulations of PSCS technique

The simulations for the evaluation of the PSCS technique performance were carried out on the 3×3 pixelated detector and a S-type AGATA detector presented in section 4.3. The simple geometry of the former helped designing the simulation and the analysis procedure. The same approach is then used to analyze the simulation results of the more complex S-type detector. In particular the simulations are performed modeling the S001 detector with which a real scan was performed as it will be shown in the next chapter. In this chapter the analysis on the simulated PSCS data for both the 3×3 pixelated and the S001 detectors will be presented.

6.1 Simulations of the PSCS technique on the 3×3 pixelated detector

A full scan of the 3×3 pixelated detector was simulated with the tools described in chapter 5. The simulated scan was performed with a pitch of $2 \times 2\,mm^2$, a collimation diameter of $1.5\,mm$ (which corresponds to the collimation diameter before the scanning-table upgrade) and a gamma-ray energy of $662\,keV$ (^{137}Cs source). For each vertical and horizontal scan line, 6000 events were used for the PSCS selection. Figure 6.1 shows the labeling of the segments of the detector and the reference frame used to present the results of the simulated scans. The different parameters extracted to quantify the quality of the PSCS technique are presented in the next sections.

6.1.1 Single-interaction events selection

The first parameter that is extracted from the simulated scan is the percentage of pulses generated by single interacting gamma rays (or single-interaction events) selected by the *pulse shape comparison* (PSC) algorithm. As mentioned at the end of section 4.1 multiple interaction events can be selected by the PSCS technique and may pollute the final database. Unfortunately there is no way to completely get rid of multiple interaction events and they can only be reduced by taking some precautions. One straightforward method is to apply the PSCS technique only to the pulses which are

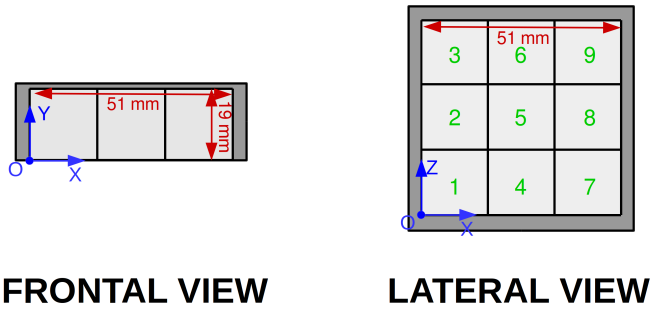

Figure 6.1: 3×3 pixelated detector: numbering of the segments and reference frame used to present the results of the simulation. More details on the 3×3 pixelated detector are in section 4.3.

generated by gamma rays which are fully absorbed in one single segment. To verify that hypothesis, some preliminary tests were made. A gamma-ray beam is shot in the middle of the detector placed both in vertical and horizontal configurations. The histogram of the total number of interactions of each gamma ray fully absorbed in *segment 5* (shown in figure 6.2a) shows that the majority of events ($\sim 91\%$) get absorbed after a maximum of 4 interactions, with an average of 2.77 interactions. By analyzing the energy spectrum of the first interaction of each gamma ray (in figures 6.2b and 6.2c) it can be noticed that only $\sim 2\%$ of the totality of gamma rays undergo a single-interaction photoelectric absorption. This percentage increases to $\sim 15\%$ if only events that are fully absorbed in a single segment are selected (see table 6.1).

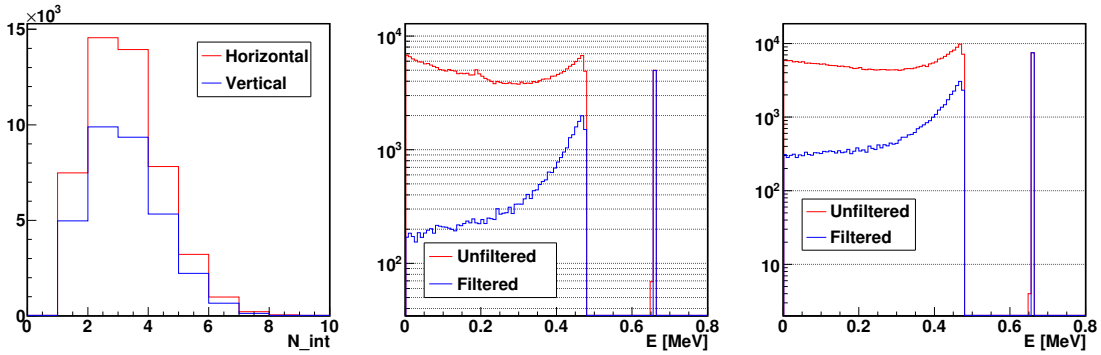

(a) (b) (c)

Figure 6.2: (a) Number of interactions for 662 keV gamma rays that are fully absorbed in *segment 5*. (b,c) Compared first-interaction energy spectra for both vertical (b) and horizontal (c) configurations of the system. The spectra in blue line are obtained considering only the gamma rays that are fully absorbed in *segment 5*. The peak at 661 keV belongs to both the blue and red spectra (even if only the blue line appears).

	$\gamma_{emitted}$	$\gamma_{detected}$	$\gamma_{full\,abs}$	γ_{single}	$\frac{\gamma_{single}}{\gamma_{detected}}$	$\frac{\gamma_{single}}{\gamma_{full\,abs}}$
Hor	685467	327179	48285	7478	2.28±0.03%	15.4±0.2%
Ver	1153784	293848	32605	4964	1.68±0.02%	15.2±0.2%

Table 6.1: Total number of gamma rays: emitted from the collimator (first column), interacting in segment *5* (second column), fully absorbed in segment *5* (third column), absorbed in one interaction (fourth column). The two lines refer, respectively, to horizontal and vertical configurations of the system. A difference in the values of the fifth column can be noted. This is due to the fact that when the detector is in vertical position the beam crosses segment *4* before entering segment *5* getting attenuated.

It is expected that the use of the PSCS technique will increase further the fraction of the selected single-interaction events. The graphs in figure 6.3 show the percentage of single events selected by PSCS. The graphs show different slices with a thickness of 1 grid unit ($2\,mm$) at different depths (Y_C) of the detector. As it can be seen the values vary from point to point in a range that goes from 5% to 57% with an average of 21%. The graphs in 6.3 also show that these values are overall homogeneous in the volume of the detector.

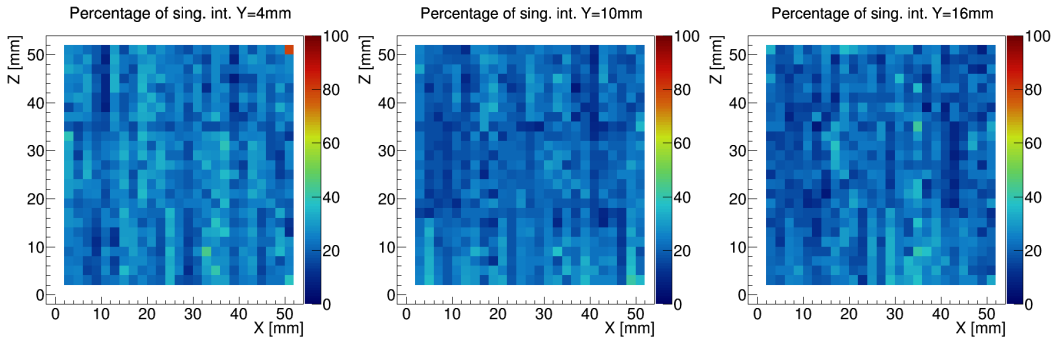

Figure 6.3: Percentage of single-interaction events selected by the PSCS technique over the total number of fully absorbed events. The graphs are relative to slices with a thickness of 1 grid unit ($2\,mm$) for Y_C =4 mm, 10 mm and 16 mm.

Finally the PSCS has not substantially increased (in average) the fraction of selected single-interaction events as expected. Moreover these values are far from the ones obtained by using the Liverpool scanning technique (taken as reference point for single interaction selection as stated in the introduction of chapter 4). In fact, a Geant4 application was designed to reproduce the Liverpool scanning technique on the 3×3 pixelated detector and it showed that the system is capable to get a single-interaction selection that ranges from 83% to 92%.

6.1.2 Interaction points parameters (IPP) search algorithm

In an attempt of improving the single-interaction event selection a complementary method, described in [49], was tested on the simulated PSCS 3 × 3 detector PSCS

dataset. The new method allows to extract the following three *interaction points parameters* (IPP) of an interacting gamma ray by analyzing the signal it generates:

- ◇ number of interactions of the incident gamma ray (IPn),
- ◇ coordinates of each interaction point and
- ◇ the energy deposited at that point.

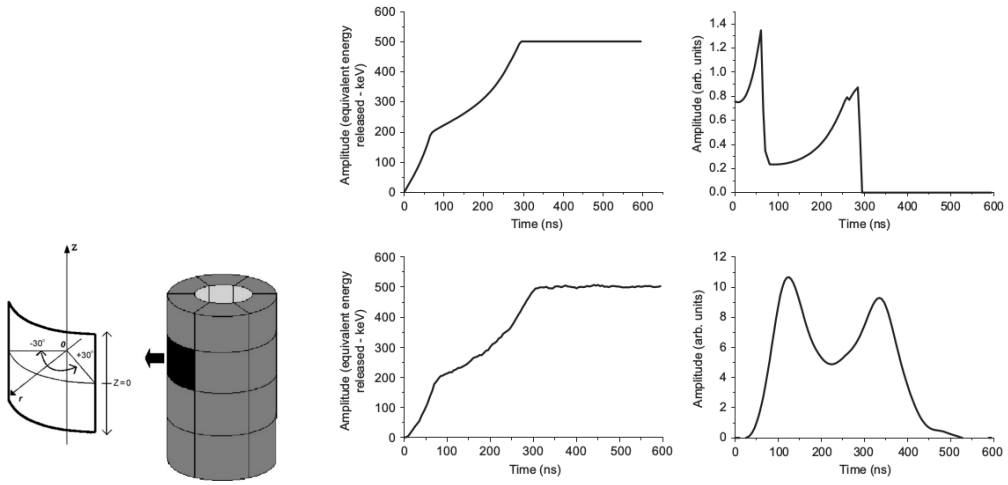

Figure 6.4: Figures from [49] reporting a study performed on a coaxial, multi-segmented MARS detector [48]. Numerically calculated pulse generated from gamma rays interacting in a segmented true coaxial detector (schematized on the left) and its respective current signal. The signal is originated by a 2-fold interacting gamma ray, depositing 60% of its energy at $R = 11.0\,mm$, $\theta = 22^\circ$ in the first interaction and the remaining 40% at $R = 31.0\,mm$, $\theta = 26^\circ$ in the second interaction. The signal on top shows the ideal case while the electrical noise, the transfer function of the preamplifier and a digital filtering where added to the calculation of the bottom signal.

The procedure was designed to pre-process data for more complex PSA routines in the AGATA PSA analysis. The IPP search algorithm exploits the feature that the slope of the net charge signal induced at the electrode of a segmented HPGe detector changes significantly as the charge is collected. These slope changes can be seen as *peak shaped structures* (PSS) in the current pulse[1] shape of a true coaxial detector, as exemplified in figure 6.4 (the following examples are taken from [49] and refers to a MARS detector [48]). From the figure, it can be seen that, in the appropriate time window, each PSS can be isolated and treated as a signal with $IPn = 1$. Moreover, the example shows also that the number of PSSs is proportional to the number of interactions, their position depends on the radius of the interaction (related to the diffusion time) and their amplitude is proportional to the energy released. The whole signal can be then decomposed and its IPP extracted by comparing each PSS with the pulses of a pre-calculated database.

[1] The current pulse is the derivative of the voltage signal at the output of the preamplifier.

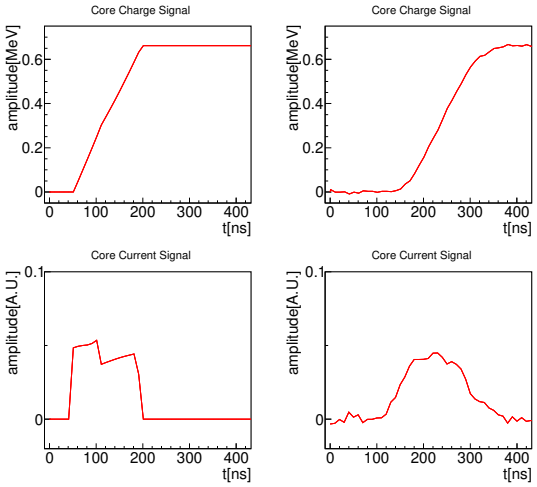

Figure 6.5: Pulse, simulated using ADL, generated by a single-interacting gamma ray in the 3×3 pixelated detector at position $X_C = 25.5$, $Y_C = 5.0$, $Z_C = 25.5$ and its respective current pulse. The signals on the left show the ideal case while a realistic electrical noise, the transfer function of the preamplifier and a digital filtering where added to the calculated signals on the right. The time shifts of the signals in the right panels is due to the introduction of the transfer function.

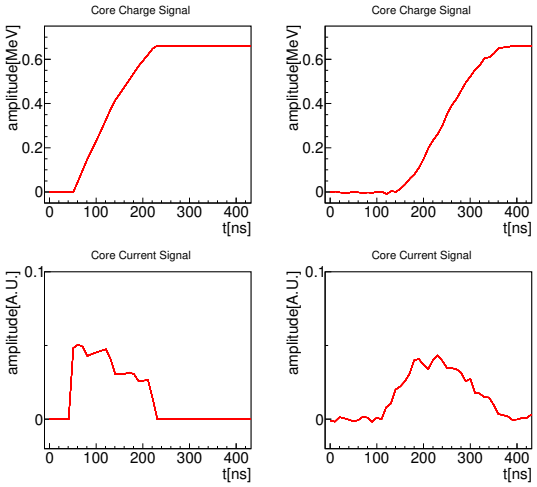

Figure 6.6: Pulse, simulated using ADL, generated by a two-fold interacting gamma ray in the 3×3 pixelated detector at positions $X = 25.5$, $Y_C = 11.0$, $Z_C = 25.5$, releasing 60% of the total energy, and $X_C = 25.5$, $Y_C = 3.0$, $Z_C = 25.5$, releasing the remaining 40%. On the bottom the respective current signal is shown. The signals on the left show the ideal case while a realistic electrical noise, the transfer function of the preamplifier and a digital filtering where added to the calculated signals on the right. The time shifts of the signals in the right panels is due to the introduction of the transfer function.

By determining the IPn for each event it would be possible, then, to raise the fraction of selected single-interaction events. For a 3×3 pixelated detector, the peaks structures are replaced by plateau-like structures which position depends on the depth of the interaction (Y_C) as can be seen in figures 6.5 and 6.6. The plateau-like structures are due to the over all linear trend of the potential of the planar detector. However the space charges in germanium bulk introduce a non-linear trend in the potential, making the plateaus not perfectly straight (in the ideal case).

From figures 6.5 and 6.6 it is seen that it is possible to disentangle (determine the IPn) a double interaction in a segment when no response function nor noise is applied and if the two interactions are well separated along Y_C direction. The task gets nearly impossible when the preamplifier response function and noise are added, as the signal lose definition with respect to its pure theoretical counterpart.

As a final test, lets consider an average pulse from a given database grid point. It is composed of single-interaction events and multiple-interaction events. In the latter there exist two-fold events exhibiting very similar voltage and current pulse shapes than single-interactions pulse, both being selected by the PSCS technique for the same grid point. From figure 6.7, it is clear that it is not possible to distinguish both types of interactions from the two current signals. In conclusion, the proposed algorithm is not effective for the purposes it was chosen for. Some explanations that help to understand why the algorithm fails will be given in the following section.

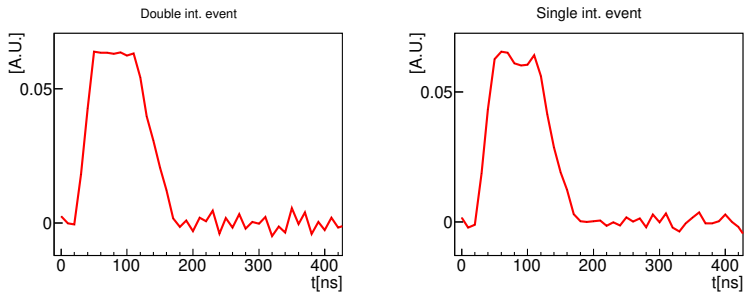

Figure 6.7: Comparison between two current pulses selected by the PSCS technique for the same grid point. The signal on the left is generated by a gamma ray interacting twice, while the signal on the right is generated by a single-interacting gamma ray.

6.1.3 Impact of multiple-interaction events on PSCS results

At the end of the previous section it was shown that the current signals coming from the PSCS selection at a given point of the database grid are basically indistinguishable. This, of course, is also true for the corresponding charge signal from which they were derived. This should come with no surprise, since the χ^2 algorithm is designed to select pulses that share the most similar shape.

To better show this feature, for each point of the database the average of all the signals generated by single-interacting gamma rays was compared with the average of all the signals generated by multiple interacting gamma rays, as shown in figure 6.8.

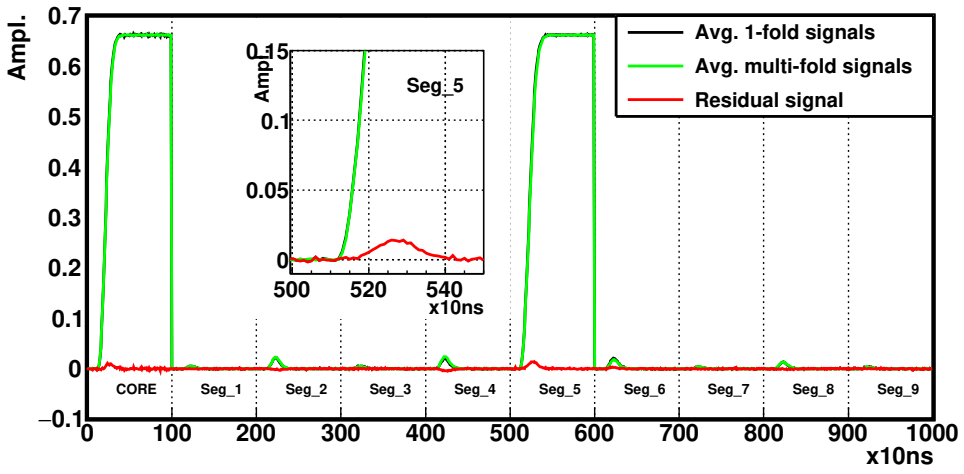

(a)

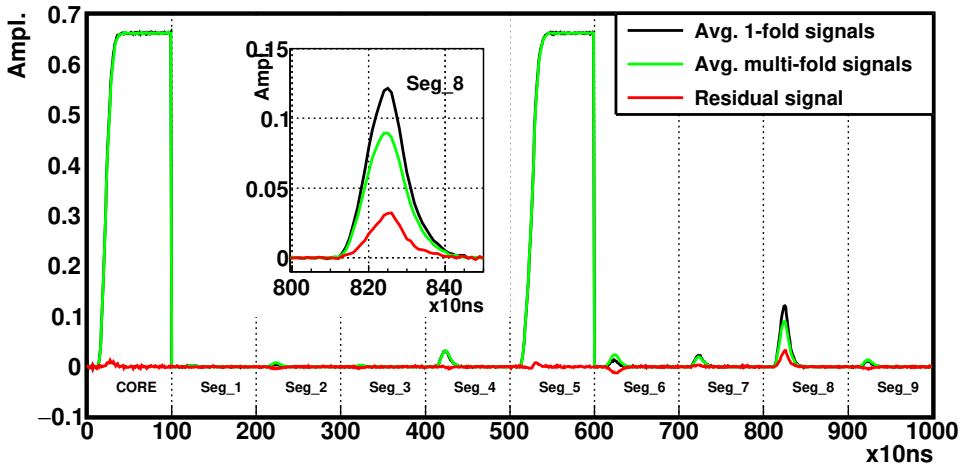

(b)

Figure 6.8: Comparison between the simulated signals generated by single-interacting and multi-interacting gamma rays, selected by the PSCS technique at a given point of the database. The trace in black is obtained by averaging the signals generated by single-interacting gamma rays, while the trace in green is obtained by averaging the signals generated by multi-interacting gamma rays. The signal in red shows the residual between the two traces. The trace shown in (a) and (b) are from the database points $X = 24.0\,mm$, $Y_C = 10.0\,mm$, $Z_C = 24.0\,mm$ and $X = 32.0\,mm$, $Y_C = 10.0\,mm$, $Z_C = 22.0\,mm$, respectively. In the first case the maximum residual is obtained by the difference of the main signals, while in the second case the maximum difference lies between two corresponding transient pulses (see inserts).

The figure shows the signals as *supertraces*, that means that the signals coming from the nine segments and the core of the detector are represented in a single compact trace. The trace in red shows the difference, or the *residuals*, between the two averaged signals[2]. The proposed examples show that the maximum value of the residual signal is around $2 \div 4\%$ of the main signal amplitude. In figure 6.8a the maximum difference is between the main pulses, while in figure 6.8b the maximum difference is between two corresponding induced pulses. It has been seen that the case shown in figure 6.8b occurs tendentially near the segmentation lines where the transient-signal amplitude changes rapidly with the position of the interactions. In the bulk of the segments, instead, the case shown in figure 6.8a is more likely to happen.

Figure 6.9 shows the maximum residual value for each point of a slice with a thickness of 1 grid unit ($2\,mm$) at a given depth position (Y_C) in the detector. It can be seen that the values are quite homogeneous across the slice, with an average value of around 3%. The figure also shows that the maximum residual value tends to be higher along the segmentation lines of the boron contact. These are border effects which are mostly due to the fact that, as previously mentioned, signals at the borders, vary very rapidly meaning that a small difference in the interaction position can lead to large difference in the pulse shape of the transient signals. If these anomalous points are ignored, the value is constant across the volume of the detector and this shows that even if conceptually pulses formed by multiple interacting gamma rays should be rejected they don't pollute the database in a sizable way.

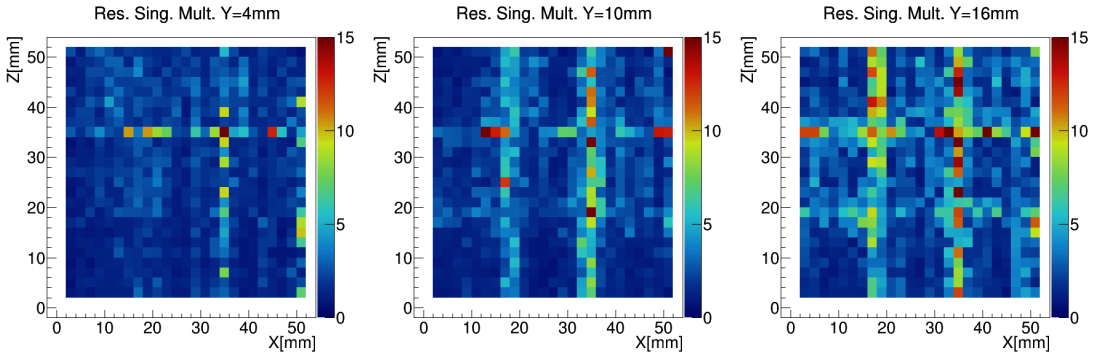

Figure 6.9: Maximum residual value, in percent with respect to the maximum amplitude of the main signal, between the averaged signals of single-interaction events and the averaged signals of multi-fold events (see also figure 6.8). The graphs are relative to slices with a thickness of 1 grid unit ($2\,mm$) for Y_C =4 mm, 10 mm and 16 mm from left to right.

Another meaningful parameter to take into account is how far, in average, are the interactions of the PSCS selected events from the position of their corresponding database point. Figure 6.10 shows the average distance values for each point of different slices

[2]The difference is performed sample by sample since all the signals calculated in the simulation by ADL are time aligned. One factor that can eventually disturb the PSCS procedure, in fact, is the time misalignment among the signals coming from a real scan. This aspect was not investigated in the simulation.

with a thickness of 1 grid unit ($2\,mm$) at different depths (Y_C) in the detector. The values are once again quite homogeneous in the volume of the detector, oscillating in a range between $3.6\,mm$ and $11.6\,mm$ with an average of $6.2\,mm$, except in the proximity of the segmentation lines where the average values raise due to the reasons previously explained.

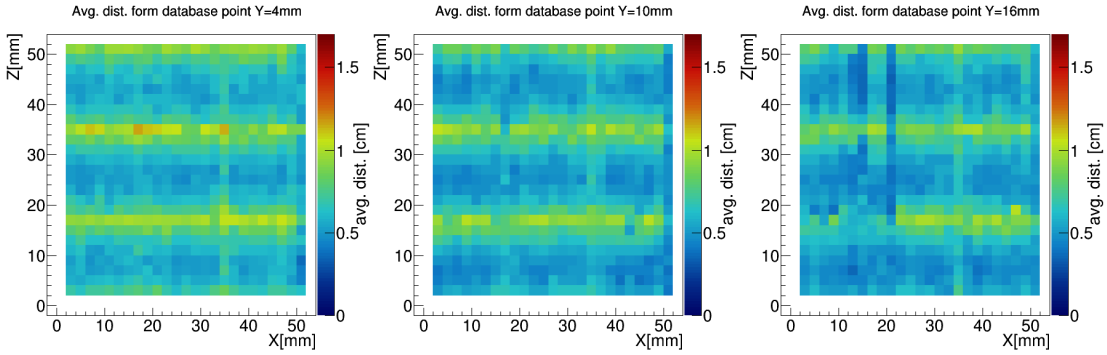

Figure 6.10: Average distance (color scale in cm) of the interactions of the PSCS selected events from the position of their database point. The graphs are relative to slices with a thickness of 1 grid unit ($2\,mm$) for Y_C =$4\,mm$, $10\,mm$ and $16\,mm$ from left to right.

This average distance can be compared with the spatial resolution of the detector. Although there are no data on the spatial resolution of the 3×3 pixelated detector, it is assumed to be worst than the spatial resolution of an AGATA detector, which is of $\sim 5\,mm$ FWHM at $1.382\,MeV$ after PSA and tracking [54, 55]. Since it was shown that the average of the interactions of the PSCS selected events from the position of their database point is of $6.2\,mm$, one can conclude that, in average, the interactions of the selected events take places within the spatial resolution of the detector. Moreover, for multiple-interaction events, the furthest interaction of an event from its first interaction position generally releases the least energy, as exemplified in figures 6.11. This means[3] that these far interactions contribute less to the signal formation and that the bulk of the signal is formed near the considered first interaction position.

As final test, the database obtained by simulating the PSCS technique was compared with the theoretical database, obtained using ADL to calculate the pulse shapes at the exact scanning grid-point positions. These theoretical pulses where convoluted with the response function of the preamplifiers. As previously done, the difference between each PSCS calculated database signal and the corresponding theoretical signal was evaluated (see figure 6.12) and the maximum value of the residual signal was extracted. The results for each point of different slices with a thickness of 1 grid unit ($2\,mm$) at different given depths (Y_C) in the detector are reported in figure 6.13. The values are homogeneous in the bulk of each segment, having an average value of 3% but they increase rapidly

[3]It is worth to remind that for multiple-interaction events, the signal is generated as the sum of single-interaction pulses calculated for each interaction position and weighted by the energy released at that point. The results shown in figure 6.11 help understanding why the selected multiple-interaction event pulses are similar to selected single-interaction pulses.

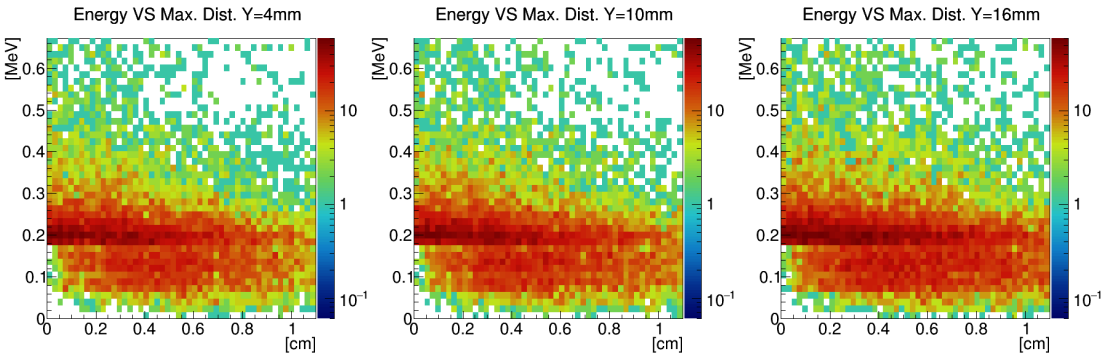

Figure 6.11: Furthest interaction distance of a multiple-interaction event from its first interaction position versus its respective released energy. Each graph gathers the interactions of all the points for a slice of the database with a thickness of 1 grid unit ($2\,mm$). The slices considered are at Y_C =$4\,mm$, $10\,mm$ and $16\,mm$ from left to right. The events concentrated around the line at $0.18\,MeV$ corresponds to the backscattering in case of 2-fold events (the large majority of multiple events). The events around $0.12\,MeV$ and $0.08\,MeV$ correspond to 3-fold and 4-fold events.

towards the segmentation lines where the average maximum residual is 16%. Moreover, right in correspondence of the segmentation lines the values spike, getting over 40% and in some cases reaching 100%. When the maximum residual amplitude reaches 100%, the main signal of the PSCS selected trace is generated in the neighboring segment with respect to the main signal of the corresponding ADL trace (as it can be seen in figure 6.14). This is due to the fact that when the gamma ray beam overlaps the border of two neighboring segments, the PSCS technique can select, somehow, pulses which are generated by interactions taking place in the "wrong" segment with respect to the segment in which the database point lies geometrically. This is especially true if the collimated beam hits one segment more than the other. This is indeed a problem of the PSCS technique that can be solved by carefully choosing the scanning grid alignment and pitch, in order to minimize the number of database points overlapping the segmentation lines. This is easy to do for a simple geometry like the one of the 3×3 pixelated detector, but less trivial for a complex geometry like the one of an AGATA detector.

In conclusion, the extracted parameters suggest that the PSCS selection, for the 3×3 pixelated detector, is reliable. It was shown that the χ^2 algorithm selects correctly similar pulses and that even if a large part of the selected events are multi-folded this doesn't affect the shape of the PSCS calculated signal due to the fact that the interactions of the selected events are in average within the spatial resolution of the detector and that the furthest interactions tendentially release the least energy contributing less to the signal formation. Moreover, the difference between the PSCS calculated database signals and the corresponding ADL signals is minimal, with the exception of some anomalies saw along the segmentation lines. A detector with a more complex geometry, like an AGATA unit detector, could lead to a better performance on the PSCS. This will be discussed in the next section.

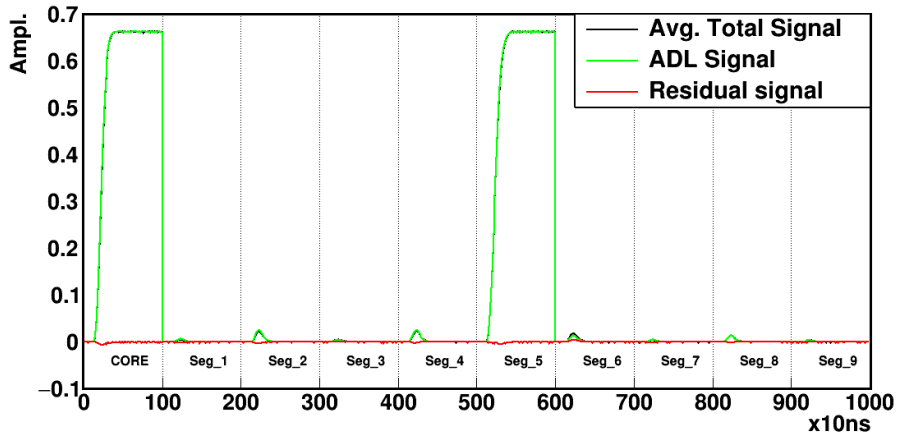

Figure 6.12: Comparison between a simulated PSCS signal and the corresponding ADL signal at $X_C = 24.0$, $Y_C = 10.0$, $Z_C = 24.0$.

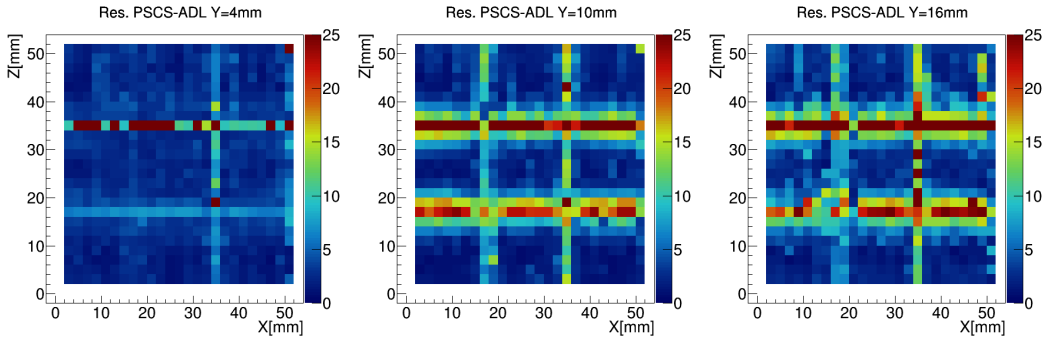

Figure 6.13: Maximum residuals between simulated PSCS signals and their corresponding ADL signals. The graphs are relative to slices with a thickness of 1 grid unit ($2\,mm$) for Y_C =$4\,mm$, $10\,mm$ and $16\,mm$ from left to right.

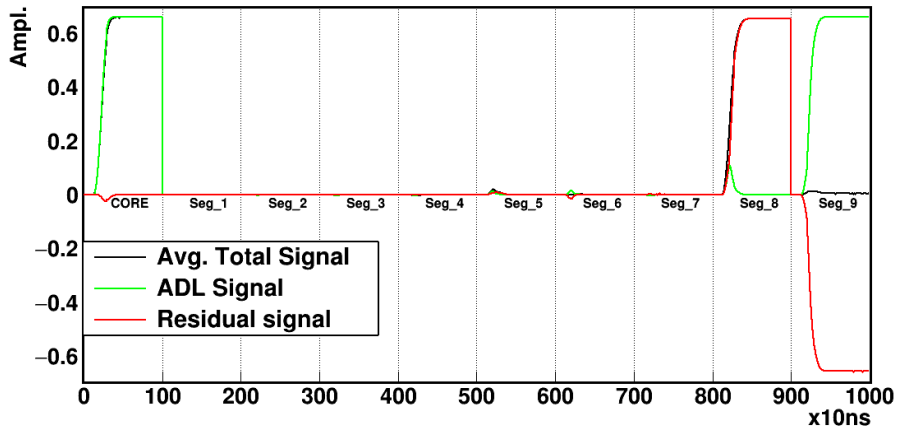

Figure 6.14: Comparison between a simulated PSCS signal and the corresponding ADL signal at $X_C = 36.0$, $Y_C = 6.0$, $Z_C = 34.0$. It can be seen that for the PSCS track (in black) the main signal is generated in segment 8 while the theoretical track (in green) has the main signal in segment 9. The maximum of the residual track (in red) is then 100% of the maximum amplitude.

6.2 Simulations of the PSCS technique on the S001 detector

As anticipated at the beginning of this chapter, the PSCS technique was tested on the S001 detector by simulating various scans. The tests aim to confirm the results obtained in section 6.1 and to explore the dependence from the energy and from the number of input events on the PSCS technique. A list of the performed simulated scans is given in table 6.2. For all the scans a collimator of $1\,mm$ diameter was used, which correspond to the upgraded version of the scanning table. Finally, in figure 6.15 the reference frame in which the results of the analysis will be presented is shown.

Description	Energy	Pitch	Events per point used for the PSCS selection	Referenced in
Full volume scan	$662\,keV$	$2 \times 2\,mm^2$	6000^2	6.2.1
Single sector scan	$122\,keV$	$2 \times 2\,mm^2$	6000^2	6.2.2
Single sector scan	$344\,keV$	$2 \times 2\,mm^2$	6000^2	6.2.2
Single sector scan	$779\,keV$	$2 \times 2\,mm^2$	6000^2	6.2.2
Single sector scan	$1408\,keV$	$2 \times 2\,mm^2$	6000^2	6.2.2
6 points scan	$779\,keV$	–	1000^2, 6000^2, 60000^2	6.2.3
6 points scan	$1408\,keV$	–	1000^2, 6000^2, 60000^2	6.2.3

Table 6.2: Summary table of the simulated scans. All scans were performed using a diameter of the collimator of $1\,mm$.

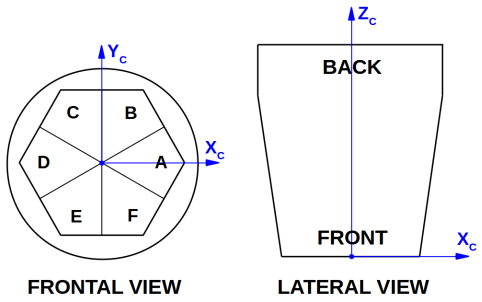

Figure 6.15: Reference frame used to present the results of the PSCS technique analysis.

6.2.1 Full volume ^{137}Cs scan

The PSCS technique applied to the S001 detector was at first tested with a simulated full volume ^{137}Cs scan. As done for the 3×3 pixelated detector in section 6.1, the first parameter extracted from the PSCS data of the full volume scan is the percentage of selected single-interaction events. It can be seen that this value is quite homogeneous across each transversal (with respect to the Z_C direction) slice of the database, as shown in figure 6.16. However, figure 6.17 shows that the average value per $2\,mm$ slice varies

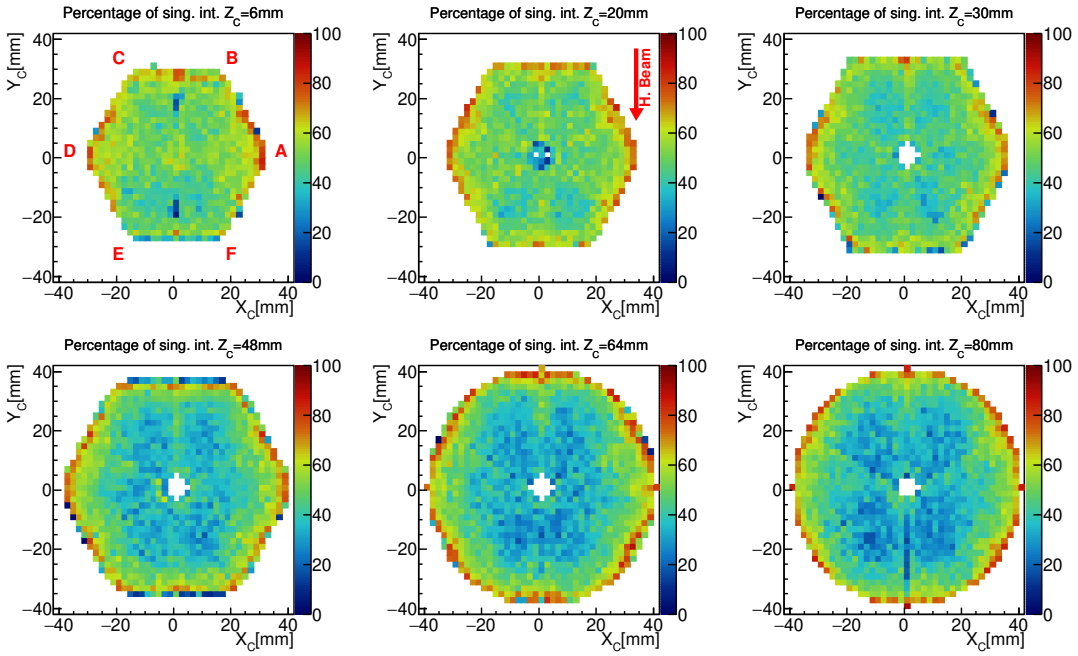

Figure 6.16: Percentage of single-interaction events selected by the PSCS technique over the total number of events. The graphs are relative to slices with a thickness of 1 grid unit (2 mm) for Z_C =6 mm, 20 mm, 30 mm, 48 mm, 64 mm and 80 mm. In the top−left panel, the segment labeling is shown while in the top−center panel the red arrow shows the horizontal beam direction.

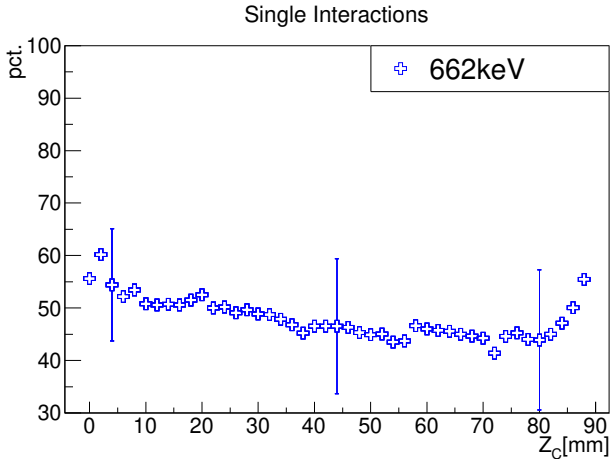

Figure 6.17: Percentage (pct.) of selected single-interaction events along the Z_C direction. The bars show the standard deviation for slices at the front, center and back of the detector.

along the depth of the detector, decreasing as Z_c increments. The maximum average value of single-interaction events is of about 60% at the front of the detector while the minimum average value is of around 40% at the back. The reasons for this trend can be found in two factors. The first one has to do with the geometrical properties of the segments: the active volume of the segments of the S001 detector increases from the front to the back of the crystal and this increases the fraction of selected multi-interaction events among the considered events that release all their energy in a single sector. The second factor concerns the absorption of gamma rays in the germanium: as the beam dips deep in the detector, the available number of events for the χ^2 selection is reduced (beam absorption) and this leads to a less efficient selection of single-interaction events (the impact of the number of events used for the χ^2 selection will be described later in section 6.2.3). These two factors were negligible for the 3×3 pixelated detector which has segments with smaller volume which are geometrically identical. In conclusion, the selection of single-interaction events for S001 detector is better than the one for the 3×3 pixelated detector but still not comparable with the values obtained by the Liverpool scanning table.

Nevertheless, as for the case of the 3×3 pixelated detector, the PSCS technique selects, for each given database point simulated, single-interaction and multiple-interaction events which are quite similar. This can also be simulated for detector S001. The average pulses of single-interaction events and multiple-interaction events, for each database point, are calculated as well as the residual supertrace (see section 3.3). The maximum residual values, in percentage with respect to the amplitude of the main signal, is shown for several database slices at different depths of the detector, in figure 6.18. The values are quite homogeneous in the volume of the detector with a global average $< 5\%$. Some anomalous high values can be registered for points that are towards the segmentation lines due to the border effects mentioned in section 6.1.3.

The similarity between the pulses generated by single-interaction events and multiple-interaction events can be understood, once again, by considering the average distance of the PSCS selected events from the position of their corresponding database point. The values for different transversal database slices at different depths of the detector (in figure 6.19) show that the average distance is homogeneous across each individual $2\,mm$ slice. The graph in figure 6.20 shows a moderate growing trend along Z_C for the values of each slice. The average distance, in fact, has a value of $\sim 2\,mm$ in the front of the detector and then rises slightly until it reaches $\sim 2.5\,mm$ at its back. These values, nevertheless, are below the nominal position resolution of an AGATA detector of $5\,mm$ (after PSA and tracking) and lower with respect to the corresponding values for the 3×3 pixelated detector (as anticipated in section 6.1.3).

A second reason that explains the similarity between the selected single-interaction events and multiple-interaction events pulses comes by considering, for multiple-interaction events, the energy released by the furthest interaction from the first interaction point related to this distance. Some examples, in figure 6.21, show that generally the furthest interaction releases the least energy and thus, as already stated in section 6.1.3, it contributes less to the signal formation. In other words the bulk of the signal is formed near the position of the first interaction.

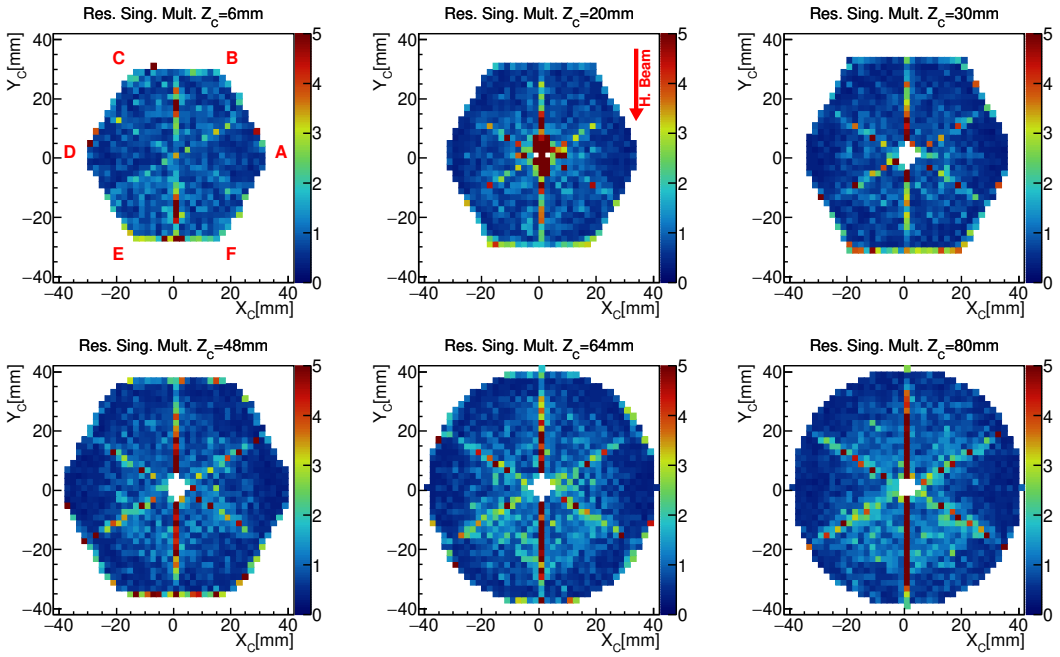

Figure 6.18: Maximum residual value, in percent with respect to the maximum amplitude of the main signal, between the averaged signals of single-interaction events and the averaged signals of multiple-interaction events. The graphs are relative to slices with a thickness of 1 grid unit (2 mm) for Z_C =6 mm, 20 mm, 30 mm, 48 mm, 64 mm and 80 mm. In the top−left panel, the segment labeling is shown while in the top−center panel the red arrow shows the horizontal beam direction.

The final test is the comparison between the database obtained by simulating the PSCS technique with the one calculated using ADL (and convoluted with the response function of the preamplifiers). For each database point the residual supertrace between the PSCS technique and the ADL calculated signals was evaluated and its maximum extracted. Figure 6.22 shows the values for several database slices along the depth of the detector. The values are, as for the case of the 3×3 pixelated detector, homogeneous in the bulk of the segments but increase rapidly towards the segments boundaries. The maximum residual can reach values of 100% (with respect to the maximum amplitude of the main signal) when the database points lay on the segmentation lines. The main reason for the anomaly, already explained in section 6.1.3, is that in these cases the PSCS technique selects in majority signals that are generated in a neighbor segment with respect to the actual segment in which the main signal should be generated. Thus the maximum difference between this "miss-selected" signal and the ADL one is the full amplitude of the main signal, as exemplified for the 3×3 detector in figure 6.14. The average value of the maximum residual varies with the depth of the detector as shown in figure 6.23. The discrepancy between the two databases is accentuated in the first slices of the databases, where it has a value comprised between 5% and 10% in the first two segment slices and then decreases towards the back part of the crystal, where it reaches a values

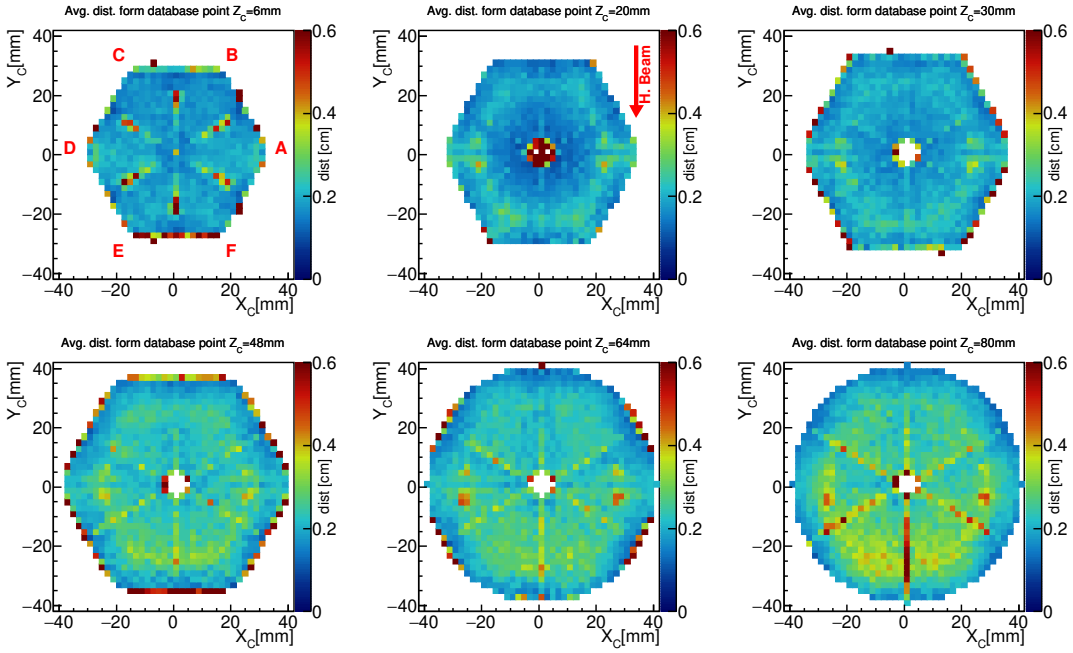

Figure 6.19: Average distance (in cm) of the interactions of the PSCS selected events from the position of their database point. The graphs are relative to slices with a thickness of 1 grid unit ($2\,mm$) for Z_C =6 mm, 20 mm, 30 mm, 48 mm, 64 mm and 80 mm. In the top−left panel, the segment labeling is shown while in the top−center panel the red arrow shows the horizontal beam direction.

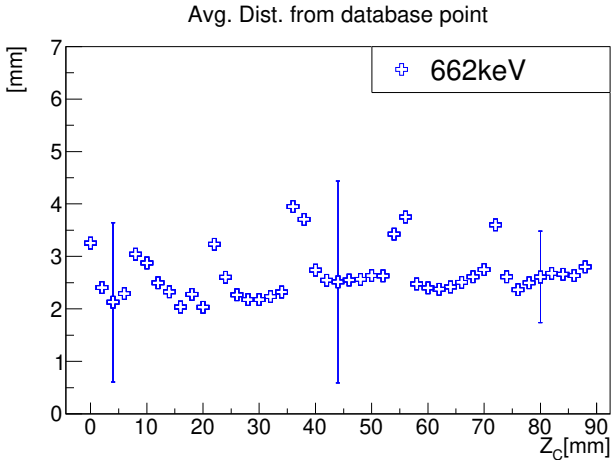

Figure 6.20: Average distance (averaged in each $2\,mm$ slice) of the interactions of PSCS selected events from the position of their database point along the Z_C direction. The bars show the standard deviation for slices at the front, center and back of the detector.

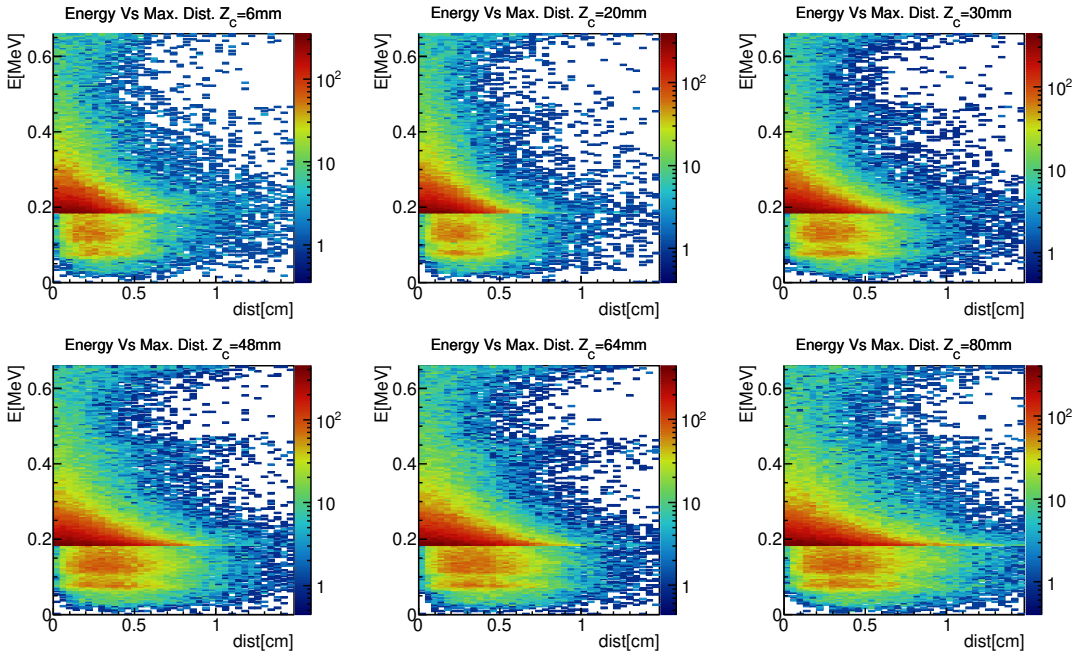

Figure 6.21: Furthest interaction distance of a multiple-interaction event from its first interaction position versus its respective released energy. Each graph gathers the interactions of all the points for a slice of the database with a thickness of 1 grid unit ($2\,mm$). The slices considered are at Z_C =$6\,mm$, $20\,mm$, $30\,mm$, $48\,mm$, $64\,mm$ and $80\,mm$.

$< 5\%$. This can be explained by the irregular geometry of the segments in the front of the detector which generates fast-changing electrical fields with respect to the one generated by the quasi-coaxial geometry of the back segments. Consequently, for the front of the detector a small variation in the position of a gamma-ray interaction can generate a big change in the resulting signal, both in the main pulse and in the induced pulses. As a final remark, the high values at $Z_C = 14\,mm$, $22\,mm$, $36\,mm$, $56\,mm$, $74\,mm$ are due to the presence, in those positions, of the boundary surfaces between segment slices. This effect is magnified by the fact that the surface of the segment-slice separation cross several $2\,mm$ slices as shown in figure 4.14. With similar argumentations given at the end of the previous section, one can conclude that the analysis of the selected parameters suggests that the PSCS technique is reliable when applied on an AGATA detector. The χ^2 algorithm selects similar pulses and even if a large part of them are generated by multiple-interaction events, this doesn't affect the final pulses that will compose the database. This is due to the fact that the interactions of the selected events are in average within the spatial resolution of the detector and that the furthest interactions tendentially release the least energy contributing less to the signal formation. Moreover the comparison between the PSCS calculated database and the ADL calculated one shows little difference with some exceptions at the boundaries between the segments of the detector.

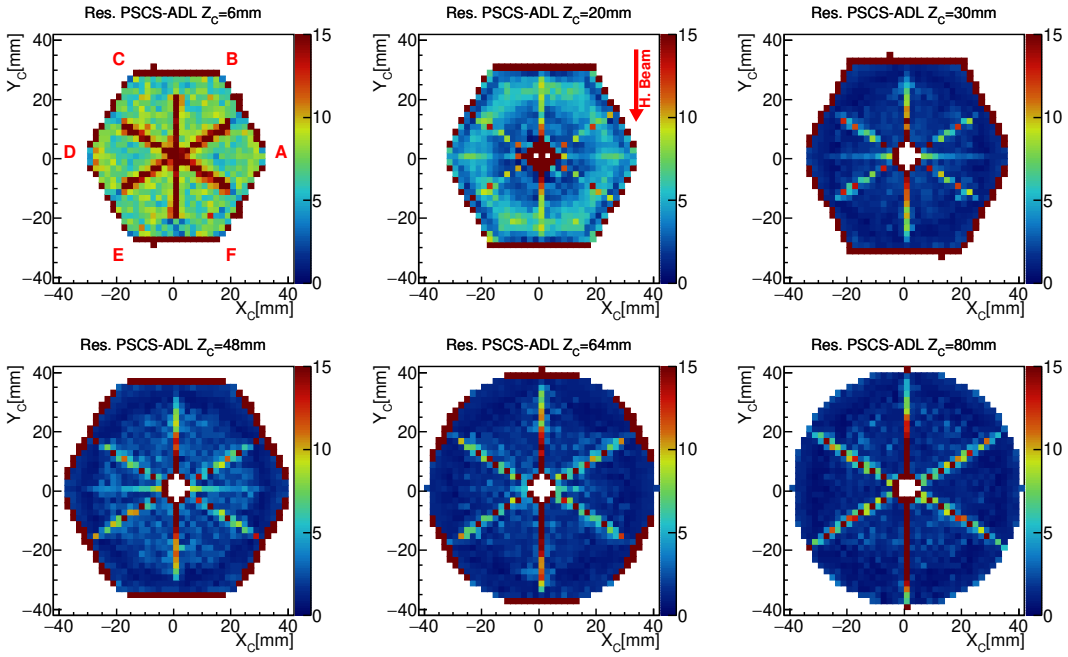

Figure 6.22: Maximum residuals between simulated PSCS signals and their corresponding ADL signals. The graphs are relative to slices with a thickness of 1 grid unit (2 mm) for Z_C =6 mm, 20 mm, 30 mm, 48 mm, 64 mm and 80 mm. In the top−left panel, the segment labeling is shown while in the top−center panel the red arrow shows the horizontal beam direction.

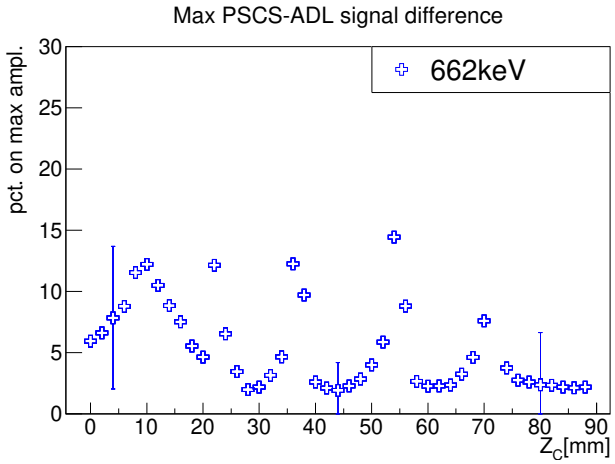

Figure 6.23: Maximum residuals, averaged for each 2 mm slice, between simulated PSCS signals and their corresponding ADL signals along the Z_C direction. The bars show the standard deviation for slices at the front, center and back of the detector.

In the next two sections the PSCS technique will be further tested with scans performed with different values for the gamma-ray energy and different number of pulses used as input of the χ^2 selection.

6.2.2 Different energies scans

As a first further test of the PSCS technique, the impact of the gamma-ray energy used for the scan was evaluated. Four simulated partial scans (only one sector of the detector was scanned) were performed with energies $122\,keV$, $344\,keV$, $779\,keV$ and $1408\,keV$ which correspond to four of the various energies of the gamma rays emitted by a ^{152}Eu source (see table 6.2). As the activity of the ^{152}Eu source is about three times smaller than the one of the ^{137}Cs source and as the branching ratio of the main ^{152}Eu gamma rays are rather low, a full scan of the S001 detector would be too long. Therefore a scan of only one sector will be performed and the results will be shown in chapter 7. The simulations here presented will be performed accordingly. The parameters considered for the present analysis are:

- ◇ the percentage of selected single-interaction events;
- ◇ the average distance of the selected events from the position of their corresponding database point;
- ◇ the maximum value of the residual signal between the simulated PSCS and ADL supertraces.

Figure 6.24a shows the percentage of selected single-interaction events at different depths of the detector for the different scanning energies. Data from the $662\,keV$ gamma-ray energy scan is added for reference. Since in the previous section it was shown that the values of the considered parameters are homogeneous in each database slice, the data represented in 6.24a refers to the average value per $2\,mm$ slice. The graphs show that data series are comparable with one another and follow the same trend. The gamma-ray energy has an impact on the PSCS results. For low energies ($122\,keV$ and $344\,keV$), the percentage of selected single interaction is sensibly larger with respect to the remaining energies above $500\,keV$ which have similar values. This result is due to the fact that at lower energies gamma rays are more likely to undergo photo-absorption as shown in section 1.1. This means that for each pool of events for a given scanned position, the fraction of single-interaction events is already larger before the χ^2 selection than for higher energies. Also, since low energy gamma rays are more likely to be absorbed in few centimeters of germanium (see section 1.5), no data is available after $Z_C = 34\,mm$ for the $122\,keV$ scan.

The average distance of the selected events from the position of their corresponding database point exhibits a tiny energy dependence, the higher energy gamma rays having the largest average distance values (figure 6.24b). However, the overall values are quite comparable, following the same trend, and range mainly between $1\,mm$ and $3\,mm$. At positions around $Z_C = 14\,mm$, $22\,mm$, $36\,mm$, $56\,mm$ and $74\,mm$ the average distance

peaks at $\sim 4\,mm$ due to the presence of the segment boundaries (see figure 6.25 in the next section). This generates anomalous data values as already explained in 6.1.3.

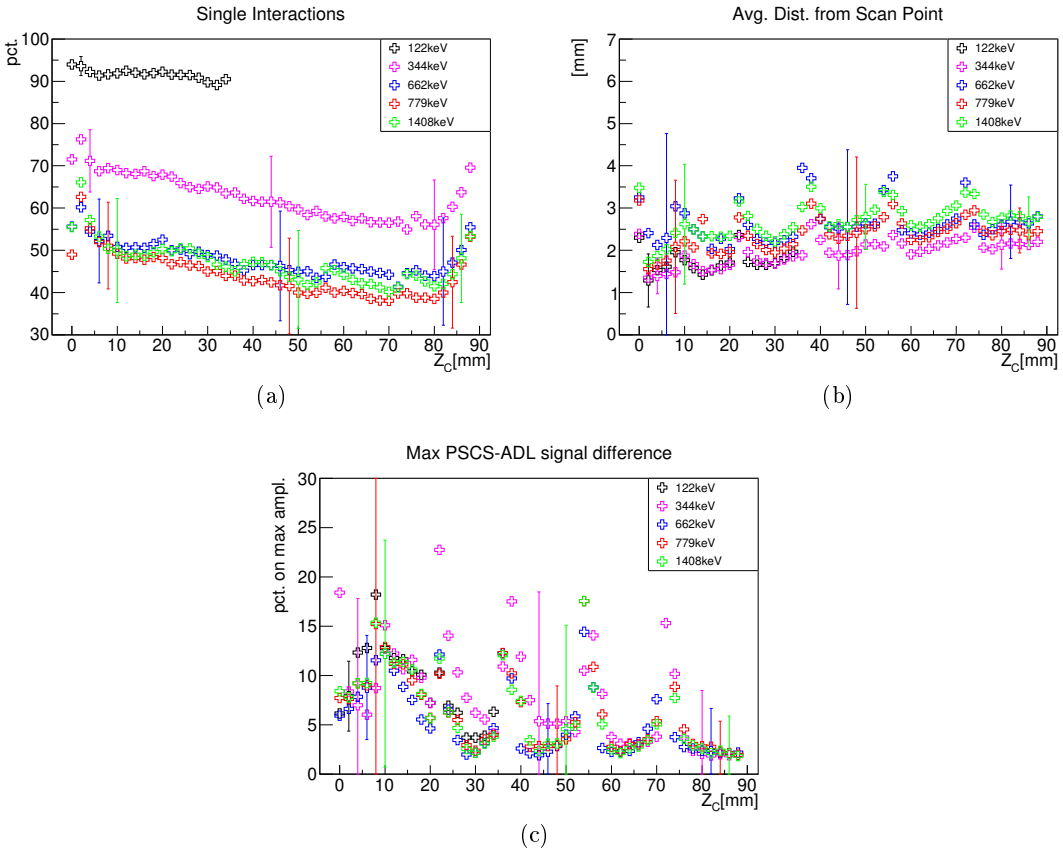

Figure 6.24: Scan results for the four considered gamma−ray energies. (a) Percentage (pct.) of selected single interaction events along the Z_C direction for different gamma−ray energies. (b) Average distance of interactions of the PSCS selected events from the position of their database point along the Z_C direction for different gamma−ray energies. (c) Maximum residuals between simulated PSCS signals and their corresponding ADL signals along the Z_C direction for different gamma−ray energies. For all the graphs, the bars show the standard deviation for slices at the front, center and back of the detector.

Finally in figure 6.24c the maximum value of the residual between the simulated PSCS and ADL supertraces is plotted for the different energies used. The data series are once again similar and the results of the PSCS technique are not affected in an appreciable way by the gamma-ray energy used. The energy independence of the parameters can be justified by the fact that the shape of the signal is in principle independent from the energy of the interacting gamma ray. This hypothesis will be tested in chapter 7 by scans of one segment sector of the S001 detector using the ^{152}Eu source.

6.2.3 Impact of the statistics on the PSCS technique performance

The impact on the PSCS technique of the number of pulses used as input for the χ^2 selection is evaluated. A scan of six points along the Z_C direction was performed, as shown in figure 6.25, so that each point is roughly in the center of the each segment of *sector D*. The χ^2 selection was performed by comparing 1000×1000 (low statistics), 6000×6000 (regular simulation statistics) and 60000×60000 (high statistics) pulses for each point of the scan. Two gamma-ray energies were used, $779\,keV$ and $1408\,keV$ and, as in the previous section, the three main parameters considered for this analysis are:

- ◇ the percentage of selected single-interaction events;
- ◇ the average distance of the selected events from the position of their corresponding database point;
- ◇ the maximum value of the residual signal between the simulated PSCS and ADL supertraces.

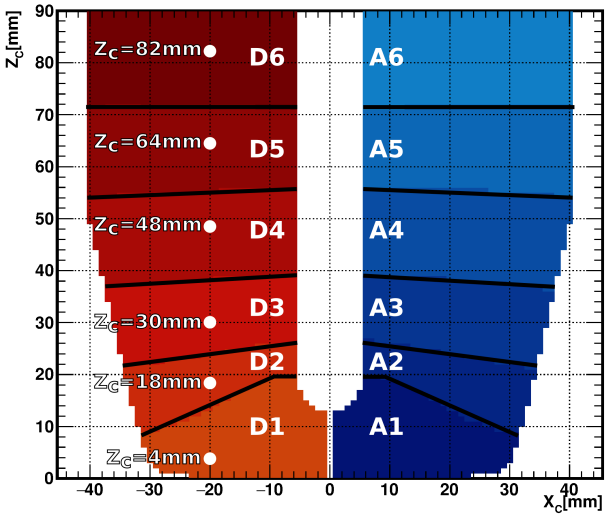

Figure 6.25: Z_C positions of the six scanned points at $X_C = -20\,mm$ and $Y_C = 0\,mm$ analyzed in this section. In the figure a lateral view of the segments boundaries is also shown.

The results, plotted in figure 6.26 for the $779\,keV$ gamma-ray energy scans and figure 6.27 for the $1408\,keV$ gamma-ray energy scans, show that statistics plays an important role in the PSCS selection. In fact, although the trends of the data series of the first two parameters previously listed is identical, their values are noticeably affected. The percentage of selected single-interaction events increases substantially and the average distance of the selected events from the position of their corresponding database point decreases, respectively, with an increasing number of pulses used for the χ^2 selection. It

is clear that for these two parameters the PSCS technique performs better when higher number of pulses are used for the χ^2 selection. Moreover it seems that there is no correlation between statistics and gamma-ray energy.

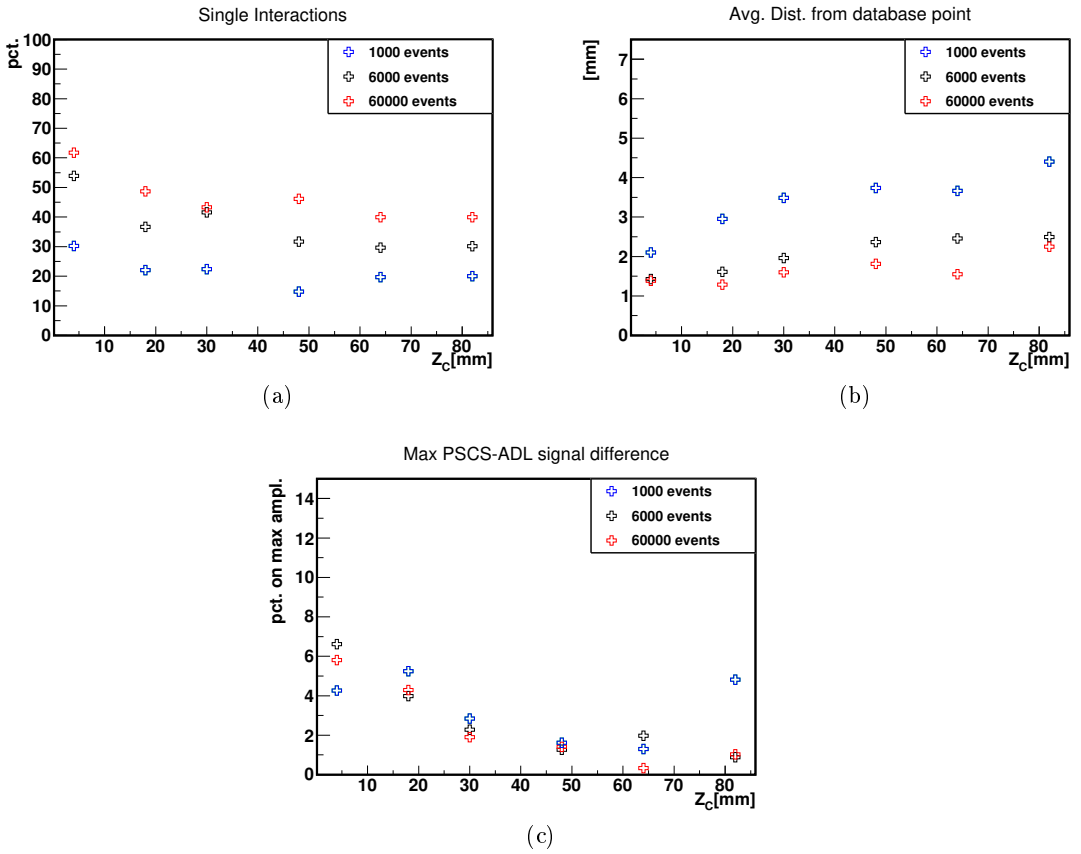

Figure 6.26: Values of the three considered parameters along the Z_C direction for the $779\,keV$ scans. (a) Percentage (pct.) of selected single-interaction events. (b) Average distance of the selected events from the position of their corresponding database point. (c) Maximum value of the residual signal between the simulated PSCS and ADL supertraces. The positions of the scanned points are given in figure 6.25.

However the maximum value of the residual between the simulated PSCS and ADL calculated supertraces doesn't seem to be significantly affected on contrary to the two previous parameters. There isn't, in fact, a noticeable change in the values except a small effect at the point of the first slice of the detector. As this third parameter is very indicative of the similarity between the simulated PSCS and ADL database pulses and as differences have been evidenced in sections 6.2.1 and 6.2.2 at the front of the detector, one can conclude that the number of events used as input for the χ^2 selection, comprised between 1000 and 60000 events, does not result in sizable changes in the construction of the database. As a further analysis it would be worth to extend the range of the test to

even lower statistics (few hundreds of events) and higher statistics (orders of magnitude $> 10^4$).

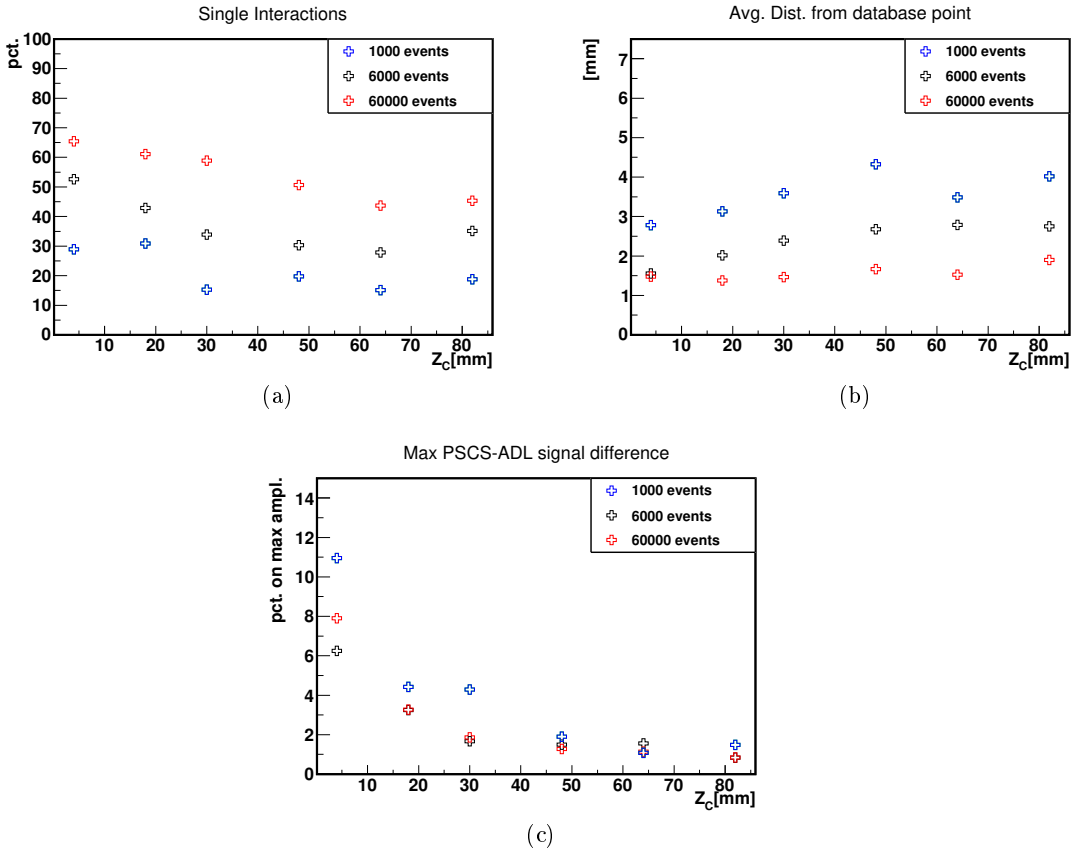

Figure 6.27: Values of the three considered parameters along the Z_C direction for the 1408 keV scans. (a) Percentage (pct.) of selected single-interaction events. (b) Average distance of the selected events from the position of their corresponding database point. (c) Maximum value of the residual signal between the simulated PSCS and ADL supertraces. The positions of the scanned points are given in figure 6.25.

Chapter 7

Real scan of the S001 detector

Along the simulation analysis, complementary work was done on the real scanning table system, a part of which was already presented in chapter 4. In this chapter the results of several 2D and 3D scans, performed on the S001 detector, will be presented. All the measurements are performed with the scanning table in the *upgraded configuration*. At first, the alignment procedure will be described. Afterwards, a 2D characterization of the detector, made with the ^{137}Cs and ^{152}Eu sources, is presented analyzed and discussed. Finally, the results of the 3D scans made with the ^{137}Cs and ^{152}Eu sources are shown and preliminary conclusions drawn.

7.1 Detector alignment procedure

The PSCS technique will always give a result from the comparison of two series of data regardless of the crossing precision. It is, then, of highest importance that the detector is well positioned and geometrically referenced on the scanning table in order to minimize the errors due to miss-alignment of the virtual scanning grid. A rough detector alignment along X_T and Y_T axes (see figure 4.2) is carried out using a square and by adjusting the micrometric screws of the adjustment frame. Then, dedicated local scans are performed to determine the position of the crystal in the scanning table reference frame. The alignment procedure is described in the following sections.

7.1.1 Vertical rotation

The scanning procedure starts by aligning the detector vertically. This means that the central axis of the detector is perpendicular with respect to the collimator moving plane. Also, in the specific case of an AGATA detector, it is required that the segmentation line between segments $E1$ and $F1$ of the detector is parallel to the Y_T axis (see figure 4.2). The alignment on Y_T axis is achieved by performing fine pitch scans (of $100\,\mu m$ using the $1\,mm$ collimator) across the $E1 - F1$ segmentation line as shown in the left panel of figure 7.1. These scans are performed with the ^{241}Am source. The graph for a

segment of the counts in the photopeak[1] as a function of the scanned point is drawn in the right panel of figure 7.1. The local photopeak efficiency stays constant (forming a

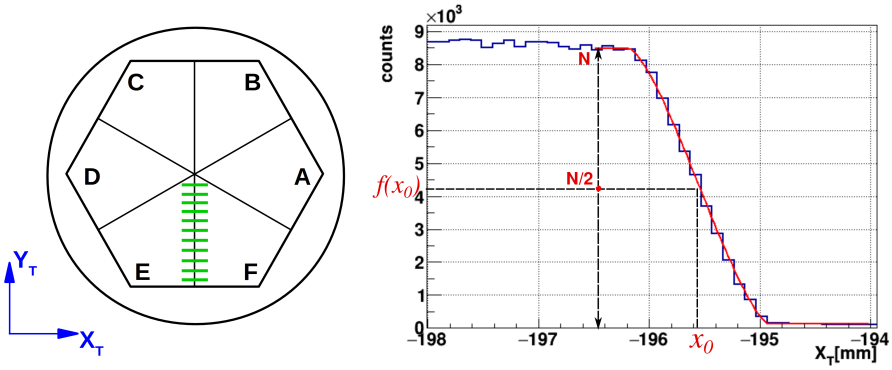

Figure 7.1: Segment $E1$ local photopeak efficiency as a function of the collimator position for a $100\,\mu m$ pitch, ^{241}Am source scan. Left panel: schematic drawing showing the 11 scans (green lines) performed across the $E1-F1$ segmentation line (the Y_T of the lines are reported in table 7.1). The beam irradiates the detector from below (parallel to the Z_T axis) and the moves from left to right for each one of the green lines. Right panel: the boundary of the segment corresponds to the abscissa x_0 of the point laying on the fit curve (solid red line) with an ordinate $f(x_0) = N/2$.

plateau) and then drops as the beam leaves the segment, until the beam is totally out of it. Similarly, the local photopeak efficiency raises as the gamma-ray beam approaches the adjacent segment until the beam is totally inside of its volume. The local photopeak efficiency profile can be fitted with the following sigmoid-like function that takes into account the finite dimensions of the beam spot entering the segment

$$f(x) = C + A\,(2 \cdot Acos\,(B \cdot (x - x_0))) - sin\,(2 \cdot Acos\,(B \cdot (x - x_0))) \qquad (7.1)$$

where A, B, C and x_0 are the fit parameters. In particular, x_0 is the abscissa of the point at half height of equation 7.1 and this value is taken as segment edge. This fitting procedure is repeated for each scan line acquired and a graph with the coordinates of the segmentation-line edge coordinates is built as in figure 7.2. From these data it is possible to extract the value of the angular correction that has to be applied to the detector in order to align it. For the S001 detector, scans at 11 different radius values, reported in table 7.1, along the $E-F$ segmentation line were performed with a collimator diameter of $1.0\,mm$ and a pitch of $100\,\mu m$. It showed a misalignment between the segmentation line and Y_T axis of $0.039° \pm 0.002°$ which is an acceptable value to consider the detector aligned, since it is below the correction precision of the adjustment frame (along the $\vec{Z_T}$ rotational direction). It corresponds to a displacement of $14\,\mu m$ between the two extreme scanned points which are spaced by $20\,mm$. This scan also allows to determine the width of the segmentation line, as exemplified in figure 7.3a. The segmentation line is measured to be in average $0.668 \pm 0.006\,mm$ (see table 7.1). An additional single scan,

[1] For simplicity the counts in the photopeak are called *local photopeak efficiency*.

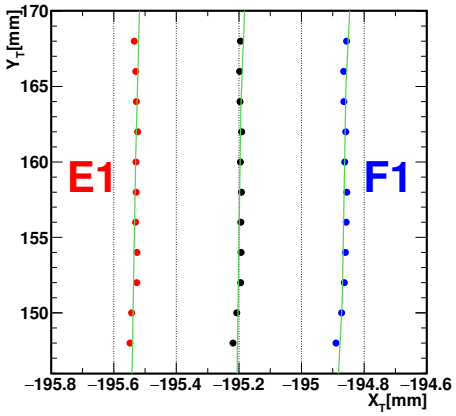

Figure 7.2: Vertical rotation alignment performed at $60\,keV$ (see table 7.2). The blue and red marks indicate the left and right delimitations of the segmentation line. The black marks in the middle indicate the barycenter of the two series and are used to determine the misalignment of the $E1 - F1$ segmentation line on the Y_T axis. The difference of the X coordinates on the blue and red marks gives the segmentation width. Error bars are smaller than the symbol size.

Y_T(mm)	Seg. Line Width (mm)	
	$\varnothing_{coll} = 1.0\,mm$	$\varnothing_{coll} = 0.5\,mm$
148	0.659 ± 0.006	
150	0.672 ± 0.006	
152	0.663 ± 0.005	
154	0.666 ± 0005	
156	0.673 ± 0.005	
158	0.673 ± 0.005	0.626 ± 0.004
160	0.667 ± 0.005	
162	0.666 ± 0.006	
164	0.663 ± 0.004	
166	0.665 ± 0.005	
168	0679 ± 0.006	
AVG	0.668 ± 0.006	

Table 7.1: Measured values of the $E1 - F1$ segmentation line width at different Y_T positions and for the two collimator diameters ($\varnothing_{coll}$) used. The average (AVG) of the eleven width values is given at the bottom line.

with a collimator diameter of $0.5\,mm$ and a pitch of $50\,\mu m$, was performed to cross check this result. As it is to be expected, a finer scan allows for a more precise determination of the segments edges[2]. Figure 7.3b shows that the edges of the efficiency graphs are

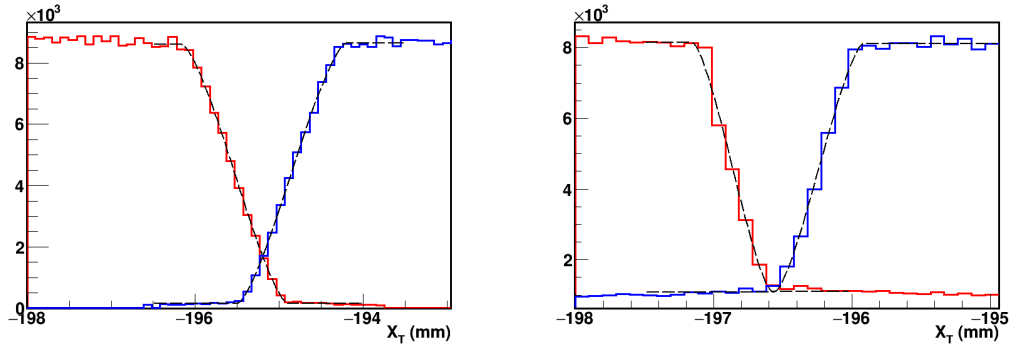

(a) (b)

Figure 7.3: Local efficiency graph of the linear scans across the $E1 - F1$ segmentation line performed at $60\,keV$ (see table 7.2) to determine its width. The graph in (a) refers to the scan performed with a $1.0\,mm$ diameter collimator and a $100\,\mu m$ pitch at $Y_T = 158\,mm$ (see table 7.1). The graph in (b) refers to the scan performed with a $0.5\,mm$ diameter collimator and a $50\,\mu m$ pitch at the same position. For both the graphs the red line refers to the data taken in segment $E1$, while the blue line refers to the data taken in segment $F1$. Note that the measurement duration was $120\,s$ for (a) and $2000\,s$ for (b). In the latter case, background from the detector-laboratory environment lead to a minimum of about 1000 counts in the energy gate.

sharper and moreover they don't overlap as for the case of figure 7.3a. This second scan gives a value for the segmentation width of $0.626 \pm 0.004\,mm$ which differs by 7% from the respective value measured with the $1.0\,mm$ diameter collimator (see table 7.1). However, a real comparison between the two values can not be done because, in order to obtain a statistically rigorous result, the measurement with the $0.5\,mm$ diameter collimator should be repeated several times. This was not done by lack of time.

7.1.2 Vertical axis alignment

Once the face of the detector is correctly oriented, the vertical alignment of the detector axis is performed. The ^{137}Cs source is used to perform fine pitch scans (of $100\,\mu m$) across the central hole of the detector. Two crossing linear scans are performed as shown in figure 7.4a. For this analysis the spectra at each scanned point were build considering only the events of total gamma-ray absorption in a single slice. Graphs of the segments efficiency as a function of the scanned points along X_T and Y_T are drawn for each of the 6 slices of the detector (right panel of figure 7.4a). As for the previous case, the efficiency stays constant when the gamma-ray beam is in the segment bulk and drops when the

[2] A study of the progressive penetration of a gamma ray beam inside the active area of a detector is presented in [24].

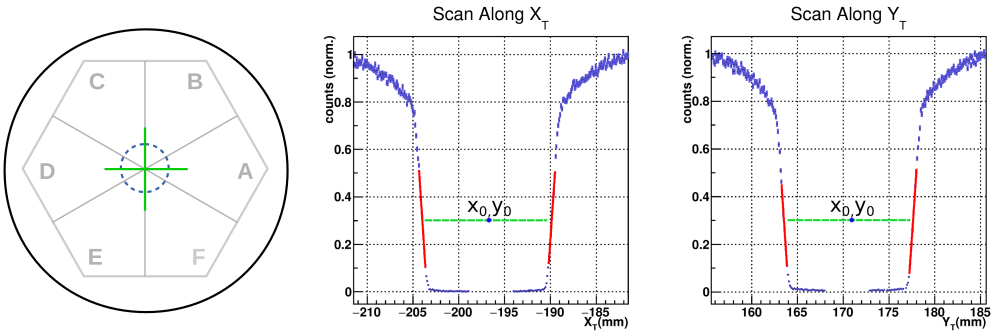

(a)

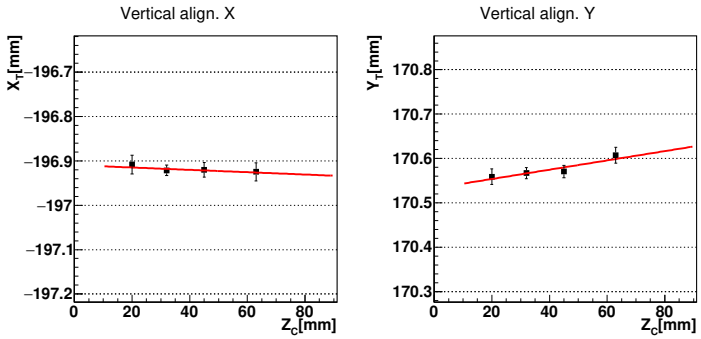

(b)

Figure 7.4: Bored-hole alignment scanning procedure (see table 7.2). (a) Cross scan and respective normalized local photopeak efficiency histograms for slice 5. The red lines represent the linear fits performed on the edges of the efficiency graphs. (b) Tilt of the vertical axes of the crystal after the alignment. Note that in this graph the ordinates refer to the scanning table reference frame (Y_T) while the abscissas refer to the crystal reference frame (Z_C). In this particular case, slice 6 was not considered for the fit. See text for more details.

beam crosses the hole. For the last 5 slices[3], the positions of the hole boundaries are determined in the following way. The positions of the hole boundaries are determined by linear fitting the edges of the efficiency graphs (see the red lines in the right panel of figure 7.4a). The linear fits are performed in the range for which y is comprised between $0.2 \cdot h$ and $0.6 \cdot h$, where h is the height of the plateau[4]. The left (right) boundary of the hole is taken as the abscissa x_l (x_r) of the point laying on the left (right) fit line with an ordinate $y = y_0 \cdot h$, where y_0 is a value taken as much closer as possible to the mid-height of the efficiency profile ($y_0 = 0.3$ in the current analysis since, to obtain a good fit, the fit ranges between the slices differ). Knowing the boundaries of the hole, its center x_0 is calculated and plotted as a function of the height of the respective slice. A linear fit of the hole boundaries in the 5 slices enables to deduce the tilt of the crystal

[3]The first slice of the detector has no hole.

[4]Generally the efficiency graphs are renormalized so that $h = 1$.

along X_T and Y_T axes. This gives the value of the two angular corrections (around the X and Y rotational axes of the adjustment frame) that have to be applied (using the micrometric screws) to the detector in order to properly align its axes on the scanning table axes (figure 7.4b).

For the S001 detector, a crossing lines scan was performed, across the bored hole, with a collimator diameter of $1.0\,mm$ and a fine pitch of $100\,\mu m$. The scan revealed that the detector had a tilt of $0.02^\circ \pm 0.02^\circ$ on the X_T axis and a tilt of $-0.42^\circ \pm 0.03^\circ$ on the Y_T axis. The detector was considered aligned on the X_T axis while the tilt on the Y_T axis was corrected. A new, similar, scan confirmed the good alignment of the detector which presented a tilt of $0.05^\circ \pm 0.02^\circ$ on the Y_T axis after correction. Finally, the shift along $X_T(Y_T)$ between points at the front and the back of the crystal is $32\,\mu m(79\,\mu m)$ only.

Such scans give also information on the diameter of the central hole of the detector that was obtained by making the difference of the values of the boundaries of the hole for each slice. The value obtained is around $14.1 \pm 0.2\,mm$ which is in agreement with the same measurements performed on the B006 detector [24]. The measured diameter is larger than expected ($10\,mm$) which is due to a combination of causes such as the width of the beam and the dead layer of the hole contact that produce a smearing effect (see discussion in chapter 4 of [24]).

Once the detector is vertically aligned, all the needed vertical scans are performed, after which the detector is prepared for horizontal positioning.

7.1.3 Horizontal alignment

While the detector is still in vertical position, the gamma source is replaced by a laser beam in order to set up the optical alignment system. The optical module consists of a pair of pin holes, spaced by $16\,cm$, attached to the side of the cryostat along its symmetry axis. The diameters of the first and second holes are $200\,\mu m$ and $50\,\mu m$, respectively. The collimator is opened, the source removed and replaced by a prism. The laser beam passes through the collimator from the bottom to the top, following the gamma-ray path. Beyond the collimator, the laser beam passes through the two holes which positions can be adjusted. The laser beam intensity is first maximized at the exit of the first hole (using a wattmeter which operates in the nW to mW range) by adjusting the pin hole position in X and Y. A similar operation is performed with the second pin hole. When the laser delivers the maximum intensity at the exit of the second hole, the optical system is set and the two holes define a direction parallel to the laser beam, i.e. the gamma-ray beam. The detector is put in horizontal position and the optical module is used to adjust its alignment with the aid of a second prism. Again the laser beam should deliver the maximum intensity at the exit of the second hole of the optical system. Since the detector is considered horizontally aligned when the axis of the detector is collinear to the X_T axis of the scanning table, the optical alignment is verified through dedicated scans with the ^{137}Cs source. The scans run transversally through the bored-hole of the detector as shown in figure 7.5a, one line for each slice. An efficiency graph is then build for each slice of the detector as shown in

figure 7.5b. The linear parts of the two joining edges is fitted with two linear fits and the abscissa at witch the two lines cross is extracted. These values are then plotted at the corresponding slice height (as shown in figure 7.5c) and a linear fit enables to deduce the horizontal misalignment of the crystal with respect to the X_T axis. For the S001 detector linear scans where performed with a collimator diameter of $1.0\,mm$ and a pitch of $100\,\mu m$ across slices 2, 3, 4 and 5. A misalignment of 0.31° was corrected to 0.02° ($32\,\mu m$ along $90\,mm$) before starting the horizontal scans.

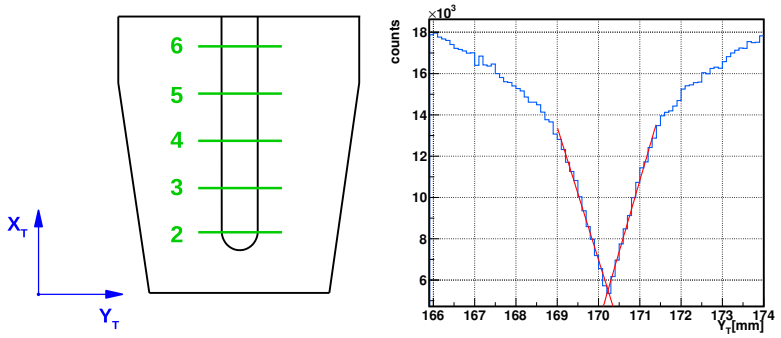

(a) (b)

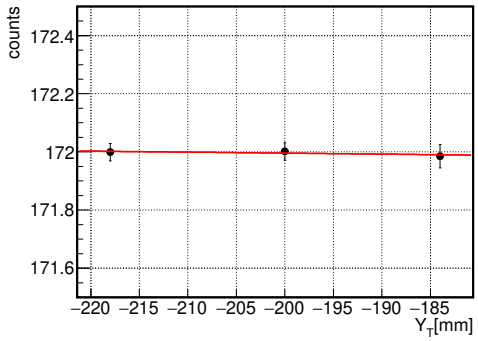

(c)

Figure 7.5: Horizontal alignment procedure. (a) linear scan along the bored-hole of the detector. (b) Efficiency graph for slice 3. The red lines represent the linear fits performed on the edges of the efficiency graphs. (c)Tilt of the vertical axes of the crystal after the alignment. In this particular case, slices 1, 2 and 6 were not considered for the fit. See text for more details.

7.2 Two-dimensional scans

With the Strasbourg scanning table it is possible to characterize a detector by performing two-dimensional (2D) scans. In the following sections the results of various 2D scans of the S001 detector, will be shown. The scans, a list of which is given in table 7.2,

are realized with the three different new sources available: ^{241}Am, ^{137}Cs and ^{152}Eu (see table 4.1). The different energy regions, in which the scans are performed, allow

Type	Source	Coll ⌀	Pitch	points	time per point	Tot time
Vert. rotation alignment	^{241}Am	$1\,mm$	$0.1\,mm$	583	$120\,s$	$22\,h$
Vert. across seg. line.	^{241}Am	$0.5\,mm$	$0.05\,mm$	61	$2000\,s$	$1.4\,d$
Vert. partial	^{241}Am	$1\,mm$	$1\times1\,mm^2$	2769	$60\,s$	$2.5\,d$
Vert. sector B	^{241}Am	$1\,mm$	$1\times1\,mm^2$	1000	$60\,s$	$20\,h$
Hori. Total Area	^{241}Am	$1\,mm$	$1\times1\,mm^2$	7448	$100\,s$	$9.9\,d$
Vert. axis alignment (1)	^{137}Cs	$1\,mm$	$0.1\,mm$	806	$240\,s$	$2.5\,d$
Vert. axis alignment (2)	^{137}Cs	$1\,mm$	$0.1\,mm$	506	$240\,s$	$1.4\,d$
Vert. axis alignment (3)	^{137}Cs	$1\,mm$	$0.1\,mm$	506	$240\,s$	$1.4\,d$
Hori. alignment (1)	^{137}Cs	$1\,mm$	$0.1\,mm$	804	$240\,s$	$2.5\,d$
Hori. alignment (2)	^{137}Cs	$1\,mm$	$0.1\,mm$	804	$240\,s$	$2.5\,d$
Vert.Total Area	^{137}Cs	$1\,mm$	$2\times2\,mm^2$	1351	$150\,s$	$2.5\,d$
Hori.Total Area	^{137}Cs	$1\,mm$	$2\times2\,mm^2$	2195	$150\,s$	$4.2\,d$
Vert.Total Area	^{152}Eu	$1\,mm$	$2\times2\,mm^2$	1355	$360\,s$	$6\,d$
Vert. sector B	^{152}Eu	$1\,mm$	$2\times2\,mm^2$	271	$1\,h$	$12\,d$
Hori. sector B	^{152}Eu	$1\,mm$	$2\times2\,mm^2$	960	$1\,h$	$40\,d$

Table 7.2: List of performed scans presented in this work. Times include the pauses for the automatized nitrogen refill (25 minutes every 8 hours).

to obtain various informations on the behavior of the detector and show the versatility of the Strasbourg scanning technique. For the first time in the AGATA and GRETA collaborations a scan with a ^{152}Eu source was performed. It is worth mentioning that the yield of the collimator (i.e. the number of gamma rays that exit the collimator with respect to the gamma rays emitted by the source) for the ^{152}Eu source is lower (due to a lower activity by a factor 2.5) than the ^{137}Cs (see chapter 4). Moreover, the yield is "divided" among the different energies of the gamma ray emitted which have different branching ratios. This means that in order to have a satisfactory amount of statistics for a given energy, the time spent to acquire data for a single point should be longer, with respect to the ^{137}Cs source, leading to time consuming scans about a factor 20 or longer. For example, a single point acquisition with a ^{137}Cs source requires, generally, $150\,sec$ while 1 hour is required for the ^{152}Eu source in order to have the same number of events that are in the photopeak of the cesium for the less intense transition considered of the ^{152}Eu source. A complete scan of S001 detector, with the ^{152}Eu source, would then last about two months.

In the following a study on the local detection efficiency, on the charge carriers behavior and imaging will be presented.

7.2.1 Local detection efficiency: ^{137}Cs source

The local detection efficiency is defined as the spectrum area around the photopeak of the energy of interest obtained at each scanned point (collimator position). The energy window is generally taken as $\pm 5\,keV$ but may be adjusted when needed. Figure 7.6 shows the results for a vertical scan realized with the ^{137}Cs source. The figures refer to the spectra obtained on the core contact requesting full absorption in the full crystal volume (figure 7.6a) and the segment contacts requesting full absorption in a single segment (figure 7.6b), respectively. Figure 7.6a shows that the core local efficiency is not homogeneous as it is larger in the bulk of the detector with respect to the borders (see color scale). This effect is due to Compton scattering, as gamma rays interacting near the border of the detector have, geometrically, a larger probability to be scattered outside the detector thus reducing the number of fully absorbed events (the photopeak area). Another drop of efficiency, located in the central part of the detector, is caused by the presence of the bored hole which reduces the active part of the crystal. A particular effect can be noted where a darker blue point marks the center of the bored hole area. This point corresponds to the position of segmentation lines crossing on the front face of the detector. The regions between the segmentation lines have very low electrical fields that lead to an incomplete charge collection. The charges will drift slowly towards the contacts increasing the probability to recombine and these areas can be thus considered inactive. This explains the sudden efficiency drop in correspondence to that specific point of the scan. As a final remark, the hexagonal shape of the front face and the tapering of the detector can be guessed by looking at figure 7.6a as the efficiency profile is directly linked to the active volume of the crystal.

Figure 7.6b shows the local efficiency of the segments of the six detector slices. For the first four slices of the detector, the hexagonal shape of the tapering is clearly visible while slice 5 exhibit a rounded hexagonal shape and slice 6 shows the overall cylindrical shape of the detector back end. The efficiency in the first slice is higher in the bulk of the segments while it decreases, towards the borders of the detector. This can be understood by looking at the horizontal profile of the slices electrical fields, schematically presented in figure 6.25. The figure shows that the first slice of the detector has a larger active volume towards the center, hence enhancing the photopeak efficiency in this area. For the second slice of the detector, the opposite phenomenon occurs, as in the same region the active volume is smaller, leading to a lower efficiency. In general, the average efficiency decreases as the slice number grows due to gamma-ray absorption along the germanium, with the only exception on the border of the slices where the beam can enter directly in the segments due to the tapering of the crystal. Finally, a significant drop in efficiency is located along the segmentation areas.

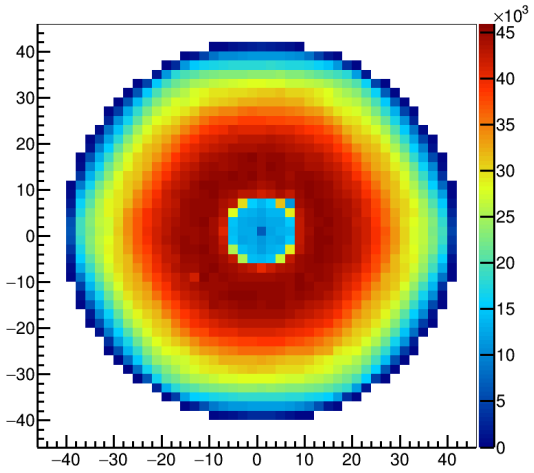

(a)

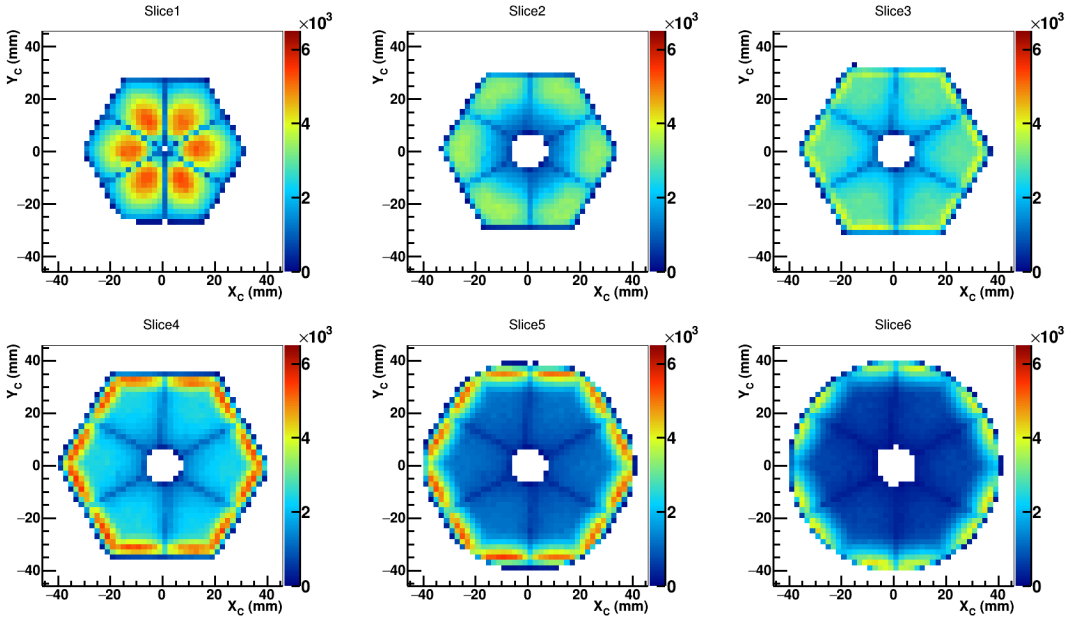

(b)

Figure 7.6: Local detection-efficiency distribution for the core (a) and the segments (b) at $662\,keV$. See text for more details.

7.2.2 Local detection efficiency: ^{152}Eu source

Since a ^{152}Eu source emits gamma rays of different energies (see chapter 4 and figure 7.7), it is possible to characterize a detector at different energies performing a single scan and selecting the events of interest by gating on the peak energies of interest. This scanning technique has never been tried with other scanning tables and is tested for the first time in Strasbourg. A vertical 2D scan of $2\,mm$ pitch, with a collimator of

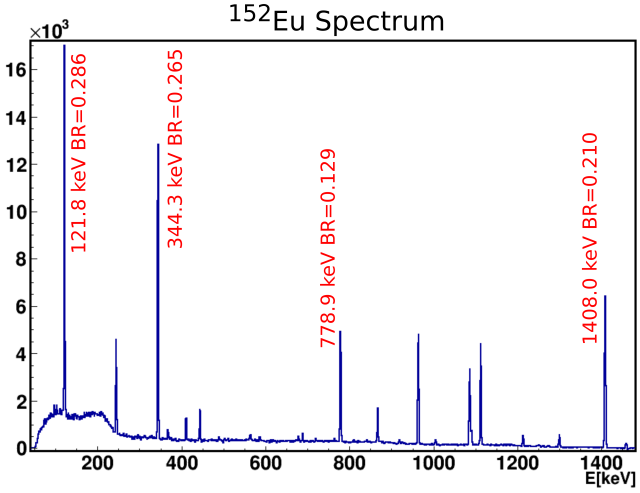

Figure 7.7: Europium core spectrum obtained from the 1 mm diameter collimator. The peaks of interest are marked by their energy and branching ratio.

$1.0\,mm$, is performed on the S001 detector with an acquisition of $360\,s$ per point which is short regarding the source activity and the branching ratio of the transitions. Gates on $122\,keV$, $344\,keV$, $779\,keV$ and $1408\,keV$ events are set and the local efficiency (defined in the previous section) distributions are plotted for each considered energy.

The results for the $122\,keV$ photopeak are shown in figure 7.8 for each one of the six slices of the detector. It can be seen that, as expected, at this energy the gamma rays are totally absorbed in the first two slices of the detector, while for the other slices events are registered only when the beam hits the tapered border of the detector. In particular, in the second slice of the detector, the only area where the local efficiency isn't zero is for $R \gtrsim 20\,mm$. As explained in the previous section, this is due to the fact that the active volume of the first slice, around the center of the detector, extends toward the Z_C direction, while the active volume of the second slice diminishes in the same radial range. Thus the gamma rays emitted by the collimator at this scanning positions are most likely to be absorbed by the first slice. Finally, in the first slice it is hard but possible to see the shadows of the contacts of the six front segments, as the material in which they are made absorbs of low-energy gamma rays. See for example the vertical line at $X_C = 8\,mm$ and $-20\,mm < Y_C < -10\,mm$.

For the next higher energy gate at $334\,keV$, the local detection efficiency is non zero for the third, the fourth and the fifth slices, as shown in figure 7.9. For the sixth slice

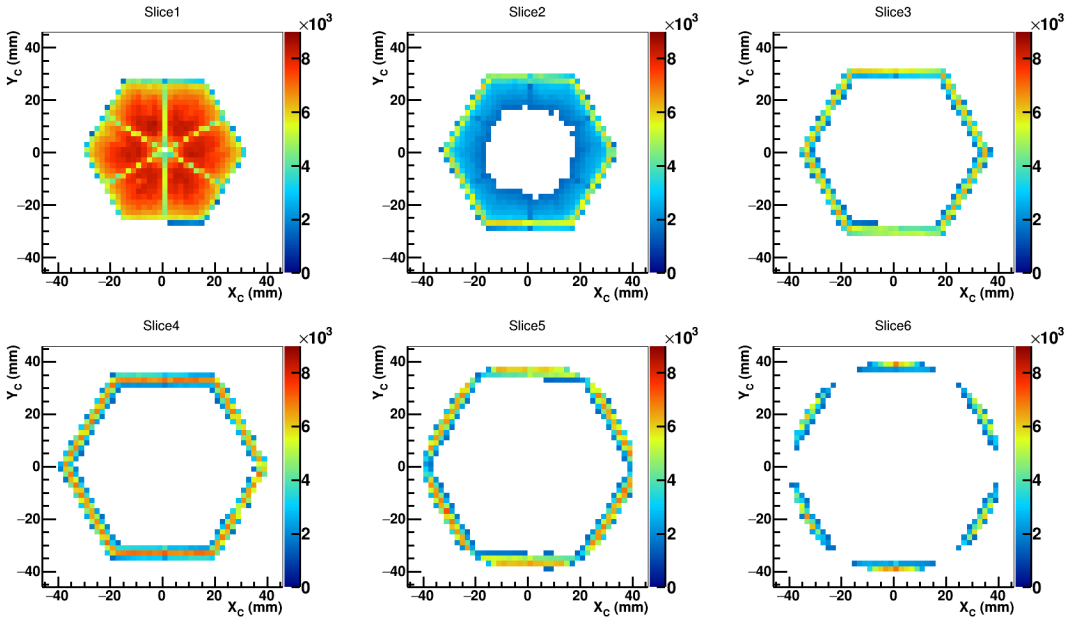

Figure 7.8: Local detection-efficiency distribution for the segments at $122\,keV$.

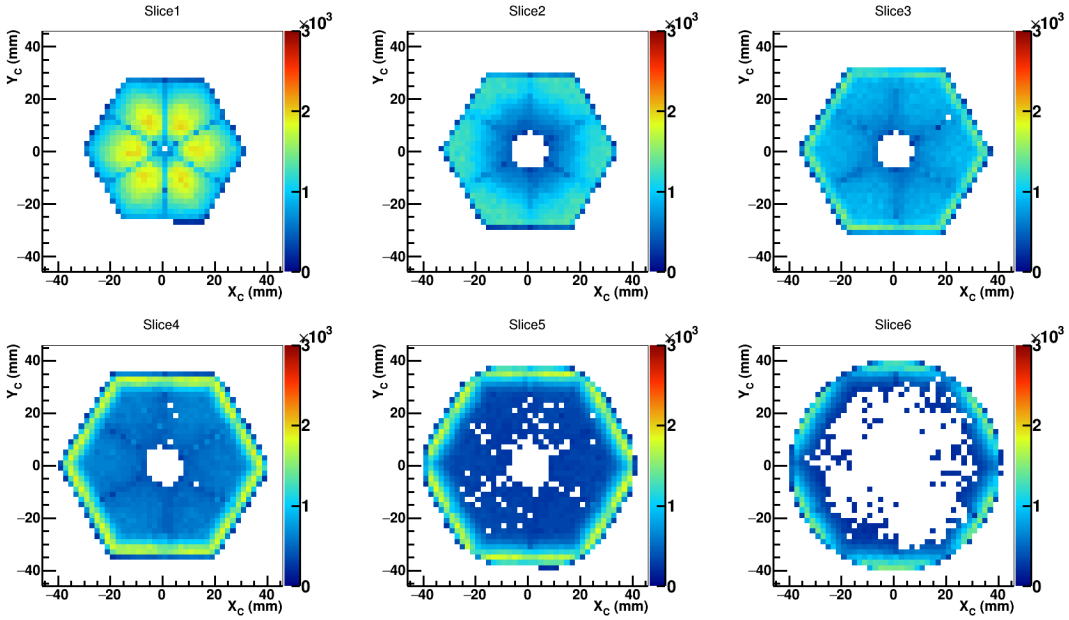

Figure 7.9: Local detection-efficiency distribution for the segments at $344\,keV$.

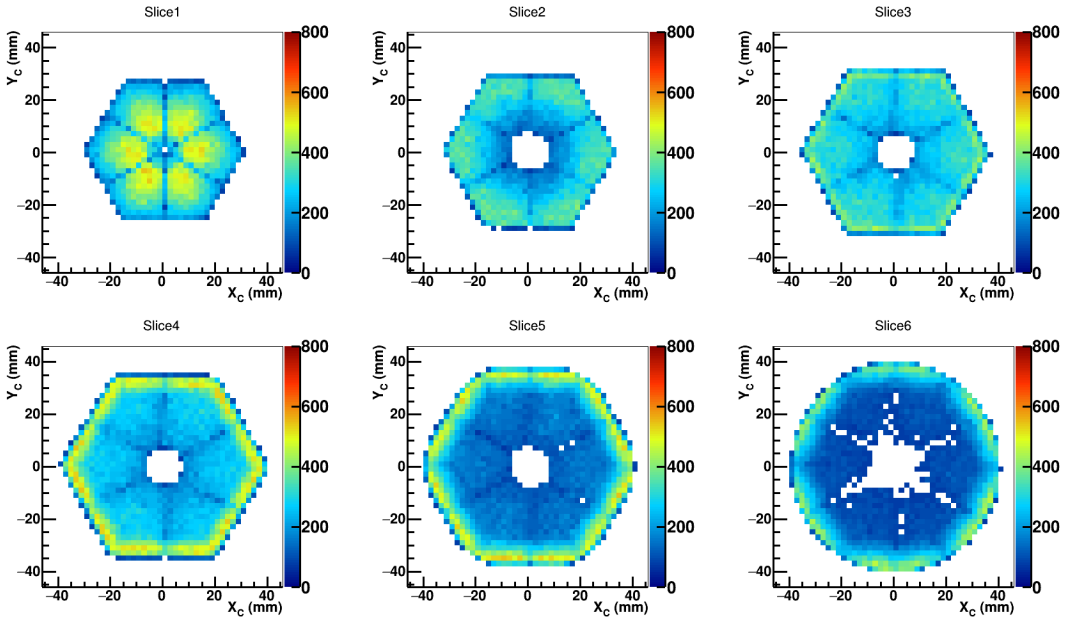

Figure 7.10: Local detection-efficiency distribution for the segments at 779 keV.

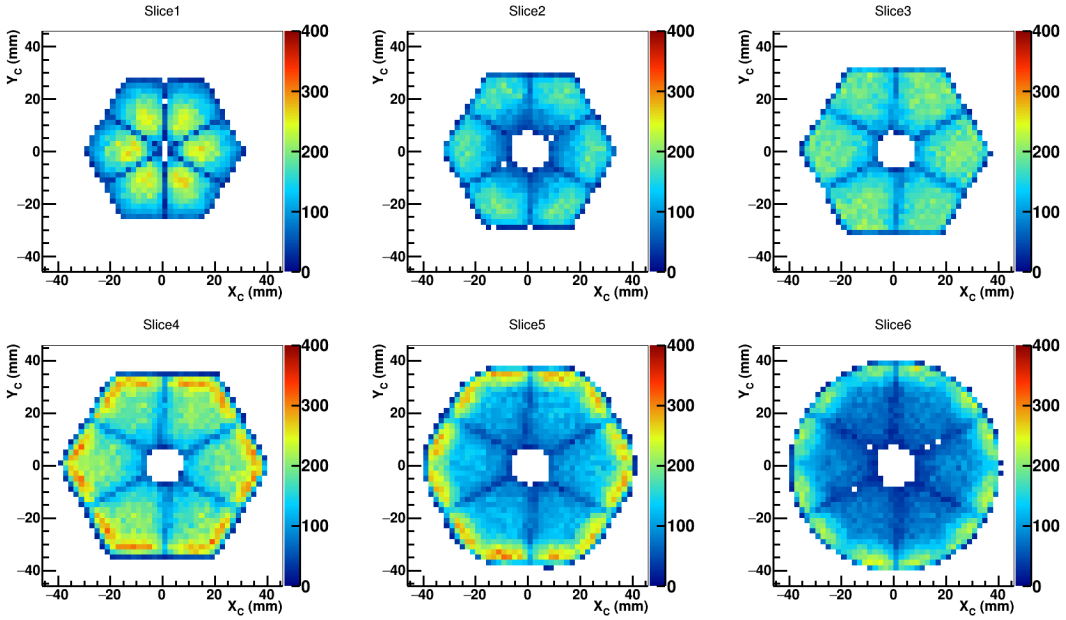

Figure 7.11: Local detection-efficiency distribution for the segments at 1408 keV.

the plot is nearly empty, except along the borders, as the beam gets mostly absorbed in the previous layers of germanium.

The results obtained gating on $779\,keV$ gamma-ray energy, in figure 7.10, should be similar to the ones obtained for the $662\,keV$ scan. However the difference in intensity between the ^{137}Cs source and the $779\,keV$ emission rate of the ^{152}Eu source (see sections 4.4 and 4.5) causes a substantial difference in the values of the local efficiency (a maximum of $5 \times 10^2\,cpp$, *count per pixel*, for the $779\,keV$ versus $6 \times 10^3\,cpp$ for the $662\,keV$ in the first slice). This leaves some empty spots around the central contact of the sixth slice as the gathered statistics in that region is poor.

Finally, the results for the $1408\,keV$ gate are shown in figure 7.11. The overall efficiency is lower than in the previous cases, but it is more homogeneous in the volume of the detector. This comes from the higher mean free path of high energy gamma rays.

In conclusion, the technique based on a multi-chromatic source seems to be effective and the method can be exploited to make 2D characterization of the detector and extended to perform 3D scans.

7.2.3 Crystal orientation

The orientation of the germanium crystal can be determined by measuring the rise time of the pulses generated for each position of the collimator. The rise time depends on the charge carrier velocity which, as said in section 2.3, depends from the orientation of the crystal. One can determine the rise time of a pulse by calculating the T_{10}^{90} as shown in section 3.3.1. For this study a ^{137}Cs scan is analyzed and, in particular, only the photopeak events absorbed in a single segment (*1-fold* events) are considered. For each collimator position, the T_{10}^{90} corresponds to the average of the T_{10}^{90} values of the events acquired at a scanned point for a given segment. Figure 7.12 shows the T_{10}^{90} distribution for the core and the segments. AGATA crystals are grown by slowly pulling it from a hot germanium bath along the $< 001 >$ crystal axis (see figure 2.2b) which is collinear to the Z_C axis. This mean that the $< 100 >$ direction lays in the $X_C Y_C$ plane and its direction can be determined from the distributions presented in figure 7.12. As charge carriers are faster along the $< 100 >$ crystal axis (see section 2.3), the corresponding T_{10}^{90} has the minimum value. For each segment slice and the core, the T_{10}^{90} values along a fixed radius are plotted as a function of the angle θ between the X_C axis and the radius direction, as shown in figure 7.13. These plots can be fitted with the function proposed in [56]

$$T_{10}^{90}(\theta) = A \cdot (1 + R_4 \cdot cos(4 \cdot (\theta - \theta_4))) \cdot (1 + R_2 \cdot cos(2 \cdot (\theta - \theta_2))) \qquad (7.2)$$

where θ_4 defines the crystal orientation relative to the detector axis X_C, the R_2 term corrects for the deviation of the 4-fold symmetry when the 6-fold geometry of the tapering is taken into account. The results of the fits are listed in table 7.3 along with the radius value for each slice at which the data are extracted. An average value for $\theta_4 = -16.7^\circ \pm 0.4^\circ$ is obtained.

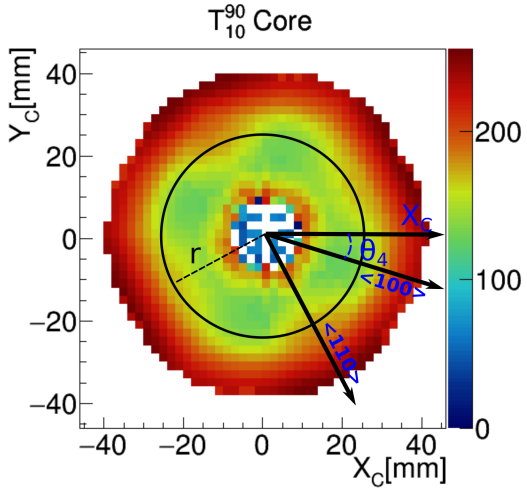

(a)

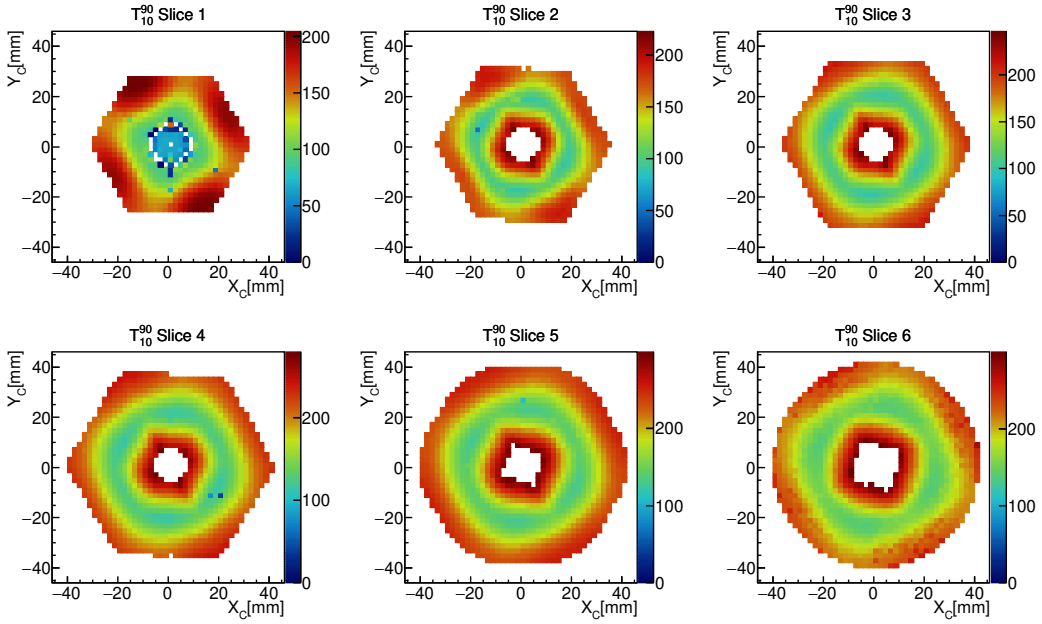

(b)

Figure 7.12: T_{10}^{90} distributions for the core (a) and the segment contacts (b) obtained with $662\,keV$ gamma rays. The segment distributions are produced by considering the T_{10}^{90} of the signals generated by the core gated on 1-fold events. Figure (a) shows the orientation of the $< 100 >$ and $< 110 >$ crystallographic axes and the angle θ_4 between the crystallographic axis $< 100 >$ and the detector axis X_C (see text for more information).

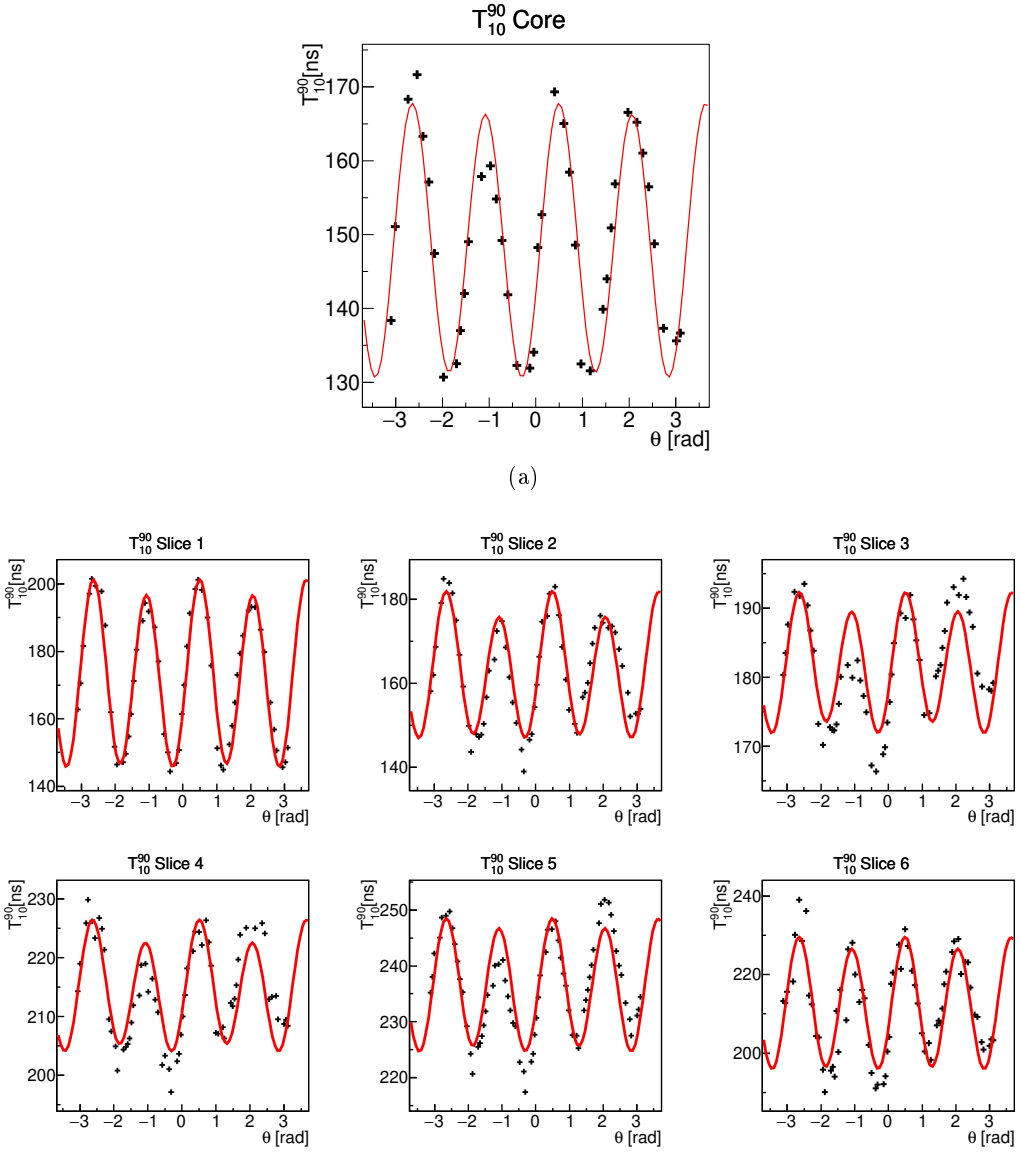

(a)

(b)

Figure 7.13: Experimental T_{10}^{90} values, for the core (a) and each segment slice (b) obtained for a fixed radius (see figure 7.12 and table 7.3). The curves are fit using equation 7.2 and θ is in radians. See text for more details.

	θ_4	r
Core	$-16.8^\circ \pm 0.7^\circ$	$r = 23\,mm$
Slice 1	$-16.7^\circ \pm 0.5^\circ$	$r = 25\,mm$
Slice 2	$-16.6^\circ \pm 0.8^\circ$	$r = 27\,mm$
Slice 3	$-17^\circ \pm 1^\circ$	$r = 31\,mm$
Slice 4	$-16^\circ \pm 1^\circ$	$r = 35\,mm$
Slice 5	$-17.0^\circ \pm 0.8^\circ$	$r = 37\,mm$
Slice 6	$-16.9^\circ \pm 0.8^\circ$	$r = 35\,mm$
AVG	$-16.7^\circ \pm 0.4^\circ$	

Table 7.3: Orientation of the crystal for the core and each slice (see text for more information). The right column displays the radius at which the data were extracted. The average (AVG) of the seven θ_4 values is given at the bottom line.

7.2.4 Core-contact charge collection

It was already observed that along the segmentation lines the charge carriers collection from the electrodes is not optimal leading to drops in the efficiency of the detector. Apart from these areas, the charge carriers collection inside a detector is generally non-homogeneous due to factors such as the non-uniformity of the electric field, trapping impurities and defects concentrations of the crystal. This is more evident for large volume crystals, such as S001, which generally present a slightly worse energy resolution compared to small volume detectors. Charge carrier collection effects can be probed by looking at detector characteristics, such as the centroid position and the full width at half maximum (FWHM), of the energy photopeak acquired at a given scan position. For this purpose a ^{137}Cs 2D vertical scan is analyzed. For each position of the collimator, the photopeaks are fitted with a Crystal Ball function [72] which consists of a Gaussian function joint with an exponential low-end tail. The function can be written in the form

$$f_{CB}(x) = \begin{cases} \frac{\left(\frac{n}{|\alpha|}\right)^n exp\left(-\frac{a^2}{2}\right)}{\left(\frac{n}{|\alpha|} - |\alpha| - x\right)^n} & \forall\, x < -|\alpha| \\ exp\left(-\frac{1}{2}\left(\frac{x-\mu}{\sigma}\right)^2\right) & \forall\, x > -|\alpha| \end{cases} \tag{7.3}$$

where μ and σ are, respectively, the mean and the standard deviation of the Gaussian function, α is the point in σ units where the Gaussian function joints the exponential part and finally n is the slope of the exponential part. As opposed to a simple Gaussian function, the exponential tail of the Crystal Ball function fits better the low end part of the photopeaks that are populated by events for which incomplete charge collection lead to an energy loss. In the large majority cases, the peaks are Gaussians, as expected, and the tail is negligible. An example of a photopeak fitted with the Crystal Ball function is shown in figure 7.14. The photopeaks are fitted in a $\pm 10\,keV$ range in order to take into account long tails.

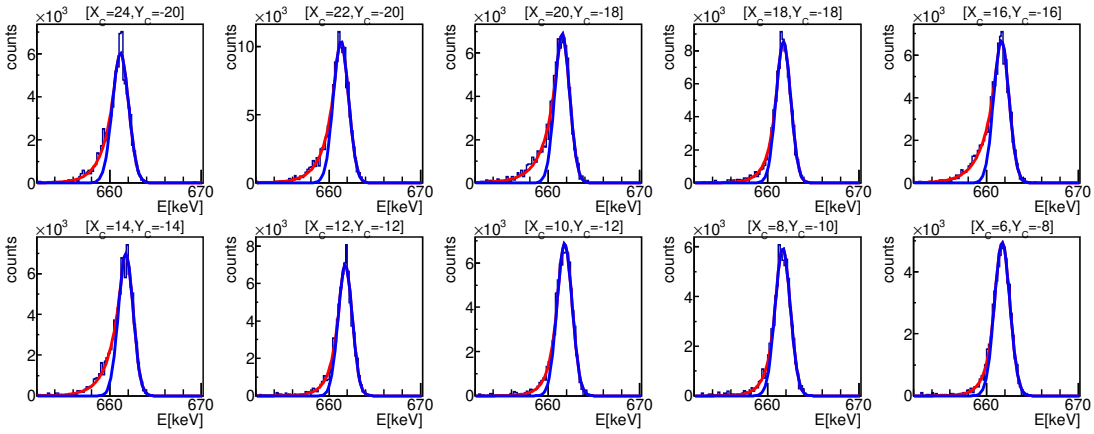

Figure 7.14: Example of photopeaks fitted with a Crystal Ball function. The Gaussian part of the function is plotted in blue and the tail in red. The spectra refers to segment $F3$ and are built with the segment energy gated on 1-fold events.

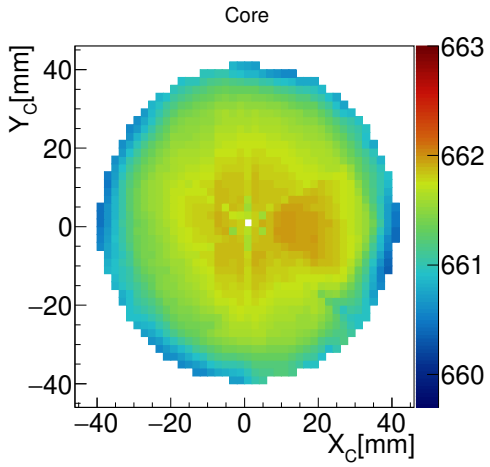

Figure 7.15: Core contact centroid-position distribution of the $662\,keV$ photopeak.

In figure 7.15 the centroid-position distribution of the photopeaks from the core contact is shown. The plot shows values of $661.7\,keV$ around the bored hole of the detector, which decrease toward the edges, with a difference between the maximum and the minimum values of about $1.3\,keV$. This behavior is due to the presence of trapping centers which capture the charge carriers without *de-trapping* them[5]. These centers are normally distributed uniformly inside the crystal, so that the probability for a charge to be trapped is mainly due to the length of drifting path. The core contact of the S001 detector collects negative charge carriers and thus, based on the Shockley-Ramo theorem, the core signals are mainly influenced by electron collection. The electron

[5] or *de-trapping* them after a time much larger than the shaping time of the digital amplifiers, $5.95\,\mu s$ for this scan (see section 4.2.4).

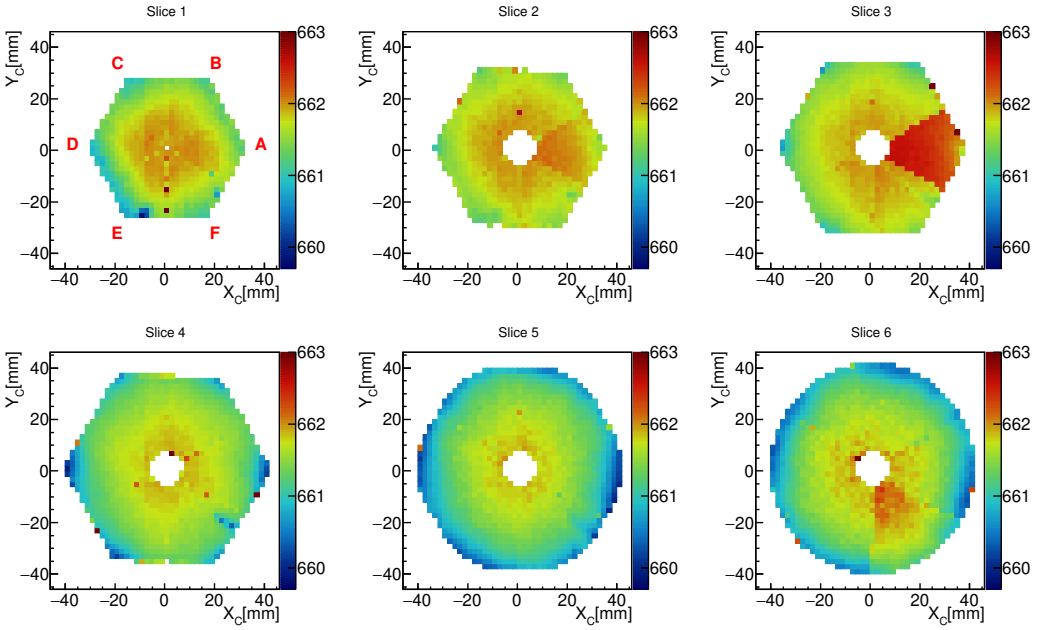

(a)

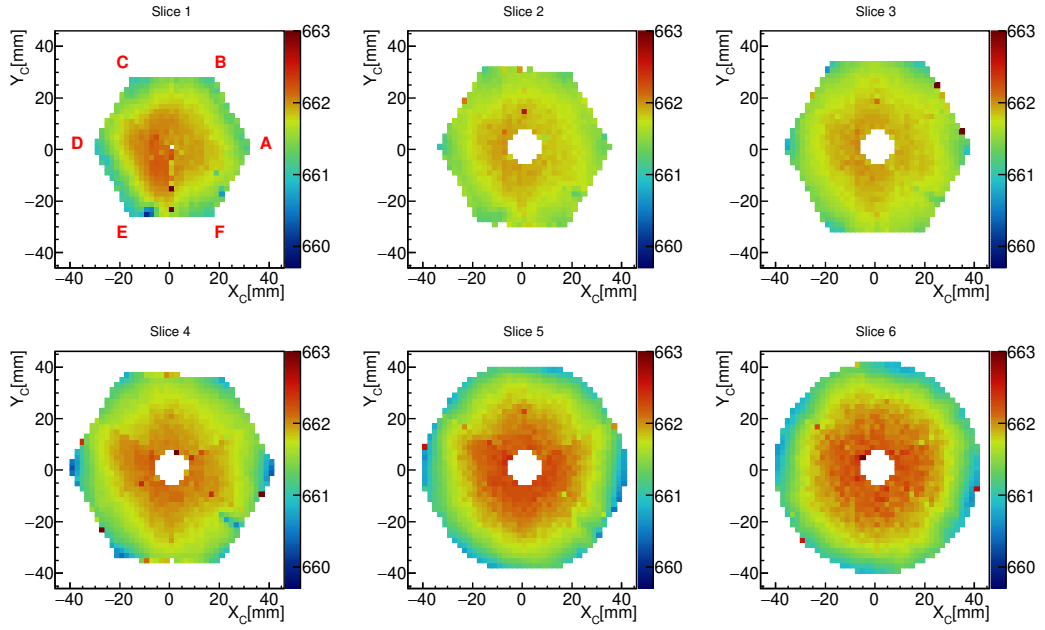

(b)

Figure 7.16: Distribution of the $662\,keV$ photopeak centroid position for the core gated on 1-fold events in the segments contacts. Panel (a) shows that the centroid-position distributions for segments $A2$, $A3$ and $F6$ are globally shifted versus the ones of the other segments. Panel (b) shows the distributions normalized at $661.7\,keV$ for each segment. See text for more detail.

trapping leads to lower signal amplitudes (see section 2.9) which in turn leads to a systematic peak shift which is larger as the distance of the interactions from the core grows. This phenomenon is well known in HPGe detectors [34, 73].

The core charge collection can be better investigated by gating the core energy on 1-fold events in the segments. The centroid distribution for the six slices of the detector is shown in figure 7.16a. Segments $A2$, $A3$ and $F6$ present higher values compared to the other segments. This behavior can't be explained by trapping and it has most likely an electrical nature. The segment distributions are uniformed by normalizing the centroid value of each segment to $661.7\,keV$. The new distributions are shown in figure 7.16b. As for the case of the core contact, the centroid position shifts toward the low end of the spectra as the collimated beam moves from the bored hole toward the edges of the detector. Figure 7.17a shows the centroid position as a function of the radius for the six slices of the detector and the core. The graphs are renormalized so that the nearest point to bored hole has a value of $661.7\,keV$. The behavior of the different slices is quite similar and matches with the one of the core. The differences among the slices are due to their slightly different dimensions and shape. In the first slice, for example, the shift of the centroid position is more pronounced because the electric-field intensity varies rapidly with the radius and the path of the charge carriers becomes longer, out of plan, approaching the slowest $< 111 >$ crystal axis (see section 2.3). The plot shows a maximum shift of $\sim 1.6\,keV$ for the centroid values of the back slices of the detector.

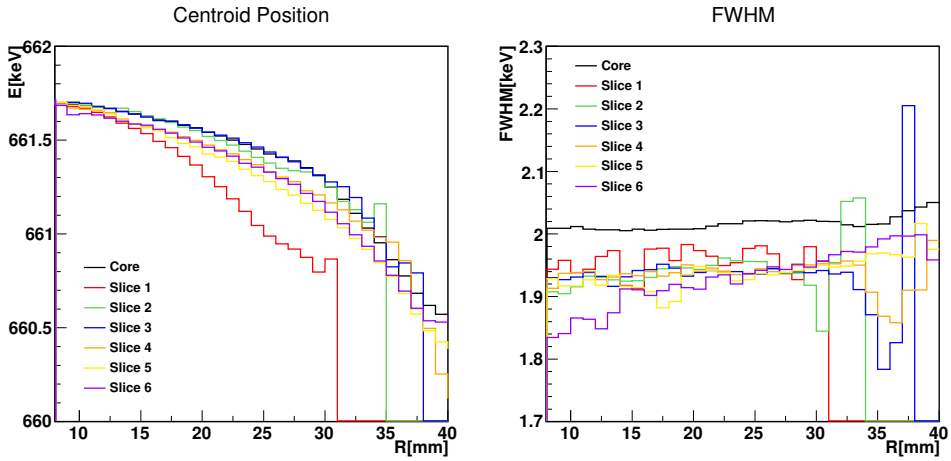

(a) (b)

Figure 7.17: (a) Distribution of the $662\,keV$ photopeak centroid position for the core gated on 1-fold events in the segments contacts as a function of the radius. The graphs are renormalized so that the nearest point to bored hole has a value of $661.7\,keV$. (b) Distribution of the $662\,keV$ photopeak FWHM values for the core gated on 1-fold events in the segment contacts as a function of the radius.

Figure 7.17b shows the FWHM average value, as a function of the radius, for the core and the slices of the detector. As it can be seen the photopeaks slightly widen

monotonously as the beam is shot far from the core contact. This behavior is coherent with examples found in literature ([33, 34]) and shows how trapping also affects the resolution of a large volume detector (see section 2.9 and figure 2.13).

7.2.5 Segment-contacts charge collection

The distributions of the centroid values obtained from segment energy spectra is investigated by gating on 1-fold events. The results are shown in figure 7.18. Once again the distribution of each segment is standardized by normalizing the centroid values at the bored hole to $661.7\,keV$. The figure shows a behavior similar to the one found for the

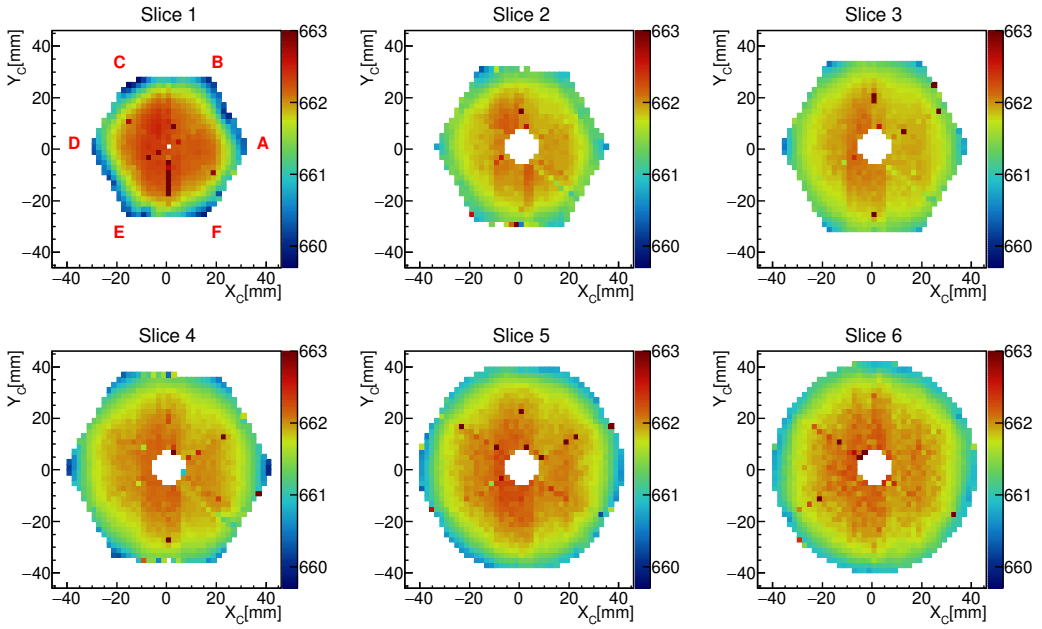

Figure 7.18: Distribution of the $662\,keV$ photopeak centroid position for the segment contacts gated on 1-fold events. The distributions are normalized at $661.7\,keV$ for each segment.

core contact (see figure 7.19a) with decreasing centroid values as the radius grows. This behavior differs from that expected. As the segment contacts collects positive charge carriers, the ballistic deficit should be mostly determined by the trapping of holes and the centroid shift should have an opposite trend than what observed or be flat when no hole trapping occurs. For example, the AGATA detector B006 was characterized in reference [24] and it was observed that the centroid position of the segment energy photopeaks is quite constant along the radius of the detector. The algorithms used to analyze the data for the detector S001 were tested on the B006 detector data and reproduced the results described in [24]. The only experimental difference between the two scans are the TNT2 trapezoid filter settings (see section 3.3.1 and figure 3.6c) for the amplification of the signals which was $\tau = 5.95\,\mu s$ ($k = 4\,\mu s$, $m = 2\,\mu s$, $s = 1.75\,\mu s$ and $w = 0.2\,\mu s$) for the S001 detector and $\tau = 8.2\,\mu s$ ($k = 6\,\mu s$, $m = 3\,\mu s$, $s = 2\,\mu s$ and

$w = 0.2\mu s$) for B006 detector. This somehow impacts the energy readout but, as no further tests with larger τ values were performed, no certain conclusion can be drawn. This opens interesting opportunities for future analyses.

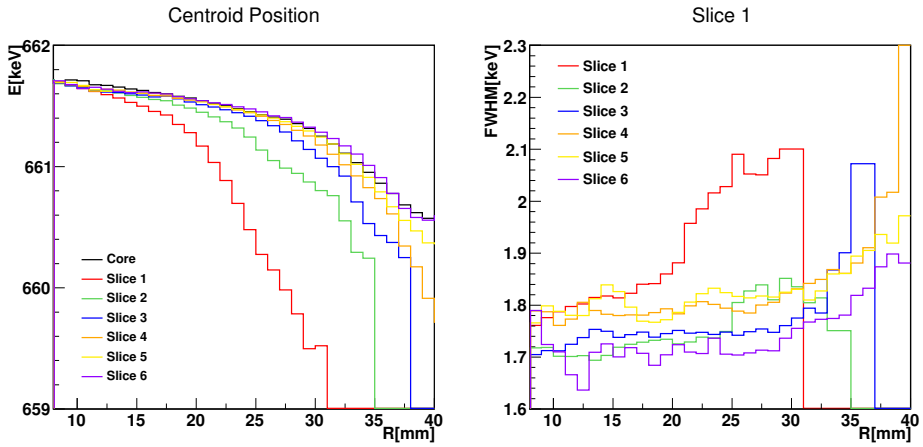

(a) (b)

Figure 7.19: (a) Distribution of the $662\,keV$ photopeak centroid position for the segment contacts gated on 1-fold events as a function of the radius. The graphs are renormalized so that the nearest point to bored hole has a value of $661.7\,keV$. (b) Distribution of the $662\,keV$ photopeak FWHM values for the segment contacts gated on 1-fold events as a function of the radius.

The value of the FWHM as a function of the radius for sector A is shown in figure 7.19b. The values are rather constant for R smaller than $25\,mm$ and an increase is observed for radii larger than $25 \div 30\,mm$ depending on the segment slice considered. The growing is unexpected and confirms the anomalous trend previously described suggesting a larger influence of the electron trapping instead of hole trapping.

Further analysis on the charge collection is done by examining the area of the exponential tail in the low end of the fitted Crystal Ball function. In fact, a large tail area could denote an anomaly in the charge collection. If $\mathcal{A}_{CB}$ is the total area of the fitted Crystal Ball function and $\mathcal{A}_{Gauss}$ the area of the Gaussian part, then the figure of merit FoM written as

$$FoM = \frac{\mathcal{A}_{CB} - \mathcal{A}_{Gaus}}{\mathcal{A}_{CB}} \tag{7.4}$$

can be used to quantify the trapping effects. The closer is FoM to 1, the largest will be the exponential component of the Crystal Ball. For a perfect Gaussian peak, $FoM = 0$. Figure 7.20 shows the distribution of FoM for the core contact and for the six segment slices of the detector. The plots show that the FoM value is globally homogeneous except in some well defined areas. A trail of anomalous values is visible in segments $F2$, $F3$ and $F4$. These anomalous points can be seen as well in the distributions of the centroids (figure 7.18). Some of the spectra extracted from the trail are shown in figure 7.14. The trail seems to follow the charge-carrier trajectory (figure 7.21) suggesting

that the trapping center is actually concentrated in a narrow area influencing the charge carriers on the path. Since, normally, trapping centers are homogeneously distributed in the crystal, the nature of this anomalous zone is not clear.

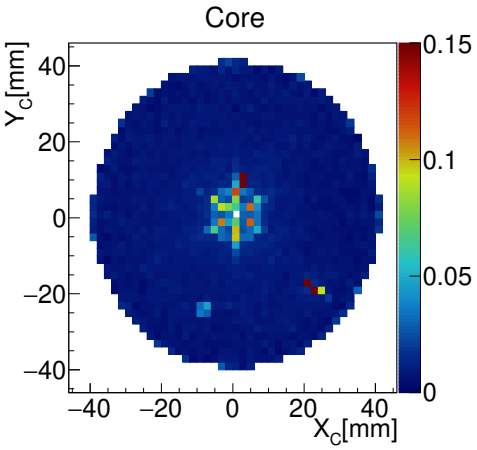

(a)

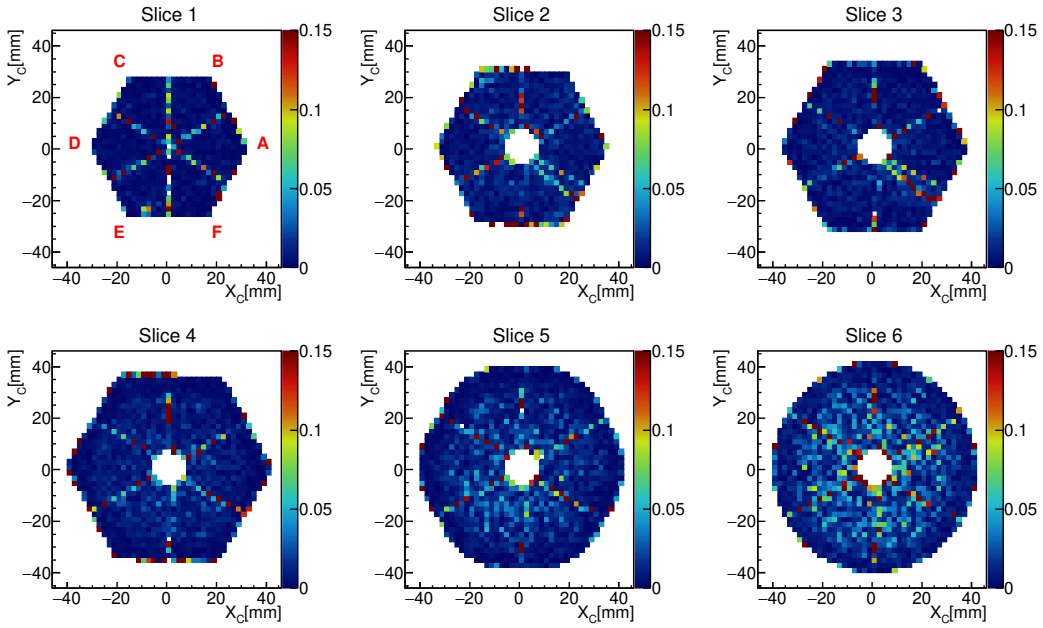

(b)

Figure 7.20: Distribution of the factor of merit FoM for the core (a) and segment contacts (b) gated on 1-fold 662 keV events.

The macroscopic models of trapping make the assumption that the peak measured at a given position is a Gaussian which centroid is shifted and width widen in case of trapping. The present shapes of the peaks along the trail lead to the belief that the

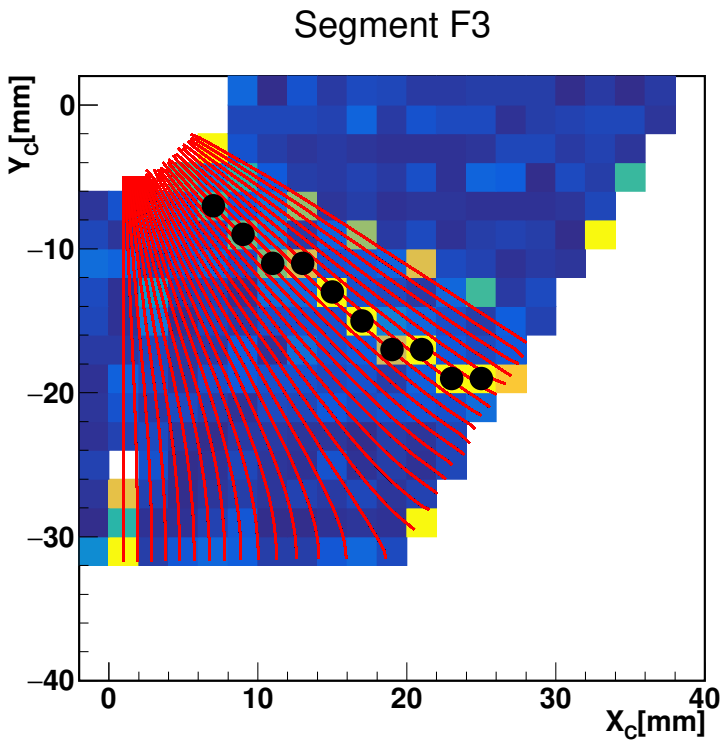

Figure 7.21: Plot of the charge-carrier trajectories in the middle of segment $F3$ thickness projected on the XY plane (red lines). The trajectories are superposed to the FoM distribution of slice 3 (see figure 7.20). The black circular markers highlight the points of the trail.

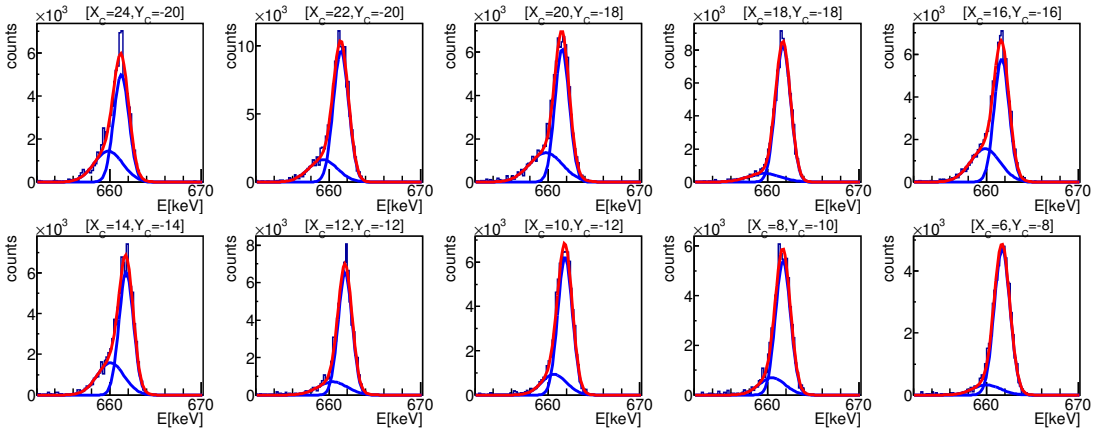

Figure 7.22: Photopeaks measured in the defective zone fitted with a double Gaussian.

extension of the zone is smaller than the spot of the gamma-ray beam ($\sim 1.5\,mm$ in the center of the crystal). If this is true, in fact, part of the gamma rays will produce

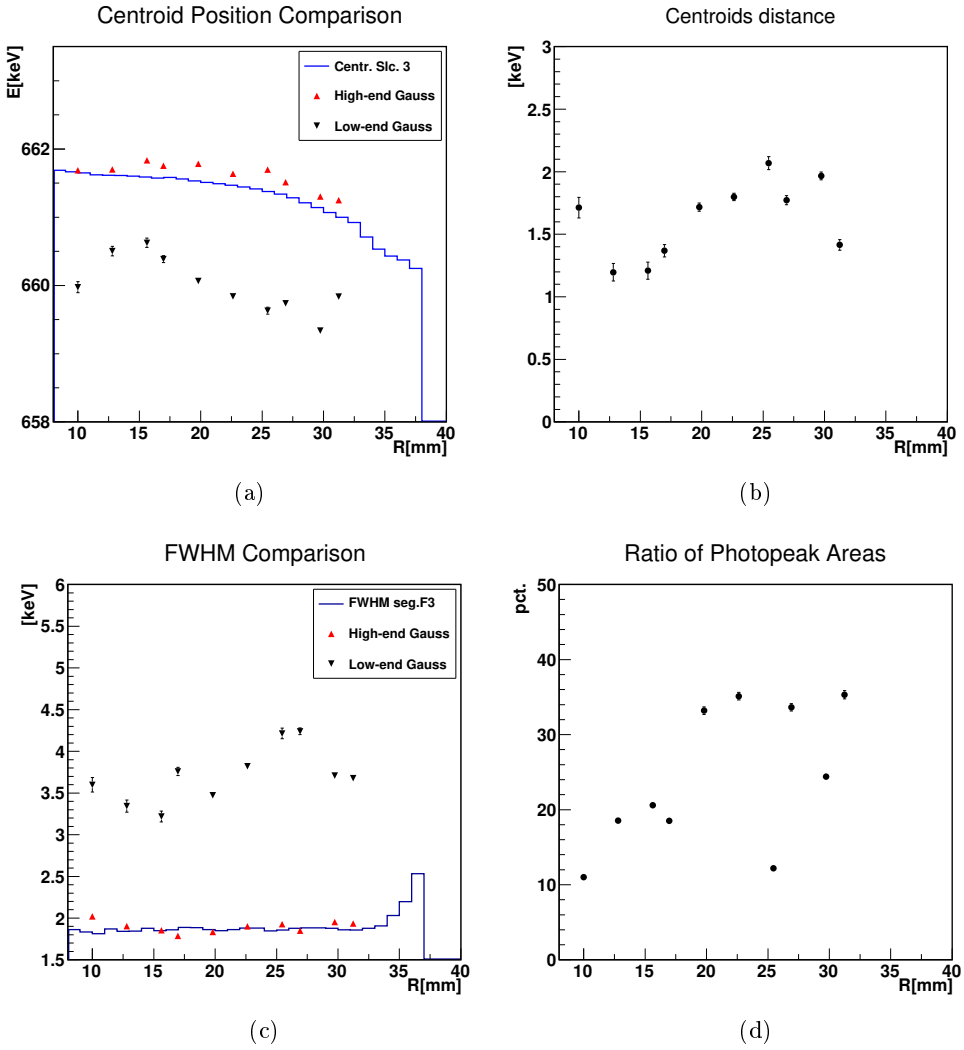

Figure 7.23: Characteristics of the two Gaussian components of the photopeak as a function of the radius. (a) Centroid positions. (b) relative distance between the two Gaussians. (c) FWHM values. (d) Ratio of the low end Gaussian area to the total peak area.

charges that will follow paths avoiding the defective zone and will be collected normally. Another part of the gamma rays, instead, will produce charges that will follow paths crossing the defective area. For the former case the photopeak will exhibit the observed electron trapping (see figure 7.19a). In the latter case, instead, additional charges are lost and thus a second peak should appear in the lower end of the peak. The spectra have been successfully fitted with a double Gaussian as shown in figure 7.22. In figure 7.23a the centroid position of the two peaks is plotted as a function of the radius together

with the average centroid value of slice 3. It can be seen that the high-energy peak follows quite nicely the values and the general trend of the slice, while the low-energy peak is shifted by, in average, $\sim 1.6\,keV$. The values are somehow flat for $R > 20\,mm$. The distance between the two Gaussian peaks is plotted in figure 7.23b and shows a growing trend which then saturates towards radii larger than $20\,mm$. The FWHM of the peaks, in figure 7.23c, also shows that the resolution of the high-energy peak follows the average of the segment ($\sim 2\,keV$) while the lower energy peak has a much larger FWHM (3.5 to $4\,keV$). Finally the ratio of the low end Gaussian area versus the full peak area, shown in figure 7.23d, indicates that the low-energy component grows from the bored hole towards $R \simeq 20\,mm$ and saturates for larger radii.

In conclusion, the plots shown previously in figure 7.23 suggest that the defective zone has a big impact on the electron collection and extends along segments $F2$, $F3$ and $F4$ from the center of the crystal to around $R = 20\,mm$ with an approximative shape of a plane of thickness smaller than the gamma beam spot ($< 1.5\,mm$). Hypothetically the crystal can be defective in that part for some structural reasons such as a major crystal-defect concentration, an anomalously large trapping center concentration or a cleavage area. More tests should be made to fully understand the phenomenon and fully characterize the properties of the defective zone.

7.2.6 2D scans with ^{241}Am source: imaging

The first layers of a detector can be explored by performing scans with low-energy gamma rays such as the ones emitted by the ^{241}Am source. In particular an imaging analysis can be performed by looking at the local efficiency profile, as already seen in the previous chapters. Hardware features of the crystal can be extracted such as the position of the segmentation lines, the position of the segments contacts and even the wiring. These kind of measurements are generally performed at the very beginning of a characterization in order to better understand the detector position on the reference frame of the table.

7.3 Three-dimensional scans

As stated in chapter 4 the main feature of the Strasbourg scanning table is the possibility to perform full volume characterization of a detector using the PSCS technique. In the following section, a description of the raw data treatment will be given and then the results of the $PSCS$ technique applied to real three-dimensional ^{137}Cs and ^{152}Eu scans will be presented.

7.3.1 Treatment of raw data

As shown in table 7.2, the cesium scan had a duration of 2.5 minutes per point, leading to a total duration of 6.7 days (2.5 days for the vertical acquisition and 4.2 days for

the horizontal acquisition, including the nitrogen refill pauses[6]). This duration assure a sufficient number of events, in the photopeak window of $662 \pm 2.0\,keV$, per point for the χ^2 selection algorithm. On the other hand, as already stated in section 7.2, acquisition times for the europium scan must be longer in order to obtain similar statistics for each one of the four photopeaks of interest ($121.8\,keV$, $344.3\,keV$, $778.9\,keV$ and $1408.0\,keV$ all gated in a $\pm 2.0\,keV$ window). A duration of 60 minutes per point was used and in order to limit the total scanning time it was chosen to scan only one single sector (sector B). Nevertheless the scan duration lasted 54 days in total (14 days for the vertical acquisition and 40 days for the horizontal acquisition, including the nitrogen refill pauses).

Before being treated with the χ^2 selection algorithm described in section 5.2, the acquired datasets are sorted and prepared. For each dataset, only 1-fold events are selected. Moreover each pulse shape is normalized and then aligned to their T^{10} (see figure 3.6b). In particular the transient pulses are normalized and aligned with respect to the signal of the hit segment[7]. The europium events, which are acquired in a single scanning procedure, are sorted in four separated datasets, one for each energy, and treated independently with the χ^2 selection algorithm, leading to the construction of four different databases.

In the following the results of the ^{137}Cs scan will be presented. They will be used as reference and will be further compared to the results obtained for the europium scan.

7.3.2 Cesium 3D scan

A full volume characterization using the PSCS technique implemented by the Strasbourg scanning table was performed and described in [24]. For that analysis, a B-type AGATA detector was scanned with a ^{137}Cs source using the $1.5\,mm$ diameter collimator (original configuration, see section 4.2). The ^{137}Cs scan presented here, instead, is realized using the new sources and the $1.0\,mm$ diameter collimator (updated configuration). In both measurements, a pitch of $2\,mm$ was used.

Once the database is created, it is important to note that some of the pulses selected by the algorithm are associated to points that lay outside the volume of the detector. Such cases can exist because the χ^2 selection algorithm is blind of the geometry of the detector[8]. It is, thus, important to clean the database from these events. Since on average the χ^2 value of these pulses is higher than the χ^2 value of the events selected inside the detector, it is possible to set a threshold in order to filter the database. Figure 7.24 shows an example of one transversal slice of the database ($2\,mm$ thick), on the tapered section of the detector, before and after the filtering.

A first test to verify the PSCS results is to check the segment map. Despite the

[6] During the nitrogen filling the scanning procedure is paused for the fill duration plus 15 minutes of waiting time after the fill (about 25 minutes in total) in order to avoid effects on the acquisition due to the bubbling of the liquid. An automatic refill is done every 8 hours.

[7] A detailed description of the time alignment is given in section 3.4.3 of [24].

[8] In fact, at the beginning of this chapter it was remarked that a precise alignment of the detector on the table is essential for the scan.

χ^2 selection algorithm being blind to the geometry of the detector, each averaged pulse shape its associated to the segment in which they are selected. The map, relative to a longitudinal slice of the database at $Y_C = 0\,mm$ is shown in figure 7.25 compared to the ADL counterpart. Even if the mesh used for the two maps is different ($2\,mm$ for the real measurements and $1\,mm$ for the ADL map) the two geometries are very similar.

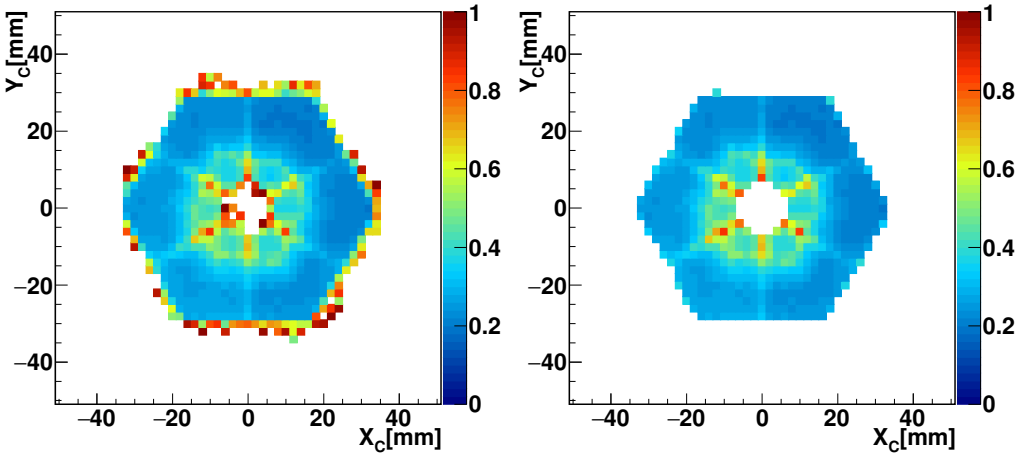

(a) (b)

Figure 7.24: A database slice at $Z_C = 14\,mm$ ($2\,mm$ thick) before and after the filtering.

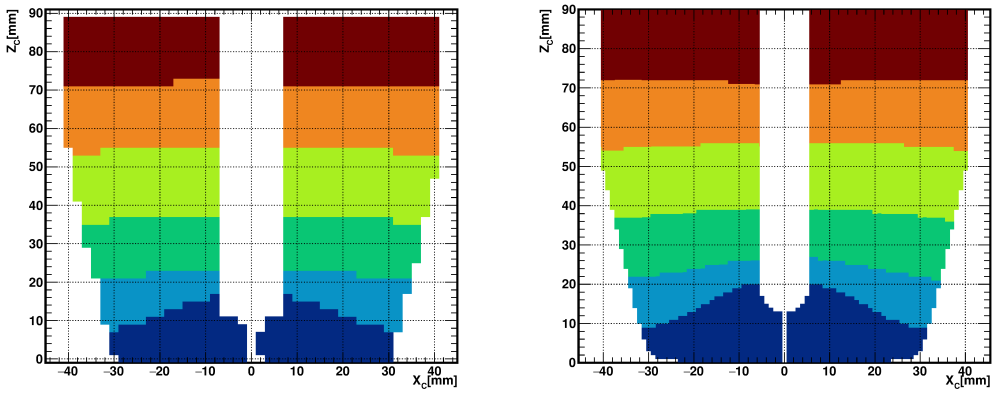

(a) (b)

Figure 7.25: Longitudinal section (for $Y_C = 0\,mm$) of the S001 segment map obtained with the PSCS technique (a) and calculated with ADL (b). In the first case the mesh of the grid is $2 \times 2\,mm^2$ while the second case has a finer $1 \times 1\,mm^2$ mesh.

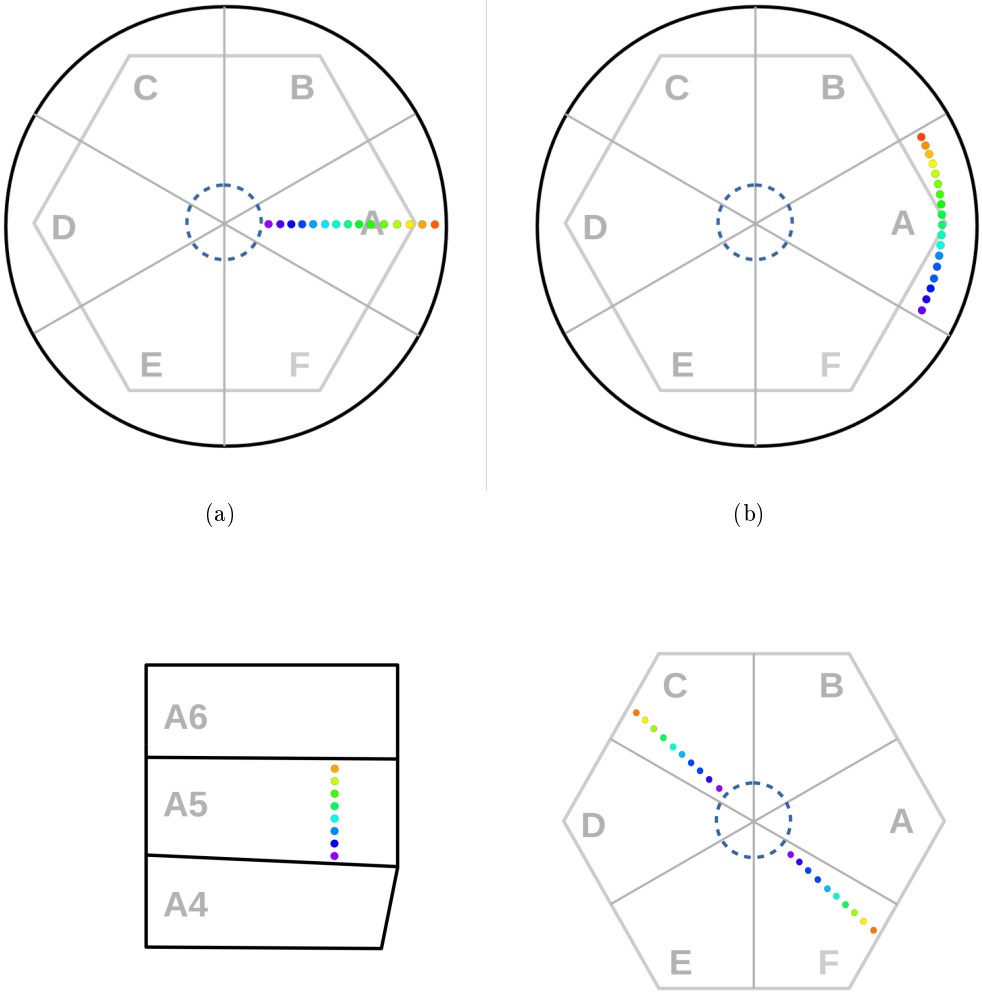

(a) (b)

(c) (d)

Figure 7.26: Schematic representation of the scanning positions for the pulses selected in figures 7.27 (top left panel), 7.28 (top right panel), 7.29 (bottom left panel) and 7.30 (bottom right panel).

The detector behavior can be verified by observing the pulse shapes at different locations (represented in figure 7.26). Figure 7.27 shows the pulse shapes relative to database points selected along a radius of the detector in segment $A5$ (see figure 7.26a). As expected, the shape of the main pulses (core and hit segment) depend from the radial position. The pulses with the slowest rise time are the one generated near the contacts (thus near the core and the $A5$ segment contact), while the pulses generated around the center of the segment have the fastest rise time. In the first case the electrons (holes) are immediately absorbed by the core (hit segment) contact and the complementary charges have to drift along the whole segment length giving rise to slow pulses. In the second case, the drift path of both types of charges is similar and they are collected at (almost) the same time leading to the minimum rise time. The behavior of the transient signals, instead, is defined by the weighting potentials. When the signal is generated near the core (hit segment) contact, the electrons (holes) are immediately collected and the holes (electrons) drift towards the opposite contact in an increasing (decreasing) weighting potential. The transient signal generation is then driven exclusively by the positive (negative) charges and reaches a positive (negative) maximum. In the center, instead, the negative and positive contribution of holes and electrons are counterbalanced and the transient signal has small amplitude and can be bipolar.

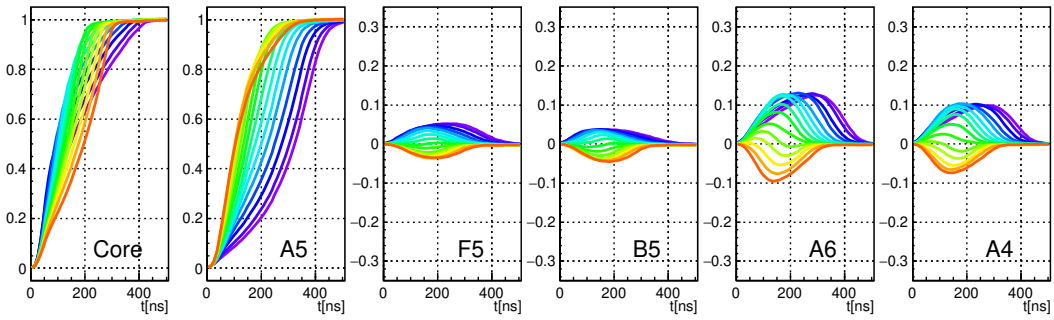

Figure 7.27: Pulses along a radius of the detector in the middle of segment $A5$.

In figure 7.28, the pulses are relative to a circumference with a fixed radius $R = 32\,mm$ and $Z_C = 60\,mm$ in segment $A5$ (see figure 7.26b). As both Z_C and R don't vary, the core and hit segment signals are not expected to change. The observed slight variation is due, in fact, to the anisotropy of the crystal between the $< 110 >$ and $< 100 >$ axes. As seen in section 7.2.3, this leads the rise time of the pulses to change as a function of the azimuthal angle. As for the transient pulses, their amplitude for the lateral segments ($B5/F5$) is bigger when the interaction is closer to the relative segment, as the weighting potential is more intense. Finally, the variation of the up/down transient pulses ($A4/A6$) is due to the anisotropy of the crystal along the $< 111 >$ direction.

Figure 7.29 shows pulses in segment $A5$ along the Z_C axis at the fixed position $X_C = 20\,mm$, $Y_C = 0\,mm$ (see figure 7.26c). Even if the radial and azimuthal positions of the points are fixed, the core and hit segment pulse shapes vary slightly. As seen in figure 7.25, the electric field presents an inclination at the bottom of slice 5 while is

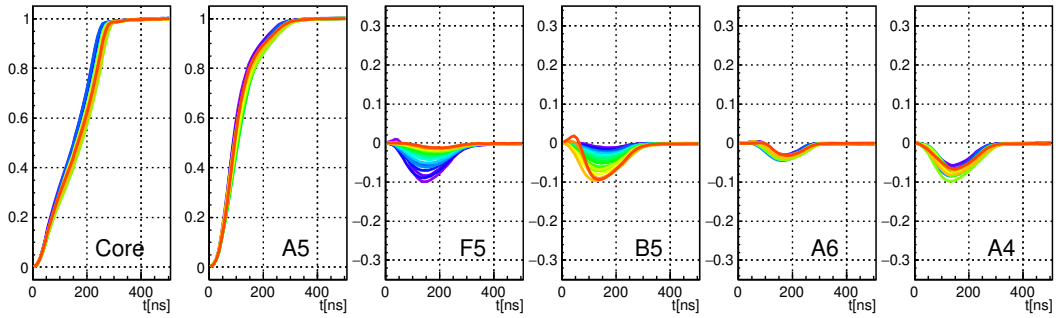

Figure 7.28: Pulses along a circumference of the detector with $R = 32\,mm$ in segment $A5$.

horizontal at its top. Consequently, the charge carrier velocities at the segment bottom are affected partially by the slower axis $< 111 >$ which is not the case for the segment top, leading to the slight changes observed. While the amplitude of the transient pulses of segments $F5/B5$ don't change, the amplitudes of pulses of segments $A6/A4$, as for the case in figure 7.28, increase or decrease depending on the distance of the interaction from the respective segment.

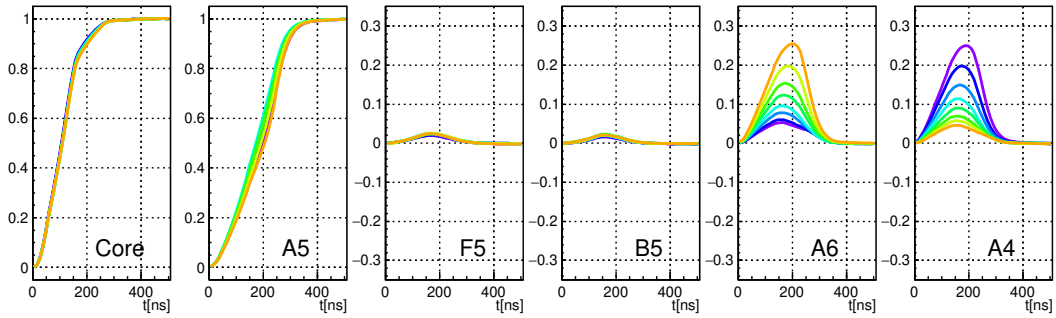

Figure 7.29: Pulses at the fixed position $X_C = 20\,mm$ and $Y_C = 0\,mm$ and along Z_C of the detector in segment $A5$.

Finally figure 7.30a shows the pulse shapes of the database points, in the segment $F3$, corresponding to the irregular trail seen in section 7.2.5 (see figure 7.26d). The pulses refers to a database slice at $Z_C = 30\,mm$. The pulse shape trend is very similar to the one shown in figure 7.27, as the points are basically aligned along the radial direction. Moreover the pulse shapes don't seem to show anomalies, meaning that the defective area affects only the amount of charges collected which doesn't have an impact on the shapes of the signals. For comparison, figure 7.30b shows the pulse shapes in segment $C3$, symmetrical to segment $F3$ relative to the bored hole, along a symmetrical path (see figure 7.26d).

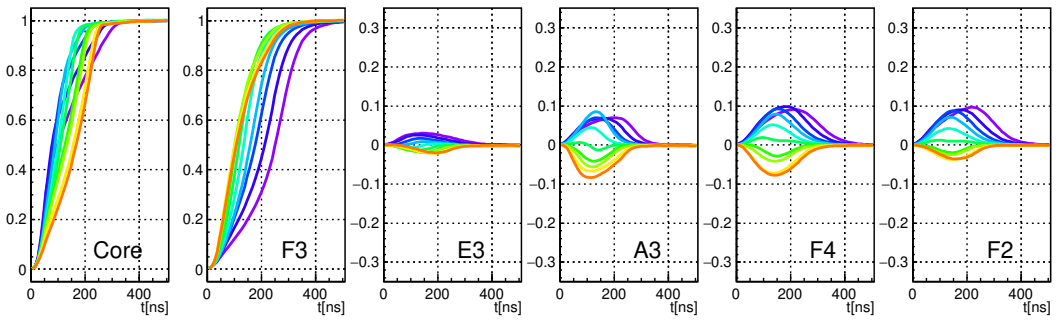

(a)

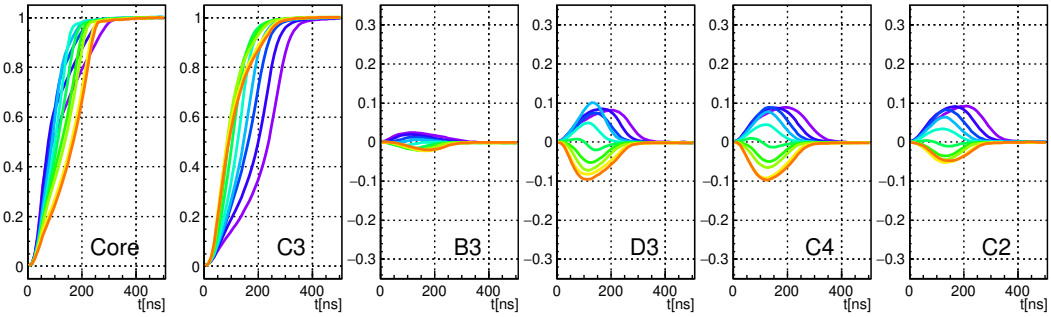

(b)

Figure 7.30: (a)Pulses along the irregular trail in segment $F3$ discussed in section 7.2.5. (b) Pulses along the symmetrical trail in segment $C3$ (see figure 7.26d). All the pulses are taken from the database slice at $Z_C = 30\,mm$.

7.3.3 Europium 3D scan

For the first time a three-dimensional scan was performed using an ^{152}Eu source. The aim of this measurement is to explore the new technique and to demonstrate that the pulse shapes are independent from the energy of the gamma ray interaction that generates them. This principle is asserted by the Shockley-Ramo theorem and it's at the base of the AGATA PSA algorithms implementation.

Unlike the ^{241}Am and ^{137}Cs source, the photopeaks of interest of the ^{152}Eu source are not isolated. In fact low energy photopeaks are build on top of a background produced by the Compton scattering of high energy gamma rays. In addition, an anomalous background bump is observed between 0 and $\sim 250\,keV$ (see figure 7.7) which is due to multi-scattered gamma rays on the wall of the collimator. Therefore an analysis of the peak to total ratio (P/T) is performed to estimate the purity of the datasets used for the χ^2 selection algorithm. The spectra generated by a vertical beam irradiating the detector in the center of sector B ($X_C = 10\,mm$ $Y_C = 20\,mm$) are build for each segment of the sector. The spectra, represented in figure 7.31 are built with 1-fold events only. Each of the photopeak of interest is fitted with a Gaussian function built on a first order

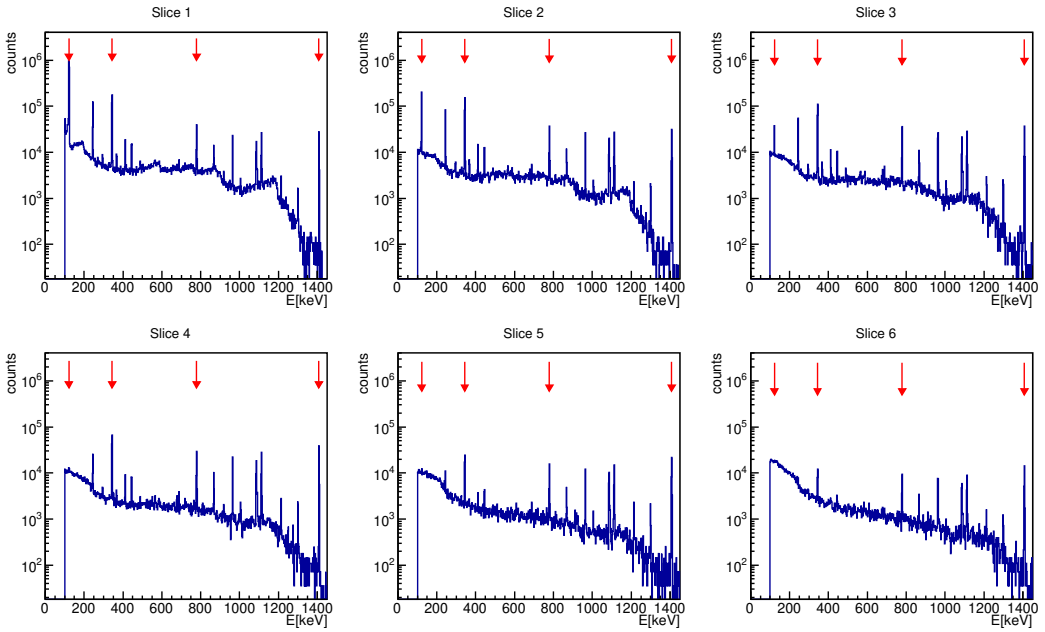

Figure 7.31: Spectra for each of the six segments of sector B of a beam irradiating the center of the sector ($X_C = 10\,mm$ $Y_C = 20\,mm$). The red arrows indicates the photopeaks of interest ($122\,keV$, $344\,keV$, $779\,keV$ and $1408\,keV$).

polynomial background. The peak is then integrated in a window of $\pm 3 \cdot \sigma\, keV$ (where σ is the standard deviation of the integrated peak) and the ratio between the Gaussian component and the full area is calculated. The results, in table 7.4 give the fraction of *good* events over the total number of selected events. The $1408\,keV$ photopeak doesn't have a meaningful background component since, being the highest energy photopeak of the source, it is isolated (contributions of the $1460\,keV$ of ^{40}K and some high energy cosmic background generate a very small background). The $779\,keV$ photopeak, on the other hand, lays on a $\sim 15\%$ background level. This is true for each slice of the sector and it's due to the relatively low branching ratio of the $779\,keV$ emission. In fact, the $344\,keV$ photopeak has a large peak component ($\sim 95\%$) due to the higher branching ratio and detection efficiency despite the fact that it lays on a background level which is two times larger. This is true for the first four segments of the sector, since, due to gamma-ray absorption, the value reach 87% and 67% levels in the fifth and sixth slices. Finally the $122\,keV$ photopeak has a large P/T ratio in the first two slices, but the value decreases rapidly to 66% in the third slice, due to gamma-ray absorption, and finally the peak disappears in slices 4, 5 and 6. Thus, for the $122\,keV$ energy it is meaningful to reliably build a database only for the first two slices.

With this premise, four databases for the four energies of interest were produced. As a first test the $779\,keV$ database is compared with the $662\,keV$ database, since they are close in energy. It is possible to make a first comparison of the two databases by looking at the distribution of parameters such as the T_{10}^{90} (defined in section 7.2.3) and

Slice (Seg)	$122\,keV$	$344\,keV$	$779\,keV$	$1408\,keV$
1(7)	$97.08 \pm 0.02\%$	$97.47 \pm 0.04\%$	$86.6 \pm 0.2\%$	$99.32 \pm 0.05\%$
2 (8)	$90.1 \pm 0.1\%$	$96.72 \pm 0.08\%$	$88.9 \pm 0.3\%$	$97.8 \pm 0.1\%$
3 (9)	$65.8 \pm 0.4\%$	$96.83 \pm 0.08\%$	$92.2 \pm 0.2\%$	$98.5 \pm 0.1\%$
4 (10)	0%	$93.4 \pm 0.1\%$	$91.4 \pm 0.3\%$	$99.02 \pm 0.8\%$
5 (11)	0%	$86.9 \pm 0.3\%$	$90.2 \pm 0.4\%$	$98.1 \pm 0.1\%$
6 (12)	0%	$66.6 \pm 0.7\%$	$82.3 \pm 0.7\%$	$96.3 \pm 0.3\%$

Table 7.4: Peak to total ratio (P/T) values of the photopeaks of interest for each of the six segments of sector B.

the Image Charge Anisotropy (ICA), the last one defined as [24]

$$ICA_{left/right} = \frac{I_{left} - I_{right}}{I_{left} + I_{right}} + 1 \tag{7.5}$$

$$ICA_{top/down} = \frac{I_{top} - I_{down}}{I_{top} + I_{down}} + 1 \tag{7.6}$$

where I_{left}, I_{right} , I_{top} and I_{down} are the integrals of the transient signal of the neighboring segments. The $+1$ is an offset to make the ICA value range in $[0, 2]$. The ICA parameters give an indication on the location of the interaction relative to the neighboring segments. Of course the $ICA_{top/down}$ signal has no meaning for the first and last slices of the detector. In these cases, the $ICA_{top/down}$ is considered as the integral of the available transient signal multiplied by a normalization factor. The distributions of the T_{10}^{90}, $ICA_{left/right}$ and $ICA_{top/down}$ values in six database slices, one for each segment of sector B, for both databases are shown in figures 7.32, 7.33 and 7.34. The distributions are very similar, hinting that the two scans are comparable.

Indeed, if two pulses with the same coordinates are compared, as in figure 7.35, it can be seen that they are almost identical. The comparison can be extended to all the points of the two databases and, as done in sections 6.1.3 and 6.2.1, the residuals of two pulse shapes, taken at the same point of the two databases, is calculated and the maximum residual value is used as comparison index (see the green signal in figure 7.35). The distribution of the residuals for some slices are shown in figure 7.36. They are quite homogeneous in each slice despite some points having high values (dark red) which appear to be concentrated near the core contact and the segmentation lines.

The average value for each slice can be calculated and the results plotted as a function of Z_C as in figure 7.37a. The graph shows that the average maximum residual per database slice has a value of 2% to 3% toward the front of the detector that increases slightly towards the back of the crystal where it reaches values up to 6% at the very back. Moreover, in correspondence of the segment separation surfaces ($Z_C = 14\,mm$, $22\,mm$, $36\,mm$, $56\,mm$, $74\,mm$) a slight value increase is observed. The same analysis can be redone by just taking into account the transient pulses. The graph, in figure 7.37b, shows that the average maximum residual between transient pulses is lower with respect to the main signals, ranging in the interval $1\% \div 3\%$. It has to be said, however,

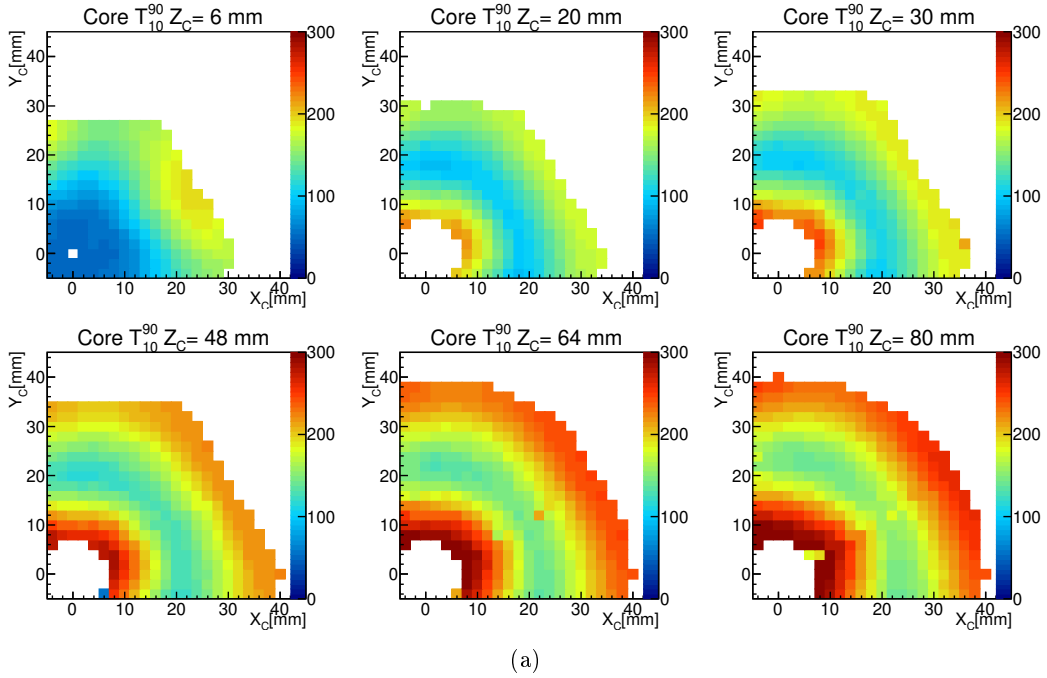

(a)

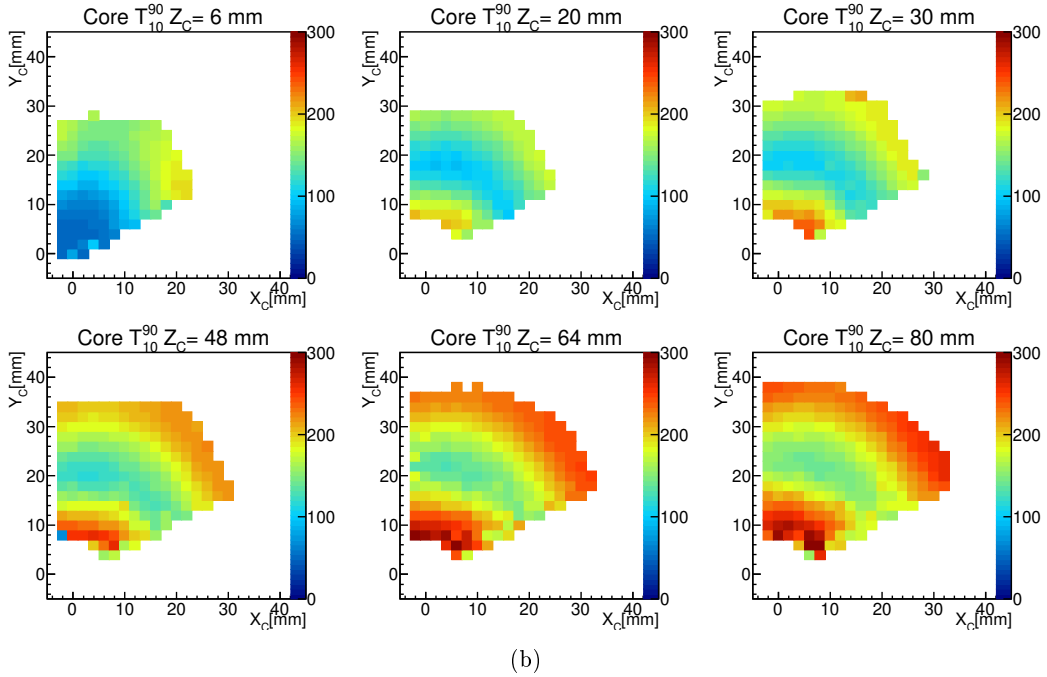

(b)

Figure 7.32: Distributions of the T_{10}^{90} in 6 slices of the $662\,keV$ database (the histograms include part of sector A and sector B) (a) and the $779\,keV$ database (sector B) (b). The slices considered are at $Z_C = 6\,mm$, $20\,mm$, $30\,mm$, $48\,mm$, $64\,mm$ and $80\,mm$.

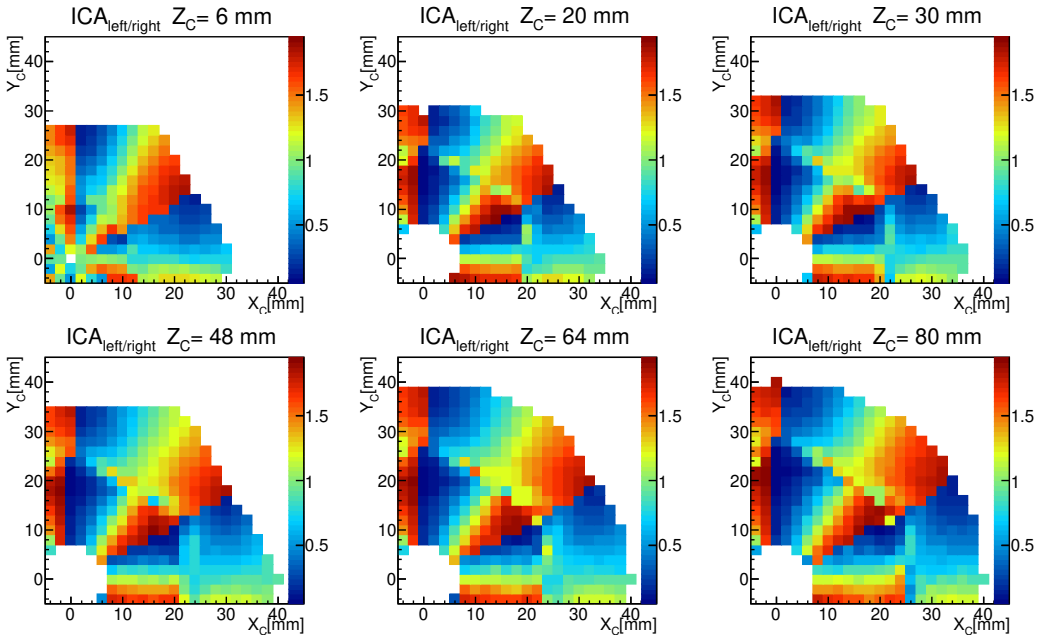

(a)

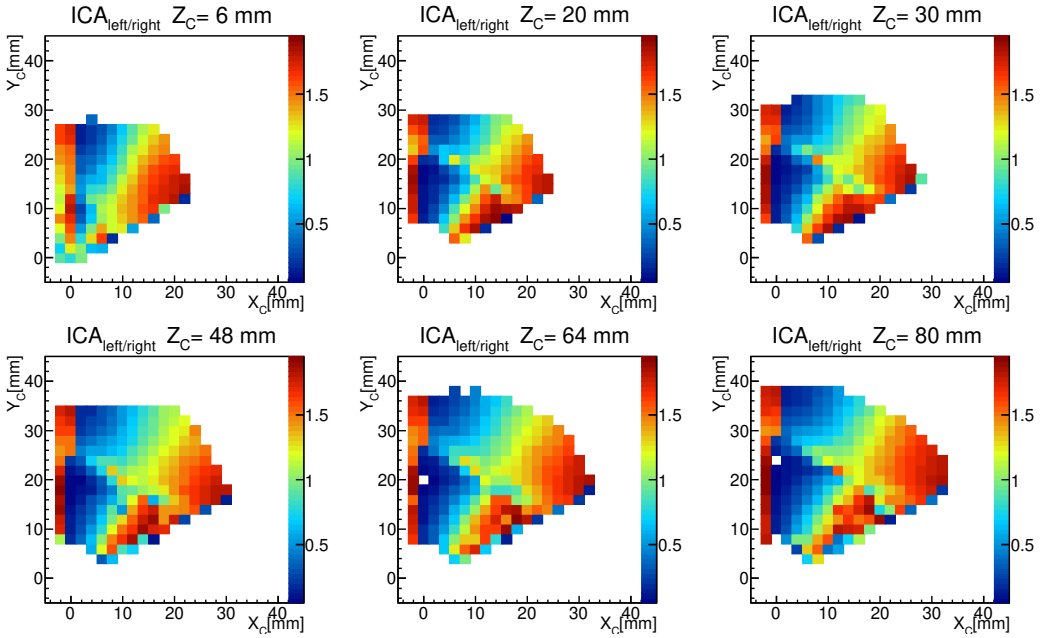

(b)

Figure 7.33: Distribution of the $ICA_{left/right}$ in 6 slices of the $662\,keV$ database (the histograms include part of sector A and sector B) (a) and the $779\,keV$ database (sector B) (b). The slices considered are at $Z_C = 6\,mm$, $20\,mm$, $30\,mm$, $48\,mm$, $64\,mm$ and $80\,mm$.

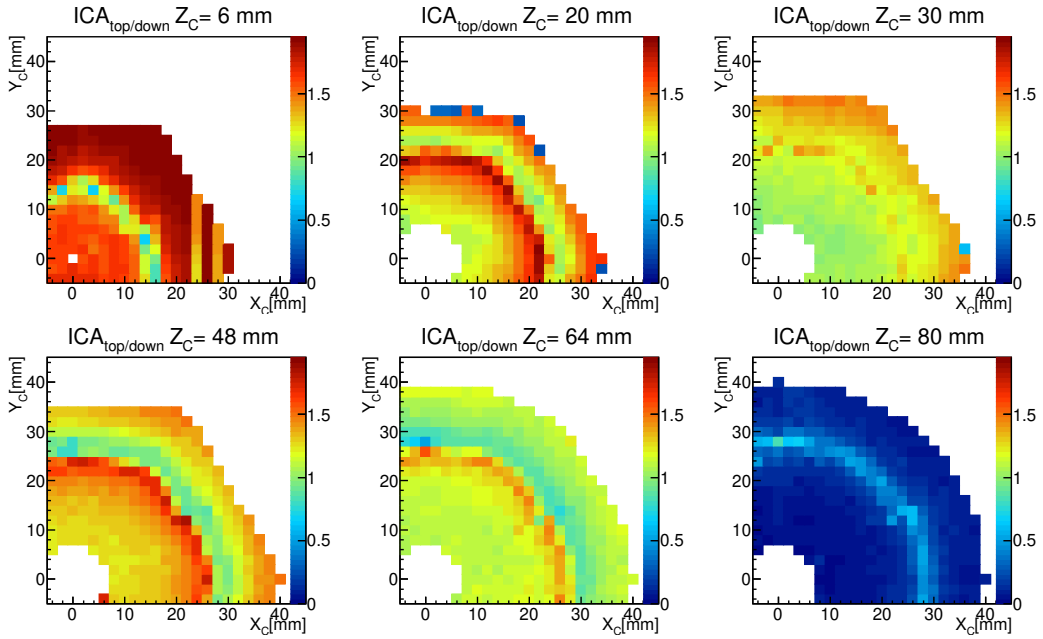

(a)

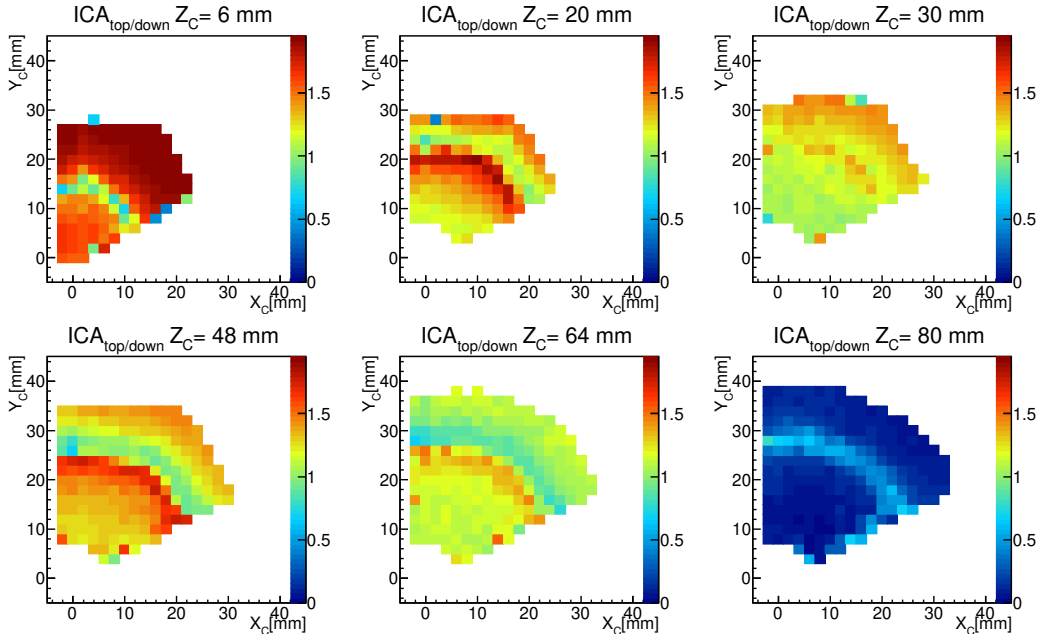

(b)

Figure 7.34: Distribution of the $ICA_{top/down}$ in 6 slices of the $662\,keV$ database (the histograms include part of sector A and sector B) (a) and the $779\,keV$ database (sector B) (b). The slices considered are at $Z_C = 6\,mm$, $20\,mm$, $30\,mm$, $48\,mm$, $64\,mm$ and $80\,mm$.

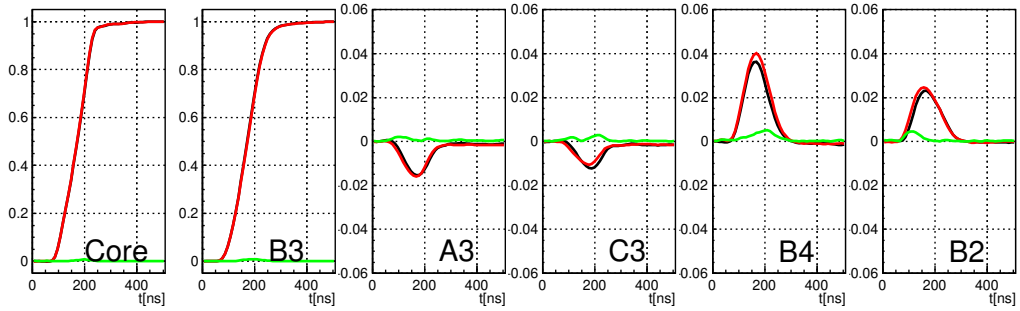

Figure 7.35: Comparison of two pulse shapes taken at the same point ($X_C = 10\,mm$, $Y_C = 20\,mm$, $Z_C = 30\,mm$) of the $662\,keV$ database (black line) and $779\,keV$ database (red line). The green line shows the residual value between the two pulses.

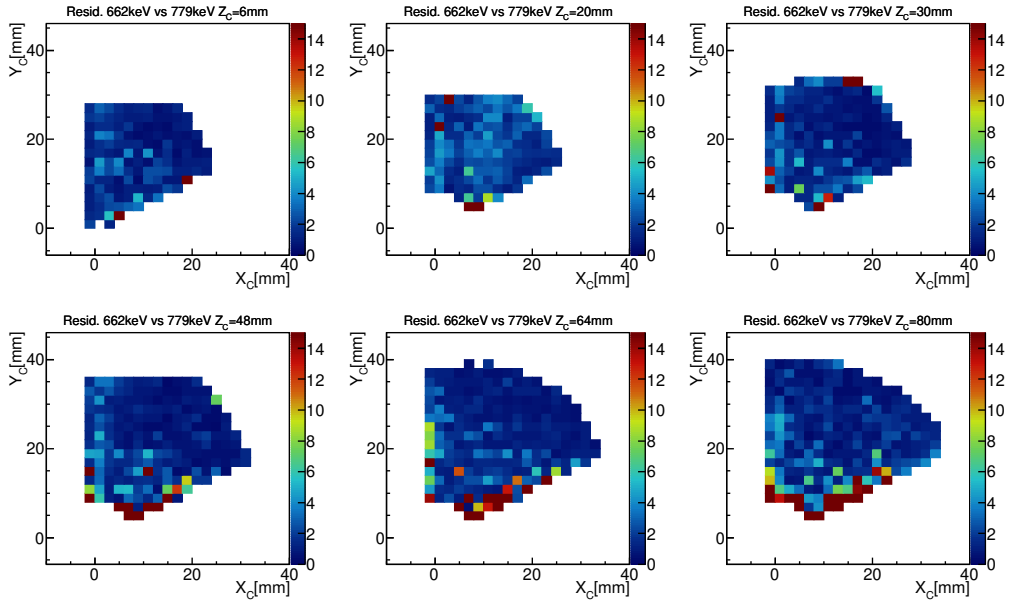

Figure 7.36: Distributions of the maximum residuals between the pulses of the $662\,keV$ and $779\,keV$ databases. The data are relative to the database slices at Z_C =6 mm, 20 mm, 30 mm, 48 mm, 64 mm and 80 mm. The color scale indicates the percentages of the residual amplitude relative to the full energies normalized to 1.

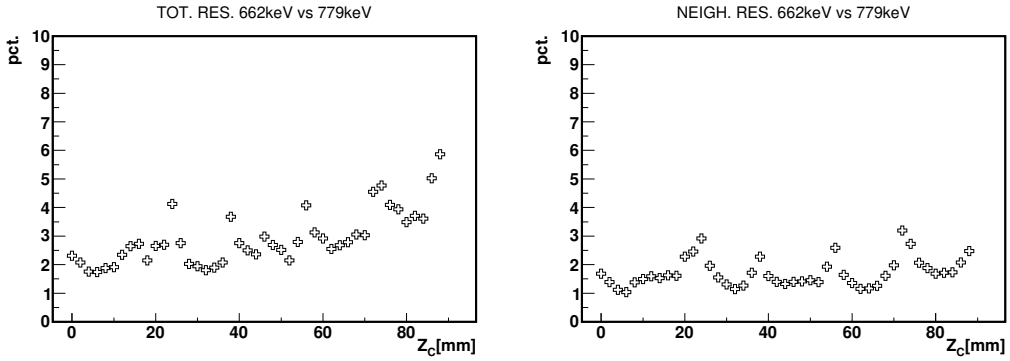

(a) (b)

Figure 7.37: Average maximum residual, as a function of Z_C, calculated comparing the $662\,keV$ and $779\,keV$ databases. In (a) the residuals are calculated with the whole supertrace while in (b) only the transient pulses are used.

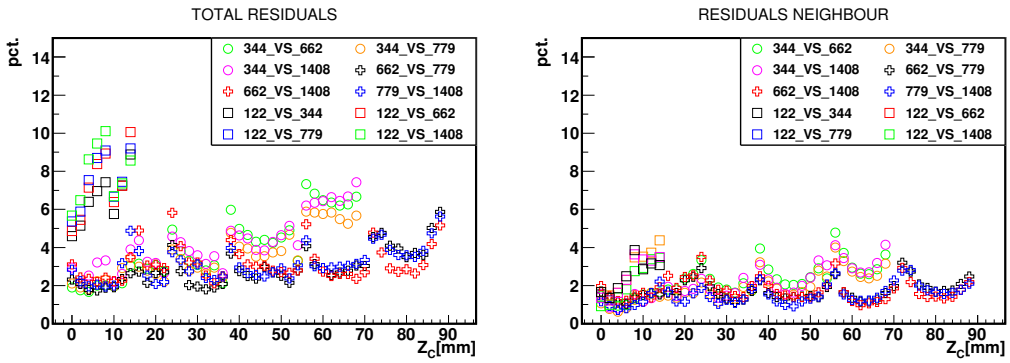

(a) (b)

Figure 7.38: Average maximum residual, as a function of Z_C, calculated comparing pair by pair the $122\,keV$, $344\,keV$, $662\,keV$, $779\,keV$ and $1408\,keV$ databases. For the data series relative to the $344\,keV$ database, data from the last slice of the detector was not taken into account as the P/T ratio drops to 67% (see figure 7.31 and table 7.4). For the same reasons, for the data series relative to the $122\,keV$ database only the data in the first two slices of the detector are considered. In (a) the residuals are calculated with the whole supertrace while in (b) only the transient pulses are used.

that these values are normalized to the maximum amplitude of the main pulses and since the amplitude of transient pulses is in relation smaller, it may mean that actually the difference between the transient pulses has a more relevant impact on the database comparison.

The above analysis can be repeated for the other databases. The databases are compared in pairs and the average maximum residuals as a function of Z_C is plotted in figure 7.38. The cross markers refer to the data series related to the comparison among high energies scans ($662\,keV$, $779\,keV$ and $1408\,keV$). They show a similar trend with comparable values. However, some discrepancies are found when comparing the high energies databases with the $344\,keV$ database (circular markers in figure 7.38). The data series relative to the $344\,keV$ database are self-consistent and follow the same trend of the high energy ones (cross markers) until $Z_C = 40\,mm$. From there on, the $344\,keV$ database and the high energy databases start to diverge. For $Z_C > 56\,mm$ the average maximum residuals reach values around 7%, which is more than a factor 2 larger than the ones for the high energy data series. Finally, the circular markers in figure 7.38 show the comparison between the $122\,keV$ and the other energies databases and as it can be seen, these data series don't follow any of the trends previously discussed. The total average maximum residuals have values of $\sim 5\%$ percent in the front slices of the database and then increase to $\sim 10\%$ toward slice 2 of the detector.

The causes of these discrepancies are most likely to be searched in the PSCS implementation or the χ^2 selection rather than in the physics of the system. However at the present state of the analysis no solid elements are found indicating where the PSCS, for low energies, lead to divergent databases. As a first hypothesis one can think that the discrepancies are due to the statistics. For example, for the series relative to the $344\,keV$ database, it can be noted that the most divergent points in slice 5 are concentrated around the core contact extending in the bulk of the detector (see figure 7.39), hinting that the discrepancies may be related to the gamma ray absorption that lowers the statistics of vertical datasets. However this hypothesis can be rejected by looking at table 7.5 where the area of the photopeaks of interest, with the background subtracted, is shown for each detector slice. In fact, for example, the number of $344\,keV$ events in the fifth slice detector is bigger than the ones of $779\,keV$ and $1408\,keV$. Another factor that can cause discrepancies is the noise level of the pulses used for the χ^2 selection. For example, the noise amplitude of the $122\,keV$ pulses is, in average, $\sim 5\,keV$ and $\sim 2\,keV$ for the core and segment contacts, respectively (see table 4.2 and figure 7.40). Such high distortion, especially on the core contact, can influence the χ^2 selection . High levels of noise can also lead the T^{10} time alignment to failure as the T^{10} value can be incorrectly found on the noise (as shown in figure 7.40) and the χ^2 selection would then be performed on events that are not properly aligned. Finally, such levels of noise can influence the selection on the transient signals which can be too noisy.

In conclusion, the analysis presented above gives elements that goes into the direction of the hypothesis that the pulse shapes are independent from the energy of the interaction. The databases calculated for energies $> 500\,keV$ match, in average, within 5% and the $344\,keV$ database follows the same trend until $Z_C = 40\,mm$. Nevertheless, further tests should be lead to improve the χ^2 selection algorithm when operating at low

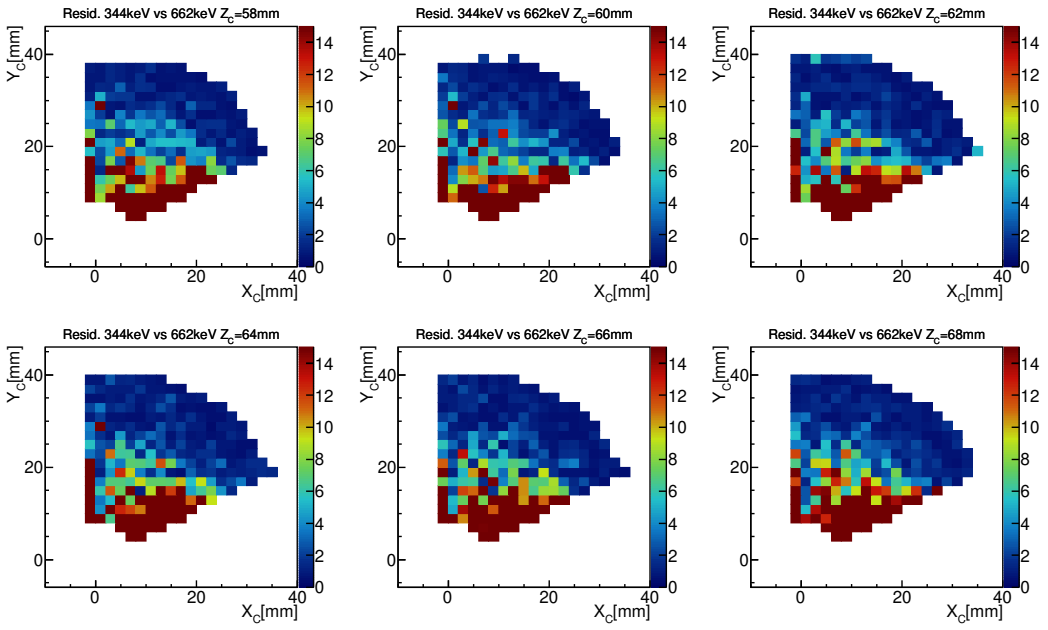

Figure 7.39: Distributions of the maximum residuals between the pulses of the $344\,keV$ and $662\,keV$ databases. The data are relative to the database slices at $Z_C = 58\,mm$, $60\,mm$, $62\,mm$, $64\,mm$, $66\,mm$ and $68\,mm$.

Slice (Seg)	$122\,keV$	$344\,keV$	$779\,keV$	$1408\,keV$
1(7)	735456	159074	26412	23445
2 (8)	55235	48437	9374	10119
3 (9)	12866	50699	13843	15915
4 (10)	0	31307	11728	15618
5 (11)	0	11524	5324	8808
6 (12)	0	4826	2864	5614

Table 7.5: Area of the photopeaks of interest, background subtracted, for each of the six segments of sector B.

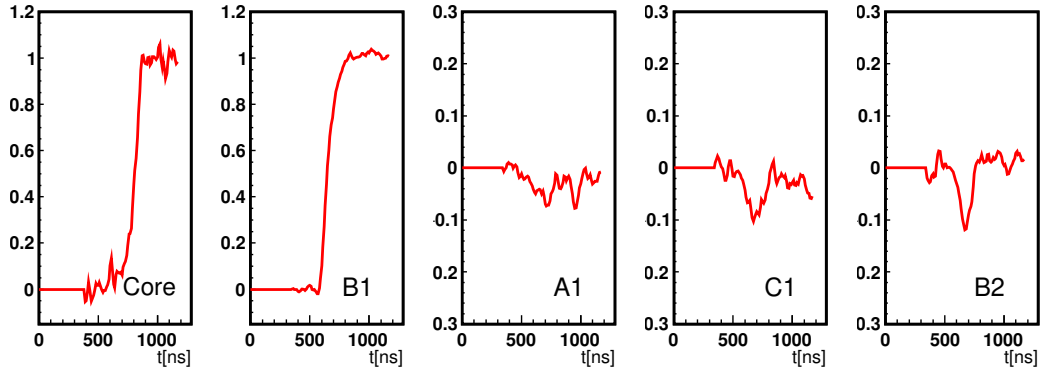

(a)

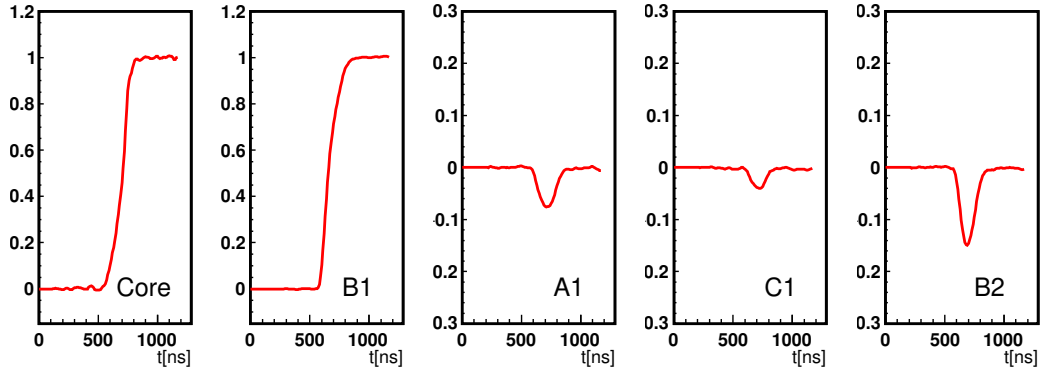

(b)

Figure 7.40: Examples of pulses used for the χ^2 selection interacting in segment $B1$. The pulse shown in (a) and (b) are relative to the 122 keV and 1408 keV datasets respectively. The noise in the 122 keV signal is non-negligible, while it has no influence on the 1408 keV signal.

energies. Some propositions, that were already made at the end of chapter 6, include using different weights for the main and transient pulses, or use non-euclidean metrics for the calculation of the χ factor. For the low energy pulse shapes, noise could be attenuated using filtering or techniques like the Fourier transform noise canceling (although this could affect the shape of the signals). Moreover, different scanning configuration could be tested, for example performing a horizontal-horizontal scan which would enable large statistics for large Z_C, keeping reasonable statistics close to the bored hole and which would enable checking the impact on the database of low energy gamma rays.

Conclusions and perspectives

A study of the PSCS technique implemented at IPHC to scan germanium detectors in 2D and 3D was performed and the results were discussed in this thesis. The aim of this work is to characterize the accuracy and the critical points of the scanning procedure in order to estimate whether the PSCS technique is able to provide full crystal volume, experimental, pulse-shape databases. The work has been carried out through the use of simulations and real measurements.

The results of the simulations of the Strasbourg scanning system were presented first. A simulation of a full volume scan of a planar 3×3 pixelated detector was performed with a gamma-ray beam energy of $662\,keV$ (^{137}Cs source). The simulation was realized with Geant4 and ADL softwares, using SIMION to calculate the electric fields and weighting potentials of the detector. The first parameter extracted from the analysis was the percentage of the selected pulses generated by a single interaction on the total number of events. The values obtained indicate a percentage of single interactions of about 21% on average, which is lower than expected. To improve the selection of single interaction events, the use of a second algorithm (IPP search algorithm) to filter the data was tested. This technique did not prove its effectiveness to select a larger percentage of single interaction events because the useful information is overwhelmed by the signal noise. Since it was not possible to reject multiple interaction events, their influence on the average pulse shape at each point of the scan grid was inquired. The analysis showed that the many interaction points of multiple interactions are placed relatively close to each other and that the average value of their distance from the point of the scan grid considered is around $6.2\,mm$. Moreover it was observed that the multiple interaction pulses selected by the PSCS technique are similar to those of single interactions. For this reason it was concluded that the multiple interaction pulses selected by the PSCS technique do not contaminate the database. Finally, the database obtained by the PSCS technique was compared with the theoretical one calculated with ADL. For the comparison, the maximum amplitude difference calculated sample-by-sample among two geometrically corresponding supertraces (ensemble of all signals, core and segments, represented in one compact signal) was taken as a quality parameter. The analysis showed that the two databases are mostly in agreement, with an average maximum residual value of 3% of the full energy in the bulk of the segments. Exceptions were found along the segmentation surfaces where edge effects, caused by limitations of the PSCS technique, increase the value up to 16%.

The same analysis was repeated with an AGATA S-type detector which was virtually

scanned with a beam energy of $662\,keV$ (^{137}Cs source). In general, the values of the parameters obtained in the analysis indicated that the PSCS technique performs better on the S-type detector than on the 3×3 segmented planar detector. The cause of this has been attributed to the much more complex segmentation geometry of the detector, which consequently provides better spatial resolution. In particular it was observed that the single interaction selection reach values that range, in average between the 55% at the front of the detector and 45% at its back. The average distance of the interactions from the scanning point was found to be around $2\,mm$. Finally the comparison between the PSCS calculated database and the ADL one showed an average maximum difference of $5\% \div 10\%$ at the very front of the detector (in the first segment slice) and then decreases rapidly to $\sim 2\%$ towards the back. Additional simulations of the S-type detector extended the analysis of the efficiency of the PSCS technique. In particular, the impact on the final results of the gamma-ray energy and the number of events used for χ^2 selection was examined at $122keV$, $344keV$, $779keV$ and $1408keV$ (^{152}Eu source energies). The analysis showed that the energy of the gamma-ray beam impacted only the percentage of selected single interaction events, enhancing this value for low energies gamma rays. The rest of the parameters were found comparable within each other and with the results obtained for the $662\,keV$ scan. The impact of the input statistics was also analyzed using different numbers of input events to be compared with the χ^2 selection algorithm for both the vertical and the horizontal datasets. The input statistics proved to have a greater impact with respect to the beam energy, as it was shown that the PSCS technique perform better with higher input statistics. However, the final comparison between the PSCS calculated database and the ADL one didn't seem to depend on this parameter.

Subsequently, the results of real measurements of a S-type detector were presented. The aim of this analysis was to test the PSCS technique performed with a ^{152}Eu source and prove, comparing different energy databases, that the pulse shapes don't depend from the interaction that generates them.

A first characterization of the detector was performed through 2D scans with the ^{241}Am, ^{137}Cs and ^{152}Eu sources. Some parameters were retrieved and discussed such as the local efficiency distribution, the crystal axis orientation, the centroid and FWHM distributions. The local efficiency distribution exhibits the expected behavior. The crystal orientation was determined, the $< 100 >$ axis being at $\theta_4 = -16.7^\circ \pm 0.4^\circ$. The centroid and FWHM distributions measured with the core contact show the known electron trapping which occurs in n-type detectors. Surprisingly, the same distributions obtained from the segment contacts present a similar trend which was not expected. This may be caused by the rather short integration time of the TNT2 digital amplifier settings ($5.95\,\mu s$) used in the scans. In addition, the centroid and FWHM distributions prompted a deeper analysis on the charge collection properties of the detector. In particular a defective zone expanding in segments $F2$, $F3$ and $F4$ was found in the detector. The energy spectra exhibit large tails towards low energy which is not expected in the several macroscopic trapping models. The charge collection properties of this zone were further analyzed and an hypothesis on the nature of the phenomenon was speculated. This unusual peak shape has been interpreted as the consequence of the presence of a second

type of electron trap, with large trap concentration, located in a thin plane of less than $1.5\,mm$ thickness. It extends from the bored-hole to a radius value of about $20\,mm$. This analysis shows the sensitivity of the scanning technique used and the interest of full crystal volume, 3D scans. Finally, the 2D scans allowed to measure some structural characteristics of the detector, such as the width of the segmentation lines at the front of the detector, the diameter of the central bored hole, the position of the contacts and the cabling of the detector (still difficult to evidence). These measurements showed the imaging capabilities of the IPHC scanning table.

Subsequently, three-dimensional scans were performed with the ^{137}Cs and ^{152}Eu sources. Due to the low activity of the source, the europium scan was restricted to one sector of the detector (sector B). The europium scan allowed to construct four different databases of pulses, with different energies, in a single measurement. The databases were built for the energies $122keV$, $344keV$, $779keV$, $1408keV$ (europium) and $662\,keV$ (cesium). A comparison was made within each other, and the maximum residual value between two signals associated to the same point of the database was chosen as comparison parameter. The databases with energy $> 500keV$ proved to be comparable within each other, with differences varying along the crystal length (front to back) from around 2% to about 3% and up to 6% at the very back, in average. Some discrepancies were instead found with the $344\,keV$ database for Z_C values larger than $40\,mm$. The residual values appeared to diverge by a factor 2 towards the back of the detector. Finally the $122\,keV$ database proved to be strongly divergent from the other databases. It was supposed that the reasons behind these divergent behaviors are to be attributed to the PSCS technique that somehow is not efficient at low energies, since the small amplitude of induced signals is strongly affected by the signal noise.

The analysis, above summarized, opens for new perspectives and research opportunities, both for simulations and measurements. The PSCS limitations shown in the analysis can be overcome by proposing improvements for the PSA. Taking inspiration from the work presented in [64], different metrics may be taken into account for the pulse selection algorithm. The χ-like formula (4.1) would then became χ^α where α is a value that can be optimized in order to maximize the fraction of selected single interactions and minimize the average distance of the interaction points from the respective database position. Another way to improve the χ^2 selection could be the use of weights for the transient signals to give them more or less impact on the database construction. This option was preliminarily tested in [24] and a more systematic study with extensive simulations could be done. Moreover the use of noise filtering techniques, such as the Fourier transform noise canceling, could be evaluated, especially for low energy pulses where the PSCS appears to be more affected. If these techniques lead to improvements on the PSCS technique, then they can be applied to real measurements to verify if the discrepancies found between the different energy databases are reduced. In order to enable measurements with low energies in a full sector volume using the ^{152}Eu source, a horizontal-horizontal configuration could be tested. It would reduce statistics issues for low energy gamma-ray beams towards the back of the detector. Finally, it would be interesting to compare the databases obtained by the IPHC scanning table with the

ones from other scanning tables exploited by the AGATA collaboration by using the same capsule mounted in a given test cryostat moved from one place to the others. The measurements performed with the ^{152}Eu source have evidenced the need to buy sources of smaller diameter ($1\,mm$ or less to be compared to $3\,mm$ for the actual ones) more compatible with the diameter of the new collimators. Keeping the same source activities would speed up the scans by a factor around 10 making europium measurements as fast as the present cesium scans.

Using these more efficient gamma-ray sources, other tests could be performed making use of the new configuration of the scanning table. In particular, the ^{152}Eu source combined with the fine collimation of gamma rays ($0.5\,mm$ and $0.2\,mm$) could be used to determine the possible impact of the charge cloud, produced by an interacting gamma ray, on the shape of the pulses. In addition, it would be possible to extract from specific measurements across a segmentation line, the size of the charge cloud which is supposed to vary with the gamma-ray energy release. This study may be performed in conjunction with dedicated COMSOL [74] calculations. Also, finer collimators could be used to perform a deep analysis on the charge carriers behavior in a large HPGe detector (as the S001 anomalous zone for further exploration).

To be complete, the IPHC scanning table could certainly be used to carry out $R\&D$ work on position-sensitive detectors. For example, the impact of more exotic geometries and segmentations on the spatial sensitivity of the detector (such as the point-like, well detector [75]), surface and crystal volume effects of new surface treatments (impact of new passivation treatments, Sb n+ contact, crystal coating as presently developed in LNL, Italy), spatial identification or even characterization of degraded charge collection areas in a defective crystal could be performed with high resolution and precision and in short times.

Appendix A

S001 Costumer Acceptance Test

When a new AGATA detector unit is delivered from the manufacturer facility, it undergoes a series of tests before getting accepted by the collaboration. In these tests, called *costumer acceptance test* (CAT), specific parameters are measured for each detector segment, such as the resolution, the current offset in function of the applied voltage and, for the full crystal, its efficiency and the FWHM/FWTM ratio. These parameters generally show if a detector presents problems or defects and in the case any is found the detector is sent back to the manufacturer for repairing. CATs are performed in few specific laboratories of the AGATA collaboration, the IPHC of Strasbourg being one of them. In addition, before a detector gets scanned with the Strasbourg scanning table, a CAT-like test is generally performed in order to verify that the detector doesn't present anomalies, or got damaged during transportation.

Tables A.1 and A.2 report the FWHM values of each segment, at low and high energies respectively, measured before the scan of the S001 detector. The tests are performed by irradiating the detector with free ^{241}Am and ^{60}Co sources. The values show that the FWHM values of segments $F2$, $F3$ and $F4$ are in line with the ones of the other segments despite the fact that, as described in section 7.2.5, anomalous values are found locally through 2D scans.

	A	B	C	D	E	F	Core
1	1.03	0.98	1.04	1.05	1.10	1.01	1.24
2	0.98	0.96	0.96	0.98	1.08	0.98	
3	1.00	0.94	1.03	1.00	1.06	1.11	
4	1.05	0.97	1.05	1.13	1.18	1.12	
5	1.02	1.03	1.05	1.10	1.15	1.11	
6	0.98	0.95	1.07	1.06	1.09	1.02	

Table A.1: Segments FWHM values at $60\,keV$ measured by irradiating the detector with a free ^{241}Am source. Units in keV. Courtesy of Marie-Hélène Sigward.

	A	B	C	D	E	F	Core
1	2.06	2.00	2.07	2.14	2.27	2.12	2.40
2	1.89	1.91	1.93	1.95	2.04	1.99	
3	2.03	1.91	2.00	1.97	2.02	2.12	
4	2.11	2.00	2.03	2.19	2.12	2.25	
5	2.11	2.05	2.14	2.16	2.12	2.04	
6	2.14	2.14	2.08	2.16	2.23	2.11	

Table A.2: Segments FWHM values at $1332\,keV$ measured by irradiating the detector with a free ^{60}Co source. Units in keV. Courtesy of Marie-Hélène Sigward.

Appendix B

Résumé en français

L'étude de la structure des noyaux loin de la vallée de stabilité par spectroscopie gamma joue un rôle très important dans la physique nucléaire moderne. Ces noyaux sont caractérisées par un rapport entre protons et neutrons qui est loin de l'unité et présentent, de ce fait, des structures particulières (eg. noyaux halo, peau de neutrons, structure en amas ou cluster, îlots d'inversion et modification des nombres magiques). De par leurs propriétés, ces noyaux sont appelés noyaux exotiques et l'étude de leur structure peut fournir des données essentielles pour améliorer les modèles de physique nucléaire existants. Il est possible de créer de tels noyaux auprès d'accélérateurs de faisceaux d'ions radioactif (Radioactive Ion Beams, RIBs) comme SPIRAL1 au GANIL, France et ISOLDE au CERN, Suisse. Des accélérateurs de nouvelle génération sont actuellement en phase de construction, comme FAIR au GSI, Allemagne SPIRAL2 au GANIL, France et SPES au LNL, Italie. Les taux de production des noyaux exotiques sont très faibles et les expériences pour l'étude de ces noyaux ont besoin de spectromètres gamma de grande efficacité et d'excellente résolution en énergie. Le multi-détecteur AGATA (Advanced GAmma Tracking Array) est un projet Européen qui implique plus de 40 instituts de 11 Pays. Le but de la collaboration est le design, la construction et le développement d'un ensemble de détecteurs HPGe (high purity germanium) de nouvelle génération avec des caractéristiques suffisantes pour l'étude des noyaux. De nombreuses campagnes expérimentales ont déjà exploité AGATA au LNL, à GSI et au GANIL. AGATA est un instrument mobile qui est installé auprès des principaux laboratoires Européens pour profiter des différents faisceaux, détecteurs ancillaires et équipements qui y sont disponibles.

Ce qui fait d'AGATA un appareillage de nouvelle génération est la nouvelle approche adoptée dans la reconstruction des événements détectés. L'ancienne génération de multi-détecteurs HPGe comme EUROBALL et GAMMASPHERE est équipée d'enceintes anti-Compton qui améliorent le rapport pic-sur-total dans les spectres gamma. Les boucliers anti-Compton sont composés de détecteurs scintillateurs BGO qui ont une faible résolution en énergie mais une grande efficacité de détection intrinsèque. Un événement est rejeté si un rayon gamma interagit par effet Compton dans un détecteur de germanium puis le quitte et interagit avec un ou plusieurs cristaux BGO environnant. Cette tech-

nique, bien qu'efficace, a deux désavantages. Le premier est que les cristaux de BGO occupent de la place et réduisent, de fait, l'angle solide occupé par les détecteurs de germanium donc leur efficacité géométrique. Le deuxième désavantage est dû à la perte intrinsèque d'efficacité quand des événements sont supprimés. Cette perte d'information peut être évitée si les rayons gamma qui s'échappent du cristal de germanium sont détectés dans un autre détecteur.

Le spectromètre AGATA complet se compose de 180 détecteurs HPGe, de grand volume, disposés dans une configuration compacte sphérique 4π qui couvre 82% de l'angle solide. Si un rayon gamma s'échappe d'un cristal, il a une grande probabilité d'être détecté dans un cristal voisin. Pour s'assurer que ces interactions dans deux cristaux voisins ne sont pas dues à deux rayonnements gamma différents, il faut reconstruire le parcours du rayon gamma dans le germanium. Comme cela sera expliqué en détail ci-dessous, le détecteur AGATA peut déterminer la position de chaque interaction d'un rayon gamma qui le parcours et déterminer si le rayonnement a été totalement absorbé ou s'il s'est échappé du spectromètre. Cette propriété de reconstruire le parcours des rayons gamma, appelée "tracking", rend superflus les boucliers anti-Compton et permet un gain d'efficacité géométrique et intrinsèque par rapport à l'ancienne génération de détecteurs. En outre, la direction de chaque rayon gamma émis par le noyaux peut être déterminée avec grande précision ce qui permet d'effectuer une excellente correction Doppler et la détermination de la position du deuxième point d'interaction permet de mesurer la polarisation linéaire du gamma.

Actuellement AGATA est en phase de construction et est composé de 41 détecteurs. Les détecteurs sont des cristaux de HPGe avec des impuretés de type n. La géométrie des détecteurs est coaxiale ($90\,mm$ de hauteur, $80\,mm$ de diamètre extérieur et $10\,mm$ de diamètre intérieur) avec la face frontale biseautée de forme hexagonale irrégulière. La surface externe est segmentée par des contacts en 6 secteurs et 6 tranches pour un total de 36 segments. L'énergie totale déposée dans le cristal est obtenue par le contact "core" qui est situé dans le trou central du détecteur.

Chacun des 37 contacts produit une impulsion quand un rayon gamma interagit dans le détecteur. Le photon ionise le cristal semi-conducteur et génère des charges négatives (électrons) et positives (trous). Sous l'action d'un champ électrique les charges sont collectées par les contacts du détecteur, c'est-à-dire le contact "core" et le contact du segment dans lequel l'interaction a eu lieu. Le contact du segment touché formera le "signal principal". Un signal identique mais de signe opposé est formé sur le contact "core". Les contacts voisins du segment touché sont sensibles aux "charges images" qui génèrent des signaux de charge totale nulle. On les appelle signaux de transit. L'amplitude de ces signaux, inférieure à celle du signal principal, dépend de la position d'interaction du rayon gamma dans le segment touché. Plus l'interaction est proche du segment voisin, plus l'amplitude du signal de transit est grande. La totalité des signaux acquis des 36 segments et du “core” donne des informations sur la position à laquelle l'interaction a eu lieu dans le cristal de germanium.

Comme mentionné ci-dessus, la caractéristique principale d'AGATA est sa capacité à reconstituer le parcours des rayons gamma. L'élaboration des données acquises par AGATA a lieu en trois phases. Au début un algorithme d'analyse des formes d'impulsion

ou PSA (Pulse Shape Analysis) détermine la position de chaque interaction qui compose un événement (c'est-à-dire l'interaction simple ou multiple d'un rayon gamma avec un détecteur Ge). L'algorithme compare la forme d'impulsion expérimentale avec une base de données de formes d'impulsion pré-calculées associées à des coordonnées spécifiques dans le volume du détecteur. Une fois que les positions de toutes les interactions sont obtenues, un autre algorithme de "clustering" groupe les interactions qui sont liées avec la plus grande probabilité au même rayon gamma. Le dernier pas est fait par un algorithme de tracking qui reconstruit la chronologie des interactions de chaque rayon gamma et, si ce rayon gamma est reconnu comme absorbé par le détecteur, l'événement associé est accepté et stocké dans le pool de données, sinon il est rejeté.

Il est clair que le PSA joue un rôle clé pour obtenir de bons résultats avec le tracking. AGATA utilise pour le PSA des algorithmes de "grid search" qui fonctionnent avec des bases de données calculées par ADL. ADL (AGATA Detector Library) est un software, développé à Cologne par la collaboration, qui calcule numériquement les formes d'impulsion générées par un détecteur une fois que les valeurs du champs électrique et des potentiels "de pondération" sont connus. Les performances de l'algorithme de tracking sont bonnes mais il présente des limitations quand les interactions ont lieu dans les parties avant et arrière du détecteur, où les formes d'impulsion sont fortement influencées par la géométrie locale (partie non-coaxiale du cristal) et par les facteurs de construction comme la surface passivée et la distribution des impuretés. Pour éviter ces problèmes, la collaboration se propose d'utiliser des bases de données de formes d'impulsion expérimentales, mesurées par une caractérisation volumétrique (3D) des détecteurs.

La caractérisation 3D des détecteurs est possible avec les "tables de scan". Cinq tables qui exploitent diverses techniques de scan sont utilisées par la collaboration AGATA. Toutefois le principe fondamental de chaque table est toujours le même. Le détecteur est fixé à la structure de la table et est irradié par une source de rayons gamma. Par des algorithmes, il est possible d'associer les formes d'impulsion enregistrées avec la position d'interaction correspondante. Les tables de scan utilisées actuellement par la collaboration sont localisées à Liverpool, Orsay, Darmstadt, Salamanca et Strasbourg.

Elles sont de deux types, les tables à coïncidences (Liverpool et Orsay) et les tables à mesures directes (Darmstadt, Salamanca et Strasbourg). Celles à coïncidences (Darmstadt et Salamanca) utilisent des détecteurs collimatés installés autour du détecteur à scanner pour déterminer les positions d'interaction des rayons gamma provenant d'un faisceau collimaté. Pour les tables à mesures directes, au contraire, une source de ^{22}Na (qui émet des rayons gamma dos à dos) est positionnée entre le détecteur à scanner et un détecteur sensible à la position qui permet de reconstruire la direction des rayons gamma émis. Le détecteur est irradié à deux positions différentes et les interactions peuvent être reconstituées en trouvant des intersections entre les deux ensembles de données de directions obtenus.

La table de scan de Strasbourg est conçue pour réaliser des scans complets avec une bonne résolution spatiale en peu de temps. Un scan 3D d'un cristal d'AGATA ($\sim$ 45000 points de scan) peut être réalisé dans un temps de l'ordre de 20 jours. La table exploite la technique PSCS (Pulse Shape Comparison Scanning) qui permet la construction d'une base de données de formes d'impulsion à partir de la comparaison

de deux ensembles de données obtenus par irradiation du détecteur avec une source collimatée de rayons gamma. Au début le détecteur est positionné verticalement sur la table et est irradié par la source collimatée qui est déplacée à intervalles réguliers sur un plan perpendiculaire à l'axe central du détecteur. Pour chaque position du collimateur tous les signaux générés par le détecteur de long du faisceau de rayons gamma sont enregistrés et un ensemble de donnée V est obtenu. Le détecteur est ensuite pivoté de 90° et mis en position horizontale. En répétant la même opération on obtient un ensemble de données H. Les points de scans V et H sont choisis pour que les axes des faisceaux gamma V et H se croisent (virtuellement) et définissent une "grille de scan" à trois dimensions (3D). Pour un détecteur sensible à la position, deux rayons gamma V et H qui interagissent à la même position, génèrent la même forme d'impulsion. La comparaison deux à deux des formes d'impulsion du jeu de données V avec celles du jeu de données H permet de sélectionner les formes d'impulsion V et H les plus similaires, de les moyenner et d'associer une forme d'impulsion moyenne à chaque coordonnées de la grille. La sélection deux à deux est effectuée par une formule de type χ^2. Plus cette valeur calculée est basse, plus les deux signaux sont similaires. Malheureusement, il n'existe pas une valeur absolue pour laquelle deux signaux peuvent être considérés identiques. Cette valeur dépend en fait des conditions expérimentales et il n'est possible d'effectuer qu'une comparaison relative des formes d'impulsion. Un autre désavantage de la technique PSCS est qu'elle ne peut pas distinguer entre des signaux générés par des événements d'interactions unique ou single et des événements d'interaction multiples. Les formes d'impulsion générées par des interactions multiples sélectionnées comme des événements d'interaction single peuvent avoir un impact négatif sur la base de données et la polluer. Des procédures ancillaires peuvent aider à améliorer la sélection, mais elles ne suffisent pas à éliminer le problème.

Une partie du travail de thèse consistait à réaliser des simulations Monte Carlo de la table de scan de Strasbourg pour extraire des valeurs de paramètres qui permettent de quantifier les performances de la technique PSCS et d'évaluer la solidité des bases de données mesurées ainsi produites.

La table de scan de Strasbourg est constituée comme suit. Un collimateur métallique est posé sur deux axes motorisés qui permettent un mouvement planaire sur un intervalle de $300\,mm$ dans chacune des deux directions. Au-dessus du collimateur, deux plateaux fixes permettent le placement du détecteur en position verticale et horizontale. Le détecteur est fixé dans un cadre de réglage (ou équerre) qui est centré sur les plateaux par des plots de centrage. Lorsque la source est retirée un système laser solidaire du collimateur envoie un faisceau dans le collimateur du point source vers le détecteur en suivant le parcours du faisceau gamma. Il permet d'aligner précisément le détecteur en position verticale et nous assure de la perpendicularité de la position horizontale. Enfin, il est possible de replacer précisément le détecteur en position verticale grâce au laser. Le collimateur est un bloc métallique cylindrique de $189\,mm$ de hauteur et de diamètre externe de $220\,mm$. Les métaux qui le constituent sont des absorbeurs de rayons gamma en tungstène, plomb et acier. Il est possible d'ouvrir le collimateur pour loger à sa base l'un des godets qui contiennent les sources. Des sources d'américium (^{241}Am, $E_\gamma = 60\,keV$), de césium (^{137}Cs, $E_\gamma = 662\,keV$) et d'europium (^{152}Eu, source de

nombreux gamma en cascade) sont à disposition pour les scans. Depuis la modification du collimateur, trois parties centrales du collimateur sont interchangeables. Elle sont constituées de cylindres de tungstène perforés de façon coaxiale par des trous de $1\,mm$, $0.5\,mm$ et $0.2\,mm$ de diamètre. L'emploi des trous de collimation dépend de l'objectif de la mesure. Le trou de $1\,mm$ permet de réaliser des scans 2D et 3D. Celui de $0.5\,mm$ permet des scans 2D pour une imagerie de précision. Celui de $0.2\,mm$ devrait servir à déterminer la taille du nuage de porteurs électrons et trous.

Le faisceau des rayons gamma qui sortent du collimateur a fait l'objet d'une étude préliminaire réalisée par simulations à l'aide de GEANT4 et par des mesures réelles. La géométrie et les matériaux du collimateur, mais aussi les dimensions et la position des sources sont reproduits fidèlement dans la simulation qui a permis d'obtenir les profils des faisceaux de rayons gamma pour les trois sources (^{241}Am, ^{137}Cs, ^{152}Eu) et d'estimer leur diamètre à différentes distances du trou de sortie. Ces résultats ont ensuite été comparés aux mesures réelles effectuées avec un capteur IPIX pixelisé (fourni par la société MIRION Technologies Canberra). Il s'agit d'un capteur CdTe de 256×256 pixels chacun ayant une taille de $55x55\mu m^2$ et de $1\,mm$ d'épaisseur. Les résultats expérimentaux trouvés sont en bon accord avec les résultats des simulations. Cette étude a permis de vérifier le bien-fondé de l'application GEANT4, qui a ensuite été utilisée pour réaliser d'autres simulations. L'étude a également permis d'obtenir des informations sur le diamètre de la tache du faisceau à n'importe quelle profondeur dans le détecteur.

Des informations sur le rendement du collimateur pour les différentes sources et leur taux d'émission ont également été extraites de la simulation. Enfin, le calcul du taux d'absorption des rayons gamma par les segments d'un détecteur de type AGATA a été mené. Les résultats de ces simulations et mesures préliminaires ont été utilisés pour concevoir les simulations complètes de la technique PSCS et les mesures réelles.

La simulation complète de la technique PSCS est réalisée à l'aide de GEANT4 et ADL. Le rôle de GEANT4 dans la simulation est de déterminer pour chaque absorption complète du rayon gamma dans un segment, les positions des point d'interaction et l'énergie déposée en chaque point. Une fois que les interactions sont simulées avec GEANT4, les signaux générés par le détecteur sont calculés grâce à ADL qui nécessite les éléments suivants: la description des champs électriques et des potentiels "de pondération" du détecteur, les paramètres de mobilité des électrons et des trous, l'orientation du cristal et la densité des impuretés. Les champs électriques et les potentiels "de pondération" peuvent être calculés par un solveur d'équation de Poisson. Dans ce travail de thèse, j'ai utilisé SIMION qui calcule les champs électriques et les potentiels à partir de la description de la géométrie du détecteur à simuler. Les autres paramètres ont été repris de la littérature. Enfin, chaque signal calculé avec ADL est convolué avec un bruit réaliste et la fonction de réponse des préamplificateurs. Le bruit réaliste a été mesuré pour les deux détecteurs étudiés dans cette thèse, un détecteur planaire et un cristal AGATA symétrique S001 (voir ci-dessous). La fonction de réponse a été mesurée pour le détecteur planaire et extraite d'AGAPRO pour S001 (voir ci-dessous).

Les données obtenues des simulations sont analysées avec un code spécialement écrit qui effectue la sélection par χ^2 pour la technique PSCS. Le fonctionnement du code

peut être résumé comme ci-dessous. Les ensemble de jeux de données V et H sont filtrés et nettoyés des signaux générés par les événements dans lesquels les rayons gamma ne sont pas absorbés par un seul segment du détecteur. Les différents fichiers des deux jeux de données sont ensuite comparés par couple en utilisant la sélection de type χ^2 à la fin de laquelle les 400 meilleurs signaux sont sélectionnés pour chaque point de la grille de scan. Ces signaux sont filtrés encore une fois (procédure de raffinement) et moyennés pour obtenir le signal au point (x,y,z) qui fera partie de la base de données. Pour chacun des signaux, les informations sur les positions des interactions qui les ont générées (positions et énergies déposées) sont enregistrées.

Les simulations de la technique PSCS ont été effectuées sur un détecteur HPGe planaire segmenté et une unité AGATA de type S. Le premier détecteur mentionné est modelé sur une copie réelle du détecteur propriété de l'IPHC. La simplicité de sa géométrie a été utile lors de la phase de conception des simulations et de l'analyse ultérieure des données. La même approche a ensuite été utilisée avec des simulations du détecteur de type S plus complexe.

Le détecteur planaire a une forme rectangulaire avec un volume actif de $51 \times 51 \times 19.9\,mm^3$. Le contact au bore est pixelisé en 3×3 générant neuf électrodes de $17 \times 17 mm^2$. Le contact opposé est diffusé au lithium et mesure l'énergie totale déposée dans le cristal. C'est le contact "core". Le scan complet de ce détecteur est simulé au pas de $2\,mm$ et pour une énergie des rayons gamma de $662\,keV$ (source de césium). Le premier paramètre extrait de l'analyse est la fraction des signaux sélectionnés générés par une interaction single sur le nombre total d'événements. Les valeurs obtenues indiquent une sélection d'interactions individuelles d'environ 21% en moyenne, une valeur bien inférieure à celle de 90% obtenue par la table de scan utilisée à Liverpool (qui est la table de scan de référence pour la collaboration AGATA). Pour essayer d'améliorer la sélection d'événements d'interactions singles, l'utilisation d'un second algorithme pour filtrer les données a été testée. Cet algorithme est en principe capable d'identifier des événements à plusieurs interactions à partir de la première dérivée des signaux, c'est à dire à partir des signaux de courant. Ces derniers présentent des sous-structures dont le nombre est proportionnel au nombre d'interactions réalisées dans un segment par le rayon gamma qui l'a produit. Toutefois cette méthode n'a pas prouvé son efficacité, car les sous-structures individuelles ne peuvent être distinguées que quand les interactions des rayons gamma sont bien espacées les unes des autres ($\sim 10mm$). De plus, le bruit du signal de courant est important. Il est donc nécessaire que les dépôts d'énergie en chaque point d'interaction soit élevé pour pouvoir les identifier.

Puisqu'il n'est pas possible de rejeter les événements d'interactions multiples, l'étude suivante a consisté à caractériser ces événements et à déterminer leur possible influence sur la forme d'impulsion moyenne en chaque point de la grille de scan. Pour les événements de diffusion multiple sélectionnés par χ^2, l'analyse montre que les interactions sont relativement proches et que la valeur moyenne de leur distance au point de la grille de scan considérée est comparable à la résolution spatiale du détecteur après analyse des formes d'impulsion et tracking gamma. Pour cette raison, les signaux d'interactions multiples sélectionnés par la technique PSCS sont similaires à ceux d'interactions single. S'il n'est pas possible de nettoyer la base de données des signaux d'interactions multi-

ples, ces derniers ne la contaminent pas. De plus, les simulations indiquent que, pour un événement de diffusion multiple, le dépôt d'énergie du point d'interaction le plus éloigné de la première interaction diminue quand la distance entre ces deux points augmente. Généralement, la plus grande libération d'énergie se produit au voisinage de la première interaction où la majeure partie du signal est générée. Ainsi, un événement de diffusion multiple dont la forme d'impulsion correspond à la somme des impulsions générées en chacun de ses points, pondérée par l'énergie partielle déposée en chaque point, présente une réponse très voisine de celle d'une interaction unique. Enfin, la base de données obtenue par la technique PSCS est comparée à la base de données théorique calculée avec ADL aux mêmes points de la grille de scan. La comparaison porte sur la différence maximale d'amplitude calculée échantillon par échantillon entre un signal obtenu avec la technique PSCS et le signal correspondant de la base de données théorique. L'analyse a montré que les deux bases de données sont pour la plupart en accord, sauf le long des lignes et surfaces de segmentation où des effets de bord sont causés par la technique PSCS. En conclusion, on peut considérer que la technique PSCS appliquée au détecteur planaire est fiable.

Comme indiqué précédemment, la même analyse a été répétée avec le détecteur AGATA de type S. Le scan est également effectué au pas de $2\,mm$ et l'énergie des rayons gamma utilisée est de $662\,keV$ (source de césium). Les résultats obtenus ont prouvé, une fois encore, l'efficacité de la technique PSCS appliquée à un détecteur sensible à la position. En général, les valeurs des paramètres obtenus pour le détecteur de type S indiquent que la technique PSCS est plus performante que pour le détecteur planaire segmenté. En particulier, le taux d'événements single sélectionné est en moyenne de $\sim 50\%$ (55% à l'avant du détecteur et 45% à l'arrière) à comparer à 21% pour le détecteur planaire. La cause peut être attribuée à la complexité accrue de la géométrie de segmentation du détecteur, qui offre par conséquent une meilleure résolution spatiale.

En prévision de la modification du collimateur (trous de collimation de $1.0\,mm$, $0.5\,mm$ et $0.2\,mm$) et de l'utilisation d'une source de ^{152}Eu, des simulations supplémentaires sur le détecteur de type S ont permis d'étendre l'analyse de l'efficacité de la technique PSCS. En particulier, l'impact de l'énergie des rayons gamma et du nombre d'événements utilisés pour la sélection de type χ^2 sur le résultat final de la technique PSCS a été examiné à $122\,keV$, $344\,keV$, $779\,keV$ et $1408\,keV$. L'analyse a montré que l'énergie du rayonnement gamma a un impact non négligeable sur la sélection des interaction single et a peu d'effet sur la distance des interactions du point de la base de données considéré, mais il n'a pratiquement aucun impact sur la comparaison des bases de données. L'impact de la statistique d'entrée a également été analysée en utilisant 1000, 6000 et 60000 événements, pour chaque jeu de données V et H, pour la procédure de χ^2. Le nombre d'événements utilisés a, en effet, un impact sur la sélection. La technique PSCS est généralement plus performante lorsque la statistique d'entrée est plus élevée. Cependant, la comparaison entre la base de données calculée par PSCS et la base théorique calculée via ADL, effectuée en extrayant le maximum de résidus entre les signaux des deux bases des données, ne semble pas dépendre de ce paramètre.

Parallèlement aux simulations, de vrais scans ont été réalisés avec le détecteur AGATA de type S, S001. Ce détecteur est un cristal quasi-coaxial de grande taille

(longueur de $9\,cm$ et diamètre de $8\,cm$) biseauté à l'avant pour prendre une forme hexagonale symétrique. Le trou central s'arrête à $13\,mm$ de la face avant du cristal. Le contact central diffusé au Li collecte toute l'énergie déposée dans le cristal. C'est le "core". Le contact externe implanté au B est segmenté électriquement en 6 tranches et 6 secteurs (36 segments). Le but de cette analyse était de tester la technique PSCS réalisée avec une source de ^{152}Eu et de prouver, en comparant différentes bases de données obtenues à différentes énergies gamma, que les formes d'impulsions ne dépendent pas de l'énergie d'interaction qui les génère. Une première caractérisation du détecteur a été réalisée par des scans 2D avec les sources ^{241}Am, ^{137}Cs et ^{152}Eu. Divers paramètres ont été extraits des mesures et discutés comme la distribution de l'efficacité locale, l'orientation de l'axe du réseau cristallin, les distributions du centroïde du pic de pleine énergie et de la largeur à mi-hauteur (FWHM) de ce pic. Les distributions des centroïdes de pic et de leur FWHM mesurées avec le contact "core" montrent le piégeage bien connu des électrons qui se produit dans les détecteurs de type n. Étonnamment, les mêmes distributions obtenues à partir des contacts des segments présentent une tendance similaire à laquelle on ne s'attendait pas. Cela peut être dû au temps d'intégration assez court ($5.95\,\mu s$) des 36 voies d'amplification numérique TNT2 utilisé pour les mesures. En outre, les distributions des centroïdes de pic et des FWHM ont incité à une analyse plus approfondie des propriétés de collection des charges du détecteur car une zone défectueuse s'étendant sur les segments F2, F3 et F4 avait été identifiée. En effet, dans l'ensemble du cristal, les spectres en énergie obtenus avec le faisceau gamma collimaté présentent des pics Gaussiens alors que, dans la zone incriminée, ils exhibent de grandes queues vers les basses énergies. Or les modèles macroscopiques de piégeage des porteurs de charges prévoient des pics Gaussiens dans le cas d'un faisceau collimaté. Pour comprendre ce comportement singulier, les propriétés de collection des charges de cette zone ont été analysées plus en détail et une hypothèse sur la nature du phénomène a été émise. Cette forme de pic inhabituelle a été interprétée comme la conséquence de la présence d'un second type de pièges à électrons, fortement concentrés, situés dans un plan fin de moins de $1.5\,mm$ d'épaisseur. Il s'étend du trou central jusqu'à une valeur de rayon d'environ $20\,mm$. Cette analyse montre la sensibilité de la technique de balayage utilisée et l'intérêt des scans 2D. Enfin, les scans 2D ont permis de mesurer certaines caractéristiques structurelles du détecteur, telles que la largeur des lignes de segmentation à l'avant du détecteur ($668 \pm 6\,\mu m$), le diamètre du trou central ($14.1 \pm 0.2\,mm$), la position des contacts et le câblage du détecteur (encore difficile à mettre en évidence). Ces mesures ont montré les capacités d'imagerie de la table de scan de l'IPHC. Par la suite, des scans tridimensionnels ont été effectués avec les sources ^{137}Cs et ^{152}Eu. En raison de l'activité limitée de la source en regard des petits diamètre des collimateurs, le scan à l'europium a été limité à un secteur du détecteur (secteur B). Ces données ont permis de construire en une seule mesure quatre bases de données de formes d'impulsions correspondant chacune à une énergie différente, $122\,keV$, $344\,keV$, $779\,keV$ et $1408\,keV$. Le scan au césium a permis de construire une base de données de référence à l'énergie de $662\,keV$. Une comparaison a été faite entre ces bases de données, et la valeur résiduelle maximale entre deux signaux associés au même point de la base de données a été choisie comme paramètre de comparaison. Les bases de données ayant une énergie $> 500\,keV$

se sont avérées comparables entre elles, les différences variant sur la longueur du cristal en moyenne d'environ 2% à l'avant, environ 3% dans le corps du cristal et jusqu'à 6% à l'arrière. Des divergences ont par contre été constatées avec la base de données de $344\,keV$ pour les valeurs le long de l'axe du crystal supérieures à $40\,mm$. Les valeurs résiduelles semblaient diverger d'un facteur 2 vers l'arrière du détecteur. Enfin, la base de données à $122\,keV$ s'est avérée très divergente des autres bases de données. Il a été supposé que les raisons de ces comportements divergeants sont à attribuer à la technique PSCS qui n'est pas efficace aux basses énergies, puisque la petite amplitude des signaux induits est fortement affectée par le bruit du signal.

L'analyse, résumée ci-dessus, ouvre de nouvelles perspectives et possibilités de recherche, tant pour les simulations que pour les mesures. Les limites du PSCS indiquées dans ce travail peuvent être surmontées en proposant des améliorations pour le PSA. En s'inspirant de travaux récents, des mesures différentes peuvent être prises en compte pour l'algorithme de sélection des impulsions. La formule de type χ^2 deviendrait alors χ^α où α est une valeur qui peut être optimisée afin de maximiser la fraction des interactions individuelles sélectionnées et, dans le cas d'interactions multiples, de minimiser la distance moyenne des points d'interaction par rapport à la position correspondante dans la base de données. Une autre façon d'améliorer la sélection χ^2 pourrait être l'utilisation de poids pour les signaux induits afin de leur donner plus ou moins d'impact sur la construction de la base de données. En outre, l'utilisation de techniques de filtrage du bruit, telles que la réduction du bruit par transformée de Fourier, pourrait être évaluée, en particulier pour les impulsions de faible énergie où le PSCS semble être plus affecté. Si ces techniques permettent d'améliorer la technique du PSCS, elles peuvent être appliquées à des mesures réelles pour vérifier si les écarts constatés entre les bases de données d'énergies différentes sont réduits.

Afin de permettre des mesures à basse énergie dans un volume de secteur complet en utilisant la source d'europium, une configuration horizontale-horizontale pourrait être testée. Elle permettrait de réduire les problèmes de statistique pour les faisceaux de rayons gamma de basse énergie vers l'arrière du détecteur.

Enfin, il serait intéressant de comparer les bases de données obtenues par la table de scan de l'IPHC avec celles d'autres tables de scan exploitées par la collaboration AGATA en utilisant la même capsule montée dans un cryostat d'essai donné.

Les mesures effectuées avec la source d'europium ont mis en évidence la nécessité d'acheter des sources de plus petit diamètre ($1\,mm$ ou moins à comparer à $3\,mm$ pour les sources actuelles) plus compatibles avec le diamètre des nouveaux collimateurs. En conservant la même activité de source, un scan à l'europium serait accéléré d'un facteur 10 environ, ce qui rendrait les mesures aussi rapides que les scans actuels au césium. Grâce à ces sources de rayons gamma plus compactes, d'autres tests pourraient être effectués en utilisant la nouvelle configuration de la table de scan. En particulier, la source d'europium combinée à la collimation fine des rayons gamma ($0.5\,mm$ et $0.2\,mm$) pourrait être utilisée pour déterminer l'impact éventuel du nuage de porteurs de charge, produit par un rayon gamma en interaction, sur la forme des impulsions. En outre, il serait possible d'extraire de mesures spécifiques à travers une ligne de segmentation, la taille du nuage de porteurs de charge qui est censée varier avec l'énergie des rayons

gamma. Cette étude peut être réalisée en conjonction avec des calculs spécifiques. De plus, des collimateurs plus fins pourraient être utilisés pour effectuer une analyse approfondie du comportement des porteurs de charge dans un grand détecteur HPGe comme la zone anormale dans S001. Enfin, la table de scan peut certainement être utilisée pour réaliser un travail de R&D sur des détecteurs sensibles à la position. Par exemple, l'impact de géométries et de segmentations plus exotiques sur la sensibilité spatiale du détecteur, les effets de surface et dans le volume du cristal de nouveaux traitements de surface, l'identification spatiale et la caractérisation de zones de collection de charges dégradée dans un cristal défectueux.

Bibliography

[1] E. M. Pell. Ion Drift in an n-p Junction. *Journal of Applied Physics*, 31(2):291–302, 1960.

[2] D. V. Freck and J. Wakefield. Gamma-Ray Spectrum obtained with a Lithium-drifted p-i-n Junction in Germanium. *Nature*, 193(4816):669–669, 1962.

[3] R. N. Hall and T. J. Soltys. High Purity Germanium for Detector Fabrication. *IEEE Transactions on Nuclear Science*, 18(1):160–165, 1971.

[4] W.L. Hansen. High-purity germanium crystal growing. *Nuclear Instruments and Methods*, 94(2):377 – 380, 1971.

[5] R. Beetz, et al. An in-beam Ge(Li)-NaI(Tl) Compton suppression spectrometer. *Nuclear Instruments and Methods*, 145(2):353 – 357, 1977.

[6] H.J.M. Aarts, et al. A Compton-suppression spectrometer for gamma-gamma coincidence measurements: Large solid angle and excellent suppression. *Nuclear Instruments and Methods*, 177(2):417 – 425, 1980.

[7] R.M. Diamond and F.S.A. Stephens. Proposal for a high resolution ball, LBNL (unpublished).

[8] R.M. Diamond. Proc. Conf. on Instr. for Heavy Ion Nucl. Res., in: D. Schapira (ed.), Nucl. Sci. Research Conf. Series, vol. 7, Harwood, p. 259.

[9] J.F. Sharpey-Schafer and J. Simpson. Escape suppressed spectrometer arrays: A revolution in gamma-ray spectroscopy. *Progress in Particle and Nuclear Physics*, 21:293 – 400, 1988.

[10] C.W. Beausang, et al. Measurements on prototype Ge and BGO detectors for the EUROGAM array. *Nuclear Instruments and Methods in Physics Research Section A: Accelerators, Spectrometers, Detectors and Associated Equipment*, 313(1):37 – 49, 1992.

[11] D. Bazzacco. Proc. Workshop on Large gamma-ray Detector Arrays, Chalk River, Canada, AECL-10613, p. 376.

[12] R.M. Diamond M.A. Deleplanque. (Eds.) Gammasphere Proposal, 1987. Preprint LBNL-5202.

[13] G. Duchêne, et al. The Clover: a new generation of composite Ge detectors. *Nuclear Instruments and Methods in Physics Research Section A: Accelerators, Spectrometers, Detectors and Associated Equipment*, 432(1):90 – 110, 1999.

[14] J. Eberth, et al. Encapsulated Ge detectors: Development and first tests. *Nuclear Instruments and Methods in Physics Research Section A: Accelerators, Spectrometers, Detectors and Associated Equipment*, 369(1):135 – 140, 1996.

[15] F.A. Beck. EUROBALL: Large gamma ray spectrometers through european collaborations. *Progress in Particle and Nuclear Physics*, 28:443 – 461, 1992.

[16] R.M. Lieder J. Gerl. (Eds.) Upgrading to Euroball III, GSI Report, 1992.

[17] J. Simpson. The EUROBALL spectrometer. *Zeitschrift für Physik A Hadrons and Nuclei*, 358(2):139–143, 1997.

[18] J. Eberth, et al. MINIBALL A Ge detector array for radioactive ion beam facilities. *Progress in Particle and Nuclear Physics*, 46(1):389 – 398, 2001.

[19] D. Habs, et al. Physics with Ge-Miniball-arrays. *Progress in Particle and Nuclear Physics*, 38:111 – 126, 1997. 4 pi High Resolution Gamma Ray Spectroscopy and Nuclear Structure.

[20] J. Simpson, et al. The EXOGAM array: A radioactive beam gamma-ray spectrometer. *Acta Physica Hungarica, Series A: Heavy Ion Physics*, 11(1-2):159–188, 2000.

[21] W.F. Mueller, et al. Thirty-two-fold segmented germanium detectors to identify gamma-rays from intermediate-energy exotic beams. *Nuclear Instruments and Methods in Physics Research Section A: Accelerators, Spectrometers, Detectors and Associated Equipment*, 466(3):492 – 498, 2001.

[22] S. Akkoyun, et al. AGATA-Advanced GAmma Tracking Array. *Nuclear Instruments and Methods in Physics Research Section A: Accelerators, Spectrometers, Detectors and Associated Equipment*, 668:26 – 58, 2012.

[23] I.Y. Lee, et al. GRETINA: A gamma ray energy tracking array. *Nuclear Physics A*, 746:255 – 259, 2004. Proceedings of the Sixth International Conference on Radioactive Nuclear Beams (RNB6).

[24] M. Ginsz. *Characterization of high-purity, multi-segmented germanium detectors.* Ph.D. thesis, University of Strasbourg, 2015.

[25] M.H. Sigward, et al. Pulse-Shape Comparison Scan of germanium detectors using the IPHC scanning table. To be published.

[26] NIST XCOM photon cross sections database (2019).

[27] G. F. Knoll. *Radiation detection and measurement*. John Wiley and sons, third edition, 2000.

[28] W. R. Leo. *Techniques for nuclear and particle physics experiments*. Springer-Verlag, second edition edition, 1994.

[29] L. Milhailescu. *Principles and Methods for gamma ray tracking with large volume Germanium Detectors*. Ph.D. thesis, University of Bonn, 2000.

[30] W. Shockley. Currents to conductors induced by a moving point charge. *Journal of Applied Physics*, 9:365–363, 1938.

[31] S. Ramo. Currents induced by electron motion. *Proceedings of the I.R.E.*, 27:584–585, 1939.

[32] Zhong He. Review of the Shockley-Ramo theorem and its application in semiconductor gamma-ray detectors. *Nuclear Instruments and Methods in Physics Research Section A: Accelerators, Spectrometers, Detectors and Associated Equipment*, 463(1):250 – 267, 2001.

[33] D. Gutknecht. *Phénoménes de capture des porteurs de charge dans les détecteurs au germanium compensé au lithium*. Ph.D. thesis, ULP Strasbourg (University of Strasbourg), 1971.

[34] Thomas W. Raudorf and Richard H. Pehl. Effect of charge carrier trapping on germanium coaxial detector line shapes. *Nuclear Instruments and Methods in Physics Research Section A: Accelerators, Spectrometers, Detectors and Associated Equipment*, 255(3):538 – 551, 1987.

[35] Korten, W., et al. Physics opportunities with the Advanced Gamma Tracking Array: AGATA. *Eur. Phys. J. A*, 56(5):137, 2020.

[36] I-Yang Lee. The GAMMASPHERE. *Nuclear Physics A*, 520:c641 – c655, 1990. Nuclear Structure in the Nineties.

[37] E. Farnea, et al. Conceptual design and Monte Carlo simulations of the AGATA array. *Nuclear Instruments and Methods in Physics Research Section A: Accelerators, Spectrometers, Detectors and Associated Equipment*, 621(1):331 – 343, 2010.

[38] The AGATA collaboration. AGATA TDR (phase 1). Technical report, 2008.

[39] Andreas Wiens, et al. The AGATA triple cluster detector. *Nuclear Instruments and Methods in Physics Research Section A: Accelerators, Spectrometers, Detectors and Associated Equipment*, 618(1):223 – 233, 2010.

[40] A. Pullia, et al. An advanced preamplifier for highly segmented germanium detectors. *IEEE Transactions on Nuclear Science*, 53(5):2869–2875, 2006.

[41] G. Pascovici, et al. Low noise, dual gain preamplifier with built in spectroscopic pulser for highly segmented high-purity germanium detectors. *WSEAS Trans. Cir. and Sys.*, 7(6):470–481, 2008.

[42] Francesca Zocca, et al. A time-over-threshold technique for wide dynamic range gamma-ray spectroscopy with the AGATA detector. *Nuclear Science, IEEE Transactions on*, 56:2384 – 2391, 2009.

[43] Valentin T. Jordanov, et al. Digital techniques for real-time pulse shaping in radiation measurements. *Nuclear Instruments and Methods in Physics Research Section A: Accelerators, Spectrometers, Detectors and Associated Equipment*, 353(1):261 – 264, 1994.

[44] A. Georgiev, et al. An analog-to-digital conversion based on a moving window deconvolution. *IEEE Transactions on Nuclear Science*, 41(4):1116–1124, 1994.

[45] R. Venturelli. and D. Bazzaco. Adaptive grid search as pulse shape analysis algorithm for gamma-tracking and results. *LNL Annual Report*, page 200, 2004.

[46] M. Schlarb, et al. Pulse shape analysis for gamma-ray tracking (Part I): Pulse shape simulation with JASS. *The European Physical Journal A*, 47(10):132–, 2011.

[47] A. Olariu, et al. Pulse shape analysis for the location of the gamma-interactions in gamma. *Nuclear Science, IEEE Transactions on*, 53:1028 – 1031, 2006.

[48] Th. Kröll and D. Bazzacco. A genetic algorithm for the decomposition of multiple hit events in the gamma-ray tracking detector MARS. *Nuclear Instruments and Methods in Physics Research Section A: Accelerators, Spectrometers, Detectors and Associated Equipment*, 565(2):691 – 703, 2006.

[49] F. Crespi, et al. A pulse shape analysis algorithm for HPGe detectors. *Nuclear Instruments and Methods in Physics Research Section A-accelerators Spectrometers Detectors and Associated Equipment*, 570:459–466, 2007.

[50] A. Lopez-Martens, et al. Gamma-ray tracking algorithms: a comparison. *Nuclear Instruments and Methods in Physics Research Section A: Accelerators, Spectrometers, Detectors and Associated Equipment*, 533(3):454 – 466, 2004.

[51] G. Suliman and D. Bucurescu. Fuzzy clustering algorithm for gamma ray tracking in segmented detectors. *Romanian Reports in Physics*, 62:27–36, 2010.

[52] F. Didierjean, et al. The Deterministic Annealing Filter: A new clustering method for gamma-ray tracking algorithms. *Nuclear Instruments and Methods in Physics Research Section A: Accelerators, Spectrometers, Detectors and Associated Equipment*, 615:188–200, 2010.

[53] S. Tashenov and J. Gerl. Tango - new tracking algorithm for gamma-rays. *Nuclear Instruments and Methods in Physics Research Section A Accelerators Spectrometers Detectors and Associated Equipment*, 622:592–601, 2010.

[54] F. Recchia, et al. Position resolution of the prototype AGATA triple-cluster detector from an in-beam experiment. *Nuclear Instruments and Methods in Physics Research Section A: Accelerators, Spectrometers, Detectors and Associated Equipment*, 604(3):555 – 562, 2009.

[55] P.-A. Soederstroem, et al. Interaction position resolution simulations and in-beam measurements of the AGATA HPGe detectors. *Nuclear Instruments and Methods in Physics Research Section A: Accelerators, Spectrometers, Detectors and Associated Equipment*, 638(1):96 – 109, 2011.

[56] B. Bruyneel, et al. Pulse shape analysis and position determination in segmented HPGe detectors: The AGATA detector library. *The European Physical Journal A*, 52(3):70–, 2016.

[57] W. Korten and The AGATA Collaboration. Annexe of AGATA white book, unpublished, private communication. 2020.

[58] J. Eberth and J. Simpson. From Ge(Li) detectors to gamma-ray tracking arrays-50 years of gamma spectroscopy with germanium detectors. *Progress in Particle and Nuclear Physics*, 60(2):283 – 337, 2008.

[59] Matthew Dimmock, et al. Validation of Pulse Shape Simulations for an AGATA prototype detector. *Nuclear Science, IEEE Transactions on*, 56:2415 – 2425, 2009.

[60] T.M.H. Ha, et al. New setup for the characterisation of the AGATA detectors. *Nuclear Instruments and Methods in Physics Research Section A: Accelerators, Spectrometers, Detectors and Associated Equipment*, 697:123 – 132, 2013.

[61] N. Goel, et al. Spatial calibration via imaging techniques of a novel scanning system for the pulse shape characterisation of position sensitive HPGe detectors. *Nuclear Instruments and Methods in Physics Research Section A: Accelerators, Spectrometers, Detectors and Associated Equipment*, 652(1):591 – 594, 2011. Symposium on Radiation Measurements and Applications (SORMA) XII 2010.

[62] A. Hernandez-Prieto, et al. Study of accuracy in the position determination with SALSA, a gamma-scanning system for the characterization of segmented HPGe detectors. *Nuclear Instruments and Methods in Physics Research Section A: Accelerators, Spectrometers, Detectors and Associated Equipment*, 823:98 – 106, 2016.

[63] F.C.L. Crespi, et al. A novel technique for the characterization of a HPGe detector response based on pulse shape comparison. *Nuclear Instruments and Methods in Physics Research Section A: Accelerators, Spectrometers, Detectors and Associated Equipment*, 593(3):440 – 447, 2008.

[64] L. Lewandowski, et al. Pulse-Shape Analysis and position resolution in highly segmented HPGe AGATA detectors. *The European Physical Journal A*, 55(5):81–, 2019.

[65] L. Arnold, et al. TNT Digital Pule Processor. In *14th IEEE-NPSS Real Time Conference, 2005.*, pages 265–269. 2005.

[66] AGAPRO section on the GSI forum `https://forum.gsi.de/index.php?t=thread&frm_id=219&rid=0`.

[67] Geant4 `https://geant4.web.cern.ch/`.

[68] The Lund/LBNL table of isotopes. `http://nucleardata.nuclear.lu.se/toi/`.

[69] P. Medina, et al. A simple method for the characterization of HPGe detectors. *Conference Record - IEEE Instrumentation and Measurement Technology Conference*, 3:1828 – 1832 Vol.3, 2004.

[70] SIMION `https://simion.com/`.

[71] Bart Bruyneel, et al. Characterization of large volume HPGe detectors. Part I: Electron and hole mobility parameterization. *Nuclear Instruments and Methods in Physics Research Section A: Accelerators, Spectrometers, Detectors and Associated Equipment*, 569(3):764 – 773, 2006.

[72] M. J. Oreglia. *A study of the reactions psi prime*. Ph.D. thesis, SLAC-R-236, 1980.

[73] B. Bruyneel, et al. Correction for hole trapping in AGATA detectors using pulse shape analysis. *The European Physical Journal A*, 49(5):61–, 2013.

[74] COMSOL `https://www.comsol.com/`.

[75] R.J. Cooper, et al. A novel HPGe detector for gamma-ray tracking and imaging. *Nuclear Instruments and Methods in Physics Research Section A: Accelerators, Spectrometers, Detectors and Associated Equipment*, 665:25 – 32, 2011.

[76] J.B. Marion and F.C. Young. *Nuclear Reaction Analysis*. North-Holland Publishing Co., 1968.

[77] L. Mihailescu, et al. The influence of anisotropic electron drift velocity on the signal shapes of closed-end HPGe detectors. *Nucl. Instrum. Meth. A*, 447:350–360, 2000.

[78] M. Moszynski and G. Duchêne. Ballistic deficit correction methods for large Ge detectors. *Nuclear Instruments and Methods in Physics Research Section A: Accelerators, Spectrometers, Detectors and Associated Equipment*, 308(3):557 – 567, 1991.

UNIVERSITÉ DE STRASBOURG

Bartolomeo DE CANDITIIS

École doctorale
Physique, chimie-physique
ED 182
Université de Strasbourg

Caractérisation 3D de détecteurs germanium hyper purs multi-segmentés – Simulation et validation de la technique de PSCS et son application à diverses énergies gamma à l'aide d'une source de ^{152}Eu

Les ensembles de détecteurs de rayon gamma de nouvelle génération, tel AGATA, utilisent des détecteurs multi-segmentés de germanium hyper-pur dans les expériences de physique nucléaire pour lesquelles une grande résolution et efficacité sont demandées. Ces caractéristiques sont obtenues par l'application des techniques d'analyse des formes d'impulsion et de tracking des rayons gamma. Ces dernières demandent une caractérisation volumétrique des détecteurs. À cet effet, l'IPHC a développé une table de scan qui utilise la technique Pulse Shape Comparison Scan (PSCS). Des simulations sont réalisées pour quantifier la précision de la technique PSCS et pour la valider. Elles sont appliquées sur un détecteur planaire pixelisé 3x3 et sur un détecteur symétrique d'AGATA de type S. La méthode est testée avec plusieurs énergies de rayons gamma et diverses statistiques d'entrée. Des scans réels sont aussi entrepris sur les deux détecteurs, qui sont totalement caractérisés. En particulier, un scan réalisé pour la première fois avec une source de rayons gamma de ^{152}Eu, prouve la validité de certaines hypothèses sur lesquelles repose la technique de tracking.

Mots clé: spectroscopie gamma, détecteurs germanium hyper pur, table de scan, analyse de formes de impulsion, multi-détecteur AGATA, caractérisation de détecteurs, technique PSCS.

New generation gamma-ray detectors arrays, such as AGATA, employ multi-segmented high purity germanium detectors in experiments of nuclear physics that require high resolution and efficiency which are obtained thanks to the application of pulse-shape analysis and gamma-ray tracking. These techniques require full volume characterization of the position sensitive detectors. The IPHC developed a scanning table that uses the Pulse Shape Comparison Scan (PSCS) technique to perform this task. Simulations are performed to quantify the accuracy of the PSCS and to validate it. They are applied on a pixelated 3x3 planar detector and a symmetrical S-type AGATA detector. The method is tested with different gamma-ray energies and input statistics. Several real scans are performed as well on both detectors, which are fully characterized. In particular a scan with a gamma-ray source of ^{152}Eu, the first ever done, prove some assumptions on which the tracking technique is based.

Keywords: gamma-ray spectroscopy, high purity germanium detectors, scanning table, pulse-shape analysis, AGATA array, detector characterization, PSCS technique.